



TEZ ŞABLONU ONAY FORMU
THESIS TEMPLATE CONFIRMATION FORM

1. Şablonda verilen yerleşim ve boşluklar değiştirilmemelidir.
2. Jüri tarihi Başlık Sayfası, İmza Sayfası, Abstract ve Öz'de ilgili yerlere yazılmalıdır.
3. İmza sayfasında jüri üyelerinin unvanları doğru olarak yazılmalıdır.
4. Tezin son sayfasının sayfa numarası Abstract ve Öz'de ilgili yerlere yazılmalıdır.
5. Bütün chapterlar, referanslar, ekler ve CV sağ sayfada başlamalıdır. Bunun için **kesmeler** kullanılmıştır. **Kesmelerin kayması** fazladan boş sayfaların oluşmasına sebep olabilir. Bu gibi durumlarda paragraf (¶) işaretine tıklayarak kesmeleri görünür hale getirin ve yerlerini **kontrol edin**.
6. Figürler ve tablolar kenar boşluklarına taşmamalıdır.
7. Şablonda yorum olarak eklenen uyarılar dikkatle okunmalı ve uygulanmalıdır.
8. Tez yazdırılmadan önce PDF olarak kaydedilmelidir. Şablonda yorum olarak eklenen uyarılar PDF dokümanında yer almamalıdır.
9. **Bu form aracılığıyla oluşturulan PDF dosyası arkalı-önlü baskı alınarak tek bir spiralli cilt haline getirilmelidir.**
10. Spiralli hale getirilen tez taslağınızdaki ilgili alanları imzalandıktan sonra, [Tez Jüri Atama Formu](#) ile birlikte bölüm sekreterliğine teslim edilmelidir.
11. Tez taslağınız bölüm sekreterliğiniz aracılığıyla format ve görünüm açısından kontrol edilmek üzere FBE'ye ulaştırılacaktır.
12. FBE tarafından kontrol işlemleri tamamlanan tez taslakları, öğrencilere teslim edilmek üzere bölüm sekreterliklerine iletilecektir.
13. Tez taslaklarının kontrol işlemleri tamamlandığında, bu durum öğrencilere METU uzantılı öğrenci e-posta adresleri aracılığıyla duyurulacaktır.
14. Tez taslakları bölüm sekreterlikleri tarafından öğrencilere iletileceği için öğrencilerimizin tez taslaklarını enstitümüzden elden alma konusunda ısrarcı olmamaları beklenmektedir.
15. Tez yazım süreci ile ilgili herhangi bir sıkıntı yaşarsanız, [Sıkça Sorulan Sorular \(SSS\)](#) sayfamızı ziyaret ederek yaşadığınız sıkıntıyla ilgili bir çözüm bulabilirsiniz.

1. Do not change the spacing and placement in the template.
2. Write defense date to the related places given on Title page, Approval page, Abstract and Öz.
3. Write the titles of the examining committee members correctly on Approval Page.
4. Write the page number of the last page in the related places given on Abstract and Öz pages.
5. All chapters, references, appendices and CV must be started on the right page. **Section Breaks** were used for this. **Change in the placement** of section breaks can result in extra blank pages. In such cases, make the section breaks visible by clicking paragraph (¶) mark and **check their position**.
6. All figures and tables must be given inside the page. Nothing must appear in the margins.
7. All the warnings given on the comments section through the thesis template must be read and applied.
8. Save your thesis as pdf and Disable all the comments before taking the printout.
9. **Print two-sided the PDF file that you have created through this form and make a single spiral bound.**
10. Once you have signed the relevant fields in your thesis draft that you spiraled, submit it to the department secretary together with your [Thesis Jury Assignment Form](#).
11. Your thesis draft will be delivered to the GSNAS via your department secretary for controlling in terms of format and appearance.
12. The thesis drafts that are controlled by GSNAS, will be sent to the department secretary to be delivered to the students.
13. This will be announced to the students via their METU students e-mail addresses when the control of the thesis drafts has been completed.
14. As the thesis drafts will be delivered to the students by the department secretaries, we are expecting from our students no to insist about getting their theses drafts from the Institute.
15. If you have any problems with the thesis writing process, you may visit our [Frequently Asked Questions \(FAQ\)](#) page and find a solution to your problem.

Yukarıda bulunan tüm maddeleri okudum, anladım ve kabul ediyorum. / I have read, understand and accept all of the items above.

Name : Atalay
Surname : Çalışan
E-Mail : e149526@metu.edu.tr
Date : 04.03.2020
Signature : _____

SUSTAINABLE HYDROGEN PRODUCTION PROCESS DEVELOPMENT
USING REDUCIBLE OXIDES

A THESIS SUBMITTED TO
THE GRADUATE SCHOOL OF NATURAL AND APPLIED SCIENCES
OF
MIDDLE EAST TECHNICAL UNIVERSITY

BY

ATALAY ÇALIŞAN

IN PARTIAL FULFILLMENT OF THE REQUIREMENTS
FOR
THE DEGREE OF DOCTOR OF PHILOSOPHY
IN
CHEMICAL ENGINEERING

FEBRUARY 2020

Approval of the thesis:

**SUSTAINABLE HYDROGEN PRODUCTION PROCESS DEVELOPMENT
USING REDUCIBLE OXIDES**

submitted by **ATALAY ÇALIŞAN** in partial fulfillment of the requirements for the degree of **Doctor of Philosophy in Chemical Engineering, Middle East Technical University** by,

Prof. Dr. Halil Kalıpçılar
Dean, Graduate School of **Natural and Applied Sciences**

Prof. Dr. Pınar Çalık
Head of the Department, **Chemical Engineering**

Prof. Dr. Deniz Üner
Supervisor, **Chemical Engineering, METU**

Examining Committee Members:

Prof. Dr. Saim Özkar
Chemistry, METU

Prof. Dr. Deniz Üner
Chemical Engineering, METU

Assoc. Prof. Dr. Alper Uzun
Chemical and Biological Eng., Koç University

Prof. Dr. Süleyman Ali Tuncel
Chemical Eng., Hacettepe University

Asist. Prof. Dr. Bahar İpek
Chemical Eng., METU

Date: 07.02.2020

I hereby declare that all information in this document has been obtained and presented in accordance with academic rules and ethical conduct. I also declare that, as required by these rules and conduct, I have fully cited and referenced all material and results that are not original to this work.

Name, Last name : Atalay Çalışan

Signature :

ABSTRACT

SUSTAINABLE HYDROGEN PRODUCTION PROCESS DEVELOPMENT USING REDUCIBLE OXIDES

Çalışan, Atalay
Doctor of Philosophy, Chemical Engineering
Supervisor : Prof. Dr. Deniz Üner

February 2020, 306 pages

The energy demand is driven by increasing world population and living standards. Sustaining this demand with available and renewable energy sources is a major challenge. The options such as solar and wind power, are unreliable for a steady energy production due to their intermittent nature. Therefore, the storage of renewable energy, such as hydrogen, gains importance. In the scope of this thesis, a sustainability barrier in front of solar integrated hydrogen production processes was addressed in terms of material development and energy utilization perspectives for the two step thermochemical cycles and methane reforming processes. From the material development perspective, thermodynamic analysis was performed for investigating the driving force towards metal oxygen bond breaking and bond formation. The effect of reaction control mechanisms on the processes is studied through temperature programmed experiments etc. Conducted experiments revealed that hydrogen yield (maximum 52.5 mL/g MO_x) was limited by heat and mass transfer resistances as well as a severe thermodynamic barrier in front of metal oxygen bond breaking. The studied red/ox couples were also investigated in conventional methane reforming process. Thereafter, solar energy integration to

methane reforming process was studied for sustaining reaction energy from solar. Simulations performed by ASPEN Plus revealed that the solar energy losses observed in a daily basis is overcome with an integrated combustion zone to solar reformer, so a unique hybrid process was proposed for uninterruptable hydrogen production. The demonstration of this proposed process under real environment was left as a future subject.

Keywords: Hydrogen, Reducible Oxides, Solar Energy Integration, Process Optimization

ÖZ

İNDİRGENEBİLİR OKSİTLER KULLANILARAK SÜRDÜRÜLEBİLİR HİDROJEN ÜRETİM SÜREÇLERİNİN GELİŞTİRİLMESİ

Çalışan, Atalay
Doktora, Kimya Mühendisliği
Tez Danışmanı: Prof. Dr. Deniz Üner

Şubat 2020, 306 sayfa

Enerjiye olan talep, yükselen dünya nüfusu ve yaşam standartları ile beraber artmaktadır. Bu talebi, uygun ve yenilenebilir enerji kaynakları ile karşılamak önemli bir problem olarak karşımıza çıkmaktadır. Güneş ya da rüzgar enerjisi gibi opsiyonlar, kesikli doğalarından dolayı sürekli enerji üretimi için uygun değildir. Bundan dolayı, yenilenebilir enerjinin hidrojen gibi yapılarda depolanması önem kazanmaktadır. Bu tez kapsamında, güneş enerjisi entegrasyonu ile hidrojen üretim teknolojilerinin önündeki sürdürülebilirlik bariyeri, iki aşamalı termokimyasal süreçler ve metan riformlama süreçleri için, malzeme geliştirme ve enerji kullanımı açılarından ele alındı. Malzeme geliştirme açısından, malzemelerin metal oksijen bağ yapma ve bağ kırmaya olan yönelimi, termodinamik analiz yardımıyla araştırıldı. Reaksiyon kontrol mekanizmalarının çalışılan süreçlere etkisi, sıcaklık programlı deneyler yardımıyla çalışıldı. Gerçekleştirilen deneyler sonucunda, hidrojen veriminin (maksimum 52.5 mL/g MO_x), ısı ve kütle transferi etkisinde olduğu kadar, metal oksijen bağ kırılmasının önündeki termodinamik bariyerin etkisinde de olduğu görüldü. Çalışılan indirgenebilir metal oksitler ayrıca konvansiyonel metan riformlama sürecinde de test edildi. Sonrasında, riformlama reaksiyonunun enerjisinin güneş enerjisinden karşılanması için, metan riformlama

sürecine güneş enerjisi entegrasyonu çalışıldı. ASPEN Plus yazılımı ile gerçekleştirilen simülasyonlar, güneş riformlama reaktörüne dahil edilecek bir yanma odası ile gün içerisindeki güneş enerjisi kayıplarının minimize edilebileceğini ortaya koydu. Böylece, kesintisiz hidrojen üretimi için eşsiz hibrit bir süre ortaya çıktı. Bu sürecin gerçek ortamda gösterimi gelecekteki çalışmalara bırakıldı.

Anahtar Kelimeler: Hidrojen, İndirgenabilir Oksitler, Güneş Enerji Entegrasyonu, Optimizasyon

To my son, ınar

ACKNOWLEDGMENTS

I would like to thank my supervisor Prof. Dr. Deniz Uner for providing and sustaining an environment where my ideas could flourish and where independence was encouraged. I am also grateful to Assoc. Prof. Dr. Serkan Kincal for his guidance during the period of his co-supervision.

I want to thank all former members of CACTUS Research Group. Main body of this thesis never will be theorized without their sleepless nights. I also wish to express my great appreciations to present members: Nevzat Can Aksu, Necip Berker Üner, Mustafa Yasin Aslan, Mert Mehmet Oymak, Veysi Halvacı, Deniz Kaya and Hale Ay. I would like to thank my bros; Güvenç Celal Oğulğöner, Turan Çağrı Arı, Görkem Türkili, İsmail Aydın and Mehmet Can Pakdil for never letting me down through my life.

The technical staff of our department Süleyman Nazif Kuşhan, Ertuğrul Özdemir, Adil Demir, Cemil Araçlı, Mustafa Cansuyu and İsa Çağlar were greatly appreciated for their expertise in reactor manufacturing.

My deepest gratitude, coming from my soul, are to my parents, my sister, and last but not the least to my wife, Deniz and my son, Çınar. Their unlimited love, support, and confidence in me throughout my life made me who I am now.

The Scientific and Research Council of Turkey (TUBITAK) are kindly acknowledged for the financial support through 1003 program (Project code: 213M006) and 2211-E PhD scholarship.

TABLE OF CONTENTS

ABSTRACT.....	v
ÖZ.....	vii
ACKNOWLEDGMENTS.....	x
TABLE OF CONTENTS.....	xi
LIST OF TABLES.....	xvi
LIST OF FIGURES.....	xvii
LIST OF ABBREVIATIONS.....	xxvii
CHAPTERS	
1 INTRODUCTION AND LITERATURE SURVEY.....	1
1.1 Energy.....	1
1.2 Thermochemical Water Splitting Processes.....	4
1.2.1 Two-Step Solar Thermochemical Cycles.....	5
1.2.2 Multi-Step Thermochemical Cycles.....	9
1.2.3 The Selection of Red/Ox Pairs.....	12
1.3 Steam Methane Reforming Technology.....	27
1.4 Hybrid Systems (Solar Reformers).....	31
1.4.1 Solar Energy Collectors and Reactors.....	33
1.4.2 Paul Scherrer Institute (PSI).....	34
1.4.3 German Aerospace Center (DLR).....	35
1.4.4 Nigata University Group.....	36
1.4.5 Tokyo Institute of Technology.....	38
1.4.6 Sandia National Laboratory.....	39

1.5	Thesis Statement.....	40
2	MATERIALS	41
2.1	Bulk Materials	41
2.2	Monolithic Samples.....	43
3	METHODS.....	45
3.1	Thermodynamics	45
3.1.1	Predominance Diagram.....	45
3.1.2	Gibbs Free Energy Minimization Analysis	46
3.2	Characterization.....	49
3.2.1	Thermogravimetric Analysis (TGA)	49
3.2.2	X-Ray Diffraction (XRD) Analysis	49
3.2.3	Surface Area Measurements	49
3.2.4	Temperature Programmed Reduction (TPR) Analysis.....	49
3.2.5	SEM Analysis	50
3.3	Instruments	50
3.3.1	Micromeritics Chemisorp 2720 Setup	50
3.3.2	Multi-Gas Analyzer	51
3.3.3	QMS 200 Mass Spectrometry Setup.....	52
3.4	Oxygen Exchange Tests	54
3.4.1	The Operating Procedure of Micromeritics Chemisorp 2720 for Thermal Stability Experiments	54
3.4.2	The Operating Procedure of Micromeritics Chemisorp 2720 for Heat Transfer Effect on Desorption and Adsorption Kinetics of Co_3O_4 and CeCoO_3	54
3.4.3	The Operating Procedure of Micromeritics Chemisorp 2720 for Film Mass Transfer Effect on Desorption and Adsorption Kinetics of Co_3O_4 and CeCoO_3	55

3.4.4	The Operating Procedure of Multi-Gas Analyzer for Thermal Stability Experiments	55
3.4.5	The Operating Procedure of Multi-Gas Analyzer for Heat Transfer Effect on Desorption Kinetics of CeFeO ₃	55
3.4.6	The Operating Procedure of Multi-Gas Analyzer for Pore Diffusion Effect on Desorption Kinetics of Co ₃ O ₄ and Co ₃ O ₄ doped Monolith	56
3.4.7	TGA Cyclic Analysis	56
3.5	Reaction Tests	57
3.5.1	Boat Reactors	57
3.5.2	Gas Bubbling Reactor	59
3.5.3	Surface Sweep Reactor.....	61
3.5.4	Reforming Experiments	61
3.6	The Concentrated Solar Energy Pilot Unit	64
3.7	Simulations	66
3.7.1	ASPEN Plus Process Built-in-Blocks	67
3.7.2	The Basis of Simulations.....	71
4	THERMODYNAMICS	75
4.1	Direct Decomposition of Water	75
4.2	Thermodynamics Behind the Two-Step Water Thermochemical Processes	76
4.2.1	Thermal Decomposition Thermodynamics	77
4.2.2	Oxidation Thermodynamics	81
4.3	Red/Ox Thermodynamics	83
4.4	Thermodynamic Efficiency of Solar Concentrators	95
5	EXPERIMENTAL FINDINGS	99
5.1	Oxygen Exchange Capability.....	99

5.1.1	Red/Ox Characteristics of Co_3O_4 as Reference Material.....	101
5.1.2	Red/ox Materials based on Perovskites; CeCoO_3 and CeFeO_3	108
5.1.3	The Effect of Heat Transfer on Oxygen Desorption and Adsorption Kinetics	116
5.1.4	Thermal Stability on Oxygen Desorption and Adsorption	120
5.2	Two-Step Thermochemical Water Splitting Cycles.....	136
5.2.1	The Performance of Co_3O_4 and 1.84% Pt- Co_3O_4 doped Monolith during Temperature Programmed Thermal Decomposition (TPtD) and Water Splitting (TPWS)	137
5.2.2	The Performance of 1% Pd- CeO_2 during TPtD and TPWS	138
5.2.3	The Performance of SCFM (6473) during TPtD and TPWS.....	145
5.2.4	The Performance of Pb at Molten State.....	148
5.3	Discussions on Hydrogen Production by Two-Step Thermochemical Water Splitting Processes.....	158
5.4	Reforming Tests	161
5.4.1	Ni- Al_2O_3 as Reference Case	161
5.4.2	The Effect of CeCoO_3 as Catalyst and Support.....	164
5.4.3	Steam Methane Reforming (SMR) Performance on Cyclic Conditions.	168
5.5	Pilot Plant Test	173
5.5.1	Characterization of Energy Utilized by Solar Concentration Plant	173
5.5.2	Steam Methane Reforming at Pilot Scale	180
5.6	Discussions on Solar Integrated Methane Reforming Process.....	192
6	OPTIMIZATION	195
6.1	Process Simulations for Solar Energy Integration to SMR Process.....	195
6.1.1	Base Simulations for SMR and ATR Process	195

6.1.2	Hybrid Solar-ATR Process Simulations	197
6.1.3	Application of Hybrid Reforming Process to Real Case Example	200
6.2	The Design of Sustainable Hydrogen Production Plant	208
7	SUMMARY	217
8	CONCLUSION	221
	REFERENCES	223
A.	A Brief Literature Survey on Red/Ox Couples	253
B.	The Operatong Procedures for Micromeritics Chemisorp 2720	267
C.	The Operating Procedures for Multi Gas Analyzer	270
D.	Ellingham Diagrams	275
E.	Coke Removal Algorithm	302
	CURRICULUM VITAE	305

LIST OF TABLES

TABLES

Table 1.1 Sustainable hydrogen production options	4
Table 1.2 Water splitting and thermal decomposition data for some metal/metal oxide pairs	7
Table 1.3 Multicycle thermochemical cycles [68]	10
Table 1.4 Reaction pathways for two step thermochemical cycles.....	11
Table 1.5 Hydrogen yields of perovskites during thermochemical water splitting processes.....	26
Table 1.6 Reaction enthalpies of methane reforming reactions	27
Table 3.1 ΔH° (kJ/mol) and ΔG° (kJ/mol) values for reactions between Pb, PbO, O ₂ , and H ₂ O [277].....	48
Table 3.2 Simulation parameters for SMR and ATR processes.....	73
Table 4.1 Categorized metals for solar thermal hydrogen production in terms of thermodynamic driving force	87
Table 4.2 The possible combination of the candidate materials	94
Table 5.1 Curve fitting parameters for TPR of Co ₃ O ₄	102
Table 5.2 Curve fitting parameters for TPO of reduced Co ₃ O ₄	103
Table 5.3 A set of plausible reactions under TPR/TPO cycling.....	111
Table 5.4 TPtD and TPO performances of Co ₃ O ₄ over 10 cycles.....	122
Table 5.5 TPtD and TPO performances of CeCoO ₃ over 10 cycles	127
Table 5.6 TPtD and TPO performances of CeFeO ₃ over 5 cycles	131
Table 5.7 The conditions for parabolic dishes-focus test	173
Table 5.8 EDS map analysis of 1.0 wt. % Pd/CeO ₂ /mullite (CeO ₂ : Mullite 20:80) after field SMR tests.....	192

LIST OF FIGURES

FIGURES

Figure 1.1. Illustration of solar peak and energy demand [7]	2
Figure 1.2. Representative schematic of C-neutral and/or C-negative process based on chemical looping technology	3
Figure 1.3. Insert Solar reactor prototype used for Zn/ZnO volatile cycles [92]....	14
Figure 1.4. An example of structured materials [96]	15
Figure 1.5. Ideal cubic form of perovskite with Pm3m structure	24
Figure 1.6. Estimated equilibrium compositions for steam methane reforming at P=1atm (a) the effect of temperature on product distribution and (b) the effect of H ₂ O/CH ₄ ratios on equilibrium conversion	28
Figure 1.7. Solar reformer designed for SOLASYS project [211]	32
Figure 1.8. Schematic of indirect solar reformer used in ASTERIX system [215]	33
Figure 1.9. Schematic of main solar concentrating technologies [251].....	34
Figure 1.10. Solar reactor with porous ceria monoliths [126]	35
Figure 1.11. Solar reactor developed for HYDROSOL project [265].....	36
Figure 1.12. Internally circulating fluidized bed reactor set-up developed by Kodama Group [270].....	37
Figure 1.13. Rotary type solar reactor developed by Tokyo Institute of Technology [272].....	38
Figure 1.14. Schematic of CR5 developed by Sandia National Laboratory [256] .	39
Figure 3.1. Micromeritics Chemisorp 2720	50
Figure 3.2. Multi-gas analyzer	51
Figure 3.3 QME 200 MS experimental setup	53
Figure 3.4. Monolith before (left) and after (right) doping procedures	56
Figure 3.5 Process flow diagram of treatment, reaction and analysis system for lab scale experiments	58
Figure 3.6 Process flow diagram of treatment, reaction and analysis system for surface sweep reactor experiments	60

Figure 3.7 Process flow diagram of treatment, reaction and analysis system for lab scale experiments.....	63
Figure 3.8. Concentrated solar energy pilot unit	64
Figure 3.9. Schematic of the solar-thermal reactor	66
Figure 3.10. Streams in Aspen Plus.....	68
Figure 3.11. Mixer (left) and Splitters (right) block in Aspen Plus	68
Figure 3.12. Reactor Blocks in Aspen Plus	69
Figure 3.13. Heater in Aspen Plus.....	70
Figure 3.14. Pressure changers in Aspen Plus.....	71
Figure 3.15. Simplified block diagram of steam reforming process	71
Figure 3.16. Simplified block diagram of autothermal reforming process	72
Figure 3.17. Simplified flow-sheet used during ASPEN Plus Simulations	74
Figure 4.1. Equilibrium composition analysis of direct decomposition of water ($P_{H_2O} = 0.1\text{bar}$ and $P_{system} = 1\text{bar}$).....	76
Figure 4.2. Gibbs free energy change during phase change reactions of single oxides	78
Figure 4.3. Ellingham Diagram of Fe, FeO, Fe ₃ O ₄ and Fe ₂ O ₃	84
Figure 4.4. Ellingham Diagram of Fe, FeO, Fe ₃ O ₄ and Fe ₂ O ₃ with H ₂	84
Figure 4.5. Categorization of red/ox materials based on Ellingham diagram in terms of oxygen desorption, water splitting and supporting materials.....	85
Figure 4.6. Thermodynamic driving force of CdWO ₄ , CoWO ₄ , CuFe ₂ O ₄ , FeWO ₄ , CoFe ₂ O ₄ , CuMoO ₄ , FeMoO ₄ and Fe ₂ MnO ₄ during water splitting reaction	90
Figure 4.7. Thermodynamic driving force of Fe ₂ NiO ₄ , Fe ₂ MgO ₄ , MnWO ₄ , Fe ₂ ZnO ₄ , MnMoO ₄ and PbMoO ₄ during water splitting.....	90
Figure 4.8. Thermodynamic driving force of CdWO ₄ , CuMoO ₄ , FeWO ₄ , CoFe ₂ O ₄ , CuFe ₂ O ₄ , CoWO ₄ , and FeMoO ₄ during thermal reduction.....	91
Figure 4.9. Thermodynamic driving force of Fe ₂ MnO ₄ , MnMoO ₄ , PbWO ₄ , Fe ₂ ZnO ₄ , MnWO ₄ , and ZnWO ₄ during thermal reduction.....	92
Figure 4.10. Thermodynamic driving force of Fe ₂ NiO ₄ , PbMoO ₄ , Fe ₂ MgO ₄ , NiWO ₄ , and MnWO ₄ during thermal reduction	92

Figure 4.11. Overall concentrator efficiency as concentration ratio increases	95
Figure 4.12. The effect of temperature of solar system efficiency	96
Figure 5.1. Temperature-programmed reduction profile of Co_3O_4 (solid line, dot and dashed lines represents experimental data, reduction of $\text{Co}^{3+,4+}$ to Co^{2+} and Co^{2+} to Co^0 respectively)	102
Figure 5.2. Temperature programmed oxidation patterns of reduced Co_3O_4 (solid line, dot and dashed lines represents experimental data, oxidation of Co^0 to Co^{2+} and Co^{2+} to $\text{Co}^{3+,4+}$ respectively)	103
Figure 5.3. XRD patterns of Co_3O_4 (a) fresh sample; (b) after TPR; (c) after TPO following TPR (Triangles label peaks due to Co_3O_4 , circles represent peaks due to Co^0)	104
Figure 5.4. Oxygen evolution during thermal decomposition (TPtD) of Co_3O_4 ..	105
Figure 5.5. Red/ox performance of 0.5% wt. Pt- Co_3O_4 (solid lines) and Co_3O_4 (dotted lines).....	106
Figure 5.6. XRD patterns of 0.5% wt. Pt- Co_3O_4 (a)empty sample holder, (b) fresh sample; (c) after TPR; (d) after TPO following TPR (Triangles label peaks due to Co_3O_4 , circles represent peaks due to Co^0).....	107
Figure 5.7. TPO after TPR Co_3O_4 , 1wt. % $\text{Co}_3\text{O}_4\text{-Al}_2\text{O}_3$, 3wt. % $\text{Co}_3\text{O}_4\text{-Al}_2\text{O}_3$, and 5wt. % $\text{Co}_3\text{O}_4\text{-Al}_2\text{O}_3$ (per gr Co basis)	108
Figure 5.8. XRD patterns of CeCoO_3 and CeFeO_3	109
Figure 5.9. TPR profiles of CeO_2 , Co_3O_4 , Fe_2O_3 , CeCoO_3 and CeFeO_3	110
Figure 5.10. TPO performances of reduced CeO_2 , Co_3O_4 , Fe_2O_3 , CeCoO_3 and CeFeO_3	111
Figure 5.11. TPtD performances of CeO_2 , Co_3O_4 , Fe_2O_3 , CeCoO_3 and CeFeO_3 .	112
Figure 5.12. The effect of film mass transfer effect on oxygen desorption of Co_3O_4	114
Figure 5.13. The effect of film mass transfer effect on oxygen adsorption of Co_3O_4	114
Figure 5.14. The effect of film mass transfer effect on oxygen desorption of CeCoO_3	115

Figure 5.15. The effect of film mass transfer effect on oxygen adsorption of CeCoO_3	115
Figure 5.16. The effect of pore diffusion resistance on oxygen desorption of Co_3O_4	116
Figure 5.17. Oxygen desorption profiles for Co_3O_4 and $\text{Co}_3\text{O}_4:\text{SiC}$ (1:1 by weight)	117
Figure 5.18. Oxygen adsorption profiles for Co_3O_4 and $\text{Co}_3\text{O}_4:\text{SiC}$ (1:1 by weight)	117
Figure 5.19. Oxygen desorption profiles for CeCoO_3 and $\text{CeCoO}_3:\text{SiC}$ (1:1 by weight).....	118
Figure 5.20. Oxygen adsorption profiles for CeCoO_3 and $\text{CeCoO}_3:\text{SiC}$ (1:1 by weight).....	119
Figure 5.21. Oxygen desorption profiles for CeFeO_3 and $\text{CeFeO}_3:\text{SiC}$ (1:1 by weight)	120
Figure 5.22. Oxygen desorption performance of Co_3O_4 over 10 cycles	121
Figure 5.23. Oxygen absorption performance of Co_3O_4 over 10 cycles	121
Figure 5.24. Cyclic oxygen exchange of Co_3O_4 based on weight change under consecutive Ar and CO_2 environments with a heating/cooling rate of $10\text{ }^\circ\text{C}/\text{min}$ (solid and dotted lines represent weight change and temperature respectively)	123
Figure 5.25. Cyclic oxygen transfer of Co_3O_4 based on weight change during heating under Ar flow to $900\text{ }^\circ\text{C}$ and cooling under CO_2 flow to $650\text{ }^\circ\text{C}$ (solid and dotted lines represent weight change and temperature respectively)	124
Figure 5.26. Cyclic oxygen exchange of 0.5 wt.%Pt- Co_3O_4 based on weight change during heating under Ar flow to $900\text{ }^\circ\text{C}$ and cooling under CO_2 flow to $650\text{ }^\circ\text{C}$. (solid and dotted lines represent weight change and temperature respectively)	125
Figure 5.27. Cyclic oxygen exchange of CeO_2 based on weight change under consecutive Ar and CO_2 environments with a heating/cooling rate of $10\text{ }^\circ\text{C}/\text{min}$ (solid and dotted lines represent weight change and temperature respectively)	126
Figure 5.28. Oxygen desorption performance of CeCoO_3 over 10 cycles	127

Figure 5.29. Oxygen adsorption performance of CeCoO ₃ over 10 cycles.....	128
Figure 5.30. Cyclic oxygen exchange of CeCoO ₃ based on weight change during heating under N ₂ flow to 1000 °C and cooling under CO ₂ flow to 400 °C (solid and dotted lines represent weight change and temperature respectively).....	129
Figure 5.31. Cyclic oxygen exchange of CeCoO ₃ based on weight change during heating under N ₂ flow to 1000 °C and cooling under dry air flow to 600 °C (solid and dotted lines represent weight change and temperature respectively).....	130
Figure 5.32. Oxygen desorption performance of CeFeO ₃ over 5 cycles	131
Figure 5.33. Oxygen adsorption performance of CeFeO ₃ over 5 cycles	132
Figure 5.34. Cyclic oxygen exchange of CeFeO ₃ based on weight change during heating under Ar flow to 1100 °C and cooling under CO ₂ flow to 500 °C (solid and dotted lines represent weight change and temperature respectively).....	133
Figure 5.35. Cyclic oxygen exchange of SCFC-6473 based on weight change during heating under Ar flow to 1100 °C and cooling under CO ₂ flow to 800 °C (solid and dotted lines represent weight change and temperature respectively).....	134
Figure 5.36. Cyclic oxygen exchange of SCFC-6473 based on weight change during heating under Ar flow to 950 °C and cooling under CO ₂ flow to 800 °C (solid and dotted lines represent weight change and temperature respectively).....	135
Figure 5.37. Cyclic oxygen exchange of SCFC-6473 based on weight change during heating under N ₂ flow to 1100 °C and cooling under CO ₂ flow to 400 °C (solid and dotted lines represent weight change and temperature respectively).....	136
Figure 5.38. O ₂ evolution profile during thermal decomposition for Co ₃ O ₄ and 1.84 Pt% Co ₃ O ₄ doped monoliths	137
Figure 5.39. H ₂ production profile by TPWS for Co ₃ O ₄ and 1.84 Pt% Co ₃ O ₄ doped monoliths.....	138
Figure 5.40. Oxygen releasing profile of 1% Pd-CeO ₂ up to 900 °C (1 st cycle)..	139
Figure 5.41. Hydrogen production profile from reduced 1% Pd-CeO ₂ at 800 °C (1 st cycle).....	139

Figure 5.42. Hydrogen production profile from reduced 1% Pd-CeO ₂ at 800 °C (2 nd cycle)	140
Figure 5.43. Oxygen releasing profile of 1% Pd-CeO ₂ up to 1150 °C during 1 st cycle (solid and dotted lines represent weight change and temperature respectively) ...	141
Figure 5.44. Hydrogen production profile at 800 °C from reduced 1% Pd-CeO ₂ at 1150 °C during 1 st cycle	141
Figure 5.45. Oxygen releasing profile of 1% Pd-CeO ₂ up to 1150 °C during 2 nd cycle (solid and dotted lines represent weight change and temperature respectively) ...	142
Figure 5.46. Hydrogen production profile at 800 °C from reduced 1% Pd-CeO ₂ at 1150 °C during 2 nd cycle	142
Figure 5.47. Oxygen releasing profile of 1% Pd-CeO ₂ up to 1150 °C during 3 rd cycle (solid and dotted lines represent weight change and temperature respectively) ...	143
Figure 5.48. Hydrogen production profile at 800 °C from reduced 1% Pd-CeO ₂ at 1150 °C during 3 rd cycle.....	143
Figure 5.49. Comparison of hydrogen production profiles of 1% Pd-CeO ₂ for 3 cycles	144
Figure 5.50. Hydrogen production profiles between 1000 to 500 °C (Thermal decomposition experiments performed at 1150 °C).....	145
Figure 5.51. 316 stainless steel cartridge with SCFM (6473) after experiment....	146
Figure 5.52. Hydrogen evolution profiles of SCFM (6473) for two cycles (left) and production profile from McDaniel <i>et al.</i> [38] (right)	146
Figure 5.53. Hydrogen signal detected by GC-TCD (left) and MS (right) of SCFM (6473)	147
Figure 5.54. O ₂ evolution profile of SCFM (6473)	147
Figure 5.55. Ceramic cartridge before and after experiment of SCFM (6473).....	148
Figure 5.56. The volatility of lead and lead monoxide at high temperatures plotted based on the data obtained from [331]	149
Figure 5.57. Predominance diagram of Pb exposed to H ₂ O/H ₂ at 1000 °C and (b) oxygen atmosphere; (c) equilibrium composition during thermal decomposition of PbO at 1 atm	150

Figure 5.58. Hydrogen production rate during water splitting	152
Figure 5.59. Estimated equilibrium conversions of H ₂ under different water vapor pressures, 1, 5, 8 and 10 bar. Pb and PbO are considered to be in vapor form.....	153
Figure 5.60. The deviation of hydrogen production (symbols) from the thermodynamic equilibrium values (line).....	154
Figure 5.61. The oxygen composition in the effluent stream during thermal decomposition.....	155
Figure 5.62. Shrinking core model for plate geometry for this experiment.....	156
Figure 5.63. The growth of PbO _x layer as a function of time, temperature and yH ₂ O	157
Figure 5.64. Methane conversion (a) and syngas composition (b) during the steam methane reforming reaction over 15 wt.% Ni/Al ₂ O ₃ powdered catalyst in a lab scale reactor.	163
Figure 5.65. TGA curve (a) and SEM image with combined EDS mapping (b) of 15wt. % Ni-Al ₂ O ₃ after being used in SMR reaction at 800 °C	164
Figure 5.66. Hydrogen (a), carbon dioxide (b) and carbon monoxide (c) signals collected during the steam methane reforming reaction	165
Figure 5.67. The TGA profile of spent catalysis after SMR reaction at 800 °C...	166
Figure 5.68. Cyclic reduction (*) and oxidation (+)performance of 13 wt.% Ni-Al ₂ O ₃ which reoxidized by water at 800 °C (Reducing was performed under 1% CH ₄ -Ar from 800 to 1000 °C with a heating rate of 20 °C/min and dwelling at 1000 °C for 20min. Oxidizing was conducted under 10% H ₂ O-Ar from 1000 to 800 °C with a cooling rate of 20 °C/min and dwelling at 800 °C for 20min.).....	170
Figure 5.69. Hydrogen production rate during reoxidation of reduced CeCoO ₃ under the flow 10% H ₂ O-Ar at 800 °C	171
Figure 5.70. Cyclic reduction (*) and oxidation (+)performance of CeCoO ₃ which reoxidized by water at 800 °C (Reducing was performed under 1% CH ₄ -Ar from 800 to 1000 °C with a heating rate of 20 °C/min and dwelling at 1000 °C for 5min. Oxidizing was conducted under 10% H ₂ O-Ar from 1000 to 800 °C with a cooling rate of 20 °C/min and dwelling at 800 °C for 5min.....	172

Figure 5.71. The shape and the size of the focus of parabolic dishes	174
Figure 5.72. The determination of concentrated Solar energy	175
Figure 5.73. The variation of air temperature with respect to solar irradiation (a) and the spiral tubing after the air heating experiments (b).....	177
Figure 5.74. Mean temperature measurements and net power estimations during heating and cooling periods of SS disk	178
Figure 5.75. The temperature-time diagram measured inside the reactor across a mullite monolith.	179
Figure 5.76. Solar reactor during the reforming operation.....	180
Figure 5.77. Solar irradiation and temperature profiles (a) and methane conversion (b) during solar steam methane reforming catalyzed by 12.8% Ni-mullite (Day 1)	182
Figure 5.78. Solar irradiation and temperature profiles (a) and methane conversion (b) during solar steam methane reforming catalyzed by 12.8% Ni-mullite (Day 2)	183
Figure 5.79. Solar irradiation and temperature profiles (a) and methane conversion (b) during solar steam methane reforming catalyzed by 1.0 wt. % Pd/CeO ₂ /mullite (CeO ₂ : Mullite 20:80) (Day 1)	185
Figure 5.80. Solar irradiation and temperature profiles (a) and methane conversion (b) during solar steam methane reforming catalyzed by 1.0 wt. % Pd/CeO ₂ /mullite (CeO ₂ : Mullite 20:80) (Day 2)	186
Figure 5.81. Solar irradiation and temperature profiles (a) and methane conversion (b) during solar steam methane reforming catalyzed by 1.0 wt. % Pd/CeO ₂ /mullite (CeO ₂ : Mullite 20:80) (Day 3)	187
Figure 5.82. Cumulative hydrogen production for (a) 12.8% Ni-mullite and (b) 1.0 wt. % Pd/CeO ₂ /mullite (CeO ₂ : Mullite 20:80) during pilot plant tests	188
Figure 5.83. Monolith pictures after the continuous SMR experiments performed at pilot scale plant.....	190
Figure 5.84. TGA curves of 12.8% Ni-mullite and 1.0 wt. % Pd/CeO ₂ /mullite (CeO ₂ : Mullite 20:80) after field SMR tests.....	191

Figure 5.85. SEM images of 1.0 wt. % Pd/CeO ₂ /mullite (CeO ₂ : Mullite 20:80) after field SMR tests.....	191
Figure 5.86. Equilibrium hydrogen production for direct water splitting, steam methane reforming and dry reforming of methane	193
Figure 6.1. Performance of SMR and ATR processes in terms of CH ₄ conversion and overall energy requirement	195
Figure 6.2. Methane requirement and CO ₂ emission of SMR and ATR processes based on 1 mol H ₂ production.....	196
Figure 6.3. Overall material and energy balance of the modified ATR system ...	198
Figure 6.4. CH ₄ requirement for producing 1 mol of H ₂ under different solar energy contributions	199
Figure 6.5. CO ₂ emission based on 1 mol of H ₂ under different solar energy contributions	200
Figure 6.6. The heat load of combustor in hybrid reforming process during solar embed methane reforming process (Ni-mullite-Day 2 (a) and Pd/CeO ₂ /mullite-Day 3 (b)).....	201
Figure 6.7. The solar energy contribution to methane conversion during solar embed methane reforming process (Ni-mullite-Day 2 (a) and Pd/CeO ₂ /mullite-Day 3 (b))	203
Figure 6.8. The CH ₄ consumption for producing 1 mol H ₂ during solar embed methane reforming process (Ni-mullite-Day 2 (a) and Pd/CeO ₂ /mullite-Day 3 (b))	204
Figure 6.9. The CO ₂ emissions for producing 1 mol H ₂ during solar embed methane reforming process (Ni-mullite-Day 2 (a) and Pd/CeO ₂ /mullite-Day 3 (b)).....	205
Figure 6.10. The cumulative H ₂ production during solar embed methane reforming process (Ni-mullite-Day 2 (a) and Pd/CeO ₂ /mullite-Day 3 (b))	207
Figure 6.11. The effect of solar energy contribution on hydrogen yield	209
Figure 6.12. Main control algorithm for reactor temperature control.....	210
Figure 6.13. Main control algorithm for oxygen plant start-up	211
Figure 6.14. Main control algorithm for steam production plant	211

Figure 6.15. Process flow diagram for the solar integrated hybrid methane reformer	212
Figure 6.16. Solar steam generation and solar reforming section of proposed process	214
Figure 6.17. Solar integrated oxygen generation plant section of proposed process	215
Figure 7.1. Block diagram of hybrid solar ATR process	219

LIST OF ABBREVIATIONS

ABBREVIATIONS

A: ampere

ALD: atomic layer deposition

ASPEN: advanced system for process engineering

ATR: autothermal reforming

a.u.: arbitrary unit

ccpm: cubic centimeter per minute

CNRS: Centre National de la Recherche Scientifique

CSIRO: The Commonwealth Scientific and Industrial Research Organisation

DME: dimethyl ether

DRM: dry reforming of methane

ID: identity

JCPDS: Joint Committee on Powder Diffraction Standards

kW: kilowatt

kW_{th}: kilowatt thermal

mA: miliamper

MFC: mass flow controller

MFCS: mass flow control station

MIT: Massachusetts Institute of Technology

MS: mass spectrometry

MW: megawatt

NDIR: non-dispersive infrared

OAPEC: Organization of Arab Petroleum Exporting Countries

PM: precious metals

PROMES-CNRS: Procédes, Matériaux, et Energie Solaire Centre National de la Recherche Scientifique

PSA: Plataforma Solar de Almería

PSI: Paul Scherrer Institute

PV: photovoltaic

Red/ox: reduction/oxidation

sccm: standart cubic centimeter per minute

SDC: $\text{Sm}_{0.15}\text{Ce}_{0.85}\text{O}_{1.925}$

SCFC-6473: $\text{Sr}_{0.6}\text{Ce}_{0.4}\text{Fe}_{0.7}\text{Co}_{0.3}\text{O}_3$

SCFM-6473: $\text{Sr}_{0.6}\text{Ce}_{0.4}\text{Fe}_{0.7}\text{Mn}_{0.3}\text{O}_3$

S-I: sulfur and iodine

SMR: steam methane reforming

TCD: thermal conductivity detector

TCT: thermal conductivity transmitter

TGA: thermal gravimetric analysis

TPO: temperature programmed oxidation

TPR: temperature programmed reduction

TPtD: temperature programmed thermal decomposition

TPx: temperature programmed experiments

TPWS: temperature programmed water splitting

TWh: terawatt hour

USD: United States Dollar

US DOE: United States Department of Energy

CHAPTER 1

INTRODUCTION AND LITERATURE SURVEY

1.1 Energy

Industrial revolution opened new era for human civilization. the technological developments and innovations have driven the changes in the fields such as factories, living standards, food, nutrition. These social effects led to unprecedented increase in the rate of world population growth (from 1 billion (1800s) to 8 billion (2018) [1,2]). In order to sustain the growth rate, the world energy consumption have been increasing tremendously from 5,600 TWh (1800s) to 162,000 TWh (2018) [3]. Currently, fossil fuel consumption is around 80% of the world energy consumption [4]. The share of natural gas and oil is nearly 55% [4]. The control of United States, Saudi Arabia and Russia on world energy production reaches to 41% [5]. Therefore, fossil fuels are generally referred as a strategic component for energy independency. Energy independency is a defined as the ability to sustain own energy demands with its own energy sources. This term is also used as a terminology to measure the reliance of an economy to imported energy sources. The economies become vulnerable to political and social crisis as this dependency increases. The 1973 and 1979 oil crises are good examples for such situation [6]. The embargo proclaimed by OAPEEC (Organization of Arab Petroleum Exporting Countries) in 1973 increased the oil prices from \$3 to \$12 in a year period. This event was followed by Iranian revolution in 1979 causing a jump in oil prices to nearly \$40. These two events triggered the global economic recessions showing the link of energy sources to national security, social stability and quality of life [6]. Therefore, producing energy with abundant and renewable sources such as solar, wind is a critical subject in terms of energy independency. However, these sources are not reliable due to their

intermittent nature. In order to overcome problems regarding intermittency, storing energy when it is available gains more importance (Figure 1.1).

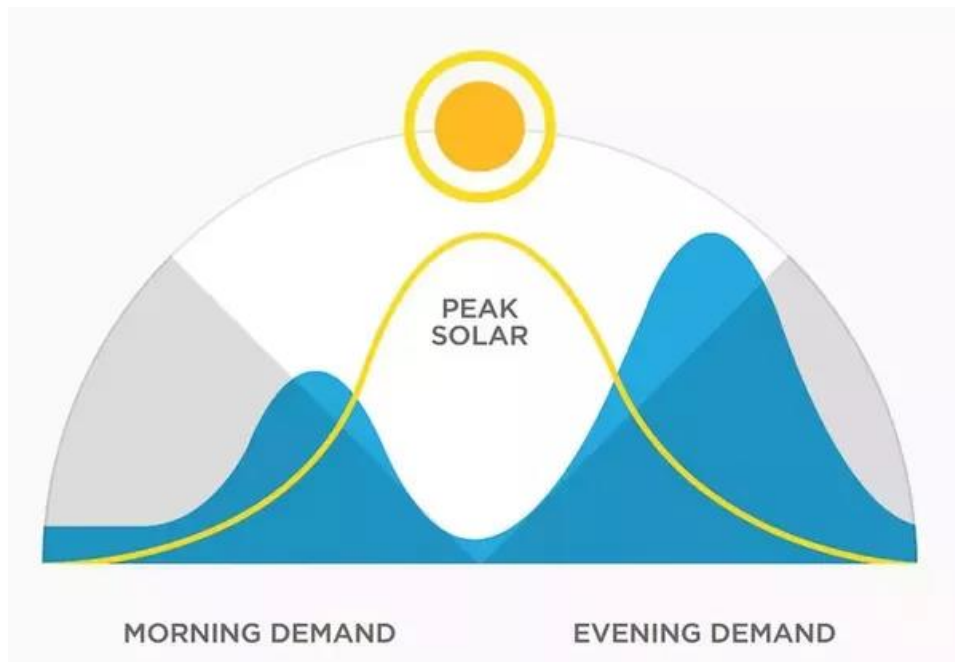


Figure 1.1. Illustration of solar peak and energy demand [7]

Hydrogen molecule, lightest element in periodic table, can be used as energy carrier according to ISO13600 [8]. In addition, the idea of using hydrogen as energy carrier was strengthened after 1974 energy crisis [9]. Hydrogen exists in the chemicals such as water, hydrocarbons, hydrogen sulfide. Today, hydrogen can be produced by various in order to meet the market demand of USD 118 billion in 2016 [10].

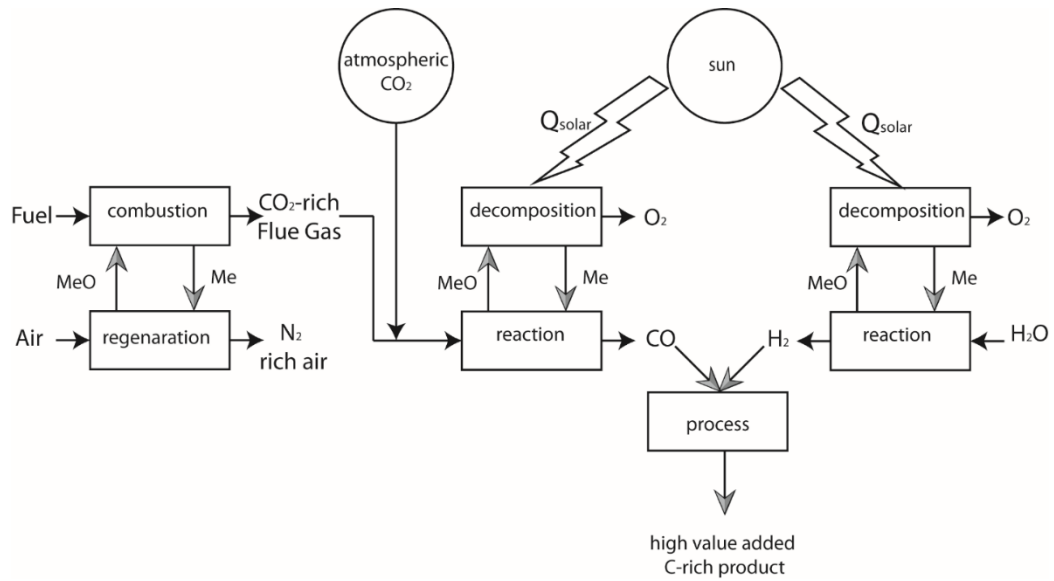


Figure 1.2. Representative schematic of C-neutral and/or C-negative process based on chemical looping technology

5% of global hydrogen demand is supplied from water electrolysis while 95% is dependent on fossil fuels [11]. For example, hydrogen sources such as alcohol, electricity, natural gas and propane are highly dependent on fossil fuels with positive carbon intensity (amount of carbon dioxide released per joule of energy produced). In order to reduce the carbon intensity, carbon neutral/negative technologies are developing by integration of renewable sources or by developing better ways instead of C sequestration. Chemical looping processes are emerging as an alternative solution for hydrogen and carbon monoxide production as well as carbon dioxide mitigation problems. The utilization of carbon dioxide and water in looping technology is shown in Figure 1.2. A reduced metal oxide splits carbon dioxide and water to oxidize itself. As the oxidation proceeds, a regeneration step is needed. Since solar energy is the most abundant source of energy in the world, this energy can be concentrated to thermally decompose the metal oxide to regenerate itself. Therefore, the regeneration of the metal oxide is the most critical step since the feasibility of the process is directly affected.

Table 1.1 Sustainable hydrogen production options

Sustainable and Renewable Energy Sources

- Solar Energy
- Hydro Power
- Ocean/Tidal Energy
- Wind Energy
- Geothermal Energy

Hydrogen Production Methods

- Electrochemical
- Thermochemical
- Hybrid
- Biochemical
- Photochemical

Sustainable Hydrogen Production Pathways

- Water Splitting
- Fossil Fuel decarbonization
- Hydrogen Sulfide Decomposition
- Waste material decomposition
- Hybrid Processes

Hydrogen-based future can be envisioned by development of sustainable hydrogen production options as given in Table 1.1. Each technology has certain advantages and disadvantages that leaves the user the choice. Under the scope of this thesis, solar thermochemical water splitting processes and hybrid processes were studied.

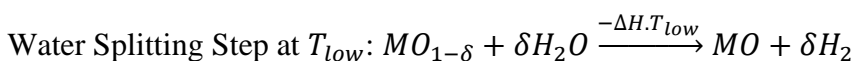
1.2 Thermochemical Water Splitting Processes

Thermochemical reaction systems process heat to drive the reaction. In this reaction systems, the reaction absorbs or desorbs energy in order to proceed the chemical transformations such as pyrolysis, combustion and gasification. In thermochemical water splitting reaction, heat is used for bond breaking and bond forming purpose as described in upcoming sections in detail.

1.2.1 Two-Step Solar Thermochemical Cycles

Storage of solar energy in chemical bonds is an important academic as well as an industrial challenge. During the solar energy storage, sunlight is utilized for synthesizing a new molecule. Among various methods proposed in the literature - such as electrochemical route from photovoltaic solar energy conversions or solar thermal power generations - the utilization of solar energy by means of two-step solar thermochemical processes was addressed in the scope of this thesis.

Two-step thermochemical water splitting technologies are broadly based on the thermal generation of oxygen imbalances, which are subsequently filled by the oxygen from water, such that hydrogen is produced as a result.



The slow reaction rates and material deactivation are the main issues of thermochemical routes. The major bottleneck in these reactions is very high temperatures needed for thermal decomposition, demanded by the energy to break metal-oxygen bond. This is the biggest challenge against the commercialization of solar thermochemical processes. These drawbacks are addressed by (i) increasing the efficiency of solar collectors for achieving high thermal decomposition temperatures, or (ii) promoting the red/ox material to fully decompose and release its oxygen at lower temperatures.

Despite the fact that thermal means of solar energy conversion has the potential of utilizing the full spectrum, the dispersed radiation is not capable of producing very high temperatures. Therefore, solar energy is concentrated by solar concentrators. By combining already existing technologies of thermal to electrical energy conversions through power cycles, such as CSIRO (Australia), PSA (Spain), PROMES-CNRS (France), solar thermal conversion pilot units have already been demonstrated [12]. It must be noted that there is a trade-off between the increased

temperatures leading to higher efficiencies and the increased cost of investment for the solar concentration. The limiting efficiencies of thermal energy conversion technologies can be considered as the Carnot cycle efficiency, defined as the maximum possible efficiency of a cycle that can convert heat to work:

$$\eta_{Carnot} = \frac{T - T_L}{T} \quad \text{Eq. 1}$$

T and T_L are the temperatures of the heat source and heat sink, in Kelvins. It is obvious from Eq. 1 that as the temperature of the heat source, T, increases, the efficiency of the cycle increases. In other words, when higher temperatures are available, it is possible to design more efficient energy conversion processes through thermal power cycles. Concentrating solar energy can increase the influx of solar radiation and as a result the temperature at the focal position with an increase in the fixed capital costs compensated by the increased efficiencies. Despite the advantage of utilization of the full solar spectrum for enhanced efficiencies, solar thermal to electrical conversions still suffer the same storage issues as PV (photovoltaic) technologies: efficient and reliable technologies for long term storage and transport of electrical energy is still a challenge, that can be overcome through storing the thermal and/or electrical energy in chemical bonds. This avenue of solar energy storage is exploited through solar thermochemical methods.

The effectiveness of a two-step thermochemical cycle can be increased by finding an appropriate red/ox material. On this front, lab scale experiments were conducted to enhance the metal oxide properties such as stability, oxygen capture capacity, thermal decomposition kinetics considering micro-to-macro relations in each cycle [13–22]. The reactivity towards oxygen desorption and thermal stability of various red/ox pairs have been studied extensively for two-step thermochemical cycles. The literature to date is classified according to the oxides in the form of single metal oxides [23–32], perovskites [15,20,33–40], spinel oxides [13,41–47], and mixed metal oxides [48–55]. The oxygen desorption reactivity of these oxides is studied under different reaction conditions. In Table 1.2, a selective summary of the some of

the materials used for solar thermochemical water splitting, along with their thermal decomposition and oxidation temperatures are presented. In the same table, the reported hydrogen rates per gram metal oxide are compared in terms of mol H₂/mol metal oxide basis. As can be seen, the extreme temperatures are a norm, due to the inherently strong oxygen to metal bond. The main drawback of proposed red/ox pairs is the temperature needed for thermal decomposition due to either low kinetics or the limitations imposed by thermodynamics.

Table 1.2 Water splitting and thermal decomposition data for some metal/metal oxide pairs

Metal Oxide (MO_x)	Thermal Decomposition/ Water Splitting Temperatures (°C)	H₂ production as reported	Converted H₂ production (mmol H₂/ mol MO_x)	Ref.
CoFe ₂ O ₄ /Al ₂ O ₃	1200/1000	0.777 mmol/g	182	[56]
CeO ₂	1400/1100	144 μmol/g	25	[57]
Ce _{0.75} Zr _{0.25} O ₂		432 μmol/g	69	
NiFe ₂ O ₄	1100	428 μmol/g	100	[58]
La _{0.9} Sr _{0.1} MnO _{3-γ}	1400/800	0.91 mL/g	9	[59]
La _{0.6} Sr _{0.4} MnO _{3-γ}		8.9 mL/g	82	
20 wt.% Fe ₃ O ₄ in 8% YSZ	1500/1200	3 mL/g	28.9	[23]
10 wt.% CoFe ₂ O ₄ in 8% YSZ		1.5 mL/g	14.6	
Ce _{0.75} Zr _{0.25} O ₂	1400/1200	468 μmol/g	74	[48]
CeO ₂	1500-750	2.12 mL/g	15.2	[28]
Ce _{0.95} Pr _{0.05} O _{2-γ}		2.1 mL/g	15	
Ce _{0.9} Pr _{0.1} O _{2-γ}		2.3 mL/g	16.5	

Table 1.2 (cont'd) Water splitting and thermal decomposition data for some metal/metal oxide pairs

Metal Oxide (MO_x)	Thermal Decomposition/ Water Splitting Temperatures (°C)	H₂ production as reported	Converted H₂ production (mmol H₂/ mol MO_x)	Ref.
CeO ₂	1500/1150	10.2 mL/g	73	[26]
5-15mol% Fe- CeO ₂		12 mL/g	84-86	
5-15mol% Co- CeO ₂		11-17.2 mL/g	78-123	
5-15mol% Ni- CeO ₂		8.5-15.4 mL/g	61-110	
5-15mol% Mn- CeO ₂		10-11 mL/g	72-79	
CeO ₂	1300-1550/400- 1000	9.3 mL/g	66.5	[25]
NiFe ₂ O ₄		11.4 mL/g	111	
NiFe ₂ O ₄ /m-ZrO ₂		11.3 mL/g	111	
NiFe ₂ O ₄ /c-YSZ		6.4 mL/g	62.4	
Ba _{0.5} Sr _{0.5} Co _{0.8} Fe _{0.2} O _{3-δ}	1000/800	83 μmol/g	18	[60]
La _{0.65} Sr _{0.35} MnO _{3-δ}	1400/1050	124 μmol/g	27	
La _{0.6} Sr _{0.4} Co _{0.2} Fe _{0.8} O _{3-δ}	1200/800	162 μmol/g	36	
LaSrCoO ₄	1300/800	164 μmol/g	57	

When the data compiled in Table 1.2 is closely examined, it can be clearly seen that both the amounts and the rates of hydrogen evolution are very low. The red/ox pairs indicated in Table 1.2 only has ZnO/Zn as a metal in the reduced state. The rest of the materials carry an oxide in their lower oxidation states, which will be the topic of further discussion in this thesis. The reactivity of a red/ox pair is measured by the oxygen exchange capability (ability to adsorb or desorb oxygen from its molecular structure) for the bulk materials. The oxygen is governed by kinetics, mass transfer, heat transfer, and thermodynamics. The governing mechanism changes with respect to temperature. At low temperatures, kinetics controls the reaction rate. As the temperature increases, the governing mechanism shifts to mass transfer, heat transfer and finally to thermodynamics. The stability of the red/ox pairs at high temperatures can be ensured by a thermally stable inert metal oxide acting as supports such as Al₂O₃, ZrO₂, TiO₂ [61–66].

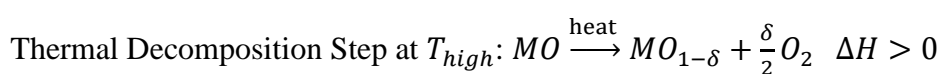
1.2.2 Multi-Step Thermochemical Cycles

Multi-step thermochemical cycles are carrying out the water splitting reaction by a series of consecutive cycles. Overall reaction is nothing but the water dissociation reaction. The multicycle (>2) thermochemical processes have been primarily developed for removing nuclear heat from the high-temperature gas-cooled reactor. They are capable of working below 1200 K. Some of these processes are given in Table 1.3. These cycles suffers from the complex reaction mechanisms, corrosive and toxic reactants, separation problems and the difficulties arisen during the utilization of solar energy [67].

Table 1.3 Multicycle thermochemical cycles [68]

No	Elements	Max Temp. (K)	# of reactions
1	Hg, Ca, Br	1050/1050	4/5
2	Cu, Ca, Br	1170	4
3	Hg, Sr, Br	1070	3
4	Mn, Na, (K)	1070	3
5	Mn, Na, (K), C	1120	4
6	V, Cl, O	1070	4
7	Fe, Cl, S	1070	4
8	Hg, Ca, Br, C	1170	5
9	Cr, Cl, Fe, (V)	1070	4
10	Cr, Cl, Fe, (V), Cu	1070	5
11	Fe, Cl	1070/1120/920/970	5/5/3-4/5
12	Mn, Cl	1170	3
13	I, S, N	1120	6
14	I, S, N, Zn	1120	4
15	S	1120	2
16	Br, S	1120	3
17	S, I	1120	3

Two step thermochemical cycles are the simplest method for water splitting. These cycles can be classified into oxide, hydride and hydroxide types as in Table 1.4. Two step thermochemical cycles are classified into oxide, hydride and hydroxide types in Table 1.4. Oxide type thermochemical cycles are studied in the scope of this thesis. Two step thermochemical processes are successive cycles of thermal decomposition and oxidation reactions. The thermal decomposition reaction is an endothermic process that requires heat to remove oxygen from metal oxide. This activation step requires higher temperatures depending on the stability of oxide.



The oxidation reaction is carried out by reacting water vapor with the reduced metal oxide at the temperatures lower than thermal decomposition step. This exothermic step splits water and produce hydrogen. This step eliminates the drawbacks coming from high temperature separation of H₂/O₂ during dissociation of water ($H_2O \xrightarrow{\text{heat}} H_2 + 0.5O_2$).

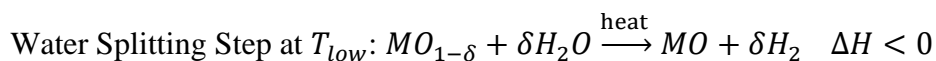


Table 1.4 Reaction pathways for two step thermochemical cycles

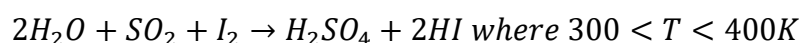
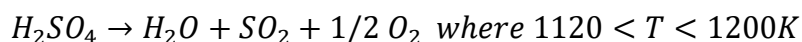
Oxide type	$MO \rightarrow M + 0.5O_2$
	$M + H_2O \rightarrow MO + H_2$
Hydride type	$MH_2 \rightarrow M + H_2$
	$M + H_2O \rightarrow MH_2 + 0.5O_2$
Hydroxide type	$2MOH \rightarrow 2M + H_2O + 0.5O_2$
	$2M + 2H_2O \rightarrow 2MOH + H_2$

The temperature interval between thermal decomposition and oxidation steps is an important parameter for overall process feasibility. Heat management between these steps determines the efficiency of the conversion of solar energy to chemical energy; that is, the ratio of solar energy utilized for chemical synthesis to total incoming solar energy. Therefore, the choice of red/ox material which directly determines the operational temperatures is the key step for maximizing the process efficiency.

1.2.3 The Selection of Red/Ox Pairs

Red/ox pairs can be grouped into three main groups as liquid-vapor, volatile and nonvolatile.

Liquid-Vapor Pairs: Redox based on sulfur and iodine (S-I) operated under harsh conditions due to the presence of sulfuric acid. This pair requires several steps including the decomposition of sulfuric acid. The operating temperature range is between 300-1000 °C [69]. The reaction mechanism was given as follows:

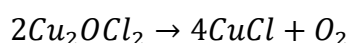
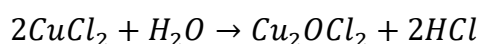
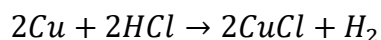


The last reaction step is called as Bunsen reaction. This reaction requires high amounts of water and iodine to produce two immiscible concentrated acid phases. Therefore, reduction of water and iodine surpluses and the distillation of H₂SO₄ and HI requires high amount of energy which is the major drawback of this process. The thermal efficiency of this reaction system was found between 33-36% based on the higher heating value where 51% is the maximum efficiency that can be obtained under ideal conditions [70].

Solar energy integration was also studied in order to overcome the energy penalty of the process. Several groups are demonstrated the utilization of solar energy at bench

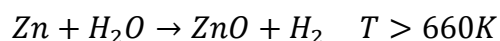
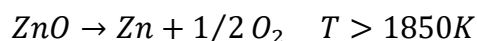
and pilot scale [71–75]. Other than the S-I pair, processes called hybrid sulfur [76–81], Outetec [82], HHLT [83], and Mark 13 [137] are also studied in literature.

Cu-Cl pair needs moderate temperatures comparing to S-I cycles [84]. The highest temperature step requires 550 °C. This moderate temperature offers an improvement in energy efficiency, and lower operational costs. The reaction steps are given as



Process begins with the exothermic reaction of Cu with HCl. This step produces hydrogen, target compound. Then, endothermic water reacts with CuCl₂ forming Cu₂OCl and HCl. During the electrolysis step, CuCl decomposes to CuCl₂ and Cu. Finally, Cu₂OCl₂ decomposes into CuCl and O₂. In these reaction steps, solids handling, product separation, presence of corrosive medium are the main challenges. Proof of principle experiments with large laboratory scale demonstrations [83] revealed that 43% efficiency based on lower heating value can be achieved during Cu-Cl cycles [85].

Volatile Cycles: A phase transition generally is seen at the thermal decomposition step due to the products that have lower boiling temperatures. In spite of thermodynamic benefits coming from entropy increase, recombination of products in gaseous phase requires fast quenching or high temperature gas separation processes.



Red/ox cycles including Zn/ZnO [86,87], Cd/CdO [88], and SnO/SnO₂ [89,90] are good examples for volatile cycles. Due to the high thermal decomposition

temperatures, solar energy utilization can be conducted by point focus systems as given in Figure 1.3. Reactants are generally isolated from the system by tubes and solar heat is transferred by means of radiation, convection and conduction [91].

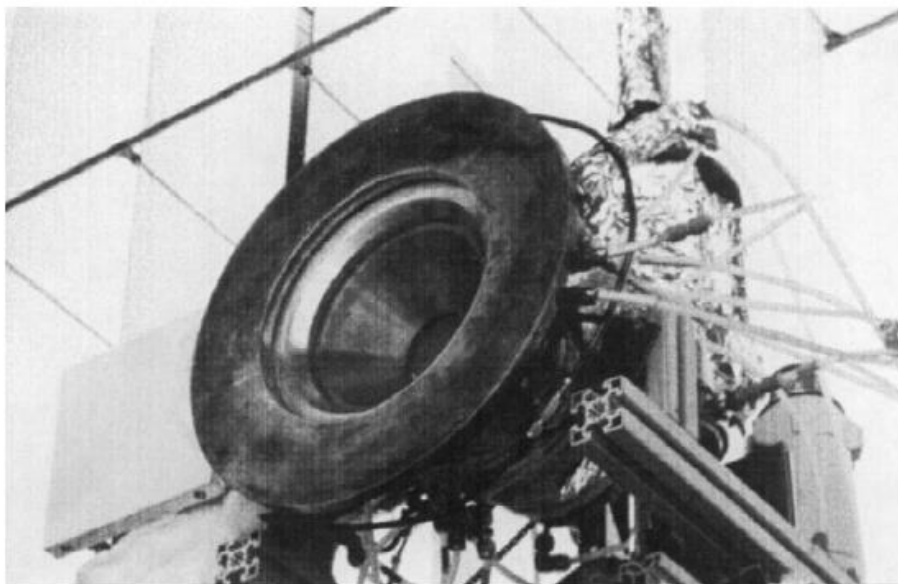


Figure 1.3. Insert Solar reactor prototype used for Zn/ZnO volatile cycles [92]

Non-volatile Cycles: Non-volatile cycles splits into two sub categories namely stoichiometric (i.e. $\text{Fe}_3\text{O}_4/\text{FeO}$ [93]) and non-stoichiometric (cycles including compounds having elemental composition that cannot be represented by natural numbers i.e. $\text{CeO}_2/\text{CeO}_{2-\delta}$ [94]) red/ox couples. In general, stoichiometric red/ox couples offer high oxygen storage capacity but slower kinetics and poor stability. Therefore, new metal atom is introduced to the system in terms of doping or substitution in order to improve kinetic and physical properties of the overall cycles [95]. Monolithic structures or coated foams are preferred during non-volatile cycles due to their structured forms and thermal stability as given in Figure 1.4.

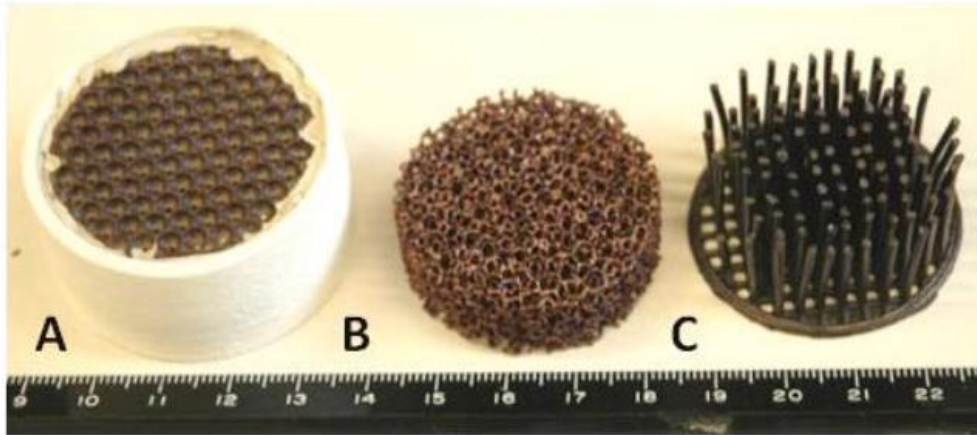
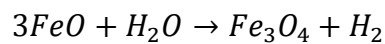
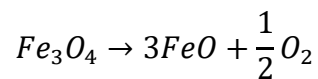
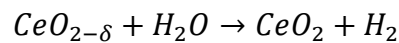
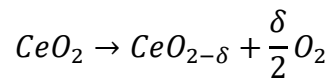


Figure 1.4. An example of structured materials [96]

Stoichiometric red/ox couple



Non-stoichiometric red/ox couple

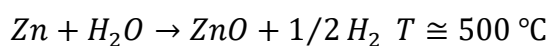
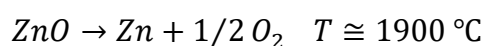


The red/ox couples that used in two step thermochemical processes are classified as pure oxides [23,27–32,97–102], mixed oxides as spinels [23,25,41,56], solid solutions [22,48,98,103,104], and perovskites [22,59,60,98,100] as well as supported [23,25,31,32,41,56,98] and unsupported oxides [22,26,27,29,32,48,56,59,60,98–105]. The preponderance of studies reported the oxides of Ce [22,24–30,48,101,104,105], Fe [22,23,25,31,32,41,56,60,97–99], Mn [59,60,98], Co [41,56,60,97,98] and Ni [97,102,104] as active red/ox metals for two step thermochemical processes. TGA [29,48,60,100,101], fixed bed reactors [22,23,29–32,41,56,59,60,98,99,102,104,105] and specialized solar reactors [22,27] were commonly used for evaluating cycle performance. Despite the fact that majority of

the red/ox couples operates at desorption temperatures higher than $>1200\text{ }^{\circ}\text{C}$ [22,23,25,27–29,41,48,56,59,60,97–101,104], few groups reported materials that has low operating temperature $<1200\text{ }^{\circ}\text{C}$ [22,60,98]. Even if a detailed analysis of the literature on two step thermochemical hydrogen production was given in Appendix A, common red/ox couples are also discussed in the following sections.

Co₃O₄/CoO: Cobalt oxides have been widely used in electrochemical [106–108] and photochemical [109,110] applications of water oxidation. The particle size [111] and surface modifications [107,112,113] were found to produce hydrogen at mild conditions. The existence of Co^{2+} controls the catalytic activity during oxygen reduction and evolution reactions [114,115]. $\text{CoO}/\text{Co}_3\text{O}_4$ was found to be thermodynamically impractical in solar thermochemical water splitting applications due to the low hydrogen yield ($4 \cdot 10^{-7}\%$ at 900K) during oxidation reaction [116,117]. Nevertheless, cobalt is widely used as a promoter to reduce the temperature in thermal decomposition step while preserving the hydrogen yield [46,56]. The inefficiency of $\text{CoO}/\text{Co}_3\text{O}_4$ stems from the reducibility of CoO by the produced hydrogen as will be discussed in the upcoming sections. Nevertheless, low temperatures required to create CoO from Co_3O_4 makes the material a favorable model system to elucidate the competing mechanistic effects and offer alternative solutions.

ZnO/Zn: ZnO/Zn red/ox couple undergoes a phase change reduction during the water splitting process. The thermal decomposition reaction is highly endothermic (450 kJ/mol) [118] and kinetically inhibited. The reasonable thermal decomposition rates can be observable after $1750\text{ }^{\circ}\text{C}$. Water splitting reaction can be operated under autothermal processes due to its exothermicity (130 kJ/mol) [118].



During the thermal decomposition, Zn evaporates and separation of O_2 and Zn becomes a technical challenge. Commonly, gaseous products immediately quenched

with an inert gas [87]. Zn recovery is controlled by changing dilution ratio and temperature. Gstoehl *et al.* demonstrated a three zone quenching apparatus for ZnO/Zn cycle [119]. After thermal decomposition of ZnO at the first zone, products pass through an intermediate zone (second zone) for suppressing the Zn(g) diffusion towards the wall. Thereafter, Zn(g) quenches with a rate of 20,000-120,000K at the third zone. 40-94% recovery of Zn was achieved with a dilution ratio (Ar/Zn) of 170 to 1,500 [87]. Exergy efficiency is predicted as 29% and percent for the cases without and with heat recovery respectively [86].

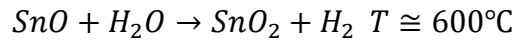
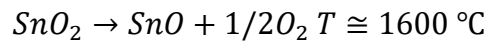
Berman and Epstein studied molten zinc oxidation by water vapor [120]. They proposed that 296 kg/h zinc is required for 100 nm³/hr H₂ production. The kinetic analysis performed at different water concentrations showed that diffusion through oxide layer is the rate limiting step [120,121].

Wegner et al. demonstrated that single pass hydrogen yield can be increased up to 70% in the tubular aerosol flow reactor [122]. The aerosol reactor consists of three temperature-controlled regions as Zn-evaporation zone, nanoparticle formation and reaction zones. Evaporated zinc contacts with water to produce Zn nanoparticles. These particles react with steam to produce hydrogen. At temperatures of 1023 to 1073K, Zn to ZnO conversion in the range of 87%-96% [123]

The industrial application of ZnO/Zn cycle has not been established yet. ETH Zurich group already demonstrated a series of rotary reactor [87,92,124,125]. One of the major problems of this cycle is coming from inert gas used for quenching purpose. After quenching Zn, inert gas mixed with oxygen. The separation step required for regeneration of inert gas is a very energy intensive process. Conducted techno-economic analysis predicted a hydrogen cost around 50 \$/kg which decreasing the competitiveness of the overall process in front of conventional hydrogen production technologies [126]. Long term potential of ZnO/Zn red/ox couple is estimated that hydrogen cost can be limited by 0.15 \$/kWth [127].

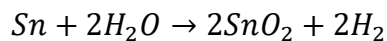
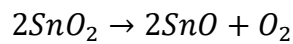
SnO₂/Sn: SnO₂/SnO red/ox couple follows a similar pattern with ZnO/Zn cycle. First process design study of SnO/SnO₂ was conducted at the CNRS [89]. The thermal

decomposition of SnO₂ requires temperatures higher than 1500 °C. Evolved gaseous mixture should be quenched to separate SnO and O₂. Quenching is much more easier than ZnO/Zn cycle due to gap between thermal decomposition temperature and condensation temperature (for Zn; T_{red}=1900 °C, T_b=900 °C, T_m=420 °C whereas for SnO; T_{red}=1600 °C, T_b=1520 °C, T_m=1040 °C) Produced SnO is thermodynamically stable under ambient conditions. Therefore, SnO can be stored to overcome for day-night operational difficulties observed in solar applications.



In lab scale, thermal decomposition experiments utilizing 1 kWth solar reactor illuminated by a 2 m-diameter parabolic dish concentrator, 54% conversion of SnO₂ was demonstrated at atmospheric pressure [128]. Water splitting kinetics is controlled by two subsequent reaction regimes: first order reaction model, diffusion mechanism at longer reaction time.

Charvin *et al.* studied the SnO₂/SnO/Sn red/ox system (Souriau cycle) for two-step thermochemical water splitting cycle [129]. Reaction order for thermal decomposition was found as zero with the kinetic parameters $E_A = 394.8 \text{ kJ/mol}$ and $k_0 = 8.32 \cdot 10^8 \text{ g/s}$ in the temperature range 1400-1600 °C. Sn and SnO₂ nanoparticles produced by solar thermal decomposition of SnO reacts with steam at 525 °C. Approximately 1h needed for 70% conversion. Same conversion was achieved at 18min for direct hydrolysis of SnO process with a peak of $13.6 \text{ mL/g}_{SnO} \text{ min}$. Apparent activation energy for the hydrolysis was found as 67.4 kJ/mol .



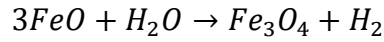
Abanades *et al.* showed that $166.3 \text{ mL}_{\text{H}_2}/\text{g}_{\text{SnO}}$ ($14.8 \text{ mg}_{\text{H}_2}/\text{g}_{\text{SnO}}$) was produced by SnO_2/SnO based thermochemical cycles [89]. The thermal decomposition step was at $1600 \text{ }^\circ\text{C}$ while hydrolysis was done $550 \text{ }^\circ\text{C}$. The oxidation mechanism of SnO was described as shrinking core model in which internal diffusion of water is the rate limiting step.

Abanades studied on the kinetic characterization of solar thermochemical CO_2 and H_2O reductions using SnO nano powders [90]. It was found that both reactions have fast chemical reaction rates followed by diffusion-controlled regime. Activation energies were found to be $51 \pm 7 \text{ kJ/mol}$ for water splitting reaction in the temperature range of 798-923 K and $88 \pm 7 \text{ kJ/mol}$ for CO_2 reduction reaction in the temperature range of 973-1173 K from thermal gravimetric analysis. Higher temperatures are needed for CO_2 reduction to achieve same conversion of SnO nano powders.

Levêque *et al.* studied on the mechanism of tin based solar thermochemical CO_2 and H_2O splitting cycles [130]. It was found that the disproportionation reaction between SnO and Sn/ SnO_2 controls the overall conversion of tin. The disproportionation reaction starts at $600 \text{ }^\circ\text{C}$ and completes at $800 \text{ }^\circ\text{C}$ by the complete oxidation of Sn. At low temperatures, the activity of tin with H_2O is higher than CO_2 . The activation energies were calculated as $53 \pm 1 \text{ kJ/mol}$ for H_2O splitting reaction and $101 \pm 10 \text{ kJ/mol}$ for CO_2 reduction reaction by assuming zeroth order reaction.

Ferrite Based Oxides: One of the first materials used for solar driven two step water splitting was magnetite/wustite red/ox couple [93]. Fe_3O_4 undergoes a phase change reaction and produce almost pure O_2 . This endothermic step requires $2300 \text{ }^\circ\text{C}$ in air [116,131]. These temperatures is higher than the melting points of Fe_3O_4 ($1530 \text{ }^\circ\text{C}$) and FeO ($1370 \text{ }^\circ\text{C}$) which decreases the surface area and deactivates the materials [132,133]. Fe-O phase diagram predicts that the thermal decomposition is only possible below $1370 \text{ }^\circ\text{C}$, melting point of FeO, if oxygen partial pressure is decreased to 10^{-7} bar [134]. Creating such an atmosphere by using either vacuum or inert gas dilution is an energy intensive process which increasing the cost of hydrogen. Water

splitting reaction, on the other hand, is much more straightforward reaction controlled by diffusion limits. This reaction step is slightly exothermic that can proceed temperature below 1000 °C.



Mn-Ferrite: Ehrensberger *et al.* studied iron manganese oxides in a temperature range of 400-900 °C [137,138]. They increased the Mn/Fe ratio from 0% to 30% by conserving the stoichiometry of Fe₃O₄. The partial substitution of Fe atoms with Mn atoms, did not change the hydrogen yield but improves the kinetic of the process in such a way that the thermodynamics starts to control the reaction.

Inoue *et al.* proposed that Zn substitution to MnFe₂O₄ mixed oxide could produce H₂ in solar thermochemical process [47]. The formed ZnO/MnFe₂O₄ was utilized for 3.5 cm³ H₂ production at 1000 °C. The material after experiment was characterized as Zn_{0.72}Mn^{II}_{0.52}Mn^{III}_{0.48}Fe₂O₄. It was also found that the degree of Zn substitution is highly depended on the water dissociation temperature.

Ni-Ferrite: During the thermal decomposition of NiFe₂O₄ products have higher melting point so that deactivation mechanism of Fe₃O₄/FeO is limited [133,142]. However, nickel ferrite undergoes a partial reduction mechanism. This limits the energy storage at the surface decreasing the conversion (NiFe₂O₄/NiFe₂O_{3.8}). Water conversion was reported as 0.3% which is very low considering energy requirement required for excess steam production [133,143].

Agrafiotis *et al.* used NiFe₂O₄ as red/ox material in the temperature range of 700-1400 °C [144]. Performed two cycle showed that an average of 74 μmol H₂/g was produced at 1100 °C while 13 μmol O₂ was evolved per one gram red/ox material. The rate constants were calculated as 0.0621 m³/min · mol for water splitting and 0.0403 L/min for thermal decomposition at same temperatures.

Gokon *et al.* showed that 45% of NiFe₂O₄/m-ZrO₂ reduced at 1400 °C under 6 kW Xe-arc lamp to simulate sun [145]. Ferrite conversion increases as the irradiation time increases. Maximum 9 cm³ H₂/g was produced at 1000 °C. It was found that 46% of the initial surface area was lost after the second cycle. Their recent study showed that the thermal stability of NiFe₂O₄/m-ZrO₂ was improved [142]. 5.06 cm³ H₂/g for NiFe₂O₄ and 6.8 cm³ H₂/g for NiFe₂O₄/m-ZrO₂ were produced during water splitting reactions.

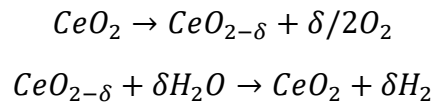
Co-Ferrite: Substitution of cobalt ions with iron increases the oxygen storage capacity. Scheffe *et al.* shows that reduction extent of Co_xFe_{3-x}O₄ increases with an increase in the cobalt content [146–148]. On the other hand, thermodynamic potential towards water splitting [145]. Allendorf *et al.* performed a systematic study on cobalt ferrite structures. They concluded that increasing oxygen capacity does not necessarily increase the hydrogen yields [146]. Therefore, finding an optimum ratio between cobalt and ferrite gains importance for thermochemical water splitting cycles.

Scheffe *et al.* proposed a cobalt ferrite-zirconia composite for solar thermochemical hydrogen production [41]. Samples synthesized by atomic layer deposition process was thermally reduced at 1450 °C. 800 μmol H₂/g was produced during the reoxidation of reduced samples in the temperature range of 900-1400 °C. It was found that the second order reaction and the diffusion mechanisms occurred simultaneously. The apparent activation energies were calculated as 53.9 kJ/mol for the second order reaction and 141 kJ/mol for the diffusion process.

Miller *et al.* studied cobalt ferrite mixed oxides on different monolithic structures [46]. The first cycle performances were measured on per gram ferrite basis as 3.8 cm³ O₂ and no hydrogen production for cast Co_{0.67}Fe_{2.33}O₄/Al₂O₃, and 14.9 cm³ O₂ and 0.15 cm³ H₂ for Co_{0.67}Fe_{2.33}O₄/TiO₂ monoliths in the temperature range of 1100-1400 °C. The cyclic performance between 1st and 4th cycle was compared as 0 to 0.035 H₂/O₂, and 0.01 to 0 H₂/O₂ respectively.

Kodama *et al.* showed that the solar thermochemical performance of ZrO₂-supported cobalt ferrite is dependent on Co/Fe ratio in the temperature range of 1000-1400 °C [117]. High and stable reactivity was achieved for Co_xFe_{3-x}O₄/ZrO₂ with the x value of 0.4-0.7. The maximum hydrogen production rates were found as 1.3 cm³/min · g for Fe₃O₄/ZrO₂, 2 cm³/min · g for Co_{0.42}Fe_{2.58}O₄/ZrO₂ and 0.3 cm³/min · g for ZrO₂.

CeO₂/CeO_{2-δ}: CeO₂ has a fluorite type structure that has a reduction extent up to Ce₂O₃. This reduction requires extreme conditions to proceed even if the total reoxidation is possible by water splitting. Cerium atoms can be found in the structure +3 and +4 oxidation states and it is possible to be reduce up to CeO_{1.65} maintaining the its original crystal structure. The complete red/ox cycle for CeO₂/CeO_{2-δ} is presented as



The solar-driven water splitting process utilizing ceria was firstly demonstrated at lab-scale fixed bed reactor by Abanades and Flamant [152]. Fast water splitting kinetics was observed in the temperature range of 400-600 °C. These fast kinetics with partial reduction capabilities increases the yield making an advantageous process for solar application [46,153]. Nonstoichiometric nature of CeO₂/CeO_{2-δ} seems to lower hydrogen yield but 0.38–0.53 mmol H₂ per gram of ceria was achieved during the thermochemical water splitting cycles [94].

The thermal decomposition of CeO₂ can be achieved at temperatures around 1400-2000 °C under reduced pressures such as 100-200mbar. These high temperatures decreases the practical implementation problems due to material selection, radiative losses, sintering etc. [46]. Therefore, thermodynamic advantage coming from environments consists low oxygen partial pressures are generally selected to decrease thermal decomposition temperature. Doping with an another metal oxide was also used as alternative to increase oxygen storage and thermal stability of CeO₂

[153,154]. Zirconia substitution, as an example, preserves the original crystal structure of CeO₂ up to certain extent and limits the sintering mechanism [48,57].

Extensive studies have been conducted to improving the reduction extent of ceria by adding other metal ions [95,155–158]. Those addition improves the reducibility, by decreasing the enthalpy of reduction, and the entropy of reduction [100] [159,160]. Le Gal et al. studied ceria-zirconia solid solutions (Ce_{1-x}Zr_xO₂) by using thermogravimetric balance method in the range of x = 0 to x = 0.5 [48]. The reduction extent increased with an increase in the Zr substitution. However, hydrogen yield did not correlate the improved from thermal decomposition performance due to chemical stability of the solid solution. Largest hydrogen yield was observed when x=0.25 [57].

The effect of transition metals on CeO₂ reduction was also reported for Mn, Fe, Ni, Cu [49][153] in the temperature range of 1000-1400 °C. Solid solutions such as CeO₂-MnO, CeO₂-NiO and CeO₂-Fe₂O₃ shows better performance when compared to non-doped CeO₂. Water splitting performance does not increase for Co- and Cu-mixed CeO₂. This was ascribed to the formation of non-active compounds such as Cu₂O and CoO although the improvement in the thermal decomposition temperature was achieved. The interactions between precious metals and ceria have been investigated in many catalytic and thermochemical cycle studies for the past decades. It is seen that the addition of low percentage precious metals (PM: Pt, Pd, Rh) on ceria and ceria-containing oxides greatly changes the red/ox properties by creating catalytically active sites at PM-CeO₂ interface. In catalytic applications, it is well-proved that ceria plays a direct role in both O₂-lean and O₂-rich conditions by cycling its oxidation state between Ce⁺³ and Ce⁺⁴ via Mars van Krevelen mechanism.

Perovskites: In the past years, perovskite type materials were used as new form of material for thermochemical two-step water splitting cycles [40,161]. Perovskites with a chemical formula ABO₃ has a cubic symmetry within the space group of pm3m as shown in Figure 1.5. A cation represents larger cation with 12-fold coordination whereas smaller cation B has 6-fold coordination. Due the possibilities

coming from A and B selection, perovskites offer large variety of electronic, ionic or magnetic properties [162].

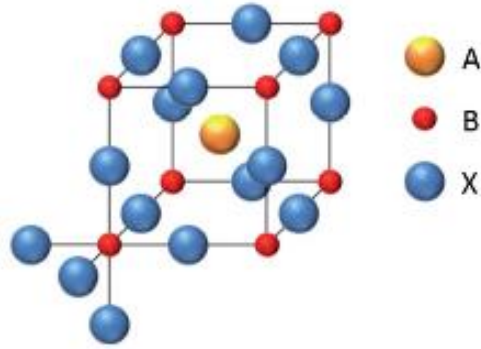


Figure 1.5. Ideal cubic form of perovskite with Pm3m structure

Goldschmidt tolerance factor is used during the characterization of perovskites. The tolerance factor, t is calculated from the ionic radii of the A and B sites of cations [163]. The correlation, tolerance factor, between structural geometry and ionic radius of the cations is calculated as

$$t = \frac{r_A + r_O}{\sqrt{2}(r_B + r_O)} \quad \text{Eq. 2}$$

Ideal cubic perovskites have a tolerance factor of 1 while the deviations from 1 simply shows the distortions in the lattice. Those distortions generates new crystallographic structures such as rhombohedral, tetragonal, monoclinic, orthorhombic, triclinic [162,164,165]. In terms of thermochemical processes, point defects in the perovskite structures are generally studied due to their effects on the equilibrium thermodynamics and reaction kinetics. Point defects can be grouped into three categories as electronic, ionic, and cationic defects. Electronic defects occur due to the excess electrons (n-type) or electron holes (p-type). Those parameters effect the surface charge transfer so that the oxygen exchange rates and bi-directional oxygen diffusion between surface and lattice. Ionic defects are well known as oxygen vacancies. Those vacancies enable oxidation and thermal decomposition of perovskites while preserving the crystal structure. Therefore, the concentration of

oxygen vacancies directly controls the hydrogen yield during water splitting [162,166,167]. Cationic defects occur due to the imbalances in the stoichiometry of A and B site. In terms of thermochemical process, cationic defects have a minor importance comparing to anionic defects [168–172].

Oxygen vacancy and nonstoichiometry are generally confusing terms. Oxygen vacancies are occurred due to charge imbalances in the crystal structure. Typically, some of the oxygen atoms that should be in metal oxide's perfect crystal structure are missing (presence of more positive ions). The vacancy formation occurred without disturbing the lattice. The charge imbalances improve the oxygen mobility for rearrangement of the charges. Oxygen non-stoichiometry occurs as the number of missing oxygen atoms increased. The missing oxygen atoms distorts, not changes, the crystal structure since the imbalance in the net charge could be sustained by the rate of oxygen mobility [173]. For example, the non-stoichiometry of ceria occurred in the range of $0.018 \leq \delta \leq 0.052$ [174]. Further loss of oxygen completely destroys the existing crystal structure and ends up with a new phase called as phase transformation at the end.

Oxygen vacancies offers a huge potential in terms of thermochemical water splitting processes. The limits are determined by the perovskite stability and the extent of phase transformation. For example, highest oxidization state for $ABO_{3-\delta}$ is achieved when $\delta=0$ while the reduction may proceed up to $\delta=0.5$ for most perovskites such as $LaSrCo_2O_5$, $SrFeO_{2.5}$, $SrMnO_{2.5}$ and $LaNiO_{2.5}$ [175–179]. In some perovskite structures ($Ba_{1-x}Sr_xCo_{1-y}Fe_yO_{3-\delta}$ etc.), non-stoichiometry may reach $\delta>0.5$ [180–182]. However, high oxygen vacancy formations can decrease the chemical stability with phase instabilities due to the lack of oxygen holding the anions and cations together [182–184]. The availability of oxygen vacancies in the perovskite structure offers a huge potential for thermochemical process. Taking CeO_2 as benchmark example, only 2-3% of the oxygen sites are used during thermochemical water splitting reactions [27,185]. However, 16.7% of total oxygen in the perovskites can be exchanged during thermal decomposition and water splitting when nonstoichiometry is in the range of $0 \leq \delta \leq 0.5$. Several p-doped perovskites based

on manganese [17,37,39,59,186–189], chromium [190], cobalt [190], or iron [60] have been investigated for thermochemical cycles [191–195] as shown in Table 1.5. The obtained mixture of electron holes with high oxygen vacancies enhances the thermal decomposition temperature. This is created commonly by Ca^{2+} , Ba^{2+} , Sr^{2+} doping to the A site [15] [17,37,39,59,186–189]. The Goldschmidt tolerance-factor was close to 1 making a structurally favorable perovskite [196]. A brief literature analysis was presented in Appendix A.

Table 1.5 Hydrogen yields of perovskites during thermochemical water splitting processes

Perovskites (x+y=1)	Temperature Range (°C)	Hydrogen yield ($\mu\text{mol H}_2/\text{g}/\text{cycle}$)	Ref
$\text{La}_x\text{Sr}_y\text{MnO}_{3-\delta}$ ($0.6 \leq x \leq 0.9$; $0.1 \leq y \leq 0.4$)	800-1400	10-102	[59]
$\text{La}_x\text{Sr}_y\text{MnO}_{3-\delta}$ ($0.5 \leq x \leq 0.65$; $0.35 \leq y \leq 0.5$)	900-1400	113-160	[60]
$\text{La}_{0.6}\text{Sr}_{0.4}\text{Cr}_{0.8}\text{Co}_{0.2}\text{O}_{3-\delta}$	800-1200	50	
$\text{Ba}_{0.5}\text{Sr}_{0.5}\text{Co}_{0.8}\text{Fe}_{0.2}\text{O}_{3-\delta}$	800-1000	83	
$\text{La}_{0.6}\text{Sr}_{0.4}\text{Cr}_{0.8}\text{Co}_{0.2}\text{O}_{3-\delta}$	800-1200	51	
$\text{La}_{0.6}\text{Sr}_{0.4}\text{CoO}_{3-\delta}$	800-1300	107	[39]
$\text{La}_{0.6}\text{Sr}_{0.4}\text{Cr}_{0.8}\text{Co}_{0.2}\text{O}_{3-\delta}$	800-1200	50	[190]

1.3 Steam Methane Reforming Technology

Almost 50% of the world's hydrogen production is supplied from methane reforming process [197,198]. The main product of the process consists of syngas (a gas mixture containing CO, H₂ and CO₂ in certain cases). Syngas production provides flexibility for the chemical industry because it could produce synthetic fuels out of methane (known as synfuel cycle) [199–202]. Steam and autothermal reforming processes are widely used in industrial syngas and hydrogen production [197,203]. The most important reactions for steam methane reforming (SMR) and autothermal reforming (ATR) reactions were presented in Table 1.6. Steam reforming, as the most preferred process for industrial syngas and hydrogen production, results in a H₂/CO ratio close to 3 [197]. For the CO free hydrogen production, steam methane reforming reaction is coupled with water gas shift reaction.

Table 1.6 Reaction enthalpies of methane reforming reactions

Reactions	ΔH_{298K}° (kJ/mole)
<i>Steam Methane Reforming</i>	
• CH ₄ + H ₂ O ⇌ CO + 3H ₂	206
• CO + H ₂ O ⇌ CO ₂ + H ₂	-41
<i>Autothermal Reforming</i>	
• CH ₄ + 1.5O ₂ ⇌ CO + 2H ₂ O	-520
• CH ₄ + H ₂ O ⇌ CO + 3H ₂	206
• CO + H ₂ O ⇌ CO ₂ + H ₂	-41

Steam reforming, as an energetically demanding reaction, is limited by thermodynamic constraints. The equilibrium conversion as a function of temperature

is shown in Figure 1.6. The reaction should be carried out at high temperatures and low pressures for maximum methane conversions. High temperatures also lead higher CO selectivity by suppressing Boudouard reaction. Steam reforming reaction is conducted at temperatures between 800 °C to 1000 °C and pressure in the range of 20-30bar to obtain industrially acceptable syngas [11]. Due to high endothermicity, large amounts of heat energy to be supplied to the reactor to maintain the conversions and prevent coke formation.

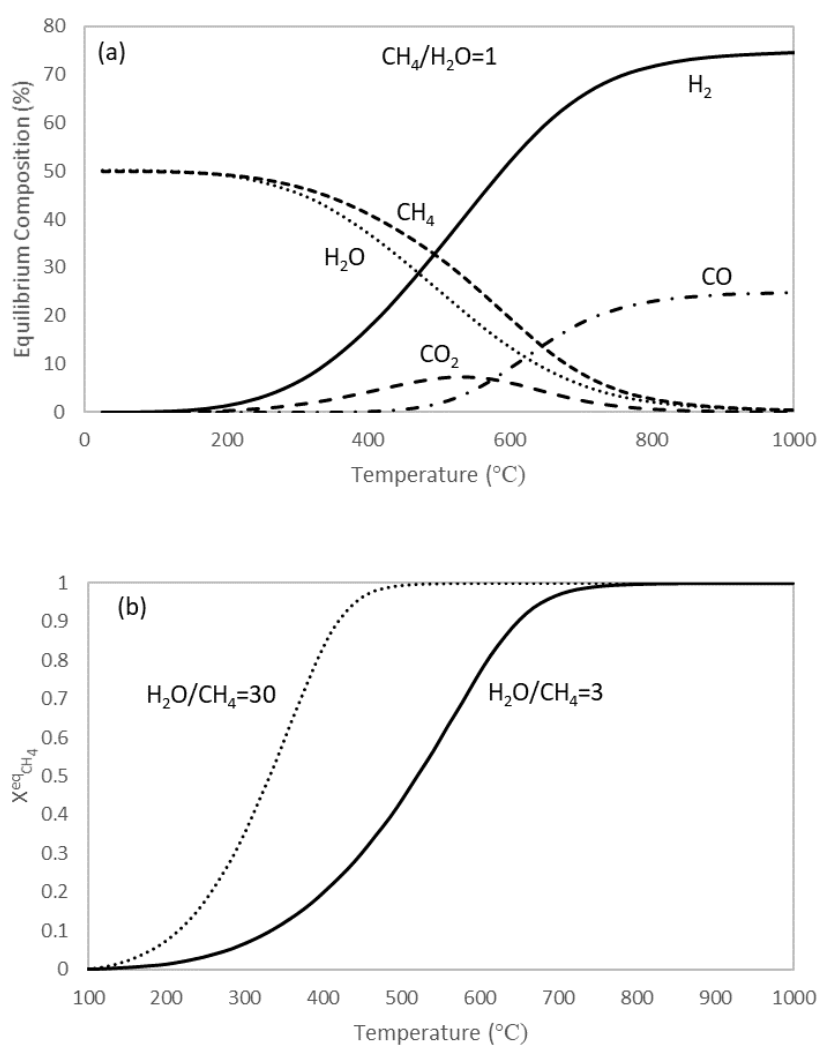


Figure 1.6. Estimated equilibrium compositions for steam methane reforming at $P=1\text{atm}$ (a) the effect of temperature on product distribution and (b) the effect of $\text{H}_2\text{O}/\text{CH}_4$ ratios on equilibrium conversion

High steam to carbon ratios (> 3) results in higher conversions at lower temperatures (Figure 1.6 (b)) but industrial plants usually operate at lower ratios (< 2.5) in order to keep the equipment sizes economically viable [204]. Consumption of methane as fuel for sustaining reaction energy requirement can reach 20% of the total methane consumption of the reforming plant depending on the downstream processes [205]. Research on combination of alternative energy sources to conventional steam methane reforming is getting more attractive for reducing the energy penalty of the process [206].

Embedding solar heat to methane reforming process has been studied in various perspectives [206–211]. Energy requirement of this reaction has been supplied by using both indirect and direct solar heating [206,209,212–214]. In direct heating systems, the reactant gas mixture and/or the catalyst are heated directly by the solar radiation using a reactor with quartz windows as aperture to run the endothermic reforming reaction [215]. The advantages of this reactor / receiver system are listed as low heat losses due to high solar flux capability, fast response to thermal transients due to compact, low mass receiver – reactors and improved overall efficiency [216]. However, major problems related to the intermittent nature of solar energy.

Nickel based catalysts is widely used in industrial steam reformers due to its optimal stability and cost [197,217]. However, high activity toward methane decomposition to carbon and hydrogen forms carbon whiskers that can influence catalytic activity and reactor performance [218,219]. On the other hand, palladium is extensively used as the active component for the total oxidation of environmentally unfriendly gaseous emissions and hydrocarbons [220,221]. Oxidation is usually described by Mars–van Krevelen mechanism [222]. The oxidation rate is dependent on the density and stability of active site pairs, PdO-Pd*, implying that the rate limiting step is the C-H bond activation. The higher stability PdO limits the partial conversion of PdO to Pd* so that less sites formed for C-H bond breakage. Strong support metal interaction between Pd and CeO₂ stabilizes the PdO which lowers the activity towards total oxidation [223].

Palladium also gives promising results during steam methane reforming reaction [224–226]. CeO₂ as a potential metal support is considered as a good candidate due to its red/ox capability and strong metal interaction [227,228]. Synergetic effect (due to Pd oxidation state modification by Pd/CeO₂ interface) between Pd and CeO₂ increases the reforming rates almost two order of magnitude comparing to Pd/Al₂O₃ [224]. In addition, the facile oxygen transfer at the Pd/CeO₂ interface results in rapid removal of coke deposited during methane decomposition, and inhibits coke build up during the reaction [229].

Steam reforming as energy intensive process [230,231] needs higher reaction temperature to increase methane conversion [232,233]. Microchannel reactor technology can be a promising technology for solving heat and mass transfer problems especially encountered in reforming processes [234]. Energy demand of reforming reaction can be sustained by coupling reforming reaction by combustor [235]. The heat released during combustion was used for maintaining the heat demand for the endothermic side of the microreactor. [236,237]. The practices were demonstrated for methane[234,238], methanol [232,239], dimethyl ether (DME) [240], glycerol [241,242] feedstocks. As the name implies, microchannel reactors are constructed by parallel, identical channels in the dimensions less than 1 mm. The length and the diameter of the channel should be carefully determined for minimizing transport limitations [232,234]. Optimized channel characteristics enhances the surface to volume ratio of the reactor so that the amount of reactant gas contacting the catalysts increases yielding higher conversions [233,240]. Loading of catalysts is another factor affecting the performance of microchannel reactors. The catalysts can either be coated on microchannels or be used in powder form. Either way, high activity, low pressure drops, no hot spots are essential factors for micro applications. Coating increases dispersion of the catalysts by minimizing pressure drop hence enhances the catalytic activity [243]. However, catalytic performance is dependent on the coating procedure and performance [236,244]. With the improvement in channel characteristics, catalysts loading, thermal conductivity, the rate of reforming reactions losses its dependency in mass and heat transfer of the system [245].

Especially for the reactions highly dependent on the energy transfer, the reaction controlled region shifts to kinetically controlled region due to minimization of transport related problems [234,243]. Despite the unique advantages mentioned above, microchannel reactors suffers from metal dusting corrosion (due to increased surface area with the reaction environment) [244], and sintering (due to narrow crystallite size distribution and high initial dispersion of the catalyst) [246,247].

1.4 Hybrid Systems (Solar Reformers)

Methane reforming is a highly endothermic process discussed in previous section. The energy requirement of the system can be sustained from solar energy by so called solar reformers. These reformers can be heated directly or indirectly with the integration of solar receivers and the reactor. Since the reforming reaction has a rate limited step which is controlled by heat transfer, temperatures around 1000 °C will be enough for controlling heat flux. CAESAR project, based on dry reforming of methane, is one of the first commercial scale demonstration in the area of solar reformers [248]. The reformer had a power input nearly 150 kW with a heat flux around 2 MW/m². Therefore, the operation temperature can easily be reached to temperatures higher than 1000 °C [249]. Similar demonstration was conducted for steam methane reforming by Weizmann Institute of Science under the project of SOLASYS [250]. In this setup, concentrated solar energy directly absorbed on the catalytic ceramic absorber. Reactant gases were introduced to the system around the quartz windows. After the reforming reaction, product gases left the system from behind where they exchange heat with fresh reactants as given in Figure 1.7. DIAPR system developed by Berman *et al.* used manganese promoted ruthenium as catalyst under direct solar radiation [211]. 92% methane conversion was sustained over 500 hours operation at 1100 °C.

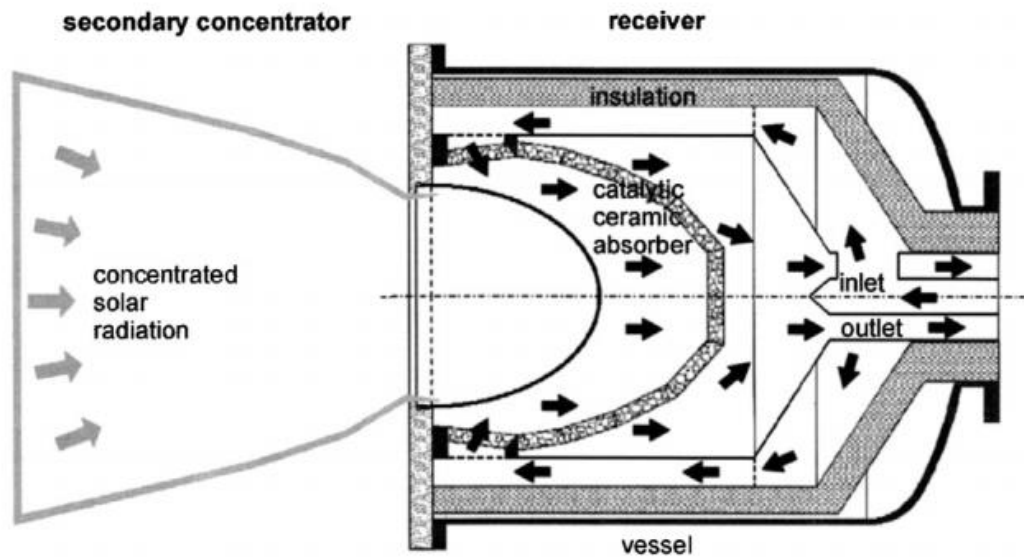


Figure 1.7. Solar reformer designed for SOLASYS project [211]

ASTERIX (Advanced Steam Reforming in Heat Exchanger) system developed under the German-Spanish Gas Cooled Solar Tower program [211]. The group aimed to maximize the solar energy absorption with methane conversion. The system was designed as a heat exchanger where air, as heat transfer agent, was heated to 1000 °C (Figure 1.8). The catalyst is packed in a tubular reactor and heated by hot air. The reactant gases enter the reactor at 500 °C and heated to 850 °C for reaching methane conversion almost 91%. Considering the pilot and commercial scale solar reformer demonstrations, the solar energy was successfully coupled to methane reforming process. Nevertheless, the effect of dynamic nature of solar irradiation on product yield has not been concluded yet.

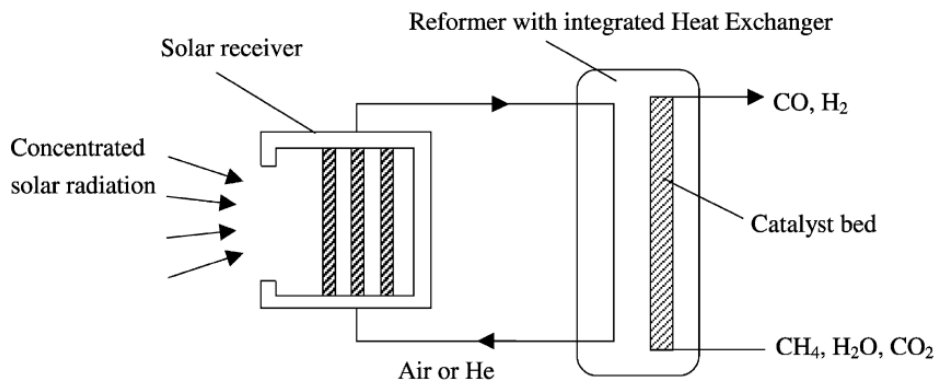


Figure 1.8. Schematic of indirect solar reformer used in ASTERIX system [215]

1.4.1 Solar Energy Collectors and Reactors

The energy requirement of thermochemical processes can be sustained by concentrating beam radiation into the reaction chamber to get high heat fluxes. Conventionally, it is done by collecting solar energy over a large area and then focusing it to a small zone. Parabolic through, tower and dish systems are generally preferred due to their availability in the market as given in Figure 1.9. Parabolic through dishes use a tubular receiver at their focal line. Tower systems, on the other hand, needs a heliostat field. The solar beams reflected from heliostats concentrated on a focus area at the top of the tower. The operation principle of parabolic dishes is very similar to parabolic trough systems. The concentrated beams are collected at the focus of the dishes.

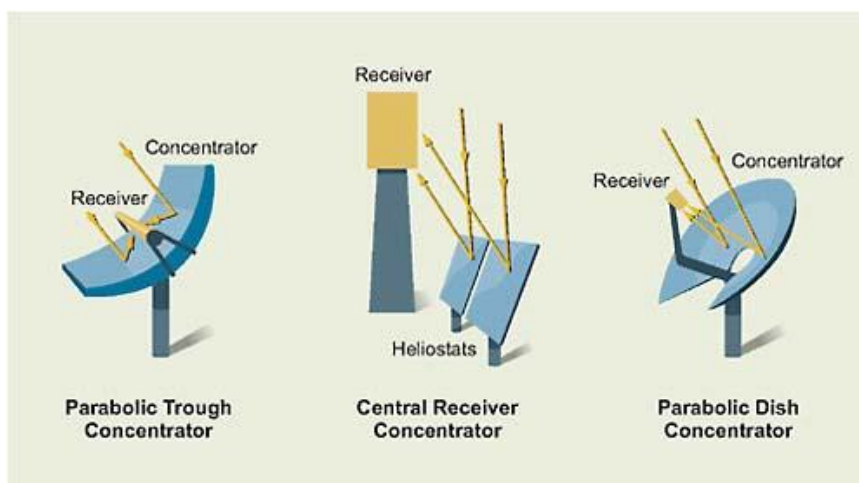


Figure 1.9. Schematic of main solar concentrating technologies [251]

After the concentration of solar energy, the beams are directed to the reactor to drive desired reaction. For this purpose, different reactor types such as multi-tubular reactors [252], fixed bed reactors [253], fluidized bed reactors [254], moving packed bed reactors [255], counter-rotating ring reactors [256], solar vortex reactors [257–259], or reactors using liquid metal for efficient heat transfer [260] are reported as pilot plant or as conceptual operations. Recent improvements in reactor design and cycle management have helped increase the total efficiency of the solar to fuel process to above 5% [261]. Studies performed by different groups on solar concentrators and reactors are summarized as follows;

1.4.2 Paul Scherrer Institute (PSI)

Small quartz packed bed reactor was tested as a primary setup in Paul Scherrer Institute (PSI) under solar radiation. The solar radiation was uniformly distributed on the red/ox material ($\text{Ni}_{0.5}\text{Mn}_{0.5}\text{Fe}_2\text{O}_4$ powder mixed with Al_2O_3) by the help of a secondary concentrator. The thermochemical water splitting reaction was performed under Ar ($>800\text{ }^\circ\text{C}$) and Ar/ H_2O ($>500^\circ\text{C}$) flows. The evolution of oxygen and hydrogen was demonstrated [262], however, the system has a certain drawback during thermal decomposition. Only a small fraction of red/ox material was reduced

due to temperature non-uniformities coming from indirect solar adsorption. Therefore, the configuration was not followed up.

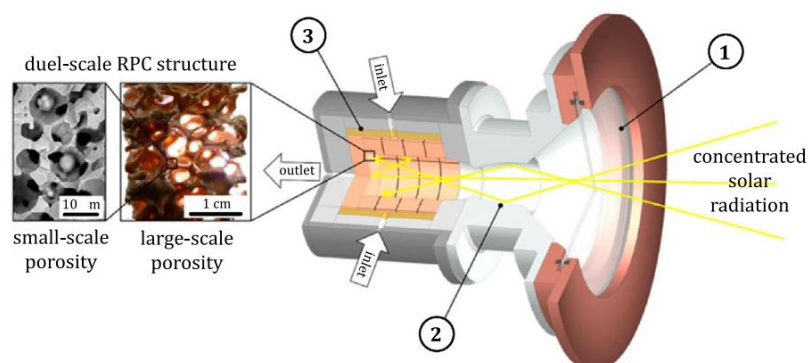


Figure 1.10. Solar reactor with porous ceria monoliths [126]

The group also built a rotary cavity type reactor for porous ceria. Direct solar radiation was passed through a quartz window so that the ceria absorbed energy as much as possible. The reactant gas entered the reactor radially as shown in Figure 1.10. The thermal decomposition step reaches to temperature as high as 1700 °C. Water was introduced to the system during cooling period which is around 900 °C. Almost 23 cycles were reported for this reactor type. The reactor suffers from thermal losses coming from radiation and conduction [27].

1.4.3 German Aerospace Center (DLR)

The DLR group has designed several prototype reactors for solar thermal processes under the scope of EU Framework Programmes for Research and Technological Development project since 2002 [263]. They were mainly coated structured materials with red/ox materials having a potential towards thermochemical processes. The first reactor was a single solar receiver reactor. The thermal decomposition and water splitting processes were taking part at the same environment. Structured supports made from silicon carbide coated with iron due to

high thermal conductivity. Uniform temperature profile at the surface of the structured material was observed around 1200 °C [264]. Thereafter, the reactions were split into two adjacent but separated cylindrical reactors as seen in Figure 1.11. Reactors were operated periodically by the help of shutter in such a case that the red/ox material in one reactor was exposed to solar irradiation for thermal decomposition (1200 °C) while water splitting process is conducted by the reduced material in the adjacent reactor (>800 °C) [265]. 100kWth solar tower coupled with reactor was installed on the Plataforma Solar de Almería (PSA) [266].

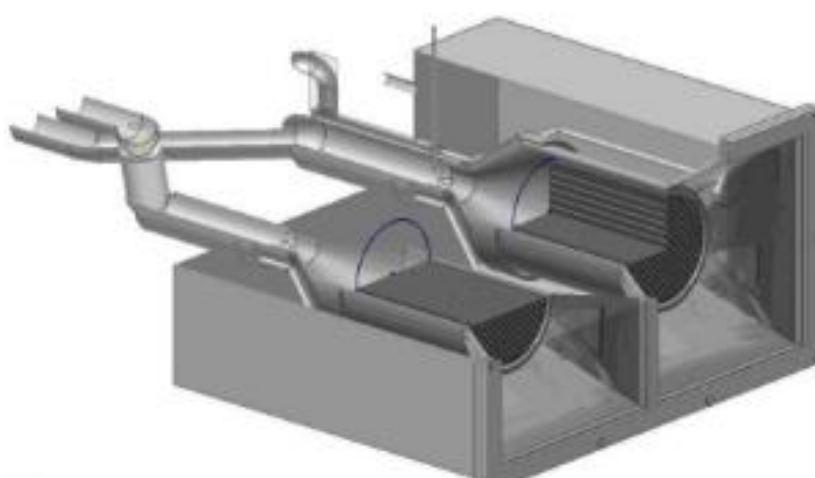


Figure 1.11. Solar reactor developed for HYDROSOL project [265]

1.4.4 Nigata University Group

Internally circulating fluidized bed reactor was proposed by Gokon et al. [267]. In this concept, solar energy was concentrated on the solar tower directing the irradiation to the reactor with quartz window. Red/Ox material was circulated up to center of the reactor in order to prevent quartz window from collision with particles. In the concept, two concentric cylinders were used where inner cylinder carries the particles upward under the flow of reaction gases. Particles then fell into annulus region. Particles absorbed the solar irradiation during the transfer from inner cylinder to annulus. Therefore, solar energy transferred from top to bottom of the reactor.

The concept was first shown in a prototype reactor with electrically heated furnace. Oxygen evolution with consecutive water splitting reaction was demonstrated with $\text{NiFe}_2\text{O}_4/\text{ZrO}_2$ [44][136]. Thereafter, heating was switched to solar simulator as given in Figure 1.12 [268]. Inhomogeneous irradiation results with a temperature gradient through the reactor resulting incomplete reduction; in other words, the reduction extent of $\text{NiFe}_2\text{O}_4/\text{ZrO}_2$ was decreased significantly. The group then studied on the coated structured materials. The coated materials were placed inside the reactor and tested under solar simulators. Thermal decomposition was conducted around 1500 °C. The reduced material then used for water splitting reaction carried out at 1200 °C. Since simulated solar energy adsorbed mainly at the top the coated material, significant temperature gradients were observed along the material [269].

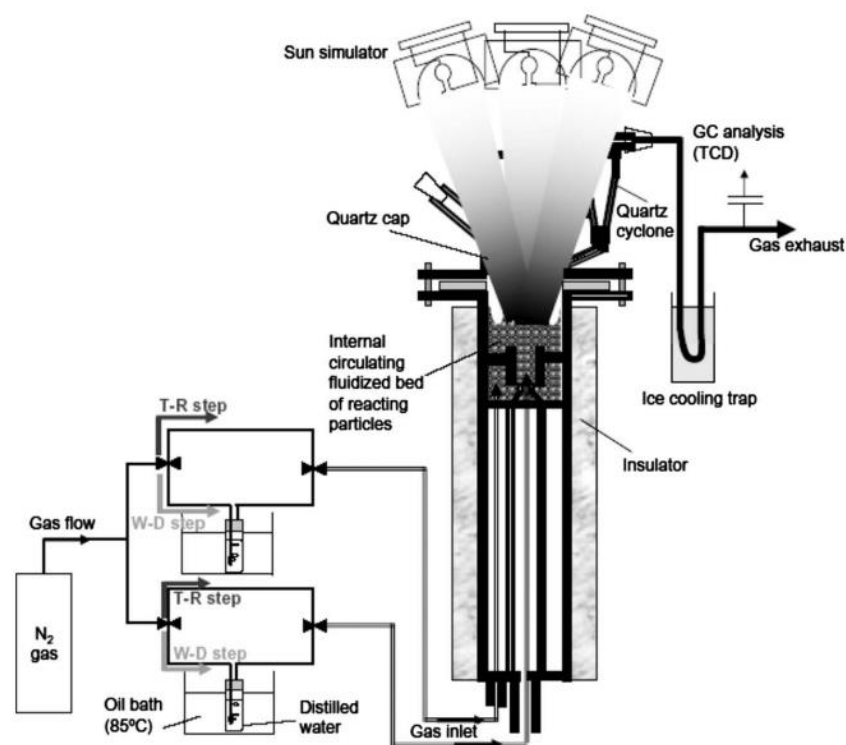


Figure 1.12. Internally circulating fluidized bed reactor set-up developed by Kodama Group [270]

1.4.5 Tokyo Institute of Technology

A rotating cylindrical reactor concept was developed for continuous hydrogen production as shown in Figure 1.13. The reactor was configured in such a way that $\text{CeO}_2/\text{ZrO}_2$ coated on ceramic rotated through thermal decomposition and water splitting cells. These cells can be named as light and dark side respectively. Thermally reduced $\text{CeO}_2/\text{ZrO}_2$ coated on ceramics in the light side was rotated to dark side where it contacts with water vapor for hydrogen production. The rotation was sustained by external electric motor. Ar was selected as inert gas as well as a sealing gas between oxygen evolution and hydrogen generation cells. Xenon lamps was used for simulating solar irradiation [271]. Coated ceramics were successfully tested for about 15mins without degradation [272]. However, ceramics were fractured over time due to the thermal expansion and contraction between oxygen evolution and hydrogen generation cells [273,274].

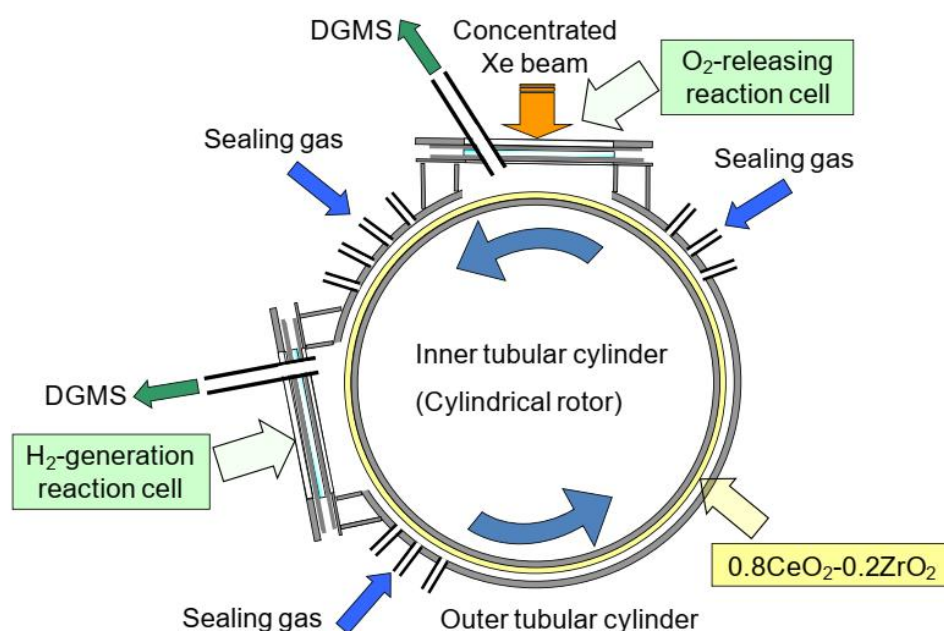


Figure 1.13. Rotary type solar reactor developed by Tokyo Institute of Technology [272]

1.4.6 Sandia National Laboratory

The research group in Sandia National Laboratory develop a rotating reactor, the Counter-Rotating-Ring Receiver/Reactor/Recuperator (CR5) as shown in Figure 1.14. The reactor consists counter rotating rings that promotes continuous hydrogen and oxygen production. Red/Ox materials coated on fins were mounted on the rings. Fins were manufacturing from ferrite and yttrium stabilized zirconia [96]. During the rotations, red/ox materials were passing through quartz window where thermal decomposition taking place (1600 °C). The reduced materials were reoxidized by water at the back side of the reactor (1100 °C) [256]. Successful continuous operations were demonstrated with CR5 reactor [275]. However, fins were not able to maintain their integrity due to high temperature difference (500 °C) over time. Thermal stresses broke the fins and the rotation ability was completely destroyed for long time tests [276].

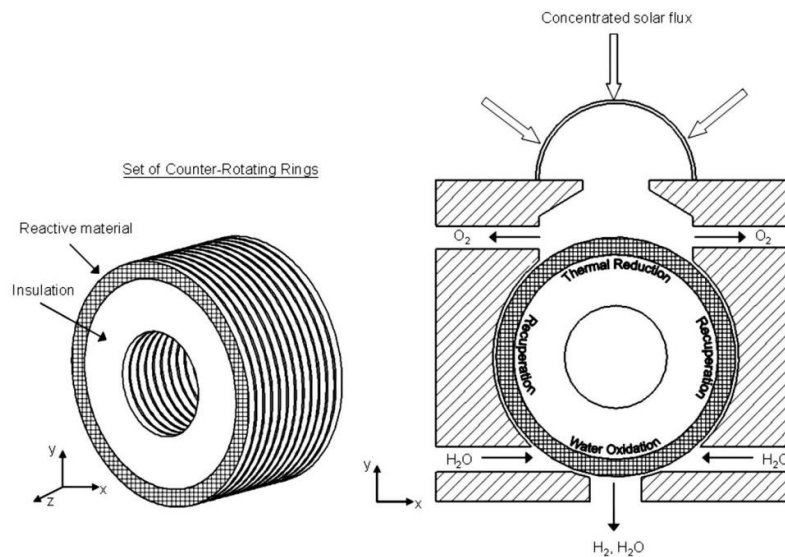


Figure 1.14. Schematic of CR5 developed by Sandia National Laboratory [256]

1.5 Thesis Statement

The sustainability towards future energy demand is dependent on the integration of renewable sources such as solar energy. Chemical looping process in the scope of thermochemical cycles offers high potential for such an integration. The potential of storing solar energy in the chemical bonds is investigated through water splitting and/or carbon dioxide reduction process where H₂ and/or CO are the value-added products of the system. In this area, several potential applications with red/ox materials were proposed. Nevertheless, the hydrogen production rates were averaged around 160 μmol/g MO_x (100 mmol H₂/mol MO_x). In addition, the temperature difference between thermal decomposition and oxidation steps was generally in the range of 200-600 °C which decreases the energy efficiency of the overall system. Methane reforming technology produces steady syngas composition around 800-1000 °C with high methane conversion. The overall process is an energy intensive process due to the high endothermicity of the reforming reaction. Conventionally, required energy to drive the process is sustained from additional methane combustion decreasing the overall yield (H₂ produced per methane used). In the past two/three decades, solar energy integration was also studied as solar reforming technology. The proposed systems enhance the energy efficiency of the conventional methane reforming. Nevertheless, the heat transfer related problems with solutions towards intermittent nature of solar energy are still awaiting solution. In the scope of this thesis, the problems related to high hydrogen yields and solar energy integration are addressed. A unique hybrid process design was also formulated.

CHAPTER 2

MATERIALS

2.1 Bulk Materials

Co_3O_4 was supplied from Ege Ferro (99.6% metal basis).

$\text{Pt-Co}_3\text{O}_4$ samples were synthesized by using incipient wetness impregnation method. First, deionized (DI) water was added dropwise to 100 mg of Co_3O_4 (Ege Ferro) until a paste was formed. The added amount was noted as V_x (milliliters DI water per 100 mg Co_3O_4). Depending on the percentage of platinum on Co_3O_4 , the volume of platinum source (0.035 M aqueous platinum solution in this thesis) was calculated as V_y (milliliters of platinum solution per 100 mg Co_3O_4). This calculated volume was diluted with DI water until total volume V_x was reached. This final solution was dropwise to 100 mg Co_3O_4 until a paste was formed. The paste was mixed with a glass rod for 30 minutes. The paste was left at room temperature overnight. The mixture was dried at 80 °C for 5 hours (Cole-Palmer Model 09015-56 Laboratory Oven). The sample was calcined at 300 °C for 3 hours (NEY 2-525 Series II Box Furnace).

$\text{Ni-Al}_2\text{O}_3$ samples were synthesized by using incipient wetness impregnation method. First, deionized (DI) water was added dropwise to 100 mg of $\gamma\text{-Al}_2\text{O}_3$ (Alfa Aesar, CAS # 1344-28-1) until a paste was formed. The added amount was noted as V_x (milliliters DI water per 100 mg $\gamma\text{-Al}_2\text{O}_3$). Depending on the percentage of nickel on $\gamma\text{-Al}_2\text{O}_3$, the amount of $\text{Ni}(\text{NO}_3)_2 \cdot 6\text{H}_2\text{O}$ (Merck CAS# 13478-00-7) salt was calculated. Then, the calculated amount of nickel salt was dissolved in DI water slowly until total volume V_x was reached. The mixture was stirred by glass rod for 15 minutes. The slurry was dried overnight at room conditions. The sample was

additionally dried at 90 °C for 2 hours (Cole-Palmer Model 09015-56 Laboratory Oven). The residue was calcined at 650 °C for 3 hours with a heating rate of 10 °C/min (NEY 2-525 Series II Box Furnace). The procedure was repeated for Ni-CeCoO₃.

3 wt.% Co-Al₂O₃ samples were synthesized by using incipient wetness impregnation method. The precursor solution was prepared by dissolving 978.3 mg Co(NO₃)₂·6H₂O (Matheson Coleman and Bell, CAS # 10026-22-9) salt into 30 mL DI water. 4.5 mL of precursor solution was added into 3 grams of γ -Al₂O₃ (Alfa Aesar, CAS # 1344-28-1) slowly. The mixture was stirred by glass rod for 15 minutes. The slurry was dried overnight at room conditions. The cobalt content of this sample was equivalent to 1 wt.% Co-Al₂O₃. An appropriate amount of precursor solution was added to increase the cobalt content to 3 wt.%. The sample was left overnight at room condition followed by a drying at 90 °C for 2 hours (Cole-Palmer Model 09015-56 Laboratory Oven). The sample was calcined at 650 °C for 3 hours with a heating rate of 10 °C/min (NEY 2-525 Series II Box Furnace).

CeCoO₃, CeFeO₃ and Sr_{0.6}Ce_{0.4}Fe_{0.7}Co_{0.3}O₃ (SCFC-6473) perovskites are synthesized by using sol-gel method. Fe(NO₃)₃·9H₂O (Sigma-Aldrich, CAS # 7782-61-8), Co(NO₃)₂·6H₂O (Matheson Coleman and Bell, CAS # 10026-22-9) and Ce(NO₃)₃·6H₂O (Merck, CAS # 10294-41-4) were used as precursors. Depending on the molar ratio of the elemental compositions (i.e. molar ratio of Ce/Co is 1 for CeCoO₃), appropriate amounts of precursors were dissolved in deionized water. The aqueous solutions of metal nitrates were mixed under continuous stirring. The amount of citric acid was determined to achieve a molar ratio of total metal ions to citric acid 1:2. Citric acid was dissolved in deionized water in the round bottom flask. After complete dissolution of precursors, precursor solution was added into the dissolved citric acid slowly at constant stirring. The condenser was attached to the round bottom flask. The final solution was stirred to give complexation for about 2 hours at 80 °C under continuous cooling at the condenser. After complexation, the solution was transferred into a beaker and kept in the oven at 80 °C overnight (Cole-Palmer Model 09015-56 Laboratory Oven). The formed cake was ground in an agate

mortar. Two stage calcination was followed during the synthesis of perovskite. The grounded cake was calcined at 350 °C for 3 hours with a heating rate of 10 °C/min. The residue was cooled down to room temperature and grounded again. Finally, the powder was calcined at 800 °C for 6 hours with a heating rate of 10 °C/min (NEY 2-525 Series II Box Furnace).

Pd/CeO₂ oxide was prepared by incipient wetness method by using palladium (II) nitrate solution (Pd(NO₃)₂, 99.95 %, Alfa Aesar) and cerium (IV) oxide powder (CeO₂, 99.9 %, Alfa Aesar). First, deionized (DI) water was added dropwise to 100 mg of CeO₂ until a paste was formed. The added amount was noted as V_x (milliliters DI water per 100mg CeO₂). Depending on the percentage of palladium on CeO₂, the amount of Pd(NO₃)₂ salt was calculated. Then, the calculated amount of palladium salt was dissolved in DI water slowly until total volume V_x was reached. The mixture was stirred by glass rod for 15 minutes. The slurry was dried overnight at room conditions. The sample was additionally dried at 90 °C for 2 hours (Cole-Palmer Model 09015-56 Laboratory Oven). The residue was calcined at 450 °C for 5 hours with a heating rate of 5 °C/min (NEY 2-525 Series II Box Furnace).

Lead rods containing 99.99 wt.% Pb (Altin Cipa) were obtained from the local market and used without further purification during the experiments.

2.2 Monolithic Samples

The 30mm x 30mm x 10mm, 200 cpsi (cells per square inch) mullite monoliths were coated by a modified incipient wetness procedure, without any wash coat layer. Prior to doping, all monoliths were etched in 2 M HCl solution for 2 hours in the ultrasonic bath (Alex Machine Ultrasonic Cleaner). Etched monoliths were washed with boiling DI water. Chlorine content in elutriated water was tested with AgNO₃ (Merck CAS # 7761-88-8). The washing procedure was repeated several times until a clear elutriated water was observed. Chlorine free etched monoliths were dried at 80 °C overnight (Cole-Palmer Model 09015-56 Laboratory Oven). Etched monoliths were

calcined at 500 °C for 3hours with a heating rate of 10 °C/min (NEY 2-525 Series II Box Furnace).

Doping Co, Pb, Ce and Ni was started by the preparation of the ionic solution. Depending on the percentage of metals on monoliths, the amounts of $\text{Co}(\text{NO}_3)_2 \cdot 6\text{H}_2\text{O}$ (Matheson Coleman and Bell, CAS # 10026-22-9), $\text{Pb}(\text{C}_2\text{H}_3\text{O}_2)_2 \cdot 3\text{H}_2\text{O}$ (Merck CAS# 6080-56-4), $\text{Ce}(\text{NO}_3)_2 \cdot 6\text{H}_2\text{O}$ (Sigma Aldrich CAS# 10294-41-4) and $\text{Ni}(\text{NO}_3)_2 \cdot 6\text{H}_2\text{O}$ (Merck CAS# 13478-00-7) was calculated. Then, precursor solution was prepared by dissolving metal salts in DI water. The solution was stirred for 30min at room conditions (Heidolph MR3001 Hot Plate Stirrer). A certain proportion of solution was taken by Pasteur pipette. The solution was dropped on each channel of the pretreated monoliths very slowly. Then, the doping was repeated for the other side of the monoliths. The doped monoliths were dried in the oven at 80 °C for 3hours (Cole-Palmer Model 09015-56 Laboratory Oven). The procedure was repeated until all solution was doped on the monoliths. After the final drying period, monoliths were calcined in the muffle at 750 °C for 5hours with a heating rate of 10 °C/min (NEY 2-525 Series II Box Furnace). Additionally, 1% Pd ($\text{Pd}(\text{NO}_3)_2$ Alfa Aesar) was impregnated on 20.0wt% CeO_2 -Mullite by following same procedure.

CHAPTER 3

METHODS

3.1 Thermodynamics

3.1.1 Predominance Diagram

The predominance diagrams express the conditions of temperature and compositions where a chemical compound has the highest potential to exist in a multicomponent reactive system. The lines on the predominance diagrams indicate the coexistence of the two chemical species while the existence of the three compounds is represented by the triple point. The predominance diagram around the equilibrium reaction of $Pb + H_2O \rightarrow PbO + H_2$ is constructed by the method described below.

The equilibrium constant of the reaction is expressed as:

$$K_{eq} = \exp\left(-\frac{\Delta G(T)}{RT}\right) = \frac{a_{PbO}a_{H_2}}{a_{Pb}a_{H_2O}} \quad \text{Eq. 3}$$

Due to the volatile nature of lead, water splitting reaction occurred at condensed and gaseous phases of Pb simultaneously. Therefore, the equilibrium constants for the reaction both in the vapor and in the liquid phase should be taken into consideration.

For the condensed phase, Pb, the corresponding equilibrium constant are given below:

$$\frac{P_{H_2}}{P_{H_2O}} = \exp\left(-\frac{\Delta G(T)}{RT}\right) \quad \text{Eq. 4}$$

For the vapor phase, the reaction and the corresponding equilibrium constants are given below:

$$\frac{P_{H_2}}{P_{H_2O}} = \frac{P_{Pb}^{vap}}{P_{PbO}^{vap}} \exp\left(-\frac{\Delta G(T)}{RT}\right) \quad \text{Eq. 5}$$

Further assumptions are as follows: The condensed phase forms an ideal mixture, i.e., all compounds in condensed phases are immiscible within each other ($a_{PbO} = 1$ and $a_{Pb} = 1$). For the vapor phase, ideal gas conditions prevail. In other words, the gas phase activities are simplified to the partial pressures of the gas phase molecules, ($a_g = \frac{f_g}{P^o} = \varphi_g \frac{P_g}{P^o}$ where φ_g is the fugacity coefficients of H_2 and H_2O ($\varphi_g = 1$) and P^o is the standard pressure ($P^o = 1bar$)). For Pb and PbO in the gaseous phase, partial pressures are equal to vapor pressures of the corresponding species.

3.1.2 Gibbs Free Energy Minimization Analysis

Predicting the equilibrium conversion in a multicomponent reactive system is critical since it hinders thermodynamic limitations. Gibbs free energy minimization (GFEM) is a powerful tool for the estimations of equilibrium composition. The calculation basis of the Gibbs free energy minimization method defined as a reactive system is in equilibrium only if total Gibbs free energy of the system becomes a minimum at system temperature and pressure. This basis is translated into mathematical form with the help of Lagrange Multipliers.

Lagrange multipliers approach is a mathematical technique for finding the minimum value of a function which consists of n variables

$$\Gamma(x_1, x_2, \dots, x_n) \rightarrow \min$$

Let us define constraints as m new relations ($m < n$).

$$\phi_k(x_1, x_2, \dots, x_n) = 0 \quad k = 1, 2, \dots, m$$

Then, the minimized function is formed by the integration of Lagrange multipliers λ_k . The final form becomes as

$$\varphi = \Gamma + \sum \lambda_k \Phi_k \quad \text{Eq. 6}$$

The application of the method to the multicomponent reactive system can be written as

$$\begin{aligned} \varphi = & \left(\sum_{i=1}^{\#C} n_i^s \left(\frac{\mu_i^o}{RT} + \ln x_i^s \right) \right)^s + \left(\sum_{i=1}^{\#C} n_i^l \left(\frac{\mu_i^o}{RT} + \ln x_i^l \right) \right)^l \\ & + \left(\sum_{i=1}^{\#C} n_i^g \left(\frac{\mu_i^o}{RT} + \ln P + \ln y_i \right) \right)^g \\ & + \sum_{k=1}^m \lambda_j \left(\sum_{j=1}^{\#P} \sum_{i=1}^{\#C} \alpha_{ik} n_i^j - \beta_k \right) \end{aligned} \quad \text{Eq. 7}$$

where n_i^j denotes the mol number of specie i in phase j , $\#C$ and $\#P$ denote the number of components and phases respectively, $x_i^{s,l}$ and y_i are the molar composition of specie i in solid/liquid and gaseous phase, μ_i^o denotes the pure component Gibbs free energy of specie i in the reference conditions, α_{ik} is the number of element k in molecule i , β_k denotes for the total amount of element k in the system.

The function φ is the under the constraints of elemental mol balance and solid, liquid and gas molar ratios as

$$\sum_{j=1}^{\#P} \frac{\beta_k}{n_{tot}^j} - \sum_{j=1}^{\#P} \sum_{i=1}^{\#C} \alpha_{ik} \frac{n_i^j}{n_{tot}^j} = 0 \quad k = 1, 2 \dots m \quad \text{Eq. 8}$$

$$\sum_{i=1}^{\#P} x_i^s = 1 \quad \text{Eq. 9}$$

$$\sum_{i=1}^{\#P} x_i^l = 1 \quad \text{Eq. 10}$$

$$\sum_{i=1}^{\#P} y_i = 1 \quad \text{Eq. 11}$$

Reactions for lead-oxygen-water reaction systems are compiled in Table 3.1 along with the relevant thermochemical information.

Table 3.1 ΔH^o (kJ/mol) and ΔG^o (kJ/mol) values for reactions between Pb, PbO, O₂, and H₂O [277]

Reactions	$\Delta H^o_{@25^\circ\text{C}}$	$\Delta G^o_{@25^\circ\text{C}}$
$\text{Pb} + \text{H}_2\text{O}(g) \rightarrow \text{PbO} + \text{H}_2(g)$	23.7	39.9
$3\text{PbO} + \text{H}_2\text{O}(g) \rightarrow \text{Pb}_3\text{O}_4 + \text{H}_2(g)$	177.3	192.9
$2\text{Pb}_3\text{O}_4 + \text{H}_2\text{O}(g) \rightarrow 3\text{Pb}_2\text{O}_3 + \text{H}_2(g)$	204.1	212.0
$\text{Pb}_2\text{O}_3 + \text{H}_2\text{O}(g) \rightarrow 2\text{PbO}_2 + \text{H}_2(g)$	184.6	204.4
$\text{PbO} \rightarrow \text{Pb} + 1/2\text{O}_2(g)$	218.1	188.6
$\text{Pb}_3\text{O}_4 \rightarrow 3\text{PbO} + 1/2\text{O}_2(g)$	64.5	35.7
$3\text{Pb}_2\text{O}_3 \rightarrow 2\text{Pb}_3\text{O}_4 + 1/2\text{O}_2(g)$	37.7	16.6
$2\text{PbO}_2 \rightarrow \text{Pb}_2\text{O}_3 + 1/2\text{O}_2(g)$	57.2	24.2

Equilibrium compositions of the reactions were estimated by using MATLAB® simulations under the following constraints:

- 1mol Pb reacted with 1 mol H₂O during water splitting reactions
- 1mol PbO was considered for the thermal decomposition reaction
- The activity of components in the condensed phase was equal to one indicating that no mutual solubility.
- The reaction was performed under atmospheric conditions

3.2 Characterization

3.2.1 Thermogravimetric Analysis (TGA)

Schimidzu DTG-60H simultaneous thermogravimetry and differential thermal analyzer was used for TGA experiments. The materials were heated up to 1000 °C with a heating rate of 10 °C/min under air atmosphere.

3.2.2 X-Ray Diffraction (XRD) Analysis

XRD patterns were measured on a Philips model PW1840 (1729) X-ray diffractometer using Ni filtered Cu-K α 945 radiation at a scan rate of 0.05 degrees/s.

3.2.3 Surface Area Measurements

The surface area of the catalysts was determined by Micromeritics Tristar II surface and porosity analyzer at 77 K. The samples were degassed for 3h at 140 °C prior to the measurements by Micromeritics VacPrep 061 Sample Degas System. The multipoint BET (Brunauer-Emmet-Teller) methodology was used for surface area measurements.

3.2.4 Temperature Programmed Reduction (TPR) Analysis

Chemisoft TPx (Micromeritics 2720) was used for TPR analysis. Approximately, 50mg sample was introduced into U-tube quartz reactor. Prior to TPR, reactor was swept under helium flow for 20min. Then sample was heated to 900 °C with a heating rate of 10 °C/min using 25sccm H₂: Ar (10:90) gas flow.

3.2.5 SEM Analysis

Morphology analysis was conducted by Phenom ProX Desktop SEM with integrated EDS. Au coated samples were analysed by high sensitivity multi-mode back scattering detector with 15kV acceleration voltage.

3.3 Instruments

3.3.1 Micromeritics Chemisorp 2720 Setup

The oxygen adsorption and desorption experiments for the materials that can decompose up to 950 °C were done by using Micromeritics Chemisorp 2720 (Figure 3.1). The reactive gases were 10% H₂ in Ar (Linde) for TPR, 2% O₂ in He (Linde) for TPO, and 99.999% He (Linde) for TPTD. The flows were set to 25 cm³/min (sccm) by built-in rotameter for all reactions. The heating rate and desired final temperature was changed depending on the oxygen adsorption and desorption performance of the material. The composition change in the flowing gas detected by built in thermal conductivity detector (TCD).



Figure 3.1. Micromeritics Chemisorp 2720

3.3.2 Multi-Gas Analyzer

The multi-gas analyzer shown in Figure 3.2 was designed and built by the help of Logos Kimya Teknolojileri. The equipment has four different sensors as 3% CO (10ppm resolution, Gascard NG/Edinburg Instruments), 10% CO₂ (0.01% resolution, Gascard NG/Edinburg Instruments), 0-1% and 0-21% O₂ (Model 3290/Teledyne Analytical Instruments), and 0-5% H₂ (Model 2000 XTC/ Teledyne Analytical Instruments). CO and CO₂ detectors have NDIR type sensors equipped with a tungsten lamp as the infrared source. The oxygen sensor is a micro-fuel cell that follows electrochemical reactions $O_2 + 2H_2O + 4e^- \rightarrow 4OH^-$ at the cathode side and $Pb + H_2O \rightarrow PbO + 2H^+ + 2e^-$ at the anode side. The hydrogen thermal conductivity transmitter (TCT) measures the concentration of a component in a binary or pseudo-binary mixture of gases by comparing the difference in thermal conductivity.



Figure 3.2. Multi-gas analyzer

Two different type of reactors were used depending on the material whether it is powder or monolith. 6mm OD quartz reactors were used for powder materials whereas 25mm OD reactors were used for monolith samples. In both reactors, materials were supported and fixed in the middle of the tube by the help of quartz

wools. The gas flow rate was adjusted by a Teledyne HFC-202 Mass Flow Controller (MFC), driven by a TERRALAB mass flow control station (MFCS). The reactant gases were 99.999% H₂ (Habas) and 99.999% dry air (Oksan) while the inert gases were 99.999% Ar (Linde) and 99.999% N₂ (Oksan). The heating rate and desired final temperature was changed depending on the tested material. Temperature of the oven is measured by K-type thermocouple.

3.3.3 QMS 200 Mass Spectrometry Setup

Balzers Prisma QME 200 mass spectrometer (MS) from Pfeiffer Vacuum was used for product gas analysis during dynamic experiments. This electric quadrupole (24V, 2A) MS is able to scan the mass to charge ratios within the range of 1-100amu. Tungsten filament was used as an ion source. Sample chamber pressure was monitored with vacuum gauge (Pfeiffer Inficon PKR 251) transmitter which is connected to Inficon Single Gauge readout. The required vacuum was sustained <10⁻⁵ torr throughout all experiments.

Synthesized bulk materials and coated monoliths were loaded into 60cm (6mmOD) and 60cm (250mm OD) quartz reactors respectively. Materials were supported by quartz wool from both sides. Reactors were put into the 1.5kW homemade tubular oven (up to 1250 °C). Oven temperature was monitored by a K-type thermocouple (ORDEL) and controlled by homemade temperature controller equipped with Delta DTB4824). Depending on the loaded material, different heating rates and reaction temperatures were used during the experiments.

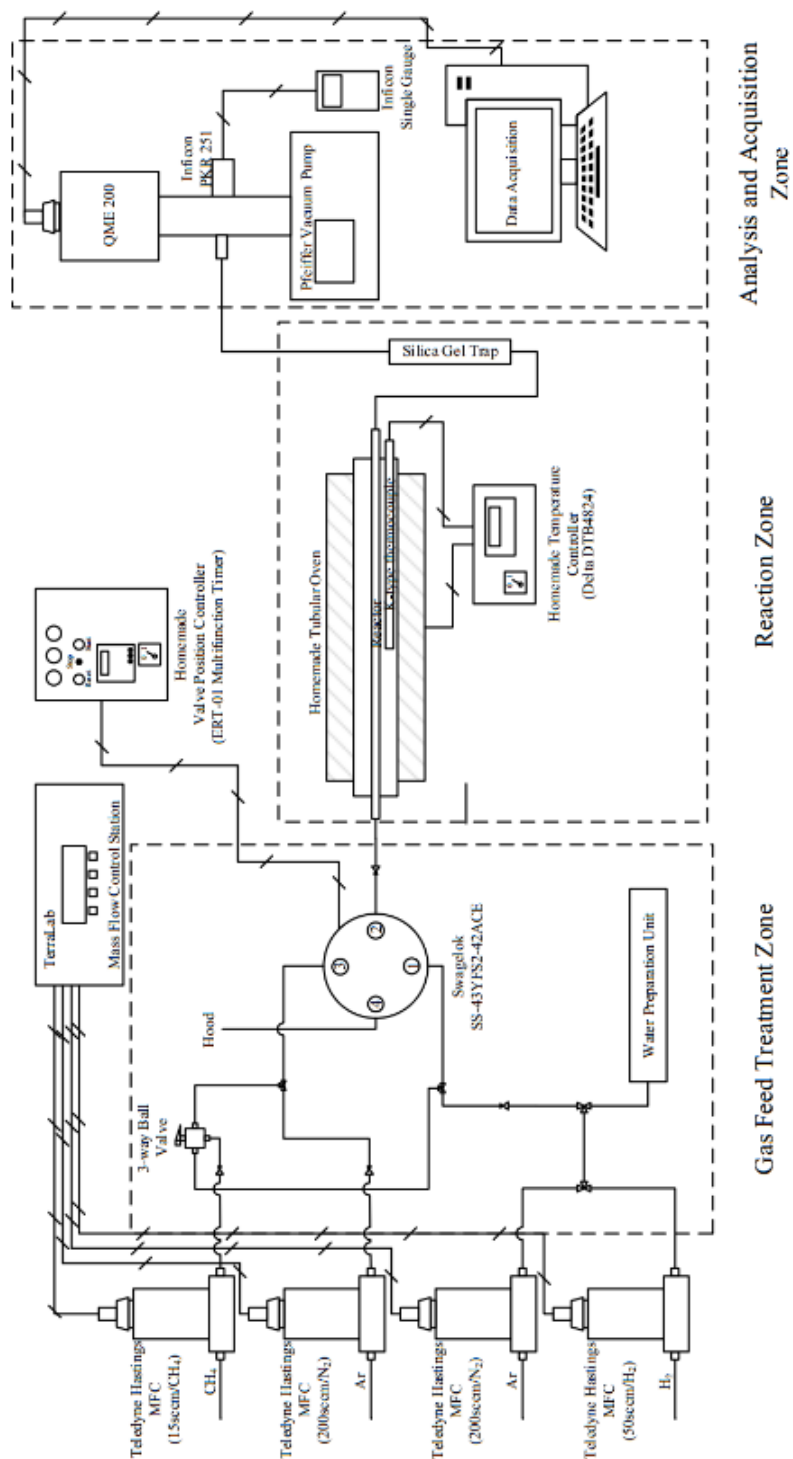


Figure 3.3 QME 200 MS experimental setup

The gas flow rate was adjusted by four Teledyne HFC-202 Mass Flow Controller (MFC) calibrated as 15 sccm/CH₄, 200 sccm/N₂ (x2) and 50 sccm/H₂. MF controllers were driven by a TERRALAB mass flow control station (MFCS). Methane and argon gasses were supplied from Linde (99.5% and 99.999% respectively) whereas hydrogen was supplied from HABAŞ (99.999%). Product gases were passed through a silica gel trap to capture water of reaction before QME 200 MS as given in Figure 3.3. Gas pretreatment system was configured in such a way that cyclic or steady state experiments can be conducted in the same experimental setup with the help of manual controlled 3-way ball valve and timer controlled 4-way ball valves. Water was supplied to the system by different techniques as temperature-controlled bubbler and a steam generator. Steam was generated by injecting liquid water by a syringe pump (Cole-Parmer) into 6 mm OD copper helix which is externally heated to 120 °C.

3.4 Oxygen Exchange Tests

3.4.1 The Operating Procedure of Micromeritics Chemisorp 2720 for Thermal Stability Experiments

Thermal stability experiments were conducted by following the procedures described in Appendix B. One cycle is defined as thermal decomposition followed by reoxidation. Thermal stability experiments were performed for 10cycles.

3.4.2 The Operating Procedure of Micromeritics Chemisorp 2720 for Heat Transfer Effect on Desorption and Adsorption Kinetics of Co₃O₄ and CeCoO₃

The effect of heat transfer was investigated for Co₃O₄ and CeCoO₃ by following the TPtD and TPO procedures described in Appendix B. The heating rate was set as 10

°C/min. SiC as high thermal conductive material was mixed with the materials as 1:1 weight ratio.

3.4.3 The Operating Procedure of Micromeritics Chemisorp 2720 for Film Mass Transfer Effect on Desorption and Adsorption Kinetics of Co_3O_4 and CeCoO_3

The effect of film mass transfer was investigated for Co_3O_4 and CeCoO_3 by following the TPtD and TPO procedures described in Appendix B. The heating rate was set as 10 °C/min. The comparative experiments were designed as decreasing the flow rate to half and doubling the amount of materials.

3.4.4 The Operating Procedure of Multi-Gas Analyzer for Thermal Stability Experiments

Thermal stability experiments were conducted by following the procedures described in Appendix C. One cycle is defined as thermal decomposition followed by reoxidation. Thermal stability experiments were performed for 5 cycles.

3.4.5 The Operating Procedure of Multi-Gas Analyzer for Heat Transfer Effect on Desorption Kinetics of CeFeO_3

The effect of heat transfer was investigated for CeFeO_3 by following the TPtD procedure described in Appendix C. The heating rate was set as 10 °C/min. SiC as high thermal conductive material was mixed with the materials as 1:1 weight ratio. The flow was kept constant at 100 ccpm Ar.

3.4.6 The Operating Procedure of Multi-Gas Analyzer for Pore Diffusion Effect on Desorption Kinetics of Co_3O_4 and Co_3O_4 doped Monolith

The effect of pore diffusion was investigated for Co_3O_4 by following the TPtD procedure described in Appendix C. The heating rate was set as $10\text{ }^\circ\text{C}/\text{min}$. Co_3O_4 and Co_3O_4 doped monolith were tested by using 6 mm and 25 mm quartz reactors respectively. Co_3O_4 doped monolith sample was put in the reactor as given in Figure 3.4.

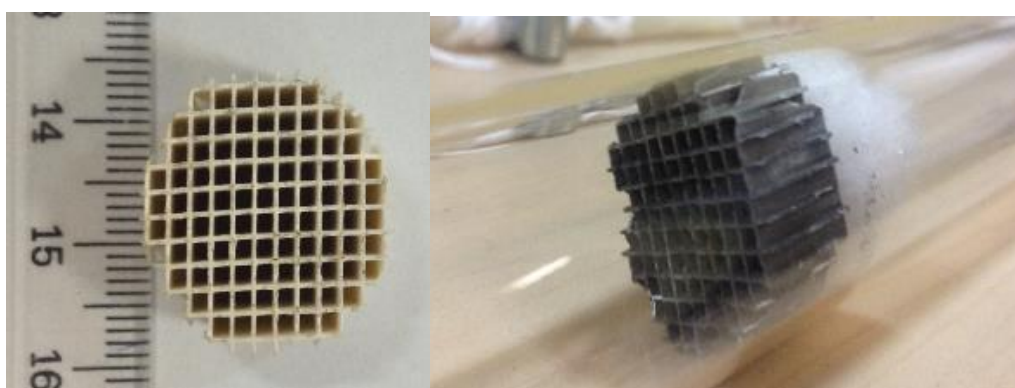


Figure 3.4. Monolith before (left) and after (right) doping procedures

3.4.7 TGA Cyclic Analysis

The red/ox properties of the materials were evaluated by thermal gravimetric analyses conducted by Shimadzu DTG-60H with simultaneous DTA-TG apparatus. The materials were put into an alumina pan. The reference material was $\alpha\text{-Al}_2\text{O}_3$. The cyclical experimental conditions were programmed by TA-60WS software. The gas flow was remotely controlled by Shimadzu FC-60A.

Thermal decomposition and reoxidation by air and CO_2 environment were conducted up to $1000\text{ }^\circ\text{C}$ with heating rates of $5\text{ }^\circ\text{C}/\text{min}$, $10\text{ }^\circ\text{C}/\text{min}$, and $15\text{ }^\circ\text{C}/\text{min}$. Argon (99.999%), nitrogen (99.999%), carbon dioxide (99.9%) gases were supplied from Linde whereas dry air (99.9%) was supplied from Oksan.

Two different cyclic experiments were conducted. In the first type, fresh material was heated under an inert atmosphere and then cooled it down under the same environment. Inert gas switched to an oxidizing gas at lower temperatures. The material heated and cooled under the flow of oxidizing gas. Second type cyclic experiments were conducted by heating under an inert atmosphere and cooling down to the preset temperature under oxidizing flow.

3.5 Reaction Tests

3.5.1 Boat Reactors

Boat reactors were manufactured from a 316-stainless steel rod (8 cm length and 1 cm OD). The rod was first cut into half, forming two semi-cylinders. Then, the semi-cylinders were machined such that a boat was formed for molten liquid handling during the reaction.

For the experiments in the boat reactor, 13gr of Pb was used. Solid Pb containing stainless steel boat was inserted into 25mm OD quartz reactor and supported by quartz wool from both sides. The sample was pretreated under 100 cm³/min argon flow (Linde, 99.999%) at 950 °C to remove any impurities. Then, the reactor was cooled to room temperature under argon flow. 100 cm³/min argon flow was directed to a water saturator kept at room temperature during the water splitting experiment. The vapor pressure of water at 25 °C is around 24 torr corresponding to 3% water vapor in the feed stream.

The excess water in the effluent from the reactor was trapped in the condenser kept in liquid nitrogen. The reactor was heated up to 800 °C at a rate of 10 °C/min. The product gas was analyzed by a home-made online multi-gas analyzer. Overall process flow diagram was given in Figure 3.5. For quantitative analysis, Teledyne XTC-2000 Hydrogen Transducer was calibrated against dilute hydrogen in the inert gas flow prior to the experiment.

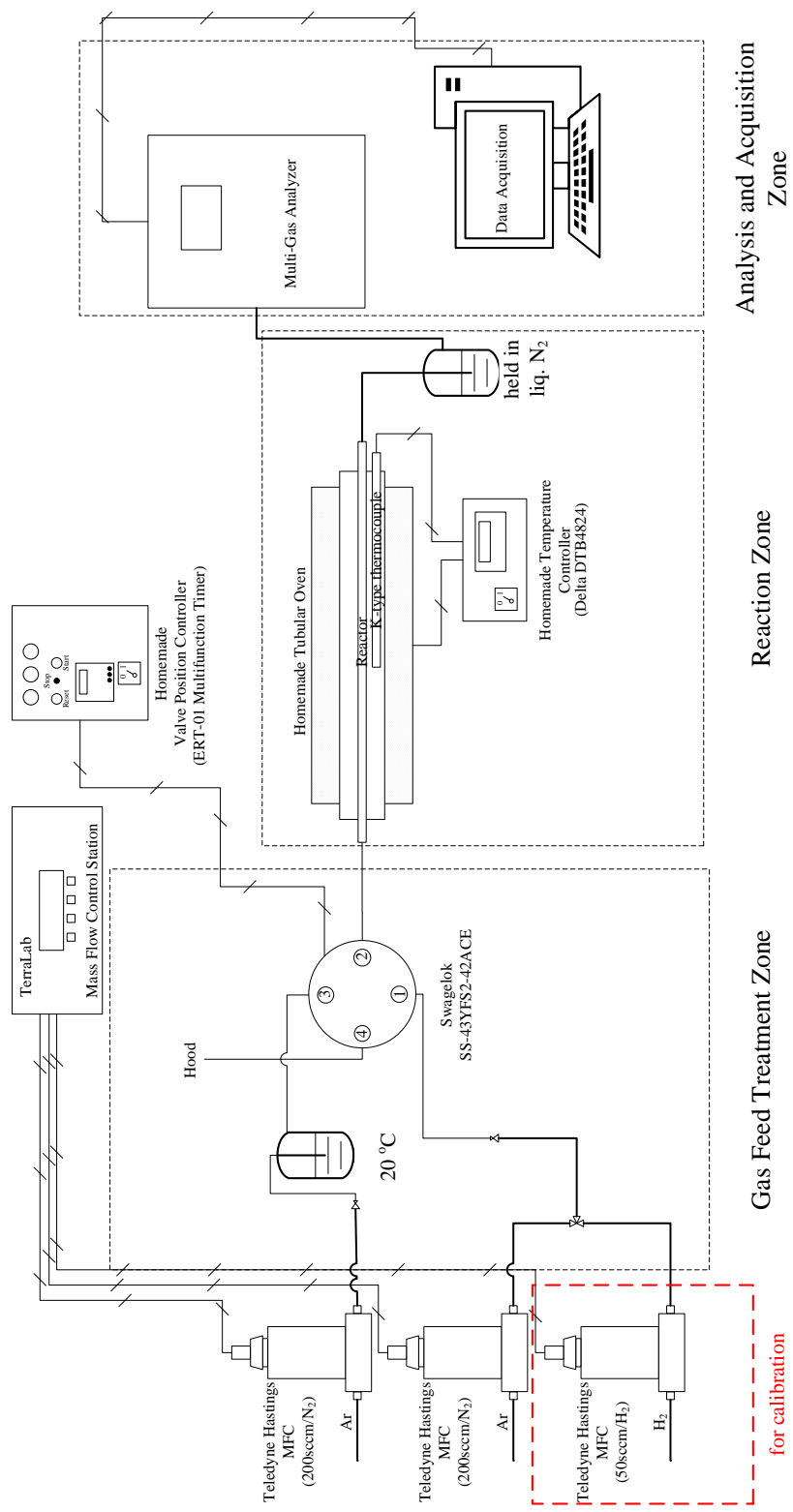


Figure 3.5 Process flow diagram of treatment, reaction and analysis system for lab scale experiments

3.5.2 Gas Bubbling Reactor

Molten metal gas bubbling reactor was also manufactured from 316 stainless steel (5.6cm ID, 30cm long). The reactor was equipped with a thermocouple and two flow lines, one for the inlet and the other for the outlet. The tubing for the inlet flow extended all the way down the reactor, such that the gas inlet was 2 cm above the bottom of the reactor. The tubing for the outlet flow was welded to the top flange. The product gasses were analyzed by a home-made low-cost hydrogen sensor. Solid-state (SnO) based detectors, MQ-4, MQ-6 and MQ-8 manufactured by Hanwei Electronics, were imbedded into a gas flow chamber constructed from a block of polyimide, the gas flow volume was minimized to ensure fast response. Sensors were supplied by a 5V signal from an independent power supply and the response was monitored by Arduino boards, digitizing the analog sensor response into a USB port on a control PC. The sensor configuration was described in detail by Ogulgonen *et. al.* [278]. The whole sensor assembly along with the data acquisition hardware is below \$100.

The reactor was loaded with ~2kg of lead (7.6 to 8.1cm height in the operating temperature range). Ar was used as carrier gas (200cm³/min), a peristaltic pump was used to supply liquid H₂O which vaporized inside the reactor and reacted with Pb. Honeywell XCD sensor was used to track combustibles (H₂ in the case) after the reactor effluent was diluted by 500 cm³/min air and passed through silica gel to remove excess water vapor.

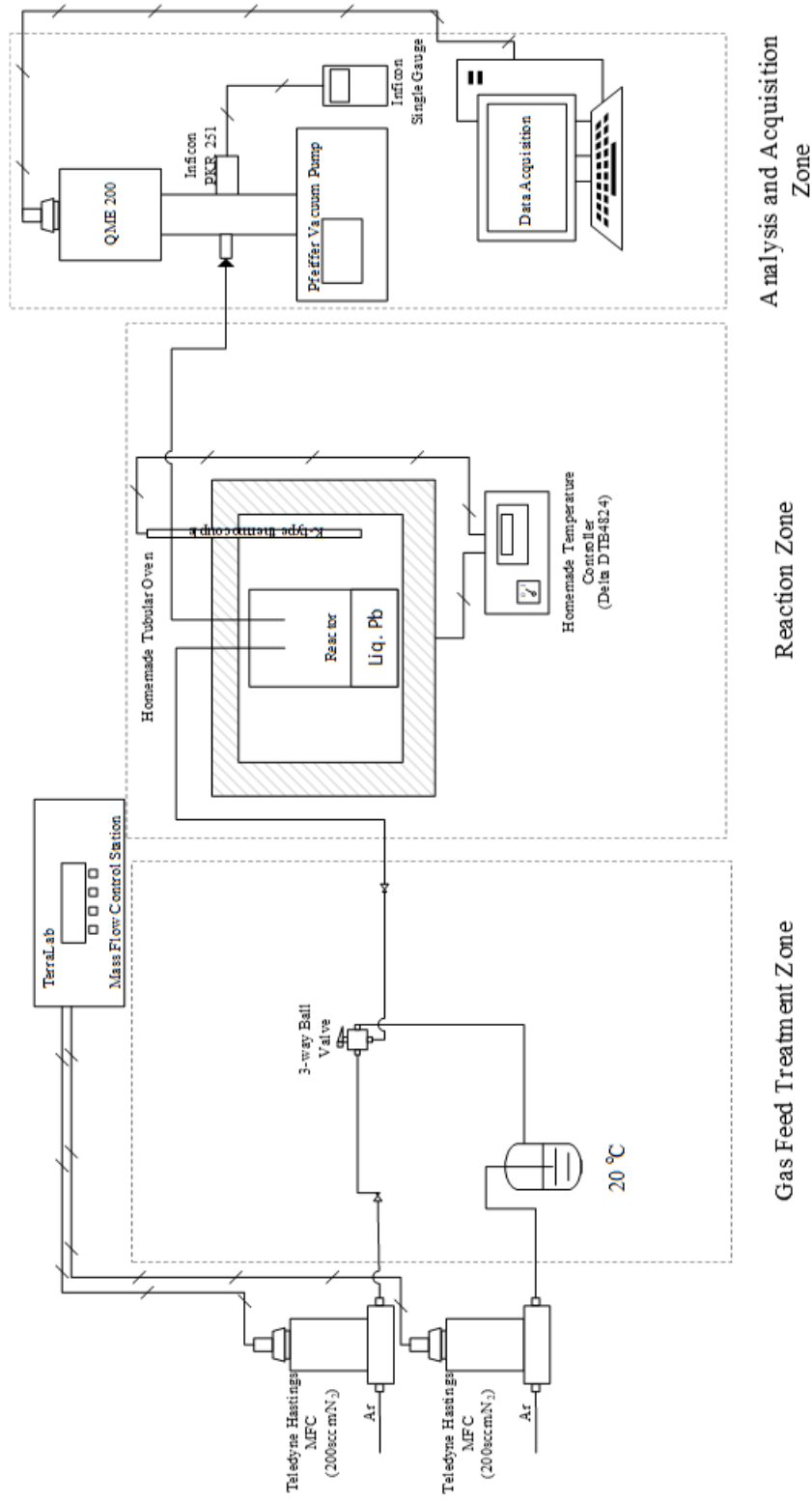


Figure 3.6 Process flow diagram of treatment, reaction and analysis system for surface sweep reactor experiments

3.5.3 Surface Sweep Reactor

Surface sweep reactor was constructed with the same principles as the molten metal gas bubbling reactor. The only difference was that the gas inlet and outlet levels were adjusted such that they both remained above the liquid level and the gas only swept the surface of the molten lead. The effluent gases were delivered to a Pfeiffer RGA QMS 200 Mass Spectrometry (Figure 3.6). Argon flow rate was adjusted by two mass flow controllers (Teledyne Hastings, calibrated to 200ccpm N₂). The flow controllers were driven by TERRALAB mass flow control station. One of the argon streams was saturated with water vapor for water splitting experiment while the other one used as a sweep gas for thermal decomposition experiment. These two feed streams were connected by three-way ball valve prior to the reactor. This valve was used to adjust the moisture level of feed stream from saturated argon flow to dry argon flow.

Thermal decomposition of lead oxide was carried out in the surface sweep reactor. Prior to the thermal decomposition, 150gr lead was loaded into the reactor. The reactor was heated up to 800 °C at a rate of 10 °C/min under 100ccpm wet Ar flow. Water was supplied to the system by bubbling dry argon through the liquid water at room conditions. After reaching the set temperature, the reactor was cooled down to room temperature naturally under the same flow. For the thermal decomposition part, the reactor was heated to 950 °C with a heating rate of 10 °C/min under 100ccpm Ar flow. The effluent gas monitored by Pfeiffer RGA QMS 200 Mass Spectrometry.

3.5.4 Reforming Experiments

Catalysis in powder form was loaded into 60cm (6mm OD) quartz reactors and supported by quartz wool from both sides. Reactors were put into the 1.5kW homemade tubular oven (up to 1250 °C). Oven temperature was monitored by a K-type thermocouple (ORDEL) and controlled by homemade temperature controller equipped with Delta DTB4824). The gas flow rate was adjusted by four Teledyne

HFC-202 Mass Flow Controller (MFC) calibrated as 15sccm/CH₄, 200sccm/N₂ (x2) and 50sccm/H₂. MF controllers were driven by a TERRALAB mass flow control station (MFCS). Methane and argon were supplied by Linde (99.5% and 99.999% respectively) whereas hydrogen was supplied by HABAŞ (99.999%). Product gases were passed through a silica gel trap to capture water of reaction before Balzers Prisma QME 200 mass spectrometer (Figure 3.7).

Prior to reforming, 100 mg sample is reduced at 100 sccm 10% H₂ – Ar flow, heating up to 700 °C with a heating rate of 10 °C/min and dwell at 700 °C for 1 hour. Steam methane reaction is conducted with 100 sccm 2.7% CH₄ 2.7% H₂O and balance Ar, at 800 °C isothermally for 3 hours. Ar is used as a sweep inert gas for the heating and cooling periods and as an internal calibration standard for quantitative analysis.

H₂ yield is calculated as the ratio of mols of H₂ produced to mols of CH₄ reacted during the reaction:

$$Y = \frac{n_{\text{H}_2}}{n_{\text{CH}_4}^{\text{in}} - n_{\text{CH}_4}^{\text{out}}} \quad \text{Eq. 12}$$

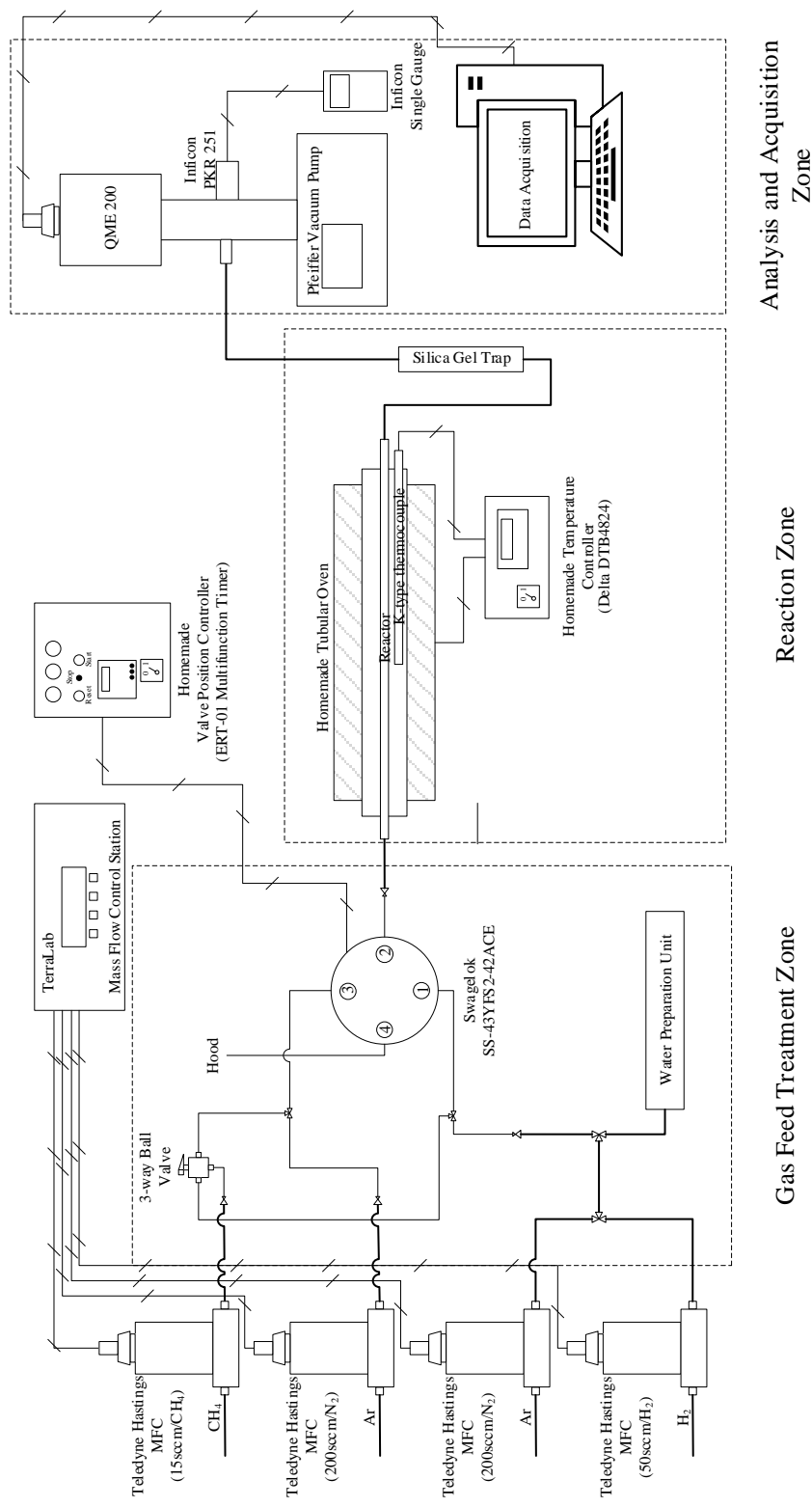


Figure 3.7 Process flow diagram of treatment, reaction and analysis system for lab scale experiments

3.6 The Concentrated Solar Energy Pilot Unit

The concentrated solar energy pilot unit consisted of four concave mirrors mounted on a dual axis solar tracking system as seen in Figure 3.8. The monoliths were loaded into the solar reactor with the open channels facing the focused solar irradiation. In this same picture, the blue tubing providing the feed gases to the front face of the monolith can be seen on the left side. The white tubing towards the back collects the effluent gases and delivers them to the gas analysis unit while monitoring the temperature of the effluent by a J-type thermocouple. The window facing the focused solar rays is a 3mm thick, 96mm diameter quartz piece. A K type thermocouple is embedded into the monolith and holds the monolith in place while monitoring its internal temperature. The parabolic dishes used for concentration are 70cm in diameter.



Figure 3.8. Concentrated solar energy pilot unit

The effluent gases are analyzed with an array of three solid-state (SnO based) sensors that have varying levels of sensitivity towards CH₄ and H₂ and allow for real-time monitoring of the gas composition (MQ4, MQ6, and MQ8 by Hanwei Electronics, China). They also pass through a more sensitive total combustible gas analyzer (Honeywell XCD) for validation. Two O₂ sensors, sensitive to ppm and percentage levels, (Southland Sensing Ltd.) connected to two EMD-485 sensor board are used to track O₂ levels. The O₂ levels are monitored prior to experimentation to confirm purging of all O₂ from the system. The entire set-up is automated through a LabVIEW interface complemented with a NI USB-6343 A/D converter with digital I/O capabilities.

30mm x 30mm x 10mm mullite monoliths coated with 12.8 wt.% Ni and 1.0 wt.% Pd/ 20.0% CeO₂ were placed into the solar reactor with the 30mm x 30mm side of the monoliths facing the focused solar irradiation, as seen in Figure 3.9. The tubing in the back collects the effluent gases and delivers them to the gas analysis unit, while monitoring the temperature of the effluent by a J-type thermocouple. Quartz window (3mm thick, 96mm-OD) was placed in the top flange for the penetration of solar rays towards to the monolith. K-type thermocouple (6mm-OD) embedded into the monolith is used for monitoring the temperature of the back side of the monolith. Front monolith temperature was predicted according to the model described in next section. The parabolic dishes used for concentration were 70cm in diameter.

Reforming reaction was conducted under 200 sccm 4 %CH₄-Ar flow. Ar is used as a sweep inert gas for the heating and cooling periods and as an internal calibration standard for quantitative analysis. The gas flow rates were adjusted by two AliCat Scientific MC-200SCCM mass flow controllers. Water was fed to the reactor in liquid form by the help of a peristaltic pump. Excess heat on the front side of the monolith (facing direct solar irradiation) was used for steam production. Reforming reaction was carried out under excess steam conditions.

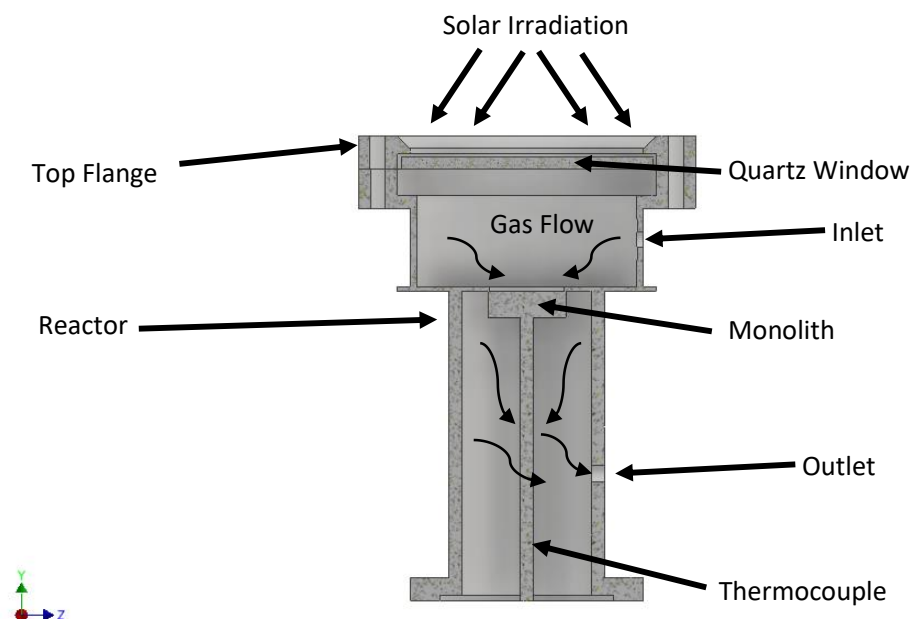


Figure 3.9. Schematic of the solar-thermal reactor

The effluent gases were analyzed with an array of 3 solid state (SnO based; MQ4, MQ6 and MQ8 by Hanwei Electronics, China) sensors that have different responses towards CH_4 and H_2 . The gaseous products also passed through a more sensitive total combustible gas analyzer (namely a Honeywell XCD) for validation. Prior to the reforming reaction, the reaction system was purged with Argon flow. Two O_2 sensors (sensitive to ppm and percentage levels by the Southland Sensing Ltd) connected to two EMD-485 sensor board were used to track O_2 levels in the effluent stream. The entire set-up was automated through a Lab-VIEW interface complemented with a NI USB-6343 A/D converter with digital I/O capabilities.

3.7 Simulations

ASPEN (Advanced System for Process Engineering) was developed by MIT and US DOE during a research project related with coal combustion. The software is used for modelling various plant operation under steady and unsteady conditions. Built in

blocks are used for modeling unit operations such as reactors, separation units, heat exchangers etc. Mass and heat balances are performed by using inlet and outlet mass and heat streams linked to that Aspen blocks. Aspen uses Fortran based codes for performing iterative calculations.

A process model for Aspen Plus is defined in three stages

- 1. Flowsheet:** The mapping of the process is the first step in Aspen Plus. The flowsheet includes unit operations, inlet, and outlet streams in terms of mass, heat and work.
- 2. Chemical Properties:** This step includes the definition of all chemical components that is expected to be present in reactants and products. The property method such as ideal gas, Peng-Robinson is also defined in this stage.
- 3. Operating Conditions:** The operating conditions such as temperature, pressure, size etc. for inlet streams and unit operations are set.

The model blocks used in the process modeling was described in the following sections.

3.7.1 ASPEN Plus Process Built-in-Blocks

Streams: Material, heat and workflow through the process are defined by using Modeling Palette as shown in Figure 3.10. Material streams are used for definition of temperature, pressure, vapor fraction, total flow rate and composition of the stream. Heat streams specifies the heat duty. Optionally, user can define initial and final temperatures corresponding heat source block. Input and/or output power is shown by work streams. Amount of power and/or driver speed for work transfer calculations can be set by using work streams.

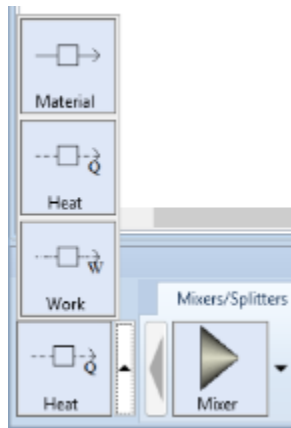


Figure 3.10. Streams in Aspen Plus

Mixer and Splitter Blocks: Mixer and splitter blocks are used for combining and dividing the streams of same type as shown in Figure 3.11. Streams in terms of material, heat and work can be combined into one outlet stream by using Mixer blocks. User can define an outlet pressure or pressure drop for material streams. The outlet stream temperature and pressure of combined stream is calculated by performing an adiabatic phase equilibrium flash calculation. Splitter takes same type of streams and divides into more streams. All outlet streams have the same composition and conditions. User can specify the outlet streams in terms of fraction or flow rate.

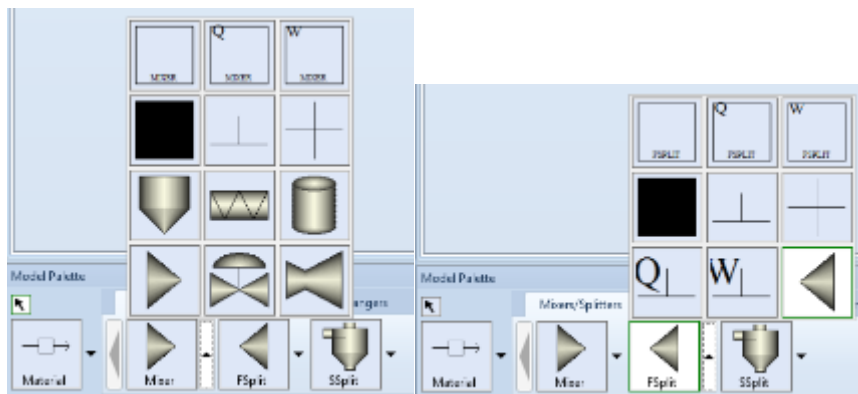


Figure 3.11. Mixer (left) and Splitters (right) block in Aspen Plus

Reactor Blocks and Rplug: Aspen Plus has several reactor blocks such as stoichiometric reactor (RStoic), yield reactor (RYield), equilibrium reactors based on stoichiometry (REquil) and Gibbs free energy minimization (RGibbs), continuous stirred tank reactor (CSTR), plug flow reactor (RPlug) and batch reactor (RBatch) as shown in Figure 3.12. In this report, RPlug and RGibbs reactor blocks were studied.

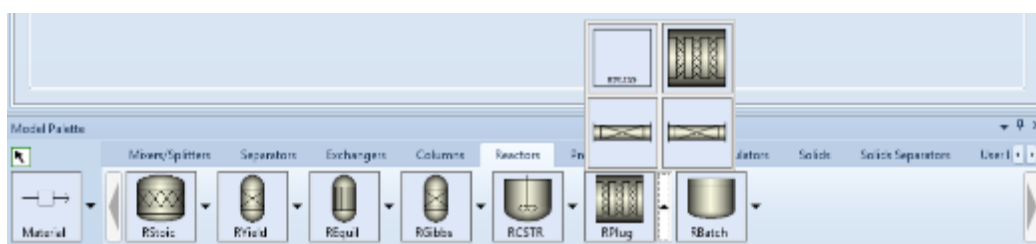


Figure 3.12. Reactor Blocks in Aspen Plus

RPlug reactor block operates by using the assumption of plug flow. This block can be used for modelling one-, two-, or three phase reactors with thermal fluids for cooling and heating purpose in co- or counter- current streams. Firstly, the thermal operation such as adiabatic, isothermal etc. is specified for RPlug block. Then, single and/or multitube configuration with specified reactor dimensions are defined. RPlug block only handle kinetic type reactions, therefore reaction sets should also be included. If necessary, pressure drop, reactor holdup, catalyst specification can also be defined for calculations.

RGibbs reactor performs chemical and phase equilibrium calculations by using Gibbs free energy minimization method. RGibbs block can model single phase equilibrium, phase equilibrium with no chemical reactions, phase and/or chemical equilibrium with solid solution phases and simultaneous phase and chemical equilibria. User should select one of the calculation options as phase equilibrium only, phase and chemical equilibrium, and restricted chemical equilibrium. User also should define the operating conditions and information related to phases.

Reactions in Aspen Plus are set in several groups as Power Law, Langmuir-Hinshelwood-Hougen-Watson, and polymer reaction types as Step-Growth, Free-Radical, Emulsion etc. In this report, power law reaction kinetics were used. In this model, stoichiometry and related exponents were set for the studied reactions.

Heat Exchangers: Heat exchange between material streams are modelled by using exchanger blocks as shown in Figure 3.13. The basic model for temperature change is called as Heater. This model can be used for modelling heaters, coolers, condensers etc. User can specify temperature, pressure, duty, vapor fraction etc. for calculation of thermal and phase conditions of outlet streams.

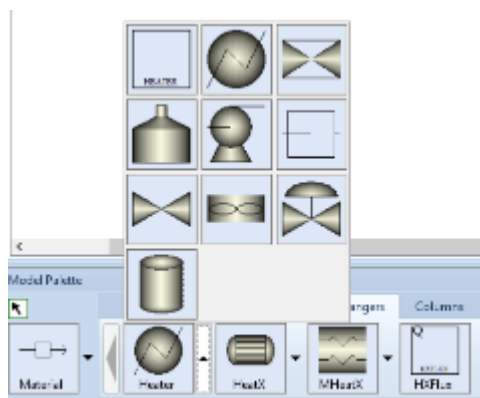


Figure 3.13. Heater in Aspen Plus

Pressure Changers: Pumps, compressors, turbines, valves, single and multiple segment pipes are present in the model palette of pressure changers as shown in Figure 3.14. Pumps and compressors change the material stream pressure. These blocks require pump/compressor outlet pressure specification in the forms of discharge pressure, pressure increase, pressure ratio and power requirement. Additionally, efficiency and type of compression can also be set by user. Valves are used for modelling the pressure drop through valve. Valves can also be used as process control equipment. Pressure drop through a single and multiple lengths are modeled by pipe and pipeline Aspen blocks.

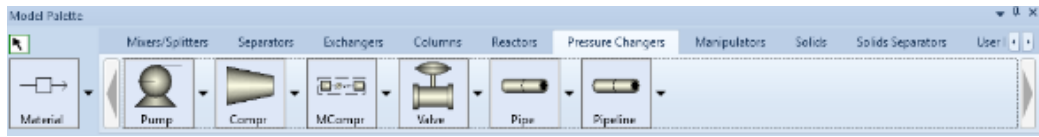


Figure 3.14. Pressure changers in Aspen Plus

3.7.2 The Basis of Simulations

The solar energy integration to steam methane reforming (SMR) was analyzed by conducting feasibility analysis on material and energy balance. In this manner, block diagram of SMR was simplified to main equipments as shown in Figure 3.15. Material and energy streams were indicated by using labels “S” and “Q” respectively throughout the analysis. Water and methane were fed to the system by streams S1 and S3 while product gas was collected from S6.

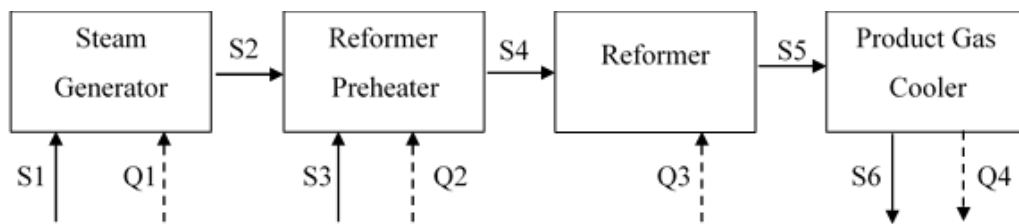


Figure 3.15. Simplified block diagram of steam reforming process

For the autothermal reforming (ATR) process, a combustor was added to the SMR block diagram as a separate box as given in Figure 3.16. Oxygen and additional methane were supplied to the combustor by the streams S7 and S8 respectively. The effluent gas stream introduced to the reformer preheated by stream S9. Combustor was assumed to be operated adiabatically; therefore, Q5 was considered as 0.

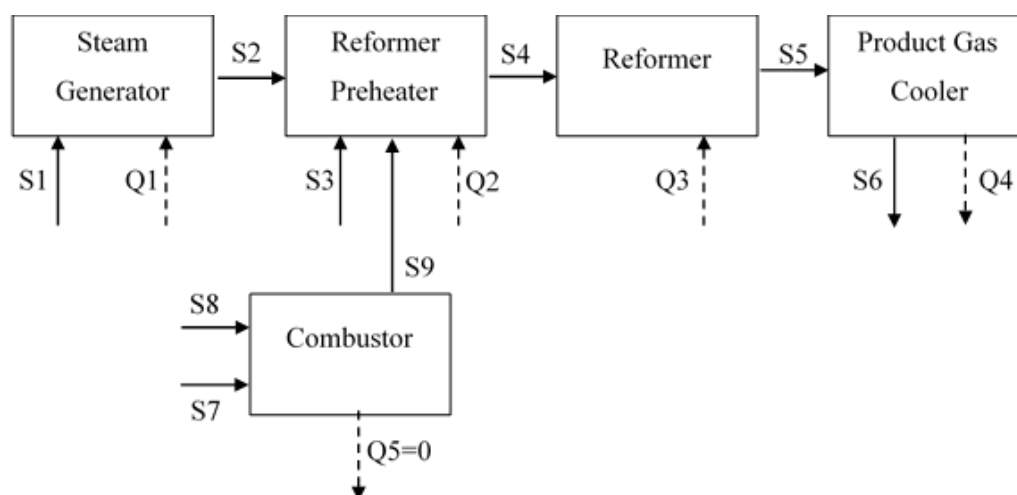


Figure 3.16. Simplified block diagram of autothermal reforming process

Simulations were conducted by using ASPEN PLUS V8.8. Simulations were based on thermodynamic equilibria. Reformer and combustor were modelled by RGIBBS module. Heat exchange simulations were done by using HEATER module. Simulations ran under atmospheric conditions. Effluent stream composition of combustor was calculated by considering total combustion of methane with stoichiometric oxygen feed. Each simulation block was studied separately in terms of heat load. The heat exchanger network was not in the scope of this study. The process feasibility was estimated by considering the total heat balance of the overall process. The feed and operational conditions for SMR and ATR simulations were given in Table 3.2. All simulations were performed under atmospheric conditions. The feed conditions in the streams S1 and S3 were kept constant during the simulation for the comparison on common basis. The performance of SMR and ATR processes were analyzed at different reformer temperatures. Therefore, temperature of the reformer preheater was changed during each case. Steam generator were assumed to be operated under isobaric conditions. Product gas cooler was used to cooled down to product streams to feed conditions so that overall energy analysis was completed at the reference of 25 °C and 1 bar. S7 (O₂ feed) and S8 (CH₄ feed) streams were fed to the combustor for sustaining overall energy demand of the ATR

process. Therefore, their amounts were changed depending on the reformer temperature during simulations.

Table 3.2 Simulation parameters for SMR and ATR processes

Streams	Module	Specifications	
		SMR	ATR
S1	-	1mol H ₂ O at 25 °C and 1 bar	
-	Steam Generator	Vaporization (Isobaric)	
S3	-	1 mol CH ₄ at 25 °C and 1 bar	
-	Reformer Preheater	Increases the temperature of the feed streams to reformer temperature (Isobaric)	
-	Reformer	Steam reforming at 1bar (Isothermal)	Steam and Dry reforming at 1 bar (Isothermal)
-	Product Gas Cooler	Decreases the temperature of the feed stream to 25 °C at 1bar	
S7	-	-	O ₂ fed at 25 °C and 1 bar
S8	-	-	CH ₄ fed as fuel at 25 °C and 1 bar
-	Combustor	-	Combustion of CH ₄ with O ₂ (Adiabatic)

Base case was simulated by considering theoretical reforming systems where energy requirement was self-sustained by the process. Hybrid solar-ATR simulations were conducted under the assumption of the external energy input (simulating solar energy) was supplied to the reforming process at certain levels. These energy levels were the ratio of solar energy to overall process energy ($Q_{\text{solar}}/Q_{\text{process}}$). Simulation of a real case example was carried out by replacing assumed Q_{solar} previously used in Hybrid solar-ATR process with the dynamic solar energy

collected on outdoor pilot scale experimental unit [279]. Due to the intermittent nature of solar energy, dynamic simulations were conducted. Built in functions of ASPEN Plus such as Sensitivity Analysis and Case Study were also used during the specified case simulations as given in Figure 3.17.

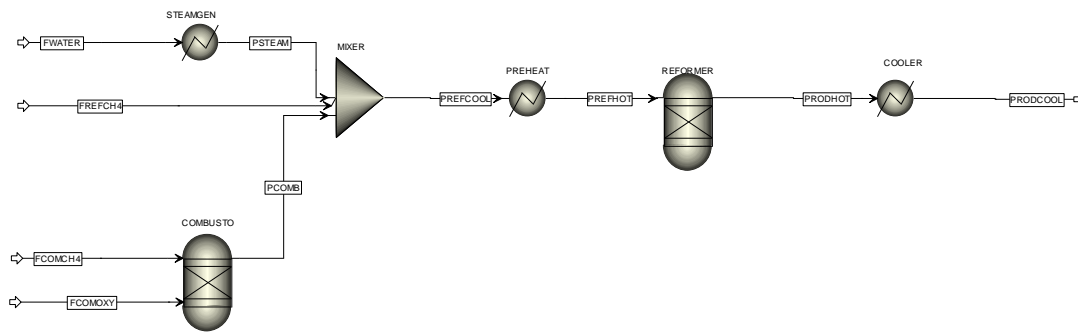


Figure 3.17. Simplified flow-sheet used during ASPEN Plus Simulations

CHAPTER 4

THERMODYNAMICS

4.1 Direct Decomposition of Water

Direct decomposition of water is the most straight forward methodology to produce hydrogen from water. The process requires extremely high temperatures due to the thermodynamic constraints. The complexity behind the direct water decomposition process was shown in Figure 4.1 by considering the compounds as H_2O , H_2 , O_2 , H , and O . During the decomposition at temperatures higher than $1200\text{ }^\circ\text{C}$, water splits into hydrogen and oxygen molecules. The products are explosive, and the separation process is very complex when the operating conditions are considered. As the temperature increases to $2000\text{ }^\circ\text{C}$, the hydrogen and oxygen molecules also splits into their atomic forms; that is, quenching the products nearly impossible. Therefore, the overall process becomes extremely difficult to operate.

Bilgen showed the 2-3% hydrogen in the product stream during the operation around $2000\text{-}2500\text{ }^\circ\text{C}$ [280]. The resulting amount is nearly 50% of equilibrium conversion. The achieved low efficiency was attributed to heat transfer related problems. The main drawback of this process is the high temperature ($>2500\text{K}$) needed for water decomposition. This temperature causes techno-economic difficulties such as separation of highly explosive mixture gas (H_2/O_2), radiative losses, material durability, high capital costs and scale up related problems. Therefore, hydrogen production at an industrial level is impractical.

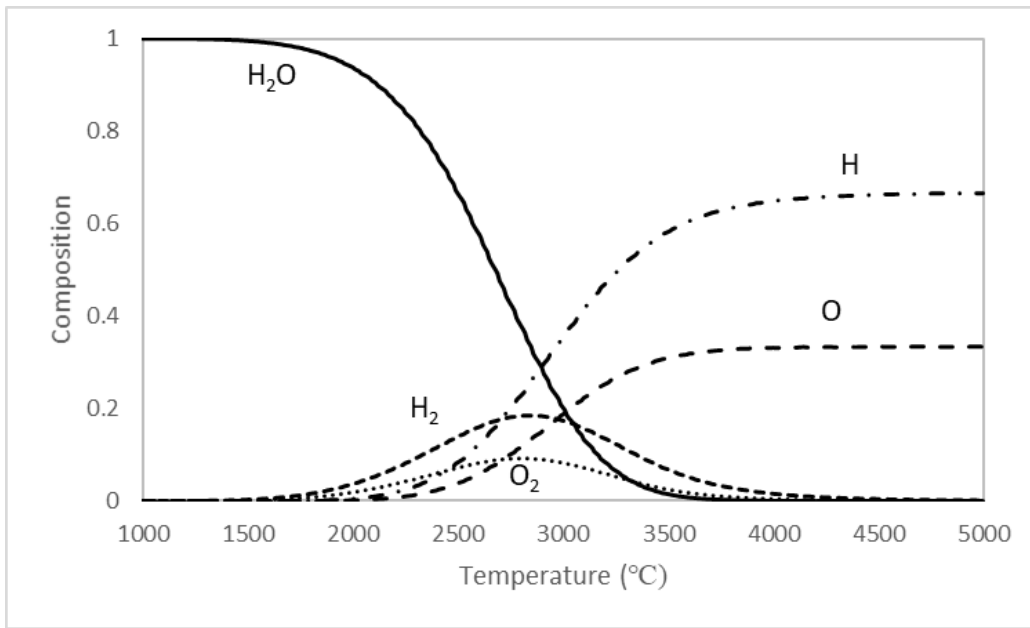


Figure 4.1. Equilibrium composition analysis of direct decomposition of water ($P_{\text{H}_2\text{O}} = 0.1\text{bar}$ and $P_{\text{system}} = 1\text{bar}$)

4.2 Thermodynamics Behind the Two-Step Water Thermochemical Processes

The thermodynamics of the reaction system are the first and most critical point which should be considered during the determination of the reaction extent and operational conditions. For the two-step thermochemical water splitting processes, thermodynamics behind the two steps should be carefully analyzed for finding promising process conditions. Promising thermodynamics generally do not offer best practical implementation due to problems coming from kinetic limitations, mass and heat transfer restrictions, material sintering, etc. Nevertheless, thermodynamics always determine the limits of reaction at process conditions; that is, maximum conversion, yield etc. are the outputs of thermodynamic analysis. For the two-step water thermochemical water splitting reaction system, the general reaction steps are defined as

Thermal Decomposition at T_{high} : $MO \xrightarrow{+\Delta H.T_{high}} MO_{1-\delta} + \frac{\delta}{2} O_2$ (ΔG_{TD})

Water Splitting at T_{low} : $MO_{1-\delta} + \delta H_2O \xrightarrow{-\Delta H.T_{low}} MO + \delta H_2$ (ΔG_{WS})

The first step during the thermodynamic analysis is to understand the change in Gibbs free energy of the reactions [281].

$$\Delta G = \Delta H - T\Delta S \quad \text{Eq. 13}$$

In the scope of this thesis, quantities are given per mol of oxygen unless otherwise is stated. The Gibbs free energy change of thermal decomposition and water splitting steps depends on the temperature, pressure, and metal oxide composition. In the reaction system of interest, ΔG_{TD} and ΔG_{WS} stand for the Gibbs free energy change for thermal decomposition and water splitting respectively. ΔG values should be negative or at least be close to zero to observe products at significant quantities at the equilibrium. Therefore, reaction conditions are selected to have spontaneity. This is why thermal decomposition reactions generally needs at the highest temperature and at the lowest oxygen content while water splitting reactions are carried out at much lower temperatures [282]. Consequently, red/ox materials for two step thermochemical water splitting reaction systems should satisfy the following criteria:

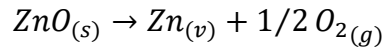
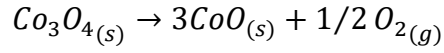
$$\Delta G_{TD}(P_{O_2}, T) < 0 \quad \text{Eq. 14}$$

$$\Delta G_{WS}(P_{O_2}, T) + \Delta G_{H_2O}(P_{O_2}, T) < 0 \quad \text{Eq. 15}$$

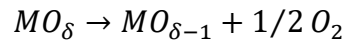
4.2.1 Thermal Decomposition Thermodynamics

Red/ox material undergoing a thermal decomposition step follows an oxygen desorption pattern such as surface oxygen release, formation of oxygen vacancies, partial reduction, and phase change reduction. For this manner, thermodynamic analysis should be applied for all these steps with the available data for the determination of limits of thermal decomposition step.

Thermal Decomposition by Phase Change : Phase change reduction occurs during the crystallography change, melting or sublimation. Depending on the reaction conditions (Figure 4.2), materials such as Co_3O_4 changes its spinel structure to rock salt whereas gaseous Zn occurs during the thermal decomposition of ZnO as



Thermodynamics of phase reduction are straightforward such that change in enthalpy and entropy can be calculated as



$$\Delta H = \Delta H_{\text{MO}_\delta} + 1/2 \Delta H_{\text{O}_2} - \Delta H_{\text{MO}_{\delta-1}} \quad \text{Eq. 16}$$

$$\Delta S = \Delta S_{\text{MO}_\delta} + 1/2 \Delta S_{\text{O}_2} - \Delta S_{\text{MO}_{\delta-1}} \quad \text{Eq. 17}$$

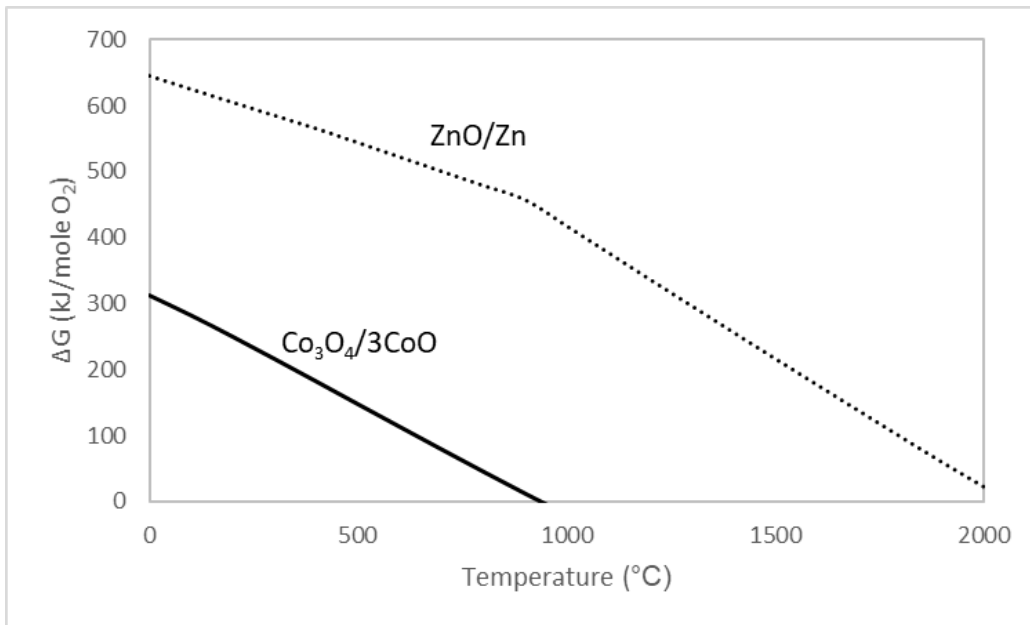


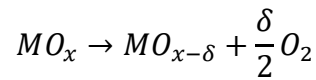
Figure 4.2. Gibbs free energy change during phase change reactions of single oxides

For the cases where sublimation occurs such as ZnO/Zn system, the dependency of partial pressure of gaseous compounds except oxygen on the change in the entropy is formulated as

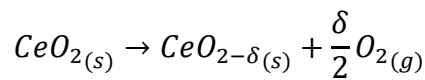
$$\Delta S = \Delta S^o - R \ln \left(\frac{\sqrt{P_{O_2}} P_{MO_{\delta-1}}}{P^o} \right) \quad \text{Eq. 18}$$

For the multicomponent oxides, such as $\text{Co}_3\text{O}_4\text{-Fe}_2\text{O}_3$, $\text{Mn}_2\text{O}_3\text{-Fe}_2\text{O}_3$, thermodynamic calculations becomes more complex due to the considerations of solid solutions, multi-phase equilibria etc. [283,284].

Thermal Decomposition by Partial Reduction: Partial reduction occurs during the reduction of red/ox materials without phase change. Oxygen leaves the red/ox material through the lattice without disturbing the crystal structure as described below;



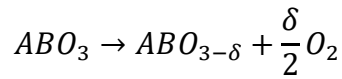
The magnitude of δ , non-stoichiometry, is strong function of the temperature and the partial pressure of oxygen. Ce based materials with perovskites are the common examples for the partial reduction [285,286]. It should be noted that phase change reduction is also expected for $\text{CeO}_2/\text{Ce}_2\text{O}_3$ only if strong reducing conditions, such as extremely high temperatures and low oxygen partial pressures, are satisfied [152,287].



The perovskites have a certain stoichiometry as ABO_3 where A and B represent two cations at different sizes. The size of A atoms are larger than B atoms and the tolerance to form a perovskite from these two atoms is determined by Goldschmidt tolerance factor, [163];

$$t = \frac{r_A + r_O}{\sqrt{2}(r_B + r_O)} \quad \text{Eq. 19}$$

The Goldschmidt tolerance factor, t , should be close to one for the formation of a perovskite. If $t = 1$, the ABO_3 has an ideal cubic perovskite structure. Orthorhombic, tetragonal, hexagonal or rhombohedral crystal structures can also be formed in the range of $1.02 < t < 1.57$ [288–290]. These structures are defined as distorted perovskites. The distorted perovskites offer an ability to tune red/ox performance by changing the A and B sites with appropriate metal cations. For example, the enthalpy of reduction can be arranged in the range of $100\text{kJ}/\text{mole} < \Delta H < 500\text{kJ}/\text{mole}$ by appropriate selection of B site [291,292]. For example, the distortion in CaMnO_3 was decreased by the addition of Sr on the A site to form $\text{Ca}_{0.8}\text{Sr}_{0.2}\text{MnO}_3$. Therefore, formation energy of oxygen vacancies is decreased with a decreased in the reduction enthalpy [293,294]. Transition metals are generally selected for the B sites metals Co [295,296], Fe [297,298], Mn [299,300], and Ti [301,302], while alkali earth metals are chosen for the A site.



Partial reduction results in oxygen defect in the lattice. The contribution of defects adds new constraints to the system for thermodynamic estimations. These constraints are accounted by using a new term as configuration entropy. Under the assumption of dilute species, the configuration entropy becomes entropy of mixing where the defects are free to move. Taking this into account, the equilibrium thermodynamic can be predicted by using partial molar quantities [185,303], as

$$\frac{\partial G^o(\delta, T)}{\partial \delta} = \frac{\partial H^o(\delta, T)}{\partial \delta} - T \frac{\partial S^o(\delta, T)}{\partial \delta} \quad \text{Eq. 20}$$

The entropy and enthalpy dependency on δ are due to the defect formation and formation energy of defects [185,304,305]. In equilibrium, the concentration of oxygen vacancies reaches a value where $\frac{\partial G(\delta, T)}{\partial \delta}$ reaches to zero.

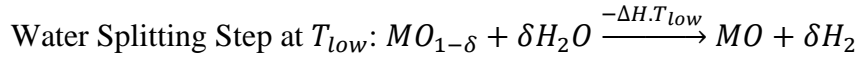
At non-standard pressures, the desired equation becomes

$$\frac{\partial S(\delta, T)}{\partial \delta} = \frac{\partial S^o(\delta, T)}{\partial \delta} + R \ln \left(\frac{\sqrt{P_{O_2}}}{P^o} \right) \quad \text{Eq. 21}$$

$$\frac{\partial G(\delta, T)}{\partial \delta} = \frac{\partial H^o(\delta, T)}{\partial \delta} - T \frac{\partial S^o(\delta, T)}{\partial \delta} + R \ln \left(\frac{\sqrt{P_{O_2}}}{P^o} \right) \quad \text{Eq. 22}$$

4.2.2 Oxidation Thermodynamics

Fuel Production: Two-step thermochemical processes consists of two reaction steps as thermal decomposition and oxidation. The oxidation step is important since it has a potential to produce hydrogen from water or carbon monoxide from carbon dioxide. Therefore, this step is often called fuel production step.



+



In terms of thermodynamics, Gibbs free energy of net reaction can be written as;

$$\Delta G_{WD} = \Delta G_{TD} + \Delta G_{WS} \quad \text{Eq. 23}$$

where subscripts *WD*, *TD*, and *WS* represent the water dissociation, thermal decomposition, and water splitting reactions respectively.

For the water splitting Gibbs free energy at non-standard pressures can be described as

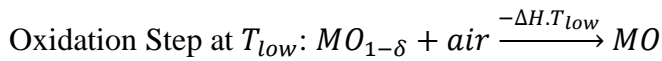
$$\Delta G_{WS} = \Delta H^o_{WS} - T\Delta S^o_{WS} + RT\ln\left(\frac{P_{H_2}}{P_{H_2O}}\right) \quad \text{Eq. 24}$$

The logarithm part of Eq. 24 can be neglected for an equilibrium conversion with 50% conversion since $\frac{P_{H_2}}{P_{H_2O}}$ reaches to 1. In addition, ΔG_{WS} can be rewritten as

$$\begin{aligned} \Delta G_{WS} &= \Delta G^o_{WD} - \Delta G^o_{TD} \\ &= (\Delta H^o_{WD} - \Delta H^o_{TD}) - T_{WS}(\Delta S^o_{WD} - \Delta S^o_{TD}) \end{aligned} \quad \text{Eq. 25}$$

During the thermal decomposition of red/ox materials, oxygen was evolved so that entropy term of Eq. 25 becomes positive. Therefore, spontaneity of oxidation reaction can be preserved only if $\Delta H^o_{TD} > \Delta H^o_{WD}$. As the ΔH^o_{TD} becomes larger, ΔG_{WS} tends to have more negative values which increases the production of H_2 . However, larger reduction enthalpies indicate more difficult reduction steps, i.e. higher temperatures during thermal decomposition. In order to overcome high ΔH^o_{TD} drawback, the driving force towards reduction can be increased by high ΔS^o_{TD} .

Oxygen Production: Two step thermochemical processes can also be utilized for oxygen production. For this purpose, an ideal red/ox material should have low reduction energy, high oxygen exchange capacity, and high driving force to capture oxygen from air. The last is directly controls the energy consumption for per mol oxygen production. This can be done by changing the reactant in the oxidation step simply to air as described below;



The red/ox materials those of which undergoes phase change reduction are generally preferred for oxygen production. For this reaction mechanism, Gibbs free energy at non-standard pressures can be written as

$$\Delta G_{OX} = \Delta H^o_{OX} - T\Delta S^o_{OX} + RT \ln \left(\frac{\sqrt{P_{O_2}}}{P^o} \right) \quad \text{Eq. 26}$$

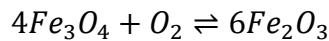
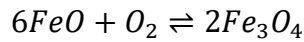
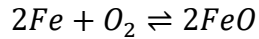
can be rewritten as

$$\frac{\sqrt{P_{O_2}}}{P^o} = \exp \left(\frac{-\Delta G_{OX}}{RT} \right) = A \exp \left(\frac{-2\Delta H_{OX}}{RT} \right) \text{ where } A = \exp \left(\frac{2\Delta S_{OX}}{R} \right) \quad \text{Eq. 27}$$

The effect of temperature on partial pressure of oxygen can be seen by utilizing the Eq. 27.

4.3 Red/Ox Thermodynamics

In the scope of this thesis, all metals in the periodic table that have enough thermodynamic data in Barin were screened [277]. After carefully examined the required oxidation steps for complete oxidation, the Gibbs free energies of the reactions were calculated and plotted. The procedure can be described by taking iron as an example. FeO, Fe₃O₄ and Fe₂O₃ are the oxidized forms of iron. The oxidation pathway of iron is written as reaction given below. Then, the reaction Gibbs free energies were calculated and plotted as shown in Figure 4.3.



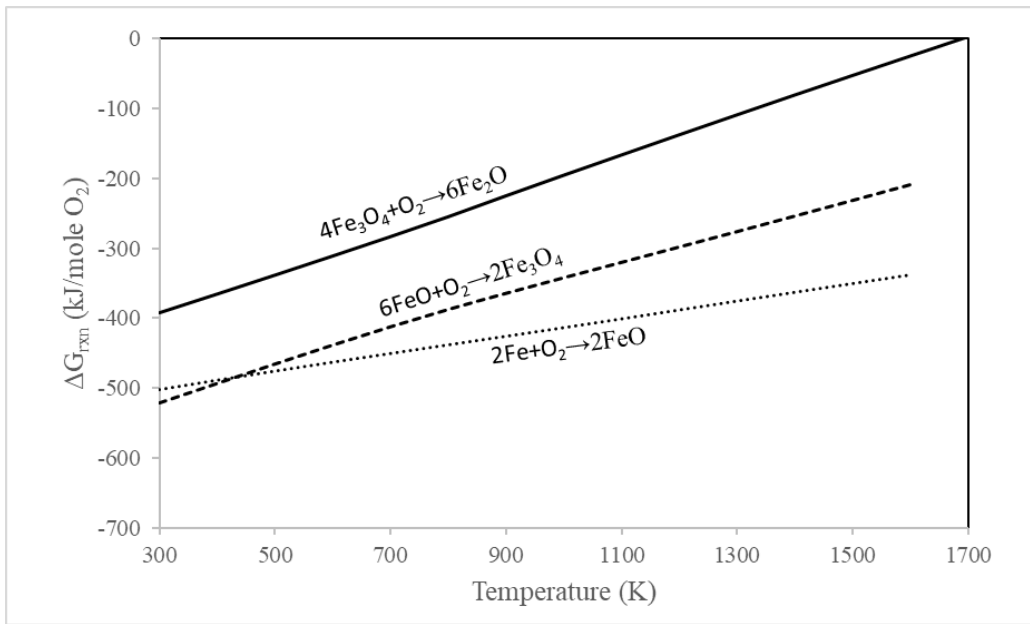


Figure 4.3. Ellingham Diagram of Fe, FeO, Fe_3O_4 and Fe_2O_3

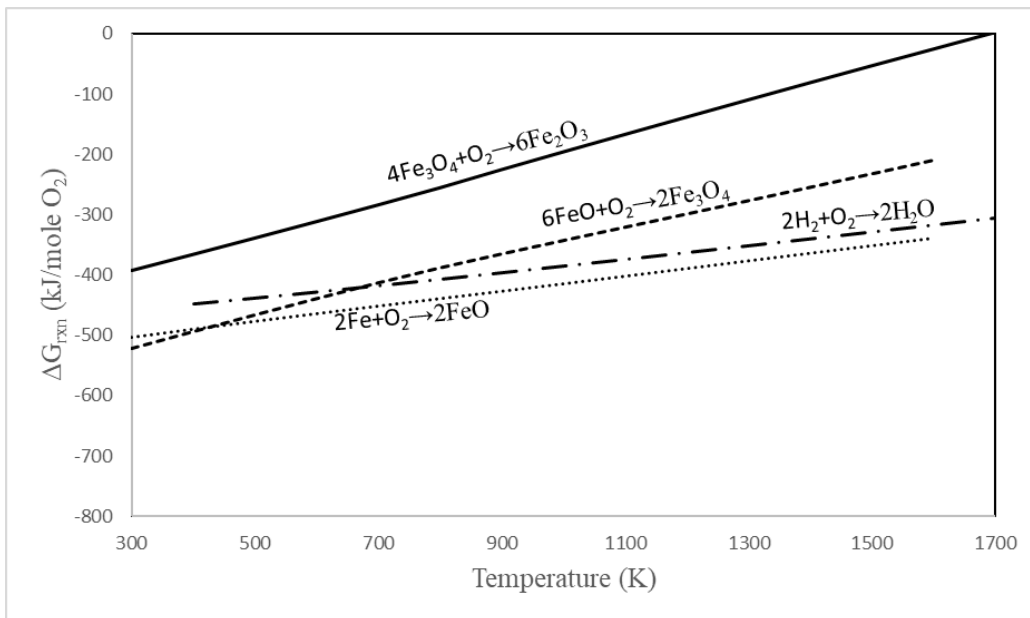


Figure 4.4. Ellingham Diagram of Fe, FeO, Fe_3O_4 and Fe_2O_3 with H_2

In the aim of material research for water splitting and carbon dioxide reduction experiments, H₂O formation lines were also drawn as shown in Figure 4.4. The possibility of thermal decomposition of Fe₂O₃ is higher than the other metals since Gibbs free energy of reaction decreases as temperature increases. Thus, $Fe_3O_4 \rightleftharpoons Fe_2O_3$ oxidation via splitting of H₂O and CO₂ is unlikely. The next reduction state of iron is the reaction $FeO \rightleftharpoons Fe_3O_4$. The Gibbs free energy line of this reaction is very close to CO, CO₂ and H₂O splitting lines. This indicates that partial conversion of FeO to Fe₃O₄ can be expected. $Fe \rightleftharpoons FeO$ which is the final reduction step seeming most active reaction since at all temperatures, its reaction Gibbs free energy is less than the CO, CO₂ and H₂O formation lines. Cho *et al.* showed that Fe₂O₃ was reduced to FeO_{0.5} by methane reforming in a three reactor chemical looping process [306]. FeO_{0.5} was partially oxidized to FeO by steam during the regeneration step due to slow kinetics. Further oxidation to Fe₂O₃ was completed by air.

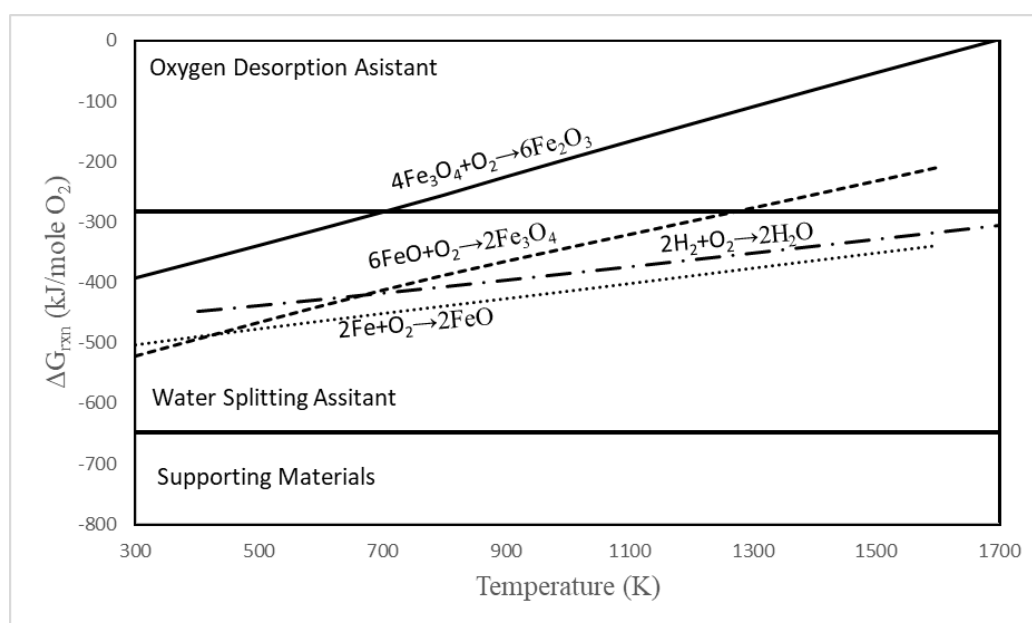


Figure 4.5. Categorization of red/ox materials based on Ellingham diagram in terms of oxygen desorption, water splitting and supporting materials

Having conducted to thermodynamic analysis (Appendix D) based on Gibbs free energy, metals in periodic table can be categorized in three groups (Figure 4.5). First

group includes the metals that have high tendency to desorb oxygen ($\Delta G > -300 \text{ kJ/mole } O_2$). The metals that can split water forms another group. These metals can be divided into two subsection ($-500 > \Delta G(\text{kJ/mole } O_2) > -300$ and $-700 > \Delta G(\text{kJ/mole } O_2) > -500$) depending on their relative thermodynamic driving force for hydrogen production. Final group consists of very stable metal oxides that can be used as support ($\Delta G < -700 \text{ kJ/mole } O_2$). These groups are shown in Table 4.1. The numbers in the parenthesis are the melting points of oxide pairs. From the thermodynamic point of view, single metal/metal oxide will not be enough to use for solar thermal processes. Single metal/metal oxide that has good oxygen desorption ability will perform negatively during the water splitting; that is, no oxidation or partial oxidation of reduced metal is expected. On the other hand, a material that splits water will need high temperatures for thermal reduction. These two conclusions explain why high temperature differences are needed for solar thermal hydrogen production processes. Charvin *et al.* showed that 75% of Fe_3O_4 was thermally reduced at 1400 °C. Reduced metal was reoxidized by steam at 575 °C [99]. Another study showed that 5% of pure ceria was reduced at 1400 °C and regenerated by steam at 1100 °C [307]. These studies showed that the cyclic temperature range should be high if single metal is selected for solar thermal hydrogen production.

Table 4.1 Categorized metals for solar thermal hydrogen production in terms of thermodynamic driving force

Oxygen Desorption	Water Splitting		Support
$\Delta G > -300$ (kJ/mole O_2)	$-500 > \Delta G > -300$ (kJ/mole O_2)	$-700 > \Delta G > -500$ (kJ/mole O_2)	$\Delta G < -700$ (kJ/mole O_2)
$Cr_2O_3 \rightarrow CrO_2$ (648K)	$CsO \rightarrow Cs_2O_3$ (?)	$B \rightarrow B_2O_3$ (723K)	$Al \rightarrow Al_2O_3$ (933K)
$BaO \rightarrow BaO_2$ (723K)	$Cs_2O_3 \rightarrow Cs_2O$ (705K)	$Cr \rightarrow Cr_2O_3$ (2180K)	$Be \rightarrow BeO$ (1560K)
$CoO \rightarrow Co_3O_4$ (1168K)	$Cd \rightarrow CdO$ (594K)	$Ce_2O_3 \rightarrow CeO_2$ (2450K)	$Ce \rightarrow Ce_2O_3$ (1068K)
$BiO \rightarrow Bi_2O_3$ (1090K)	$Co \rightarrow CoO$ (1768K)	$Cs \rightarrow Cs_2O$ (302K)	$Hf \rightarrow HfO_2$ (2506K)
$Cu_2O \rightarrow CuO$ (1505K) $Cu \rightarrow Cu_2O$ (1358K)	$FeO \rightarrow Fe_3O_4$ (1650K) $Fe \rightarrow FeO$ (1650K)	$Ga_2O \rightarrow Ga_2O_3$ (?) $Ga \rightarrow Ga_2O$ (?)	$Gd \rightarrow Gd_2O_3$ (1585K)
$Fe_3O_4 \rightarrow Fe_2O_3$ (1811K)	$In \rightarrow In_2O_3$ (430K)	$Mn \rightarrow MnO$ (1519K)	$Ho \rightarrow Ho_2O_3$ (1734K)
$Ir \rightarrow IrO_2$ (1370K)	$Ge \rightarrow GeO_2$ (1211K)	$Nb \rightarrow NbO$ (2210K)	$Li \rightarrow Li_2O$ (454K)
$Li_2O \rightarrow Li_2O_2$ (468K)	$K \rightarrow K_2O$ (337K)	$Rb \rightarrow Rb_2O$ (312K)	$La \rightarrow La_2O_3$ (1193K)
$K_2O_2 \rightarrow KO_2$ (763K) $K_2O \rightarrow K_2O_2$ (763K)	$NbO_2 \rightarrow Nb_2O_5$ (1785K) $NbO \rightarrow NbO_2$ (2188K)	$VO \rightarrow V_2O_3$ (2062K) $V \rightarrow VO$ (2062K)	$Lu \rightarrow Lu_2O_3$ (1925K)
$Mn_2O_3 \rightarrow MnO_2$ (808K) $Mn_3O_4 \rightarrow Mn_2O_3$ (1161K) $MnO \rightarrow Mn_3O_4$ (1840K)	$Ni \rightarrow NiO$ (1728K)	$Ti_4O_7 \rightarrow TiO_2$ (2116K) $Ti_2O_3 \rightarrow Ti_3O_5$ (?) $Ti_3O_5 \rightarrow Ti_4O_7$ (?) $TiO \rightarrow Ti_2O_3$ (2020K)	$Mg \rightarrow MgO$ (923K)
$MoO_2 \rightarrow MoO_3$ (1068K)	$Mo \rightarrow MoO_2$ (1370K)	$Ta \rightarrow Ta_2O_5$ (2145K)	$Np \rightarrow NpO_2$ (909K)
$Na_2O \rightarrow Na_2O_2$ (733K)	$Na \rightarrow Na_2O$ (371K)	$Zn \rightarrow ZnO$ (693K)	$Nd \rightarrow Nd_2O_3$ (1297K)
$Os \rightarrow OsO_2$ (773K)	$Sb \rightarrow Sb_2O_3$ (904K)		$Pr \rightarrow Pr_2O_3$ (1208K)

Table 4.1 (cont'd) Categorized metals for solar thermal hydrogen production in terms of thermodynamic driving force

Oxygen Desorption	Water Splitting		Support
	$-500 > \Delta G > -300$ (kJ/mole O_2)	$-700 > \Delta G > -500$ (kJ/mole O_2)	
Pb ₃ O ₄ →PbO ₂ (563K) PbO→Pb ₃ O ₄ (773K) Pb→PbO (601K)	SnO→SnO ₂ (1350K) Sn→SnO (505K)		Si→SiO ₂ (1687K)
Pr ₇ O ₁₂ →PrO ₂ Pr ₂ O ₃ →Pr ₇ O ₁₂	WO ₂ →WO ₃ (1746K) W→WO ₂ (1970K)		Sm→Sm ₂ O ₃ (1345K)
Pd→PdO (1020K)			Sc→Sc ₂ O ₃ (1814K)
Rb ₂ O→RbO ₂ (705K)			Sr→SrO (1050K)
ReO ₃ →Re ₂ O ₇ (633K) ReO ₂ →ReO ₃ (673K) Re→ReO ₂ (1273K)			Tb→Tb ₂ O ₃ (1629K)
Rh→Rh ₂ O ₃ (1370K)			Ti→TiO (1941K)
Ru→RuO ₂ (1473K)			Yb→Yb ₂ O ₃ (1097K)
Sb ₂ O ₄ →Sb ₂ O ₅ (653K) Sb ₂ O ₃ →Sb ₂ O ₄ (929K)			Tm→Tm ₂ O ₃ (1818K)
Se→SeO ₂ (494K)			Y→Y ₂ O ₃ (1799K)
SrO→SrO ₂ (488K)			Zr→ZrO ₂ (2128K)
Tb ₂ O ₃ →TbO ₂ (?)			Ca→CaO (1115K)

Table 4.1 (cont'd) Categorized metals for solar thermal hydrogen production in terms of thermodynamic driving force

Oxygen Desorption	Water Splitting		Support
$\Delta G > -300$ (kJ/mole O_2)	$-500 > \Delta G > -300$ (kJ/mole O_2)	$-700 > \Delta G > -500$ (kJ/mole O_2)	$\Delta G < -700$ (kJ/mole O_2)
Tl ₂ O → Tl ₂ O ₃ (869K) Tl → Tl ₂ O (577K)			
Te → TeO ₂ (723K)			
V ₂ O ₄ → V ₂ O ₅ (963K) V ₂ O ₃ → V ₂ O ₄ (2210K)			

The thermodynamic possibility of mixed metal oxides which have enough thermodynamic data in Barin was also investigated [277]. The water splitting properties of these oxides are shown in Figure 4.6 and Figure 4.7. The formations of CoWO₄, FeWO₄, PbWO₄, CdWO₄, MnWO₄, PbMoO₄, NiWO₄, ZnWO₄ by water splitting are thermodynamically feasible between 400 K and 1600 K. The thermodynamic driving force for oxidation to CoFe₂O₄, Fe₂MnO₄, Fe₂NiO₄, Fe₂MgO₄ and Fe₂ZnO₄ decreases as temperature increases. Therefore, these mixed metal oxides can suffer from high temperature water splitting reactions. It is found that the formations of CuMoO₄, FeMoO₄, CuFe₂O₄ and MnMoO₄ are thermodynamically unfavorable; that is, these reactions can be completed under oxygen atmosphere. One can suggest that the formation mixed metal oxides that consist of tungsten have high thermodynamic tendency to occur while the occurrence iron containing mixed oxides by water splitting is depended on temperature.

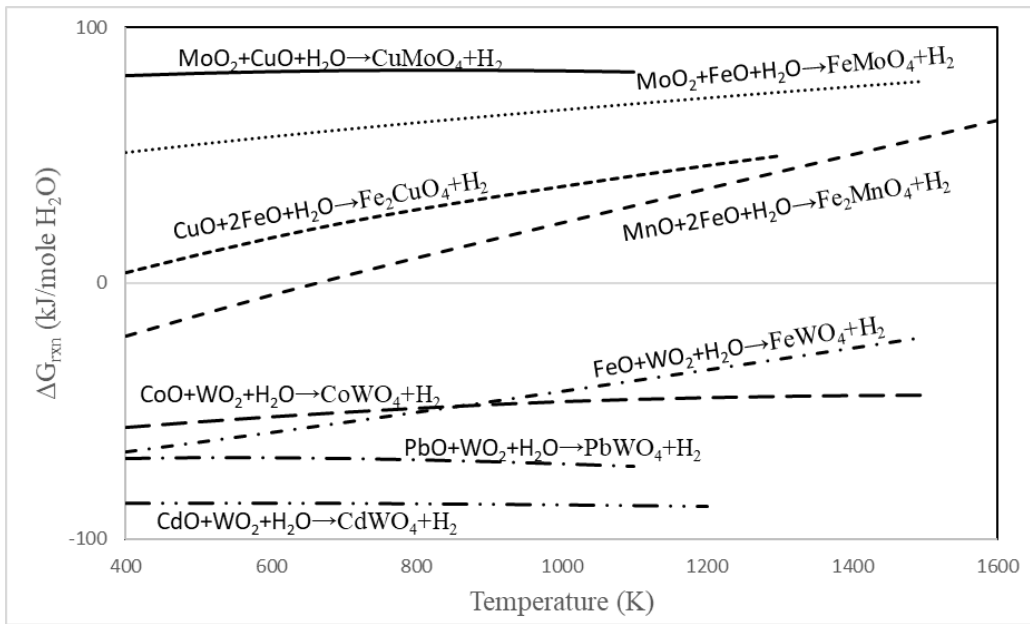


Figure 4.6. Thermodynamic driving force of CdWO_4 , CoWO_4 , CuFe_2O_4 , FeWO_4 , CoFe_2O_4 , CuMoO_4 , FeMoO_4 and Fe_2MnO_4 during water splitting reaction

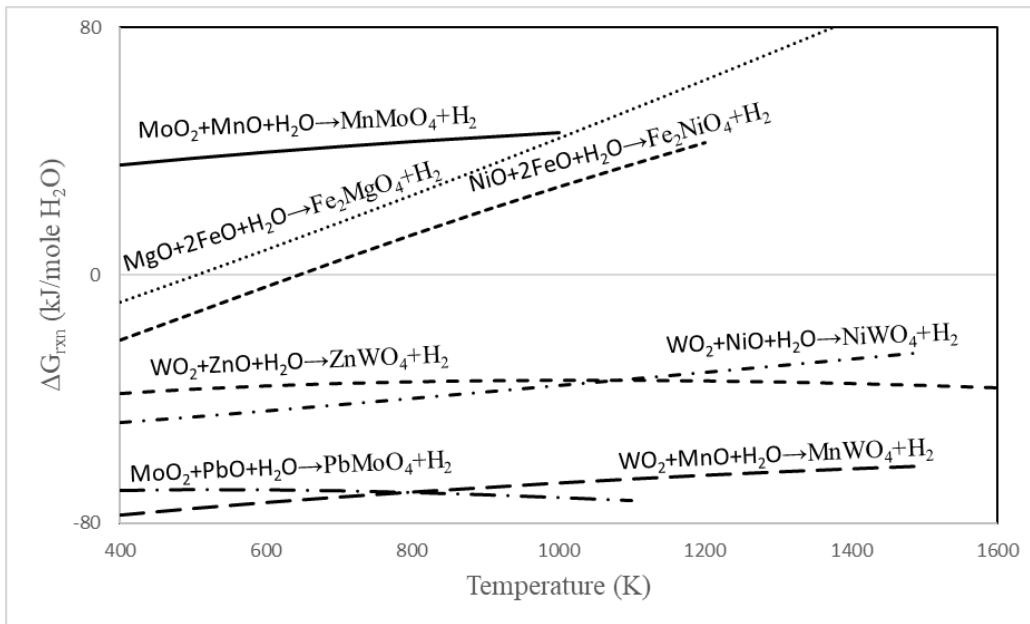


Figure 4.7. Thermodynamic driving force of Fe_2NiO_4 , Fe_2MgO_4 , MnWO_4 , Fe_2ZnO_4 , MnMoO_4 and PbMoO_4 during water splitting

In the thermal decomposition point of view, it is expected that all transformations have positive reaction Gibbs free energies as shown in Figure 4.8, Figure 4.9 and Figure 4.10. The comparison of these reactions is done in terms of the magnitude of reaction Gibbs free energies. It is found that the materials that are thermodynamically favorable for water splitting needs higher temperature for thermal decomposition. There is a certain difference between mixed metal oxides and metal oxides in terms of the magnitude of the reaction Gibbs free energies. For example, the magnitude of the reaction Gibbs free energy of certain materials at 1000K can be written as follows; $\Delta G_{CoO \rightleftharpoons Co_3O_4} = 70.3 \text{ kJ/mol } O_2$, $\Delta G_{FeO \rightleftharpoons Fe_3O_4} = 342.4 \text{ kJ/mol } O_2$ and $\Delta G_{CoFe_2O_4 \rightleftharpoons CoO, FeO} = 327.8 \text{ kJ/mol } O_2$. The thermodynamic probability of $CoFe_2O_4$ to decompose is higher than the Fe_3O_4 and lower than Co_3O_4 . There is a certain advantage for water splitting when $CoFe_2O_4$ is used since the reaction Gibbs free energy is negative while it is positive for FeO and CoO oxidation by water. Aston *et al.* studied the performances of Fe_2O_3 , $NiFe_2O_4$ and $CoFe_2O_4$ for pure H_2 and CO_2 production. Materials were reduced to FeO, $NiFe_2O_{4-x}$ and $CoFe_2O_{4-x}$ by syngas and then, reoxidized by water at 600 °C. It was found that reduced mixed oxides fully regenerated while the conversion of Fe_2O_3 was limited to 22%.

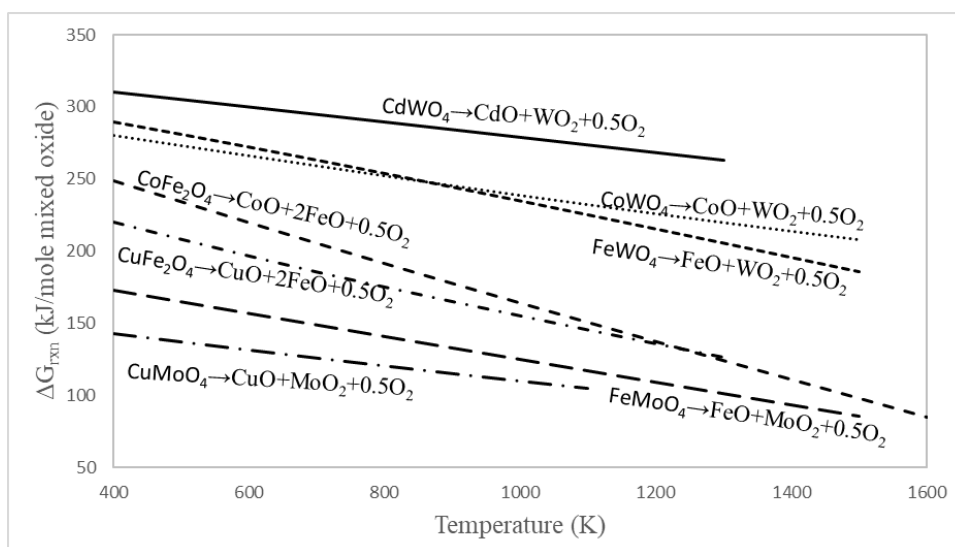


Figure 4.8. Thermodynamic driving force of $CdWO_4$, $CuMoO_4$, $FeWO_4$, $CoFe_2O_4$, $CuFe_2O_4$, $CoWO_4$, and $FeMoO_4$ during thermal reduction

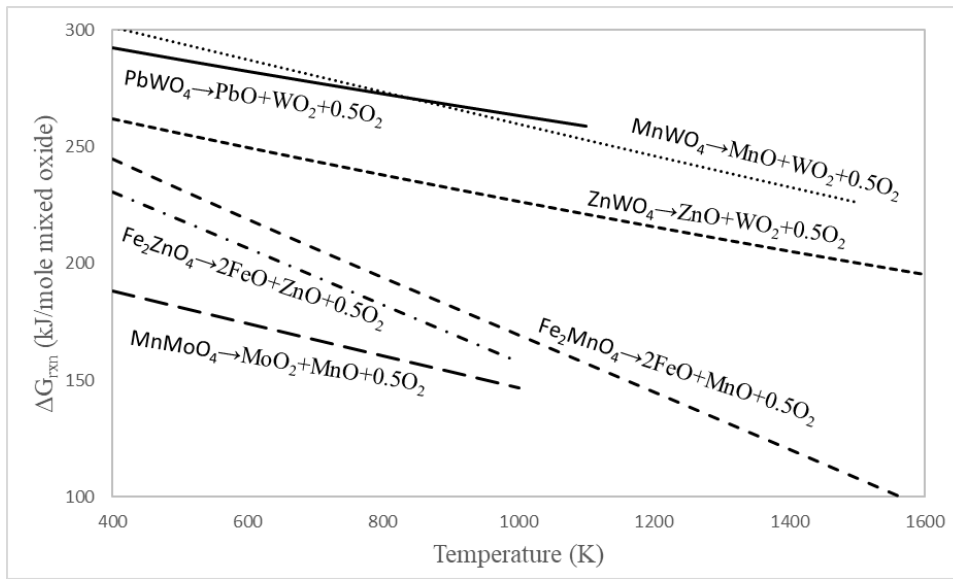


Figure 4.9. Thermodynamic driving force of Fe_2MnO_4 , MnMoO_4 , PbWO_4 , Fe_2ZnO_4 , MnWO_4 , and ZnWO_4 during thermal reduction

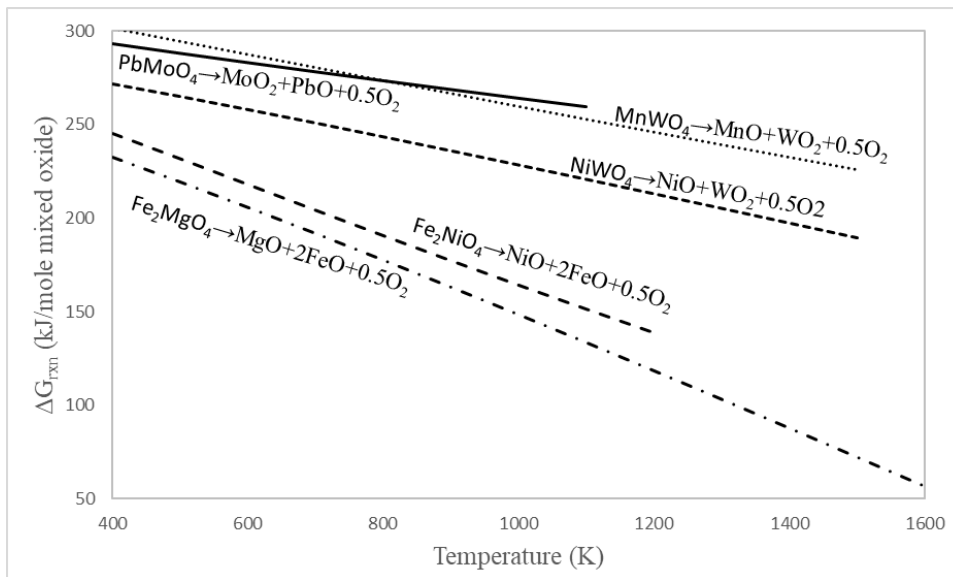


Figure 4.10. Thermodynamic driving force of Fe_2NiO_4 , PbMoO_4 , Fe_2MgO_4 , NiWO_4 , and MnWO_4 during thermal reduction

The temperature range of thermal reduction and oxidation steps is higher when single metal is used, and it decreases for bimetallic oxides. The phase transformation between oxidation and thermal reduction steps needs an assistant from a more stable oxide; that is, minimum three metals are needed for sufficient improvement in solar thermochemical hydrogen production. Each metal will assist the process by their thermodynamic properties. First metal should improve the oxygen desorption rates, so the temperature of the thermal reduction step will eventually decrease. The second metal should be stable enough to split water. The third metal which is the most important metal should work as a support while it should also help the solid state oxygen diffusion mechanism; that is, this metal will keep the metals in the reduced states so that during the oxidation it will help to form new phase which will have less oxide stability. This instability will help to decrease the temperature of the thermal reduction step. In order to test this hypothesis, certain candidate materials are selected depending on the availability of the thermodynamic data in the reference book [277]. The study performed by Munich *et al.* supports this theory [308]. They deposited CoFe_2O_4 spinel oxide to Al_2O_3 by atomic layer deposition. Material is cycled at 1350 °C isothermally between water splitting and thermal reduction. The desorbed oxygen from CoFe_2O_4 structure makes the structure instable. This instability balances with the oxygen coming from Al_2O_3 since the thermodynamic driving force between Co and Fe is less than Co-Al and Fe-Al at the studied temperature range. The steam injection to the system increases the oxidation state of the iron from +2 to +3 so that the thermodynamic driving force shift from Co-Al and Fe-Al to Co-Fe. The first testing group was shown in Table 4.2.

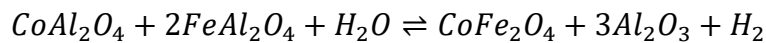
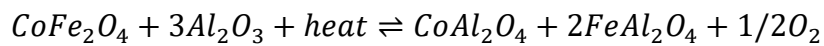


Table 4.2 The possible combination of the candidate materials

	Oxygen Desorption Assistant				Water Splitting Assistant				Solid State Oxygen Diffusion Assistant					
	Co	Ba	Mn	Sr	V	W	Fe	Ce	Ti	Al	Si	Zr	Mg	Zn
Co						CoWO ₄	CoFe ₂ O ₄		CoTiO ₃ ; Co ₂ TiO ₄		Co ₂ SiO ₄			
Ba						BaWO ₄			BaTiO ₃ ; Ba ₃ TiO ₄	BaAl ₂ O ₄ ; Ba ₃ Al ₂ O ₆	BaSiO ₃ ; BaSi ₂ O ₅ ; Ba ₂ SiO ₄ ; Ba ₂ Si ₃ O ₅	BaZrO ₃		
Mn						MnWO ₄	FeMnO ₄			MnAl ₂ O ₄	MnSiO ₃ ; Mn ₂ SiO ₄	MnTiO ₃ ; Mn ₂ TiO ₄		
Sr						SrWO ₄			SrTiO ₃ ; SrTiO ₄ ; Sr ₄ Ti ₃ O ₁₀	SrAl ₂ O ₄	SrSiO ₃ ; Sr ₂ SiO ₄	SrZrO ₃		
V							FeV ₂ O ₄ ; Fe(VO ₃) ₂						Mg(VO ₃) ₂ ; Mg ₂ V ₂ O ₇	
W	CoWO ₄	BaWO ₄	MnWO ₄	SrWO ₄			FeWO ₄						MgWO ₄	ZnWO ₄
Fe	CoFe ₂ O ₄		FeMnO ₄		FeV ₂ O ₄ ; Fe(VO ₃) ₂	FeWO ₄			FeTiO ₃ ; FeTiO ₄	FeAl ₂ O ₄	FeSiO ₃ ; FeSiO ₄			Fe ₂ ZnO ₄
Ce										CeAlO ₃				
Ti	CoTiO ₃ ; Co ₂ TiO ₄	BaTiO ₃ ; Ba ₂ TiO ₄	MnTiO ₃ ; Mn ₂ TiO ₄	SrTiO ₃ ; SrTiO ₄ ; Sr ₄ Ti ₃ O ₁₀			FeTiO ₃ ; FeTiO ₄			Al ₂ TiO ₅				MgTiO ₃ ; Mg ₂ TiO ₄
Al		BaAl ₂ O ₄ ; Ba ₃ Al ₂ O ₆	MnAl ₂ O ₄	SrAl ₂ O ₄		FeAl ₂ O ₄	CeAlO ₃	Al ₂ TiO ₅						
Si	Co ₂ SiO ₄	BaSiO ₃ ; BaSi ₂ O ₅ ; Ba ₂ SiO ₄ ; Ba ₂ Si ₃ O ₅	MnSiO ₃ ; Mn ₂ SiO ₄	SrSiO ₃ ; Sr ₂ SiO ₄		FeSiO ₃ ; FeSiO ₄								
Zr		BaZrO ₃		SrZrO ₃										
Mg					Mg(VO ₃) ₂ ; Mg ₂ V ₂ O ₇	MgWO ₄			MgTiO ₃ ; Mg ₂ Ti ₂ O ₅ ; Mg ₂ TiO ₄					
Zn						ZnWO ₄	Fe ₂ ZnO ₄	Zn ₂ TiO ₄						

4.4 Thermodynamic Efficiency of Solar Concentrators

Solar energy can be utilized by sustaining the energy requirement of the reduction reaction. This process can be described as solar energy storage at chemical bonds; that is, the product can be used for simply heat generation. Water splitting reaction ($H_2O \rightarrow H_2 + 0.5O_2$) needs 484kJ/mol O_2 to complete the reaction. This energy can be supplied from the solar energy. In addition, the products (H_2 and O_2) can be transported and stored in suitable environments for certain period of time. This process is described as the solar energy storage in chemical bonds. During a demand, this stored energy can be used for heat generation or work production. The efficiency of chemical energy storage can be defined as the percentage of solar energy utilized for products. The thermodynamic limit for this efficiency is very close to 100% at ideal conditions. However, the high temperature requirement of thermochemical processes decreases this efficiency due to the radiative losses from the receiver. Therefore, absorption efficiency is preferred for the prediction of solar thermochemical efficiency.

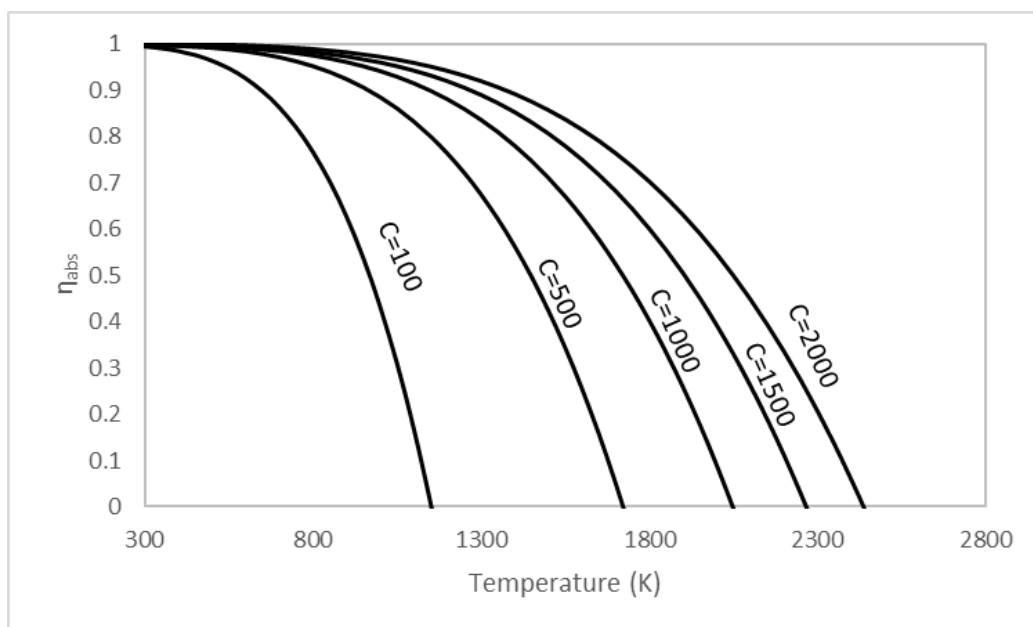


Figure 4.11. Overall concentrator efficiency as concentration ratio increases

Under the assumption of negligible conduction and convectional losses, absorption efficiency is described as [309]

$$\eta_{abs} = \frac{\alpha_s IC - \varepsilon \sigma T^4}{IC} \quad \text{Eq. 28}$$

where I is the solar radiation intensity, C ; concentration ratio, T ; receiver temperature, α_s ; solar radiation absorbance, ε ; emittance, σ ; Stefan-Boltzman constant. As solar energy is concerned, higher concentration ratios for higher thermal energy decreases the absorption efficiency as shown in Figure 4.11.

Carnot efficiency (Eq. 1) is another important parameter for predicting the limits of chemical energy storage in the chemical form. After defining η_{abs} and η_{Carnot} , the overall system efficiency, efficiency of solar system, is estimated from

$$\eta_{system} = \eta_{abs} \eta_{Carnot} \quad \text{Eq. 29}$$

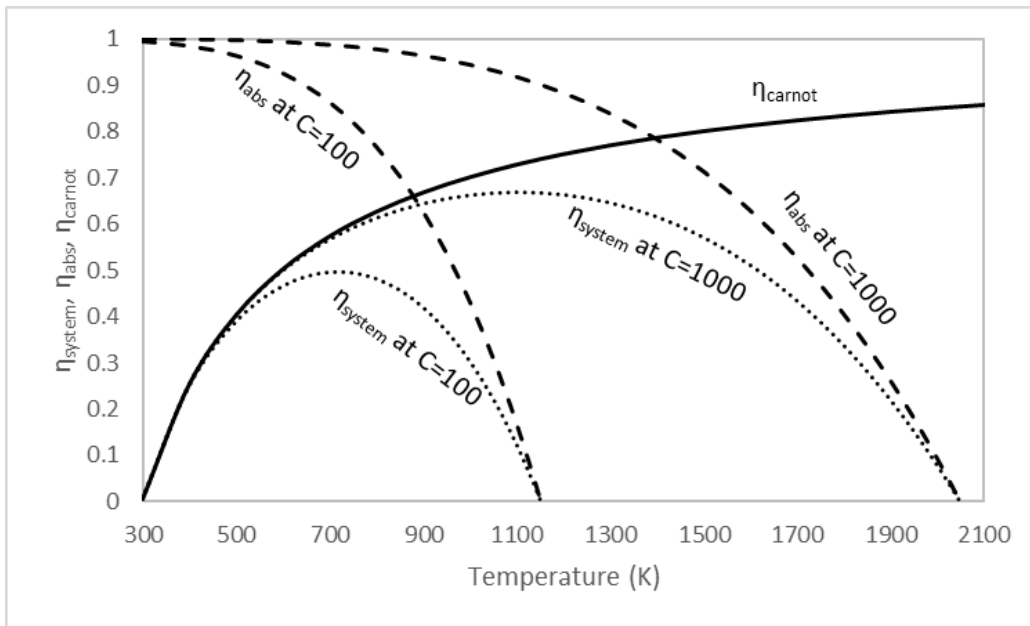


Figure 4.12. The effect of temperature of solar system efficiency

The maximum solar system efficiency was shown in Figure 4.12 under the following assumptions, $\alpha_s = \varepsilon = 1$, $I = 1 \text{ kW/m}^2$, $T_L = 298\text{K}$. The efficiencies are changing from 40% to 60% at the temperature range of 700K to 1100K. Therefore, for mid

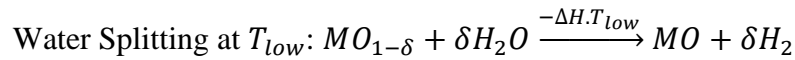
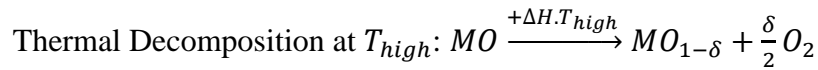
and low temperature operations ($T < 1100\text{K}$ with $C < 1000$), solar system efficiency can not exceed 60%. The magnitude of this efficiency is should be carefully taking into account for determining the overall system feasibility.

CHAPTER 5

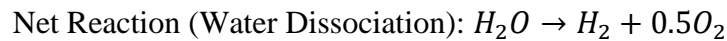
EXPERIMENTAL FINDINGS

5.1 Oxygen Exchange Capability

Thermochemical red/ox processes are based on the oxygen exchange properties of the red/ox materials. Oxygen exchange properties is defined as the ability to absorb/adsorb and desorb oxygen from environment consisting oxygen such as air, water, carbon dioxide. For the two-step thermochemical water splitting reactions, red/ox materials undergo a thermal decomposition reaction followed by oxidation by water as given;



+ _____



The products of these reaction system are oxygen and hydrogen at different steps. The amount of hydrogen is proportional to oxygen produced in the thermal decomposition step which is directly related to reduction extent of the red/ox material at T_{high} . In other words, the net reaction (water dissociation) yield is controlled by the oxygen exchange properties of the red/ox materials. Therefore, red/ox materials must be carefully chosen to maximize the yield.

On this front, the best red/ox material for two step thermochemical water splitting reaction can be defined as a red/ox material that can completely decompose, release all of its oxygen, and can reoxidized by water to reach its initial oxidation state. For the aim of finding better red/ox materials, the initial step, thermal decomposition

properties, was studied for CoO/Co₃O₄ system. CoO/Co₃O₄ was found to be thermodynamically favorable for complete reduction to CoO. However, this red/ox pair is thermodynamically impractical in solar thermochemical water splitting applications due to the low hydrogen yield (the ratio of formed hydrogen to maximum hydrogen that can be produced from water $H_2(\text{formed})/H_2(\text{max}) = 4 \cdot 10^{-7}\%$ at 900K) during oxidation reaction [116,117]. The, red/ox behavior of cobalt spinel oxide covers a full span of Co⁰ in the metallic cobalt, Co⁺² in CoO to Co⁺³ in Co₃O₄. Coexistence of the different oxidation states in the same material provides the opportunity to exploit the material as an excellent red/ox mediator. Therefore, CoO/Co₃O₄ was selected as a reference red/ox pair.

The rate of oxygen desorption and adsorption process is expected to be driven by kinetics, mass transfer, heat transfer and thermodynamics. The existence of active sites determines the rate of oxygen desorption and adsorption at low temperatures. As the temperature increases, reaction occurs instantaneously at the active sites so overall rate is controlled by transport of evolved or consumed oxygen. Further increase in temperature also enhances the diffusion constants on the order of 1.5 using Chapman-Enskog theory. In mid-temperatures, mass transfer and heat transfer compete each other. Careful investigation of overall rates is needed to exactly define the main resistance. At high temperatures, thermodynamic driving force for metal oxygen transfer; that is; the rate of phase transformation controls the red/ox cycles. Investigation of the phase transformation conditions can help us to understand process constraints. The change in oxidation state of active sites, the structural reorganization during phase transformation or exothermicity/endothemicity of the reaction creates new active sites, alters the resistance of mass and heat transfer respectively.

The effect of kinetic, mass, heat and thermodynamic resistances on rates was investigated by careful designed experiments as follows:

Kinetically Controlled Region: The red/ox material is diluted with an inert material. The rate dependency on dilution verifies the kinetic controlled region.

Mass Transfer Limited Region: The resistance of film mass transfer depends on the gaseous film that surrounds the particle. The thickness of this layer changes in the reverse order of Reynolds number. The effect of film mass transfer can be eliminated by increasing velocity while keeping volumetric flow rate constant by changing L/D ratio of the reactor. Pore diffusion resistance is investigated by changing the particle sizes. To see the effect of pore diffusion limitations, bulk and monolith doped materials can be tested at constant space-time.

Heat Transfer Limited Region: The heat transfer from oven to reactor and internal temperature gradient in the material bed are two main resistances. The heating rate of oven can be changed to see the effect of heat transfer from oven to reactor. The possible shifts indicate the resistance of exterior heat transfer resistance. The effect of interior heat transfer effect is tested by diluting the red/ox couple with an inert material that has high thermal conductivity. Enhancement in the rate of conversion is an indication of interior heat transfer resistance.

5.1.1 Red/Ox Characteristics of Co_3O_4 as Reference Material

Red/ox characteristics of Co_3O_4 was investigated by TPR and TPO analysis. The temperature programmed reduction (TPR) profile of Co_3O_4 conducted under 10% H_2 -Ar was given in Figure 5.1. The reduction of Co_3O_4 took place in the temperature range of 250 to 500 °C. The total hydrogen consumption was calculated as 4mol H_2 /mol Co_3O_4 . This amount is consistent with the overall reduction of the spinel oxide to metallic cobalt.

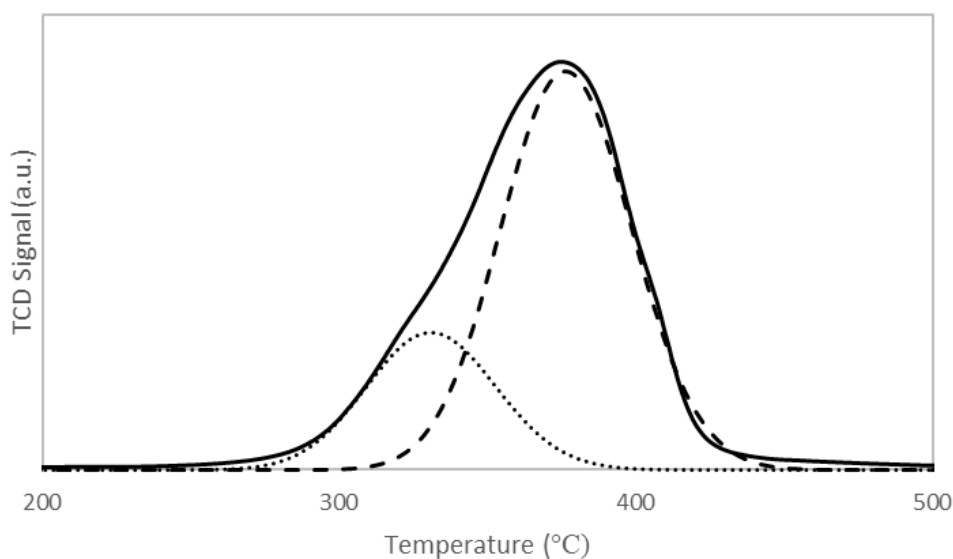


Figure 5.1. Temperature-programmed reduction profile of Co_3O_4 (solid line, dot and dashed lines represents experimental data, reduction of $\text{Co}^{3+,4+}$ to Co^{2+} and Co^{2+} to Co^0 respectively)

Two peaks identified in the TPR profile (Figure 5.1) indicated the existence of two events. The simulated peaks are symmetric in nature indicating a second order process was prevailing [310]. Dissociative adsorption of hydrogen is inherently a second order process. A symmetric Gaussian peak was used to represent the second order behavior for peak fitting. The fitting parameters are summarized in Table 5.1.

Table 5.1 Curve fitting parameters for TPR of Co_3O_4

Reaction	μ	σ	α_1	Area
$\text{Co}_3\text{O}_4 + \text{H}_2 \rightarrow 3\text{CoO} + \text{H}_2\text{O}$	330 °C	22 °C	0.29	1.7
$3\text{CoO} + 3\text{H}_2 \rightarrow 3\text{Co} + 3\text{H}_2\text{O}$	375 °C	22 °C	0.87	4.9

The relative amounts of hydrogen consumption estimated by the simulated peaks were close to 1:3, as expected from the stoichiometry of the reactions indicated in Table 5.1.

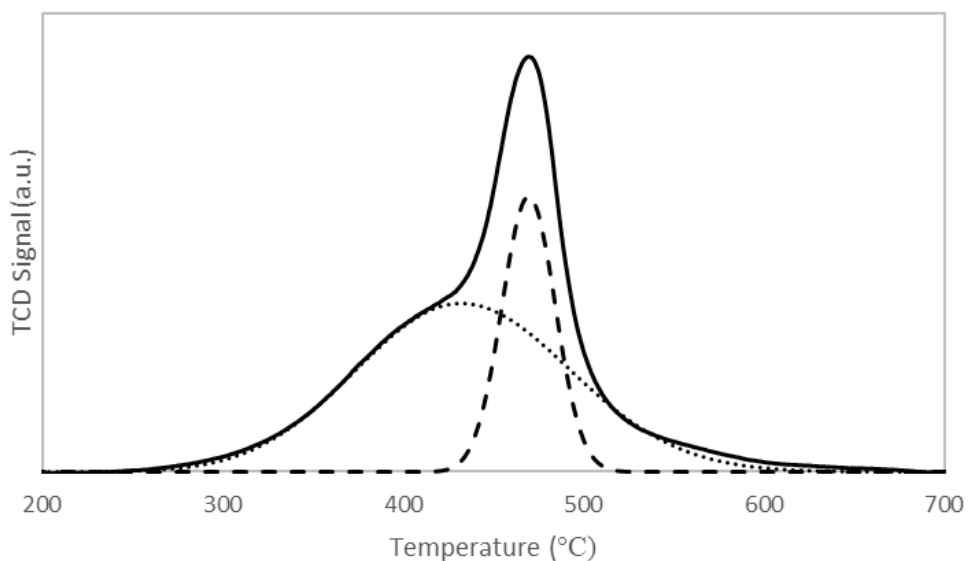


Figure 5.2. Temperature programmed oxidation patterns of reduced Co_3O_4 (solid line, dot and dashed lines represents experimental data, oxidation of Co^0 to Co^{2+} and Co^{2+} to $\text{Co}^{3+,4+}$ respectively)

Reduced samples were cooled to room temperature under 10% H_2 -Ar flow. Temperature programmed oxidation experiments were carried out under 2% O_2 -He flow after purging the reactor with helium. Reoxidation patterns of reduced Co_3O_4 were illustrated in Figure 5.2. A broad reoxidation peak was observed in the temperature range of 250-700 °C. This broad peak is coupled to a sharp peak centered about 470 °C. The fitting parameters are given in Table 5.2.

Table 5.2 Curve fitting parameters for TPO of reduced Co_3O_4

Reaction	μ	σ	α_1	Area
$3\text{Co} + 3/2 \text{O}_2 \rightarrow 3\text{CoO}$	432 °C	60 °C	0.033	0.5
$3\text{CoO} + 1/2 \text{O}_2 \rightarrow \text{Co}_3\text{O}_4$	470 °C	15 °C	0.054	0.2

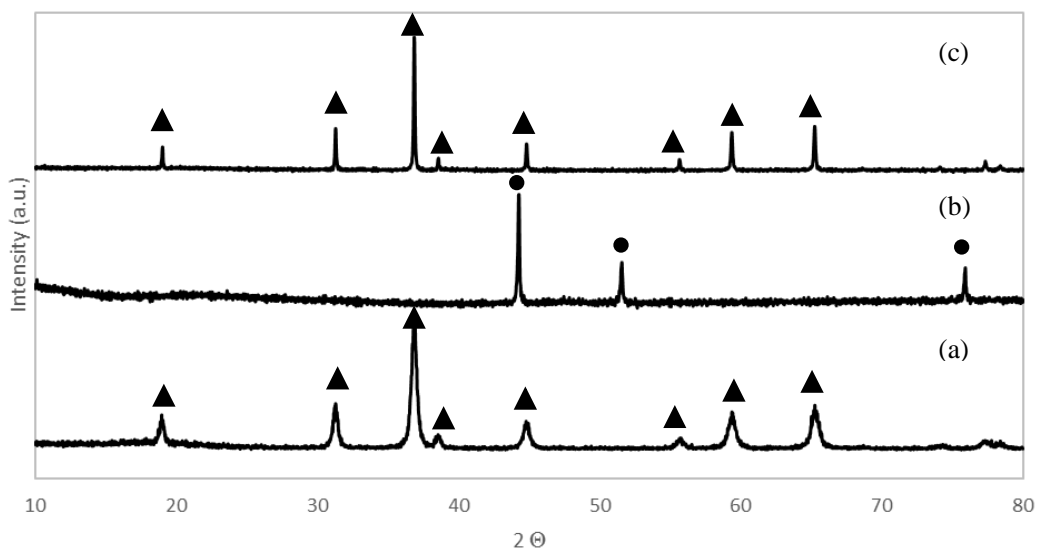


Figure 5.3. XRD patterns of Co_3O_4 (a) fresh sample; (b) after TPR; (c) after TPO following TPR (Triangles label peaks due to Co_3O_4 , circles represent peaks due to Co^0)

The reduction and oxidation processes were also monitored by XRD. The change in the crystal structure of Co_3O_4 during red/ox experiments were given in Figure 5.3. The fresh sample has the diffraction peaks of Co_3O_4 (JCPDS card No. 42-1467). After the TPR analysis, the sample was identified as Co (ICSD 44989) indicating complete reduction of Co_3O_4 . The diffraction peaks obtained after TPO following TPR was belong to Co_3O_4 (JCPDS card No. 42-1467), demonstrating full reoxidation of sample. The broader peaks observed for fresh sample indicates the formation of nanoparticles due to less lattice interactions.

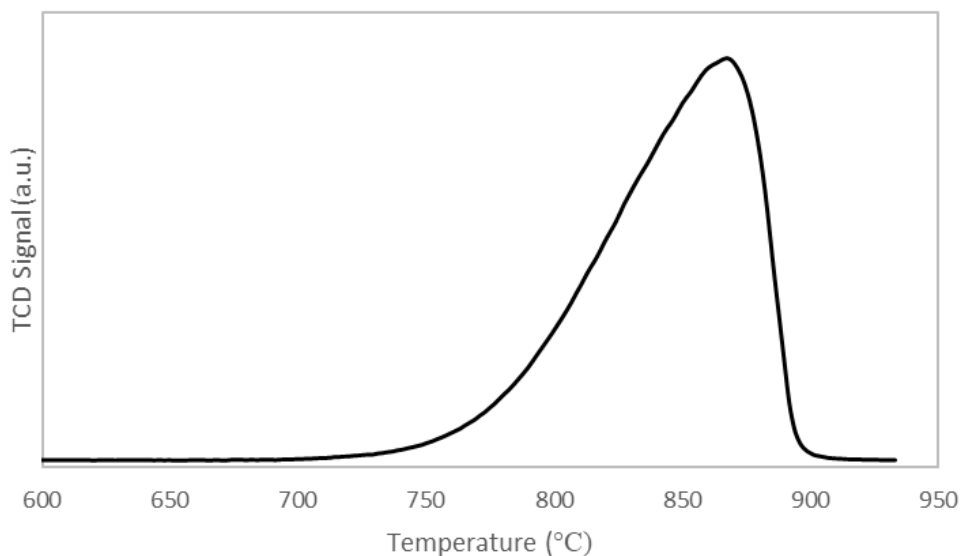


Figure 5.4. Oxygen evolution during thermal decomposition (TPtD) of Co_3O_4

Having evaluated the red/ox properties of Co_3O_4 , temperature programmed thermal decomposition experiment was performed (Figure 5.4). Oxygen evolution was detected after 700 °C and gave a maximum around 870 °C. Evolved oxygen was 25% of the total oxygen uptake during TPO after TPR corresponding to the reaction of $\text{Co}_3\text{O}_4 \rightarrow 3\text{CoO} + 1/2\text{O}_2$. The oxygen evolution peak is asymmetric indicating first order desorption process [310].

Thermal gravimetric analysis revealed that around 6.5% weight was lost due to thermal decomposition of Co_3O_4 . The calculate weight loss is exactly equal to 0.5 mol O_2 /mol Co_3O_4 corresponding to the reaction of $\text{Co}_3\text{O}_4 \rightarrow 3\text{CoO} + 0.5 \text{O}_2$.

The Effect of Bi-Metallic Interaction on Red/Ox Performance: Having evaluated the temperature programmed reduction, oxidation and thermal decomposition profiles of Co_3O_4 , the effect of doping with another metal was also investigated. For this purpose, 0.5wt. % Pt- Co_3O_4 was tested in terms of temperature programmed experiments. The reducibility of Co_3O_4 was enhanced in the presence of platinum as given in Figure 5.5. The reduction of Co^{3+} to Co^{2+} was completed around 240 °C. Further reduction to Co^0 was completed at 420 °C. The hydrogen consumption was calculated as 4 mol H_2 /mol Co_3O_4 which is well agree with stoichiometry. The

reduction of platinum was not observed probably due to the low loading amount (less than 0.13 mg in 25 mg total sample).

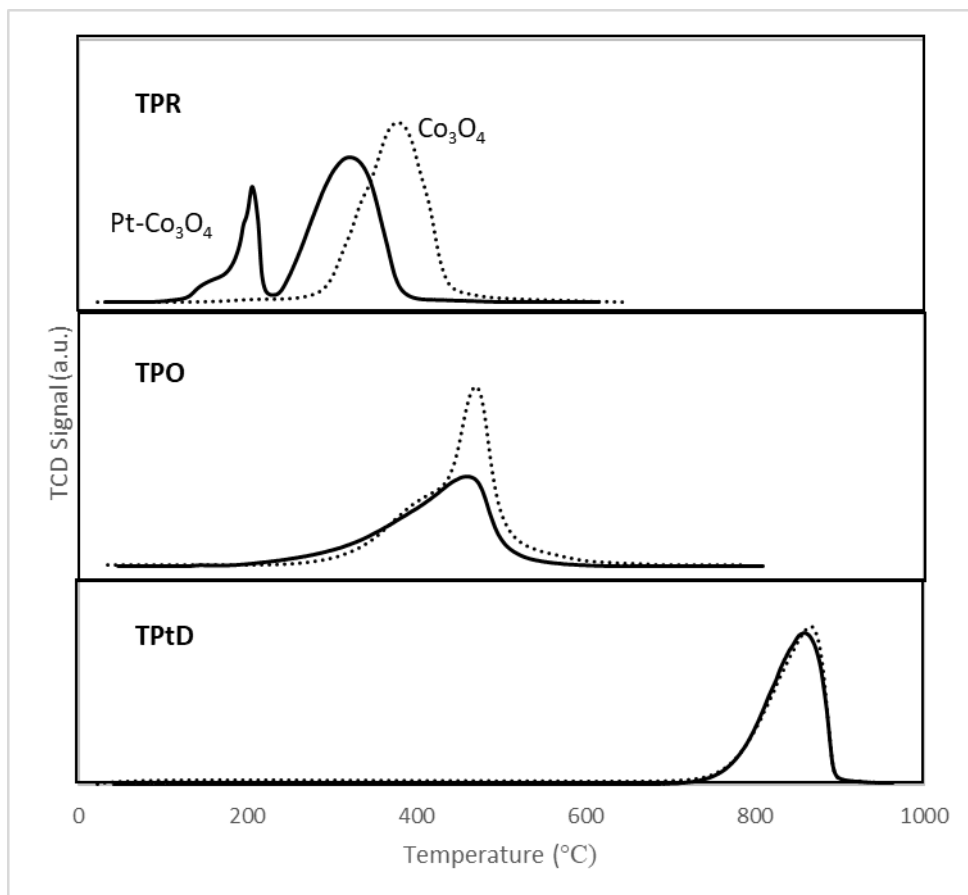


Figure 5.5. Red/ox performance of 0.5% wt. Pt-Co₃O₄ (solid lines) and Co₃O₄ (dotted lines)

After the reduction of 0.5% wt. Pt-Co₃O₄, residue consists of Co⁰ as shown in Figure 5.6. These metals were reoxidized under 2% O₂-He flow. The oxygen uptake profile of reduced sample (Figure 5.5) becomes broader when compared to reduced form of Co₃O₄. The oxidation starts around 120 °C which is 100 °C lower than Co₃O₄ (Figure 5.2). After the completion of oxidation, the crystallography changed to its initial state which is Co₃O₄ (Figure 5.6). Due to limited residue obtained after oxidation, some of the characteristic peaks of Co₃O₄ were stayed under the noise. The oxygen

desorption profile was not change significantly from unpromoted Co_3O_4 during the thermal decomposition.

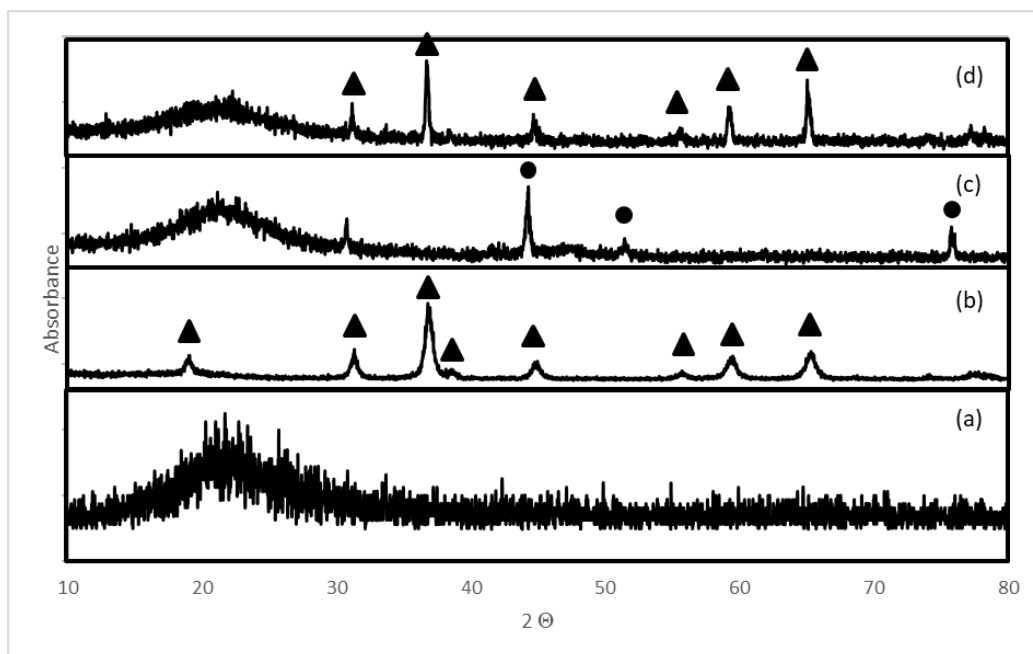


Figure 5.6. XRD patterns of 0.5% wt. Pt- Co_3O_4 (a)empty sample holder, (b) fresh sample; (c) after TPR; (d) after TPO following TPR (Triangles label peaks due to Co_3O_4 , circles represent peaks due to Co^0)

The Enhancement of Surface Area of Co_3O_4 : Having assessed the effect of bimetallic interaction, the effect of surface area on the oxygen adsorption and desorption was also investigated by dispersing Co_3O_4 on high surface area alumina. The cobalt was doped on alumina in the ratios of 1wt. % $\text{Co}_3\text{O}_4\text{-Al}_2\text{O}_3$ (CA1), 3wt. % $\text{Co}_3\text{O}_4\text{-Al}_2\text{O}_3$ (CA3) and 5wt. % $\text{Co}_3\text{O}_4\text{-Al}_2\text{O}_3$ (CA5). Same TPx experiments performed on the undoped and Pt doped Co_3O_4 were applied on Co doped alumina samples in the same order (TPR, TPO, TPtD).

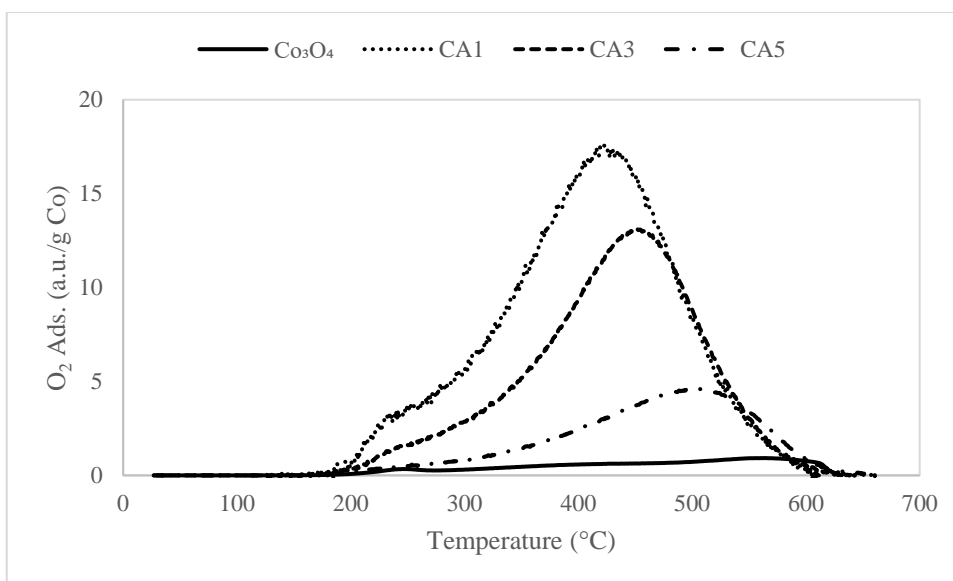


Figure 5.7. TPO after TPR Co_3O_4 , 1wt. % $\text{Co}_3\text{O}_4\text{-Al}_2\text{O}_3$, 3wt. % $\text{Co}_3\text{O}_4\text{-Al}_2\text{O}_3$, and 5wt. % $\text{Co}_3\text{O}_4\text{-Al}_2\text{O}_3$ (per gr Co basis)

The dispersion of cobalt on alumina increases the reduction rate in the order of four when compared with the bulk Co_3O_4 . As the cobalt content increases in the alumina, the rate of reduction approaches to bulk as shown in Figure 5.7. During reoxidation the magnitude of reoxidation was found in the order of $\text{CA1} > \text{CA3} > \text{CA5} > \text{Co}_3\text{O}_4$. The similar rates were also observed during thermal decomposition of decomposed samples.

5.1.2 Red/ox Materials based on Perovskites; CeCoO_3 and CeFeO_3

The oxygen exchange properties of cerium were can be increased by addition of new metal site. For this purpose, cobalt and iron were selected to form a perovskite type structure as CeCoO_3 and CeFeO_3 respectively. Synthesis procedure was given in Chapter 2. XRD spectrum shown in Figure 5.8 reveals that all diffraction patterns can be assigned to a single-phase orthorhombic perovskite structure with space group $Pbnm$. The lattice parameters were obtained as $a = 5.5214(9) \text{ \AA}$, $b = 5.5704(0) \text{ \AA}$, and $c = 7.8185(2) \text{ \AA}$.

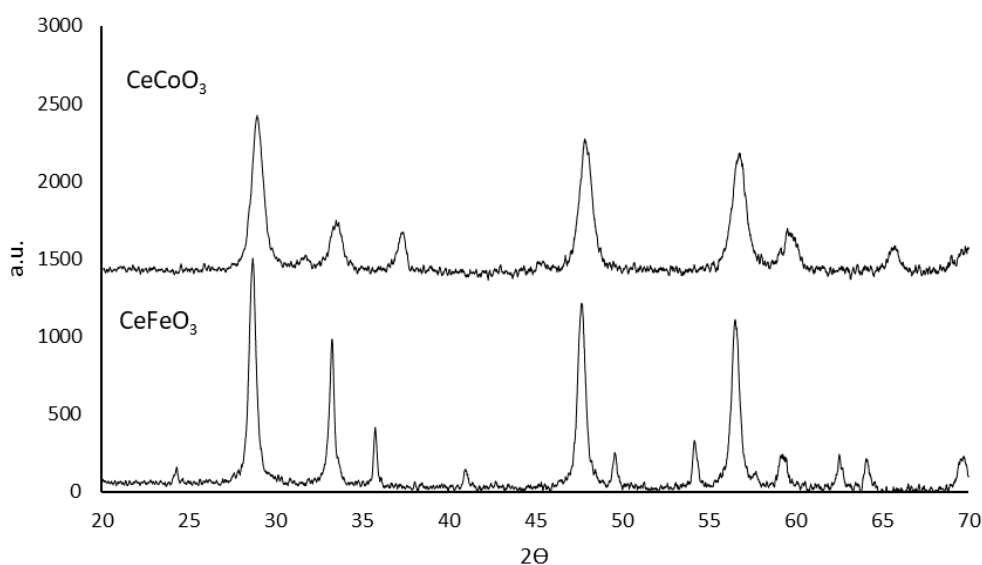


Figure 5.8. XRD patterns of CeCoO₃ and CeFeO₃

The specific surface area of the CeCoO₃ and CeFeO₃ nanoparticles was measured by BET as 24.56 and 17.66 m²/g respectively. The reduction behavior in H₂ was monitored by TPR. The TPR patterns of CeO₂, Co₃O₄, Fe₂O₃, CeCoO₃ and CeFeO₃ were presented in Figure 5.9. The reduction profile of CeO₂ has two broad regions. First region is attributed as the reduction of surface oxygen while the second reduction region with a peak around 880 °C is attributed to bulk Ce⁴⁺-Ce³⁺ transformation [311,312]. The first peak at 350 °C in TPR pattern of Fe₂O₃ shows the transformation of $3Fe_2O_3 + H_2 \rightarrow 2Fe_3O_4 + H_2O$ [313]. The increased H₂ consumption indicates further reduction of $Fe_3O_4 \rightarrow Fe_xO \rightarrow Fe$ [314,315]. Co₃O₄ shows two reduction steps at 326 °C and 376 °C for the reduction reactions $Co_3O_4 + H_2 \rightarrow 3CoO + H_2O$ and $3CoO + 3H_2 \rightarrow 3Co + 3H_2O$ respectively [316]. CeCoO₃ and CeFeO₃ shows higher reducibility due to lower reduction temperatures. By comparing the reduction patterns with the synthesized perovskite structures, it was found that CeFeO₃ can be represented by $Ce_2O_3 + Fe_2O_3$ and $CeO_2 + FeO$ while CeCoO₃ is mixture of $Ce_2O_3 + Co_2O_3$ and $CeO_2 + CoO$ due to spinel structure of Co₃O₄ (Co²⁺-Co³⁺). These oxide mixtures explains the whole TPR profile with the

small hydrogen consumption region appeared after 650 °C that ascribed to CeO₂ since it is well known that reduction of Ce₂O₃ is nearly impossible at the studied temperature range [317].

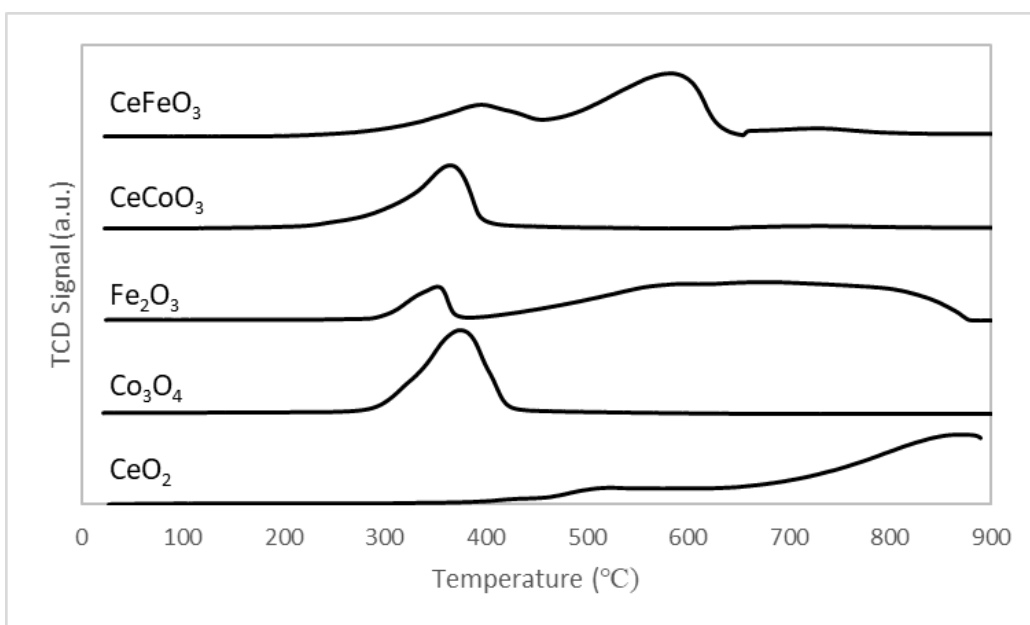


Figure 5.9. TPR profiles of CeO₂, Co₃O₄, Fe₂O₃, CeCoO₃ and CeFeO₃

The reoxidation patterns of the materials after reduction was shown in Figure 5.10. The reduced CeO₂ reoxidized its final oxidation state up to 200 °C [318]. The reoxidation of reduced Co₃O₄ appears in the temperature range of 250 to 500 °C which corresponds to total oxidation of Co to Co₃O₄ [318,319]. The distinct peak around 760 °C in the TPO pattern of Fe₂O₃ attributes to $Fe_3O_4 \rightarrow Fe_2O_3$ [320]. Both of the perovskites show a low temperature reoxidation around 70 °C due to oxygen consumption by the reduced CeO₂ as given in Figure 5.9. Further reoxidation in higher temperatures occurs by the contribution of reduced iron and cobalt in the structure.

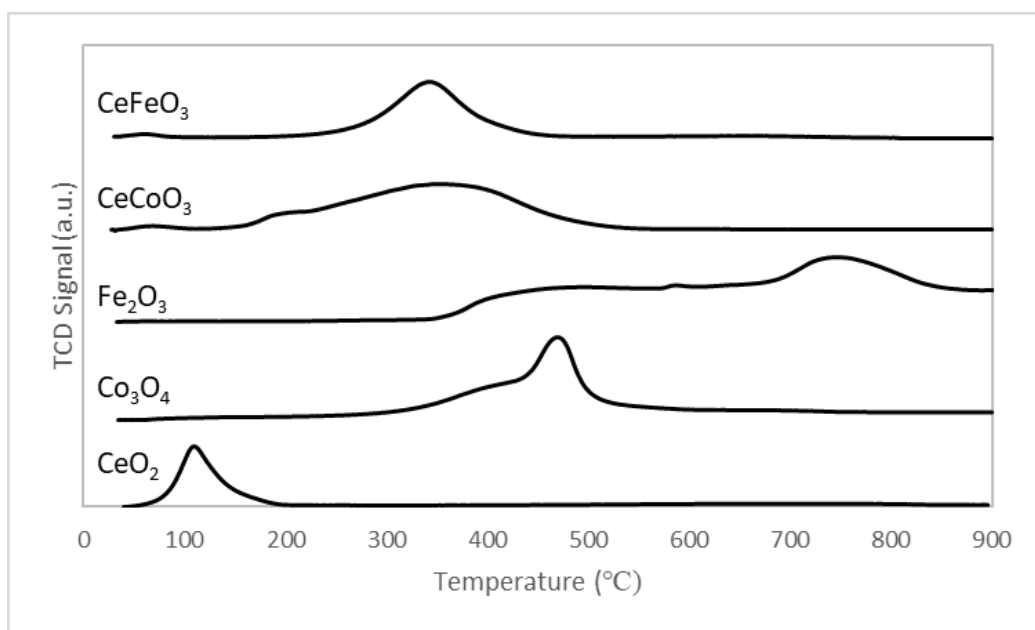


Figure 5.10. TPO performances of reduced CeO_2 , Co_3O_4 , Fe_2O_3 , CeCoO_3 and CeFeO_3

During the reoxidation after TPR, possible oxidation reactions were listed in Table 5.3. TPO mechanism of CeFeO_3 was suggested as given in reaction IDs 1 to 3. The low temperature reoxidation of CeCoO_3 follows the reaction route of reaction ID 4. As the temperature increases, oxygen competitively consumes by the routes that represents the oxidation states in reaction IDs 5 to 7.

Table 5.3 A set of plausible reactions under TPR/TPO cycling

Reaction ID	Reactions
1	$\text{Ce}_2\text{O}_3 \cdot \text{FeO} + 1/2 \text{O}_2 \rightarrow \text{CeO}_2 \cdot \text{FeO} \rightarrow \text{CeFeO}_3$
2	$(\text{Ce}_2\text{O}_3)_3 \cdot (\text{FeO})_6 + 1/2 \text{O}_2 \rightarrow (\text{Ce}_2\text{O}_3)_3 \cdot (\text{Fe}_3\text{O}_4)_2$
3	$(\text{Ce}_2\text{O}_3)_3 \cdot (\text{Fe}_3\text{O}_4)_2 + 1/2 \text{O}_2 \rightarrow (\text{Ce}_2\text{O}_3 \cdot \text{Fe}_2\text{O}_3)_3 \rightarrow 3\text{CeFeO}_3$
4	$\text{Ce}_2\text{O}_3 \cdot \text{Co} + 1/2 \text{O}_2 \rightarrow \text{CeO}_2 \cdot \text{Co}$
5	$\text{CeO}_2 \cdot \text{Co} + 1/2 \text{O}_2 \rightarrow \text{CeO}_2 \cdot \text{CoO} \rightarrow \text{CeCoO}_3$
6	$\text{Ce}_2\text{O}_3 \cdot (\text{Co})_2 + \text{O}_2 \rightarrow \text{Ce}_2\text{O}_3 \cdot (\text{CoO})_2$
7	$\text{Ce}_2\text{O}_3 \cdot (\text{CoO})_2 + 1/2 \text{O}_2 \rightarrow \text{Ce}_2\text{O}_3 \cdot \text{Co}_2\text{O}_3 \rightarrow 3\text{CeCoO}_3$

Oxygen Desorption Profiles of CeCoO₃ and CeFeO₃: Oxygen desorption of species CeO₂, Co₃O₄, Fe₂O₃, CeCoO₃ and CeFeO₃ during the thermal reduction was shown in Figure 5.11. The TPtD experiments for CeO₂, Fe₂O₃ and CeFeO₃ was performed by using Multi-Gas analyzer because its furnace can provide temperatures up to 1250 °C. No oxygen evolution was detected for CeO₂ while Co₃O₄ thermally decomposes after 700 °C. Similar desorption profile for CeCoO₃ was achieved at 685 °C. Iron containing materials needs higher temperatures to produce oxygen. Oxygen desorption patterns show that Fe₂O₃ and CeFeO₃ thermally reduce after 1100 °C. By comparing the oxygen desorption patterns of materials that have same atoms, it can be said that oxygen desorption step takes place the atoms of cobalt and iron. Therefore, it is possible to conclude that Ce site in CeFeO₃ and CeCoO₃ increases the rate of oxygen desorption at same temperature.

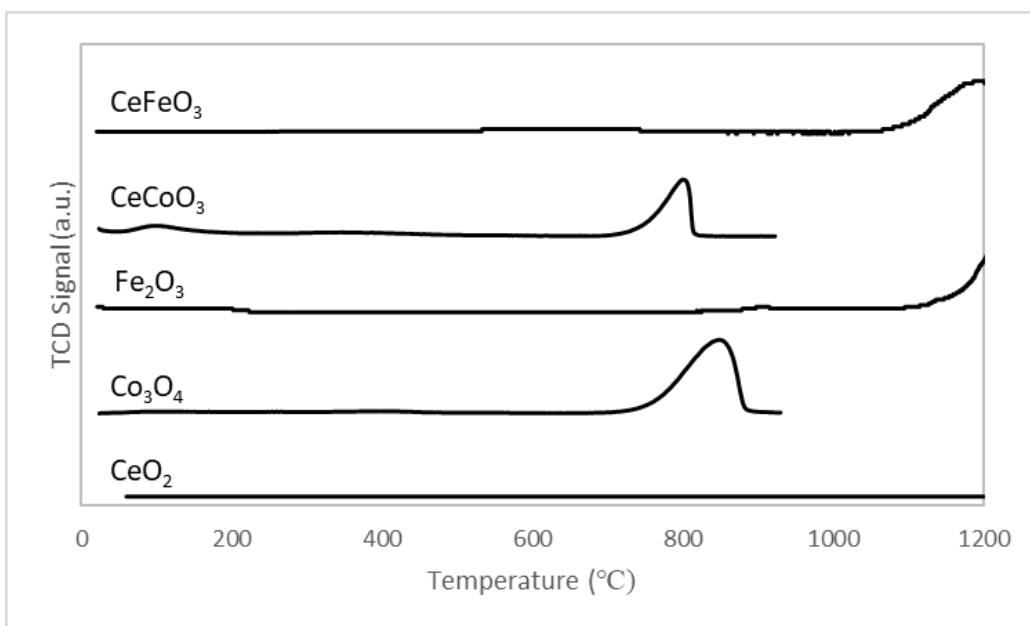


Figure 5.11. TPD performances of CeO₂, Co₃O₄, Fe₂O₃, CeCoO₃ and CeFeO₃

The Effect of Mass Transfer on Oxygen Desorption and Adsorption Kinetics: Film mass transfer and pore diffusion resistance are two governing control mechanisms expected to occur during solid-gas reactions. Evolved O₂ during thermal decomposition or O₂ molecule that gets closer for reoxidation of the reduced material has to penetrate through the gas-film barrier that surrounds metal oxide. The resistance applied by this barrier is defined as film mass transfer effect. Film mass transfer coefficient is proportional to Reynolds number. Therefore, increase in the gas flow rate lowers the thickness of this barrier which results in less film mass transfer resistance. Pore diffusion is the movement of O₂ molecule into pores of the material either for decomposition or reoxidation. The existence of this barrier can be tested by performing experiments on different particle sizes. Larger pores will decrease the resistance by increasing rate of oxygen adsorption or desorption.

The Effect of Film Mass Transfer on Oxygen Desorption and Adsorption Kinetics of Co₃O₄ and CeCoO₃: The oxygen desorption and adsorption patterns of Co₃O₄ was shown in Figure 5.12 and Figure 5.13. The experiments were performed by keeping mass-flow value constant. The change in operating parameters significantly changes the reducibility and oxidizability of Co₃O₄. This rate dependency confirms the film mass transfer resistance.

The oxygen desorption and adsorption patterns of CeCoO₃ was shown in Figure 5.14 and Figure 5.15. The effect of film mass transfer resistance on oxygen desorption and adsorption patterns was also confirmed for CeCoO₃. This rate dependency confirms the film mass transfer resistance.

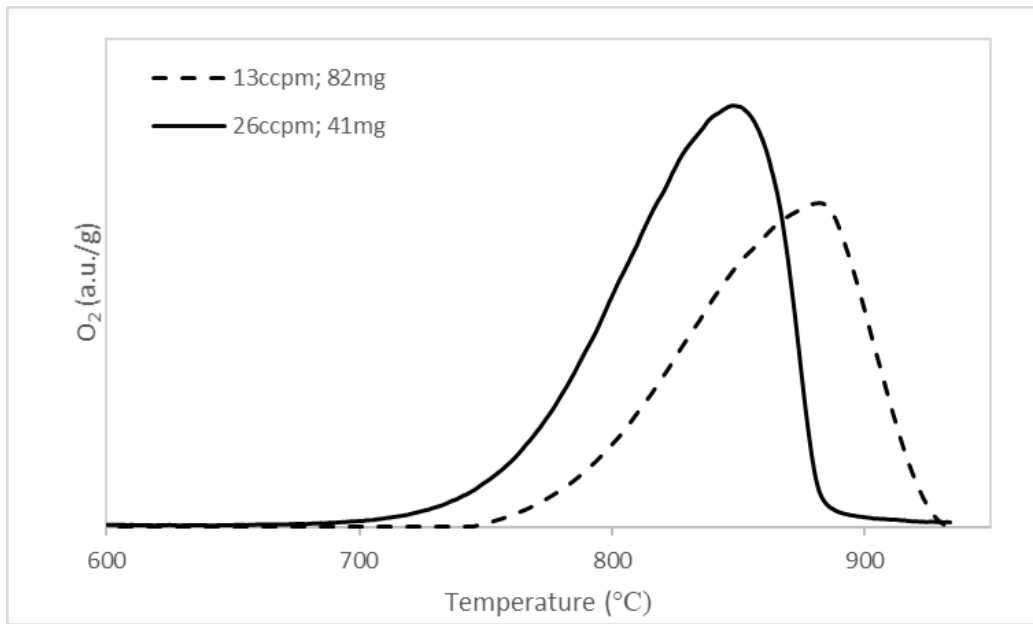


Figure 5.12. The effect of film mass transfer effect on oxygen desorption of Co_3O_4

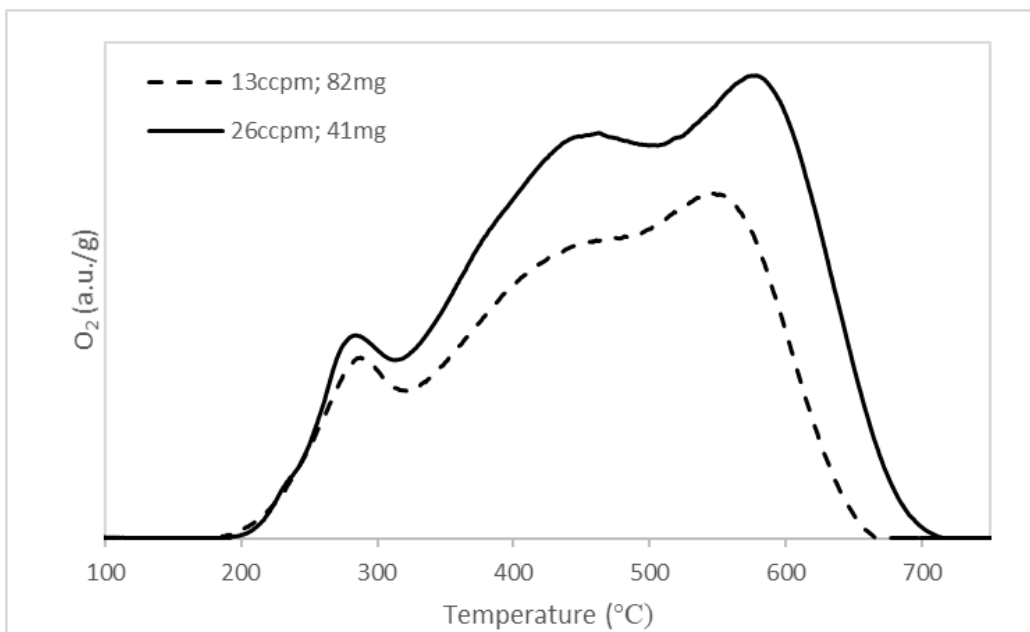


Figure 5.13. The effect of film mass transfer effect on oxygen adsorption of Co_3O_4

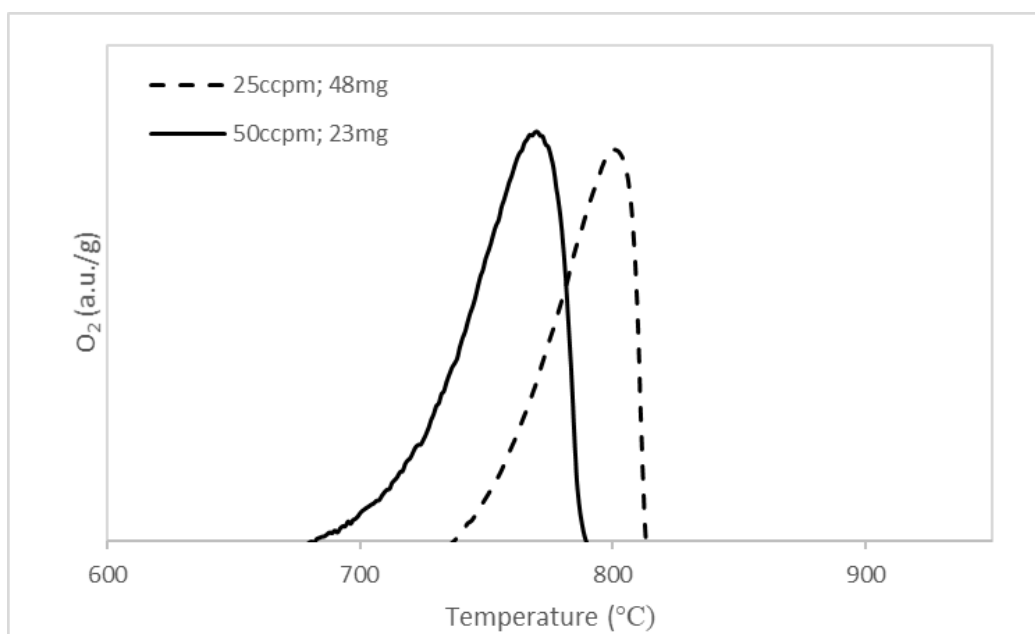


Figure 5.14. The effect of film mass transfer effect on oxygen desorption of CeCoO_3

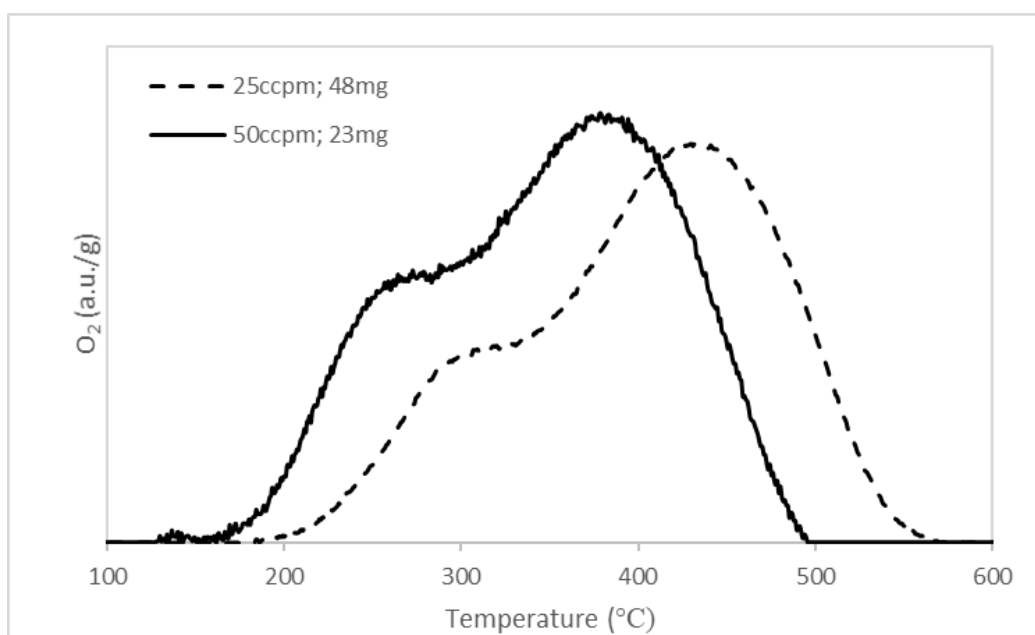


Figure 5.15. The effect of film mass transfer effect on oxygen adsorption of CeCoO_3

The Effect of Pore Diffusion on Oxygen Desorption Kinetics of Co_3O_4 : The effect of pore diffusion resistance on oxygen desorption kinetics was shown in Figure 5.16. Higher rates and conversions were observed for Co_3O_4 monolith samples due to more structured and wide pores, confirming pore diffusion resistance.

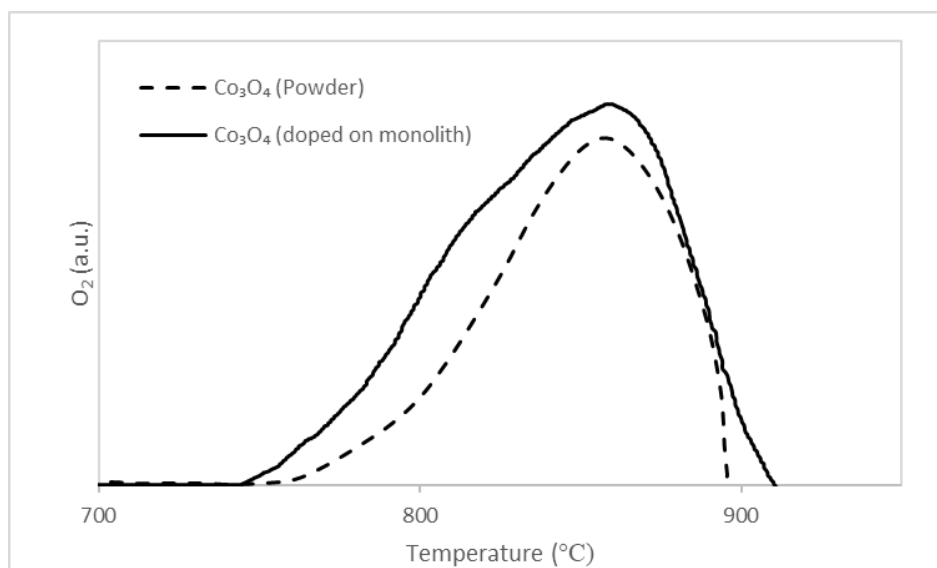


Figure 5.16. The effect of pore diffusion resistance on oxygen desorption of Co_3O_4

5.1.3 The Effect of Heat Transfer on Oxygen Desorption and Adsorption Kinetics

The Effect of Heat Transfer on Oxygen Desorption and Adsorption Performance of Co_3O_4 : The decomposition reaction of $2\text{Co}_3\text{O}_4 \rightarrow 6\text{CoO} + \text{O}_2$ is highly endothermic with 403.5 kJ/mol O_2 at 800 °C. The transfer of such energy can be affected by heat transfer related problems. The oxygen desorption and adsorption patterns of Co_3O_4 and $\text{Co}_3\text{O}_4:\text{SiC}$ (1:1 by weight) were shown in Figure 5.17 and Figure 5.18 respectively. By comparing desorption and adsorption profiles, transport capability of Co_3O_4 increased which indicates heat transfer problem.

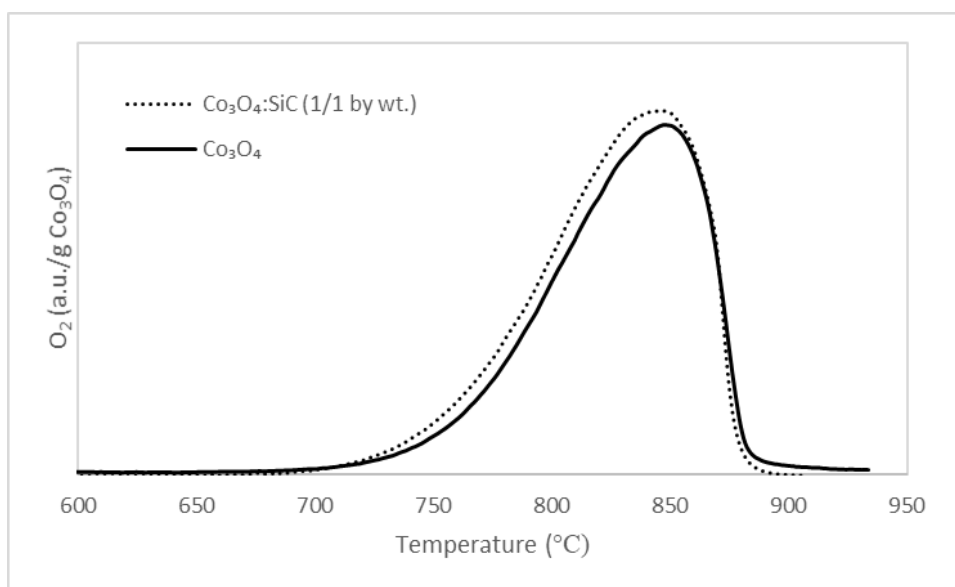


Figure 5.17. Oxygen desorption profiles for Co_3O_4 and $\text{Co}_3\text{O}_4:\text{SiC}$ (1:1 by weight)

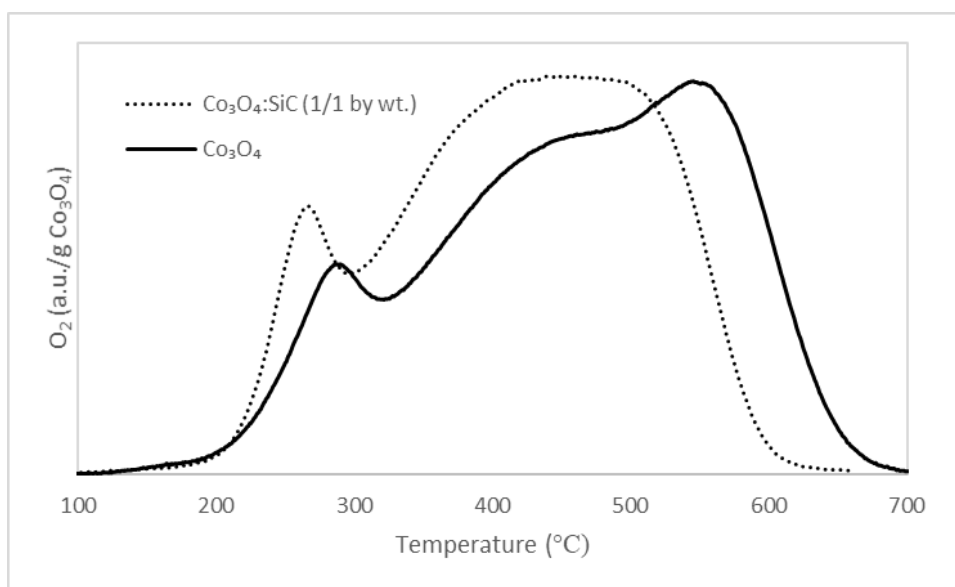


Figure 5.18. Oxygen adsorption profiles for Co_3O_4 and $\text{Co}_3\text{O}_4:\text{SiC}$ (1:1 by weight)

The Effect of Heat Transfer on Oxygen Desorption and Adsorption Performance of CeCoO₃: By knowing that oxygen evolution by thermal decomposition is endothermic for all the materials, the transfer of this energy can be affected by heat transfer related problems. By using a proper inert and thermal conductive material as SiC, the effect of heat transfer was investigated by assuming uniform heat transfer in the material bed. The oxygen desorption and adsorption patterns of CeCoO₃ and CeCoO₃:SiC (1:1 by weight) were shown in Figure 5.19 and Figure 5.20 respectively. The effect of heat transfer was significant during oxygen evolution which is an indication of heat transfer related problems. Negligible change was observed between the oxygen profiles of CeCoO₃ and CeCoO₃:SiC. The reaction is controlled by oxidation kinetics, not heat transfer.

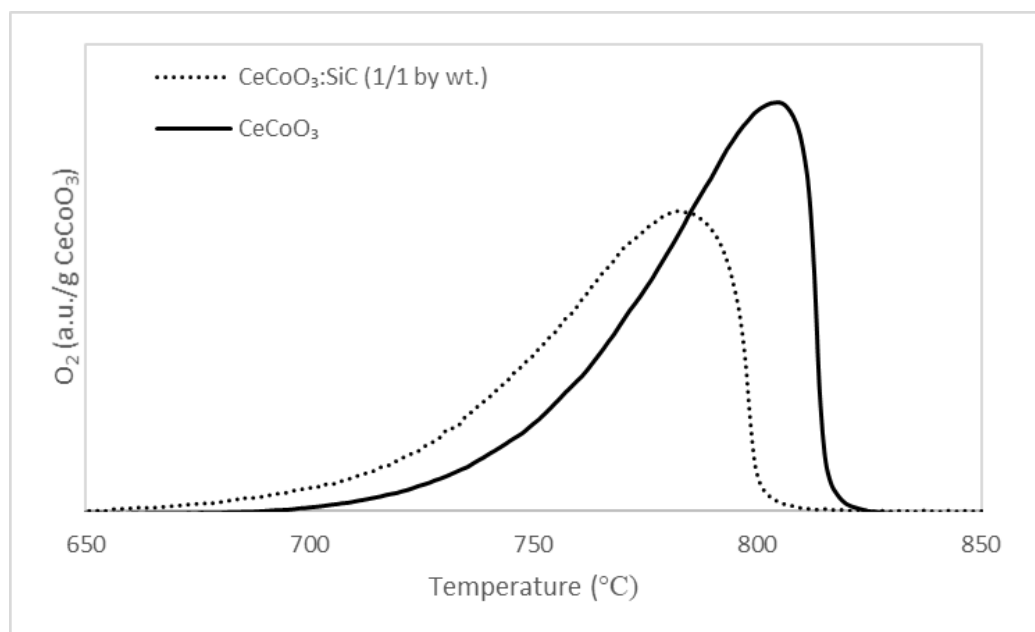


Figure 5.19. Oxygen desorption profiles for CeCoO₃ and CeCoO₃:SiC (1:1 by weight)

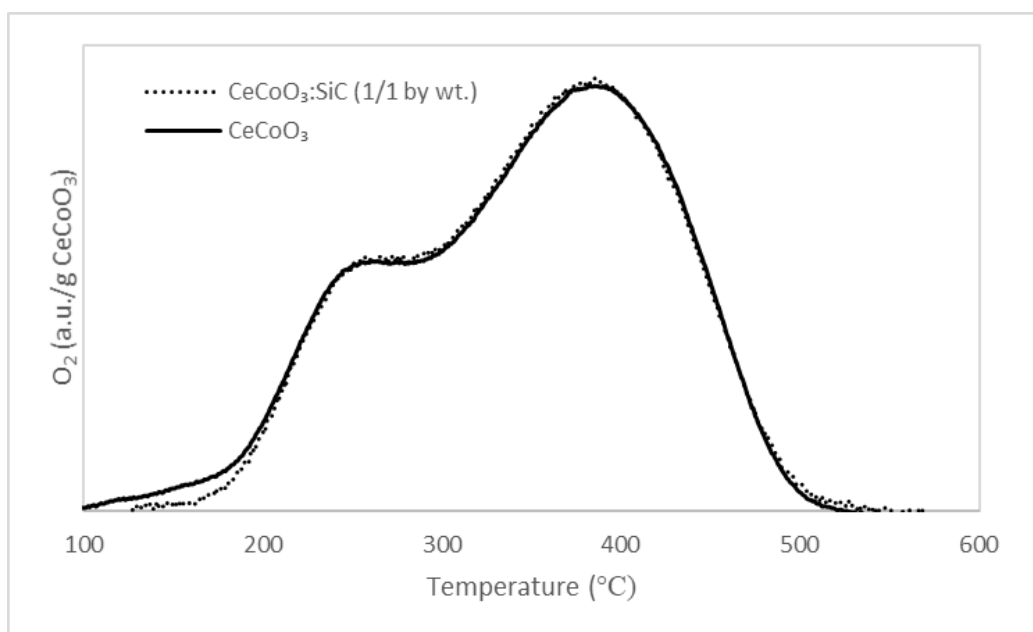


Figure 5.20. Oxygen adsorption profiles for CeCoO_3 and $\text{CeCoO}_3:\text{SiC}$ (1:1 by weight)

The Effect of Heat Transfer on Oxygen Desorption and Adsorption Performance of CeFeO_3 : By knowing that oxygen evolution by thermal decomposition is endothermic for all the materials, the transfer of this energy can be affected by heat transfer related problems. By using a proper inert and thermal conductive material as SiC, the effect of heat transfer was investigated by assuming uniform heat transfer in the material bed. The oxygen desorption pattern of CeFeO_3 and $\text{CeFeO}_3:\text{SiC}$ (1:1 by weight) was shown in Figure 5.21. The effect of heat transfer was significant during oxygen evolution which is an indication of heat transfer related problems.

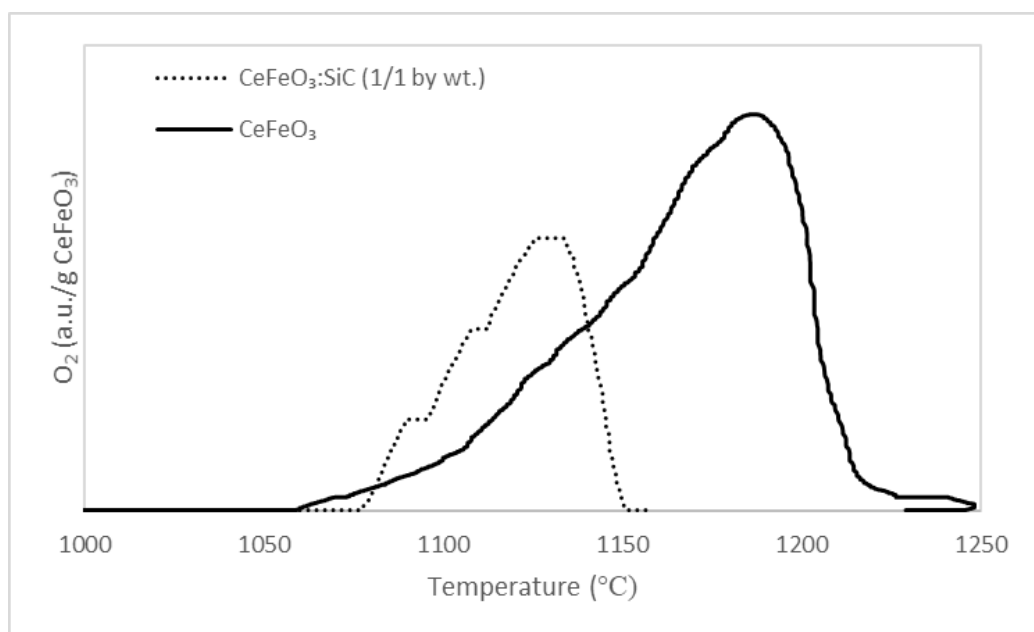


Figure 5.21. Oxygen desorption profiles for CeFeO_3 and $\text{CeFeO}_3:\text{SiC}$ (1:1 by weight)

5.1.4 Thermal Stability on Oxygen Desorption and Adsorption

Thermal Stability of Co_3O_4 : The oxygen desorption and adsorption performances over repeated cycles for Co_3O_4 was shown in Figure 5.22 and Figure 5.23 respectively. The data in the 4th cycle was incomplete due to power outage. The effect of power outage was minimum since the data obtained in the 5th cycle has the trend of second and the third cycles. The amount of desorbed and adsorbed oxygen and the temperature of maximum oxygen evolution and consumption occurs was given in Table 5.4. It was found that the amount of transportable oxygen during thermal decomposition and reoxidation was conserved over 10 cycles. The shift in temperatures of TPtD and TPO was calculated as 30 °C and 68 °C respectively. These shifts can be explained by aggregation and agglomeration problems. By comparing 9th and 10th cycles, it can be said that Co_3O_4 reaches its thermal stability and transports nearly same amount of oxygen at similar temperatures.

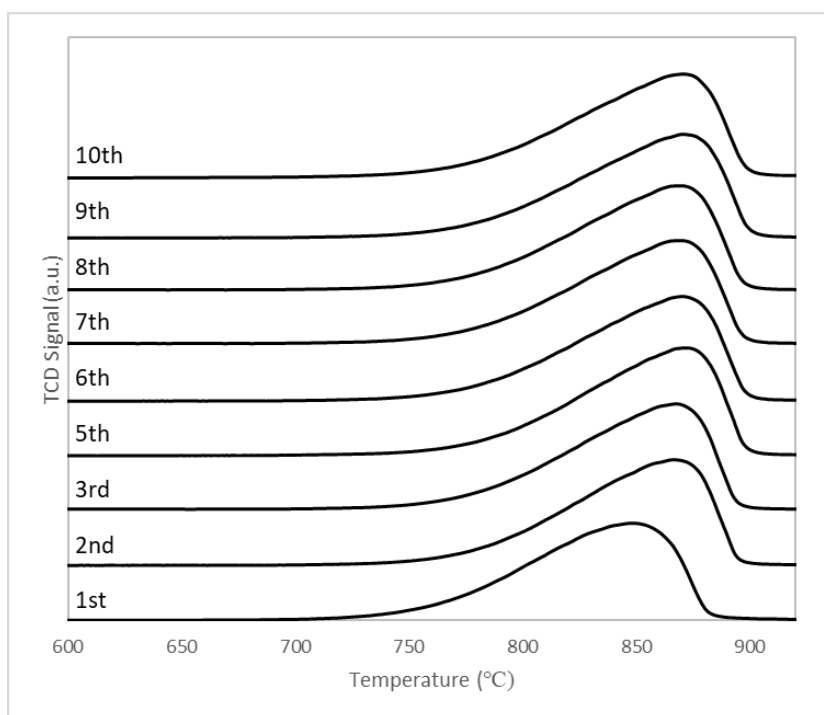


Figure 5.22. Oxygen desorption performance of Co_3O_4 over 10 cycles

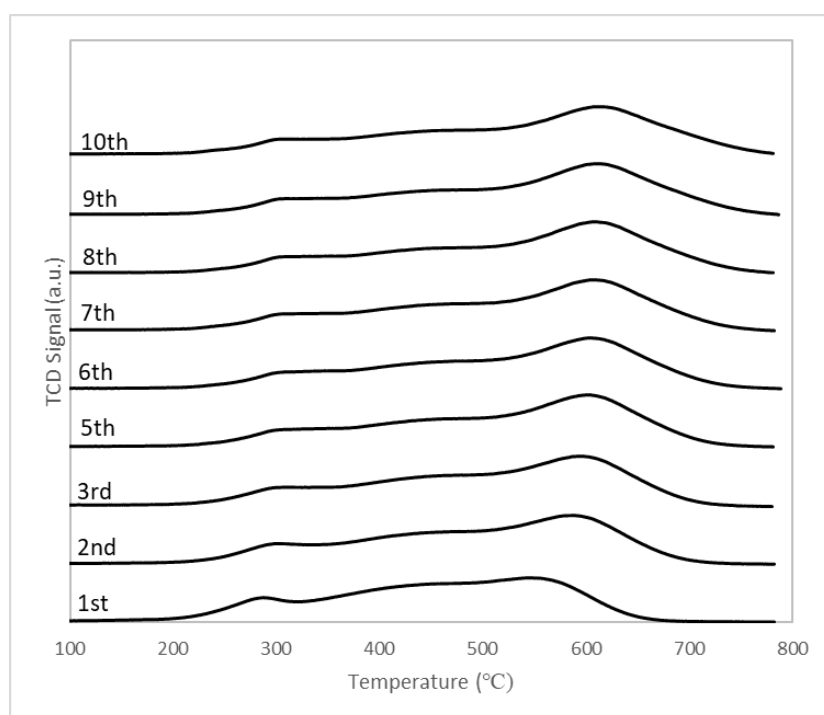


Figure 5.23. Oxygen absorption performance of Co_3O_4 over 10 cycles

Table 5.4 TPtD and TPO performances of Co_3O_4 over 10 cycles

Cycle #		1	2	3	4	5	6	7	8	9	10
TPtD	T_{max}	848	866	868	Power Outage	872	870	870	871	871	871
	O_2 (a.u.)	0.49	0.41	0.41		0.41	0.41	0.41	0.41	0.41	0.41
TPO	T_{max}	545	589	594		602	604	606	609	614	613
	O_2 (a.u.)	0.41	0.41	0.41		0.42	0.42	0.41	0.41	0.42	0.41

Consecutive Cycles in TGA: Having evaluated the thermal decomposition behavior of Co_3O_4 , red/ox performance was also conducted by TGA under CO_2 and Ar atmospheres. Cyclic tests were performed by using fresh Co_3O_4 . The red/ox pair is heated to 1000 °C with a heating rate of 10 °C/min under argon flow. Then, the material was cooled down to 130 °C with 10 °C/min under same flow. The second cycle was performed by following same heating and cooling periods under CO_2 atmospheres. Consecutive cycles were repeated several times. The red/ox cycle performance was given in Figure 5.24. Weight change of Co_3O_4 and temperature were shown by solid line and dashed line respectively. Reaction environment was labeled on the corresponding illustration.

In the first cycle, fresh Co_3O_4 was thermally decomposed around 800 °C with a 6.5% weight loss. During the cooling period, 0.6wt% was regained which is in the range of instrumental error. After thermal decomposition cycle, red/ox pair reoxidized by CO_2 . 2.8% increase in weight was observed up to 800 °C. At high temperatures, red/ox pair decomposes again. Decomposed material reoxidized during the cooling period under CO_2 atmosphere. Similar decomposition and oxidation behavior was observed throughout consecutive cycles. The time between thermal decomposition and reoxidation was reduced by reorganizing the experimental conditions as heating under Ar atmosphere and cooling under CO_2 atmosphere.

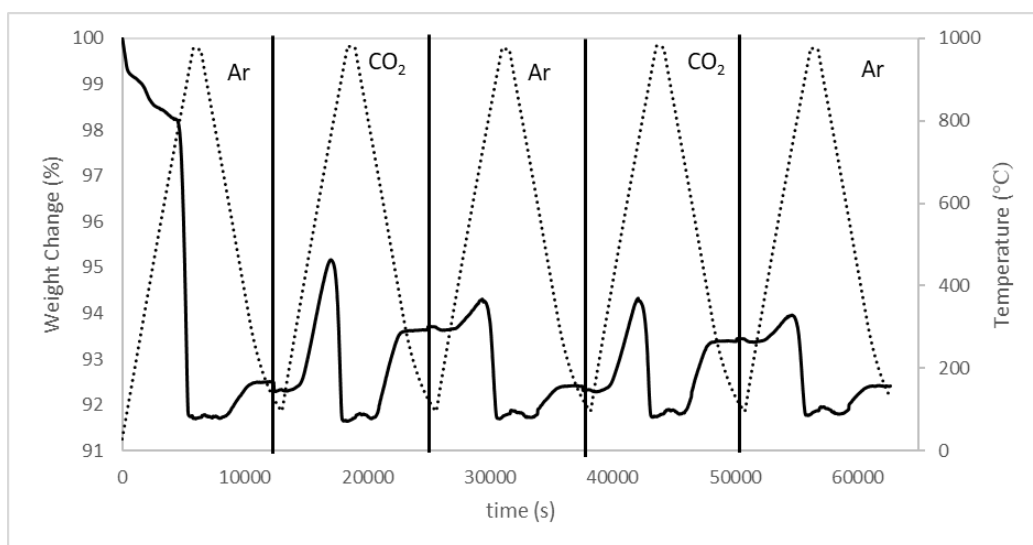


Figure 5.24. Cyclic oxygen exchange of Co_3O_4 based on weight change under consecutive Ar and CO_2 environments with a heating/cooling rate of $10\text{ }^\circ\text{C}/\text{min}$ (solid and dotted lines represent weight change and temperature respectively)

Red/ox performance of Co_3O_4 was also tested by heating under Ar atmosphere and cooling down under CO_2 atmosphere. Cyclic tests were performed by using fresh Co_3O_4 . The red/ox pair is heated to $900\text{ }^\circ\text{C}$ with a heating rate of $10\text{ }^\circ\text{C}/\text{min}$ under argon flow. Then, the material was cooled down to $650\text{ }^\circ\text{C}$ with $10\text{ }^\circ\text{C}/\text{min}$ under CO_2 flow. Consecutive cycles were repeated several times. The red/ox cycle performance was given in Figure 5.25. Weight change of Co_3O_4 and temperature were shown by solid line and dashed line respectively.

The red/ox ability of Co_3O_4 was tested by configuring cycles as heating under Ar atmosphere to thermal decomposition temperature ($900\text{ }^\circ\text{C}$) and cooling under CO_2 atmosphere to the temperature where oxidation rate reaches its maximum rate ($650\text{ }^\circ\text{C}$) as can be seen in Figure 5.25. The oxygen uptake of thermally decomposed Co_3O_4 was found very similar during the first three cycles. As the cycle number increases, the red/ox ability of Co_3O_4 reduced significantly. The temperature to regain same desorbed oxygen was shifted to lower temperatures as the cycle number increases. During the 17th cycle, oxygen equivalent to 0.3 wt.% of initial Co_3O_4 was exchanged between thermal decomposition and reoxidation by CO_2 .

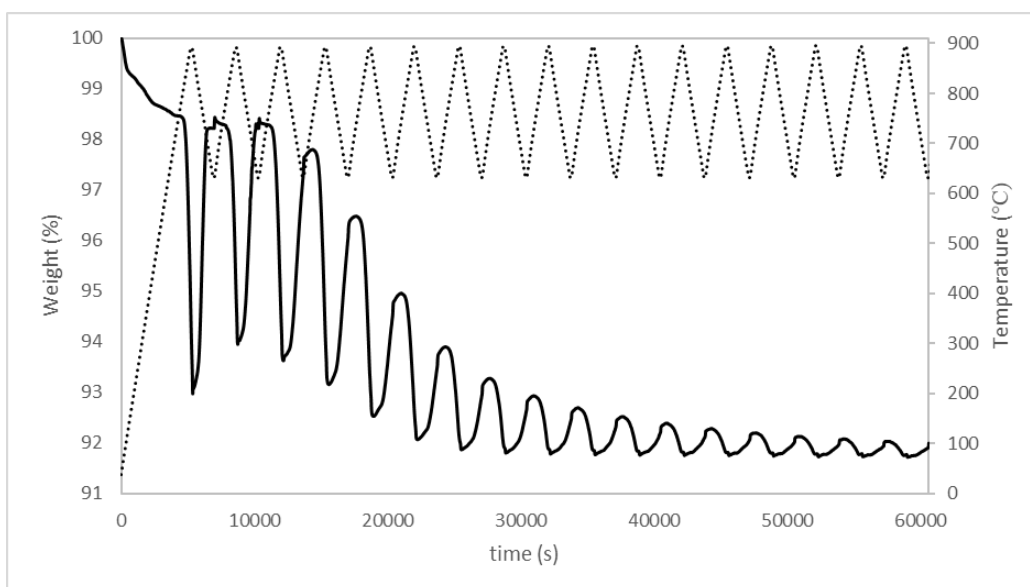


Figure 5.25. Cyclic oxygen transfer of Co_3O_4 based on weight change during heating under Ar flow to 900 °C and cooling under CO_2 flow to 650 °C (solid and dotted lines represent weight change and temperature respectively)

Thermal Stability of 0.5% Pt- Co_3O_4 : Red/ox performance of 0.5 wt.% Pt- Co_3O_4 was tested by heating under Ar atmosphere and cooling down under CO_2 atmosphere. Cyclic tests were performed by using fresh 0.5 wt.% Pt- Co_3O_4 . The red/ox pair is heated to 900 °C with a heating rate of 10 °C/min under argon flow. Then, the material was cooled down to 650 °C with 10 °C/min under CO_2 flow. Consecutive cycles were repeated several times. The red/ox cycle performance was given in Figure 5.26. Weight change of 0.5 wt.% Pt- Co_3O_4 and temperature were shown by solid line and dashed line respectively. Reaction environment was labeled on each excursion.

The effect of platinum on the oxygen transport mechanism of Co_3O_4 was also tested under same experimental conditions with Co_3O_4 as shown in Figure 5.26. Fresh 0.5 wt.% Pt- Co_3O_4 was thermally decomposed during the first heating period. Following the cooling under the CO_2 atmosphere, 0.8 wt.% initial weight was regained. Similar weight changes were observed for the next two cycles. The effect of temperature on reoxidation was also tested with fresh 0.5 wt.% Pt- Co_3O_4 . The reoxidation under

CO₂ atmosphere was continued down to 200 °C. Nevertheless, the red/ox performance of Pt-Co₃O₄ did not change. Therefore, the addition of platinum on Co₃O₄ reduces the reoxidation performance under CO₂ atmosphere.

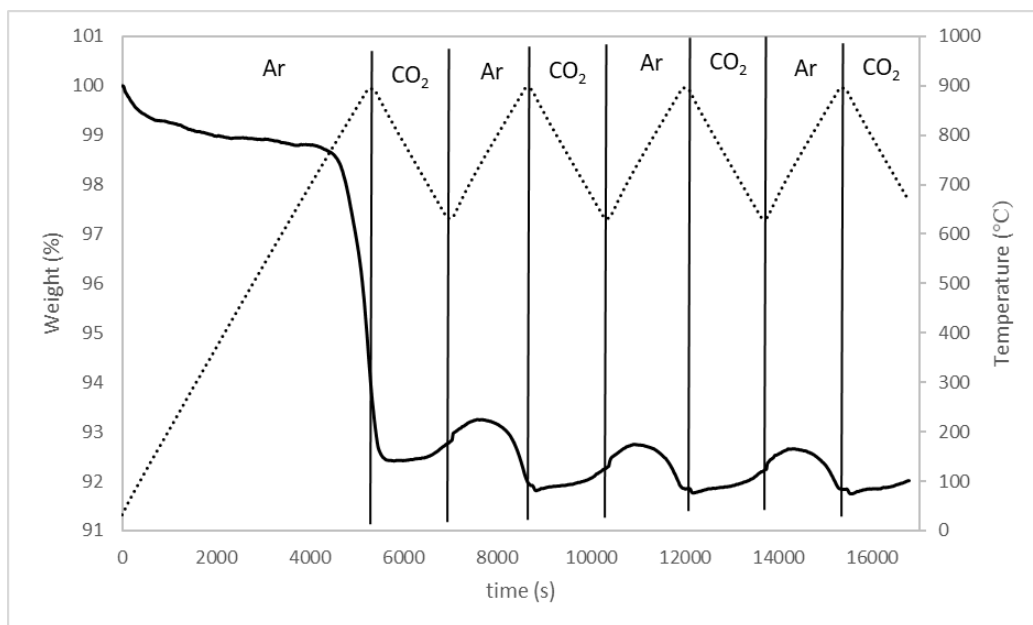


Figure 5.26. Cyclic oxygen exchange of 0.5 wt.%Pt- Co₃O₄ based on weight change during heating under Ar flow to 900 °C and cooling under CO₂ flow to 650 °C. (solid and dotted lines represent weight change and temperature respectively)

Thermal Stability of CeO₂: Red/ox performance of CeO₂ was conducted by TGA under CO₂ and Ar atmospheres. Cyclic tests were performed by using fresh CeO₂. The oxide was heated to 1050 °C with a heating rate of 10 °C/min under argon flow. Then, the material was cooled down to 130 °C with 10 °C/min under same flow. The second cycle was performed by following same heating and cooling periods under CO₂ atmospheres as given in Figure 5.27. Weight change of CeO₂ and temperature were shown by solid line and dashed line respectively. Reaction environment was labeled on the corresponding illustration.

Fresh CeO₂ was not decomposed thermally up to 1050 °C as can be seen in Figure 5.27. The weight gain under the inert atmosphere is attributed to instrumental error. After reaching 1050 °C, the material was cooled under CO₂ flow. Overall weight did

not change significantly during the experiment indicating that CeO_2 cannot be reactivated thermally by oxygen exchange up to 1050 °C.

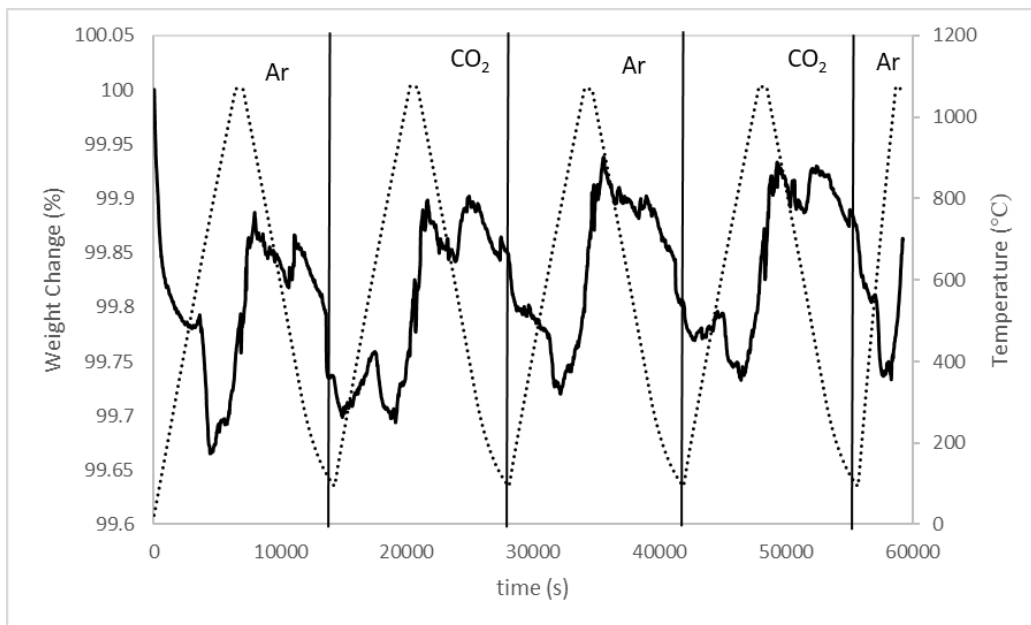


Figure 5.27. Cyclic oxygen exchange of CeO_2 based on weight change under consecutive Ar and CO_2 environments with a heating/cooling rate of 10 °C/min (solid and dotted lines represent weight change and temperature respectively)

Thermal Stability of CeCoO_3 :

The oxygen desorption and adsorption performances over repeated cycles for CeCoO_3 was shown in Figure 5.28 and Figure 5.29 respectively. The amount of desorbed and adsorbed oxygen and the temperature of maximum oxygen evolution and consumption by the material was given in Table 5.4. It was found that the amount of transportable oxygen during thermal decomposition and reoxidation was conserved over 10 cycles. The shift in temperatures of TPtD and TPO was calculated as 13 °C and 96 °C respectively. This shift can be explained by aggregation and agglomeration problems. By comparing 8th to 10th cycles, it can be said that CeCoO_3 reaches its thermal stability and transports nearly same amount of oxygen at similar temperatures.

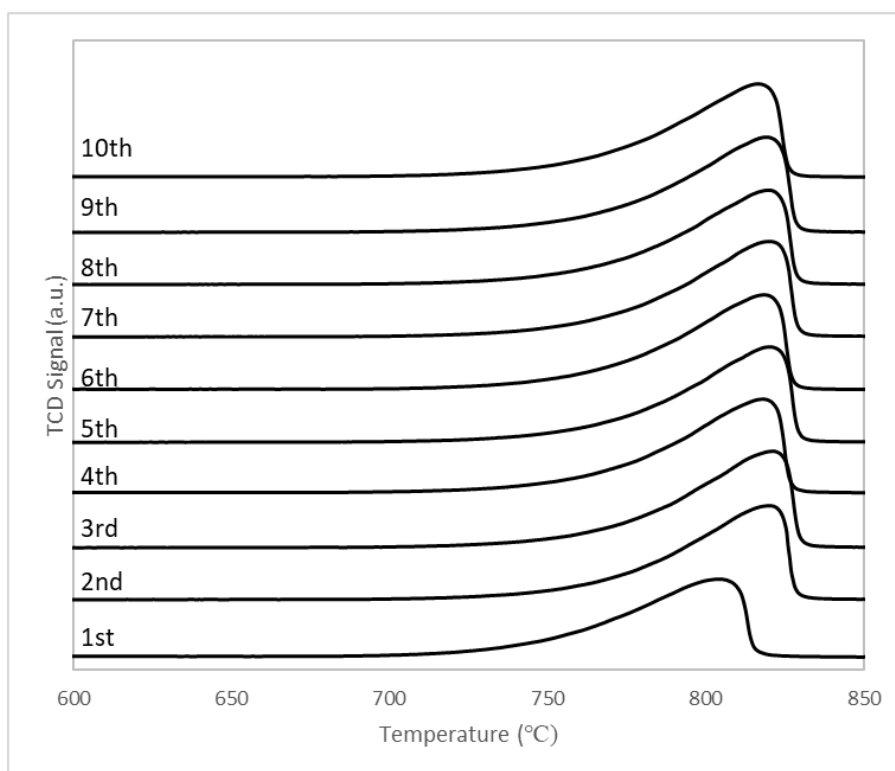


Figure 5.28. Oxygen desorption performance of CeCoO₃ over 10 cycles

Table 5.5 TPtD and TPO performances of CeCoO₃ over 10 cycles

Cycle #		1	2	3	4	5	6	7	8	9	10
TPtD	T _{max}	804	820	821	818	820	818	820	820	819	817
	O ₂ (a.u.)	0.19	0.21	0.22	0.21	0.22	0.21	0.22	0.22	0.22	0.21
TPO	T _{max}	386	425	451	461	469	469	474	479	481	482
	O ₂ (a.u.)	0.21	0.20	0.21	0.21	0.21	0.21	0.21	0.22	0.21	0.21

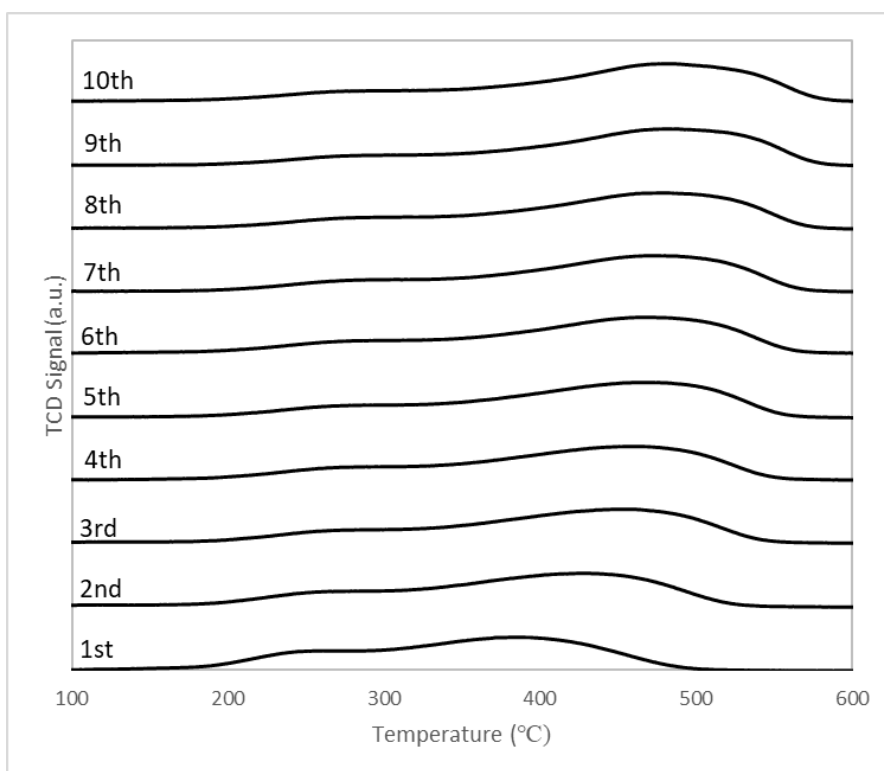


Figure 5.29. Oxygen adsorption performance of CeCoO_3 over 10 cycles

Red/ox performance of CeCoO_3 was tested by heating under N_2 atmosphere and cooling down under CO_2 atmosphere. Cyclic tests were performed by using fresh CeCoO_3 . The red/ox pair was heated to $1000\text{ }^\circ\text{C}$ with a heating rate of $10\text{ }^\circ\text{C}/\text{min}$ under argon flow. Then, the material was cooled to $400\text{ }^\circ\text{C}$ with $10\text{ }^\circ\text{C}/\text{min}$ under CO_2 flow. The red/ox cycle performance was given in Figure 5.30. Weight change of CeCoO_3 and temperature were shown by solid and dashed lines respectively.

Oxygen equivalent to 2 wt.% of initial weight was evolved during the first thermal decomposition period after $850\text{ }^\circ\text{C}$. Same amount of oxygen was regained during the consecutive reoxidation step after $750\text{ }^\circ\text{C}$. The amount of oxygen exchanged between thermal decomposition and reoxidation was decreased to 1.4 wt.% of initial weight as the cycle number increases. The temperature to regain same desorbed oxygen was shifted to lower temperatures as the cycle number increases. However, the oxygen evolution temperature of CeCoO_3 did not change significantly during

five cycles. The effect of oxidizing gas to the performance of CeCoO_3 was also studied by changing oxidizing gas from CO_2 to dry air.

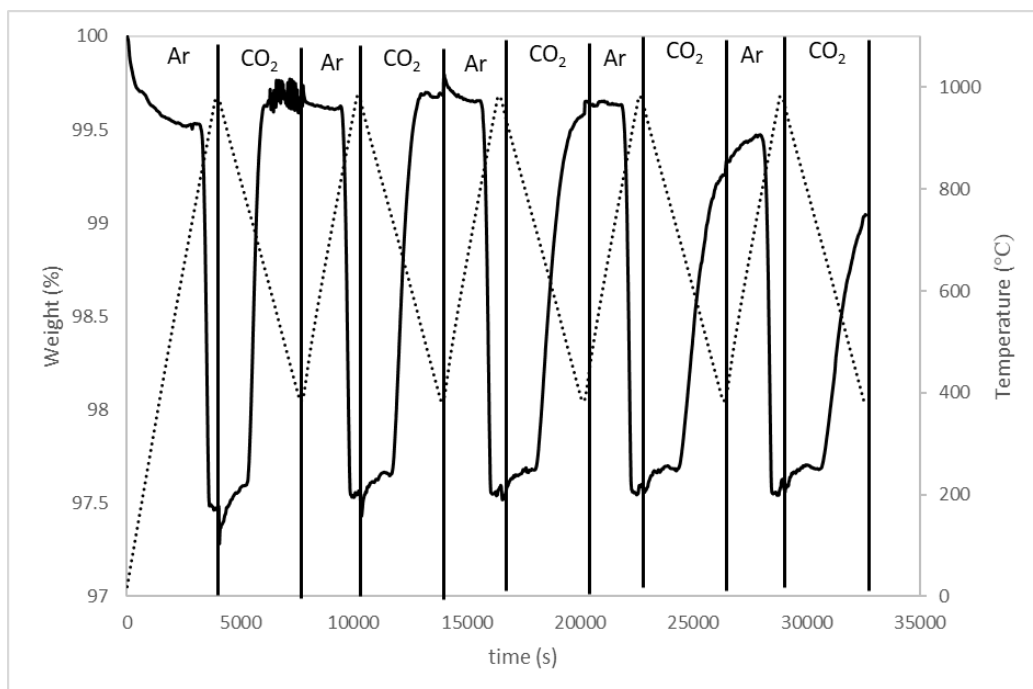


Figure 5.30. Cyclic oxygen exchange of CeCoO_3 based on weight change during heating under N_2 flow to $1000\text{ }^\circ\text{C}$ and cooling under CO_2 flow to $400\text{ }^\circ\text{C}$ (solid and dotted lines represent weight change and temperature respectively)

Additional TGA experiment was conducted by increasing the lower temperature limit of oxidation step $400\text{ }^\circ\text{C}$ to $600\text{ }^\circ\text{C}$ and by changing oxidizing flow from CO_2 to dry air. The remaining operational parameters were kept the same. The red/ox cycle performance of CeCoO_3 between 600 and $1000\text{ }^\circ\text{C}$ under air flow was given in Figure 5.31. Weight change of CeCoO_3 and temperature were shown by solid line and dashed line respectively. Oxygen equivalent to $2\text{ wt.}\%$ of the initial weight evolved during the first thermal decomposition period after $850\text{ }^\circ\text{C}$. Same amount of oxygen was regained sharply during the following reoxidation step after $800\text{ }^\circ\text{C}$. The amount of oxygen exchanged between thermal decomposition and reoxidation was not changed during twelve cycles. The oxygen release and uptake profiles were

almost identical. The oxygen exchange performance of CeCoO_3 was improved by changing oxidizing flow from CO_2 to dry air.

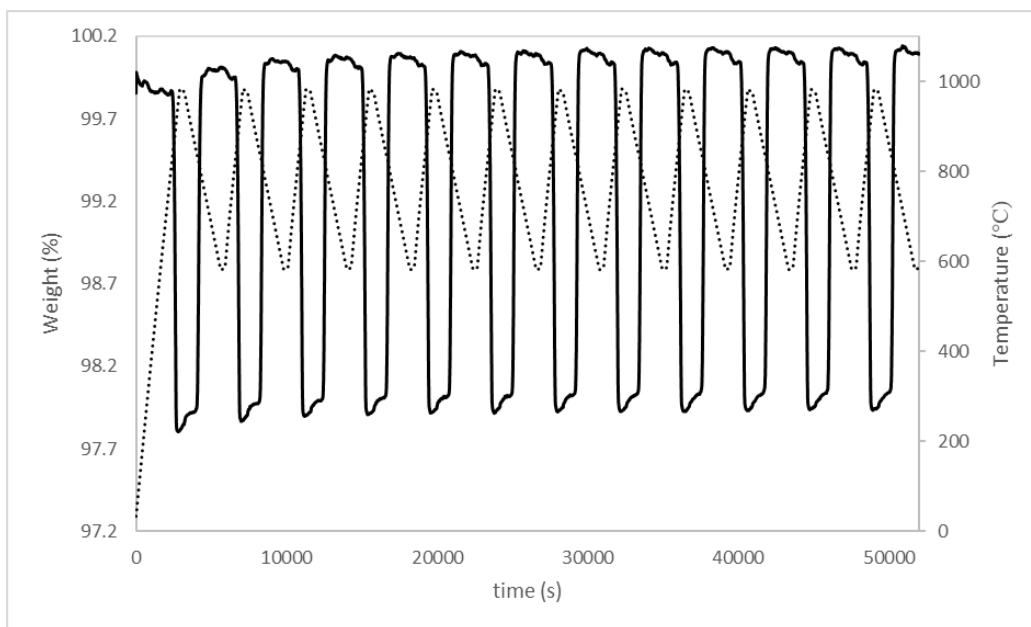


Figure 5.31. Cyclic oxygen exchange of CeCoO_3 based on weight change during heating under N_2 flow to $1000\text{ }^\circ\text{C}$ and cooling under dry air flow to $600\text{ }^\circ\text{C}$ (solid and dotted lines represent weight change and temperature respectively)

Thermal Stability of CeFeO_3 : The oxygen desorption and adsorption performances over repeated cycles for CeFeO_3 was shown in Figure 5.32 and Figure 5.33 respectively. The amount of desorbed and adsorbed oxygen and the temperature of maximum oxygen evolution and consumption by the material was given in Table 5.6. These experiments were conducted by using Multi-Gas analyzer since its oven can reach up to $1250\text{ }^\circ\text{C}$. There are some fluctuations over repeated cycles since the transportable oxygen of CeFeO_3 increases the response time of the sensor. This effect results with plateaus as can be seen in the corresponding figures. It was found that the amount of transportable oxygen during thermal decomposition and reoxidation was conserved over 5 cycles with a temperature fluctuation in the range of 5 to $10\text{ }^\circ\text{C}$.

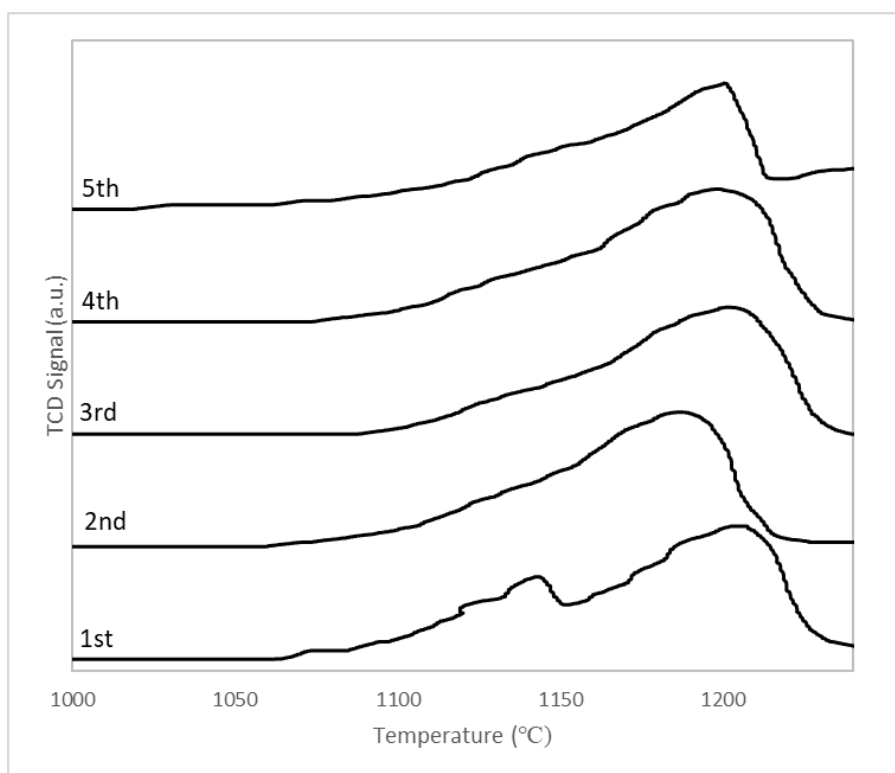


Figure 5.32. Oxygen desorption performance of CeFeO_3 over 5 cycles

Table 5.6 TPtD and TPO performances of CeFeO_3 over 5 cycles

Cycle #		1.	2.	3.	4.	5.
TPtD	T_{\max}	1205	1196	1202	1200	1201
	O_2 (cm^3)	0.94	0.82	0.77	0.85	0.84
TPO	T_{\max}	424	433	429	428	429
	O_2 (a.u.)	0.73	0.66	0.66	0.56	0.55

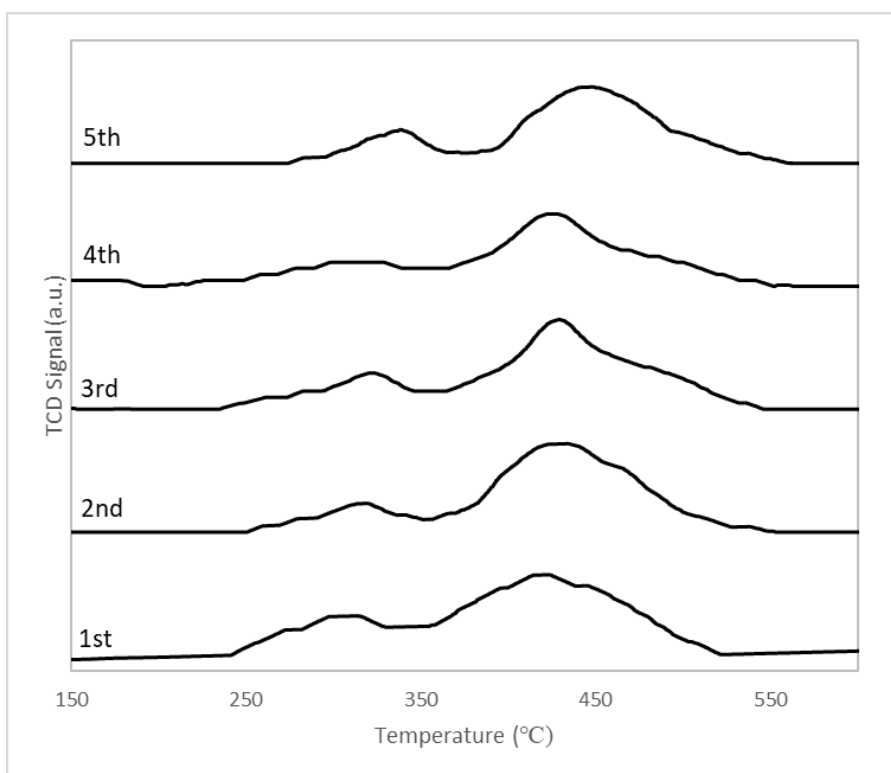


Figure 5.33. Oxygen adsorption performance of CeFeO_3 over 5 cycles

Red/ox performance of CeFeO_3 was tested by heating under Ar atmosphere and cooling down under CO_2 atmosphere. Cyclic tests were performed by using fresh CeFeO_3 . The red/ox pair is heated to $1100\text{ }^\circ\text{C}$ with a heating rate of $10\text{ }^\circ\text{C}/\text{min}$ under Ar flow. Then, the material was cooled down to $500\text{ }^\circ\text{C}$ with $10\text{ }^\circ\text{C}/\text{min}$ under CO_2 flow. The red/ox cycle performance was given in Figure 5.34. Weight change of CeFeO_3 and temperature were shown by solid line and dashed line respectively. Reaction sequence was labeled on the corresponding illustration.

Fresh CeFeO_3 could not decompose thermally up to $1100\text{ }^\circ\text{C}$ as can be seen in Figure 5.34. The increase in the weight under the inert atmosphere was due to instrumental error. After reaching $1100\text{ }^\circ\text{C}$, the material was cooled under CO_2 flow. Overall weight did not change significantly during the experiment indicating that CeFeO_3 cannot be activated thermally in terms of oxygen exchange up to $1100\text{ }^\circ\text{C}$.

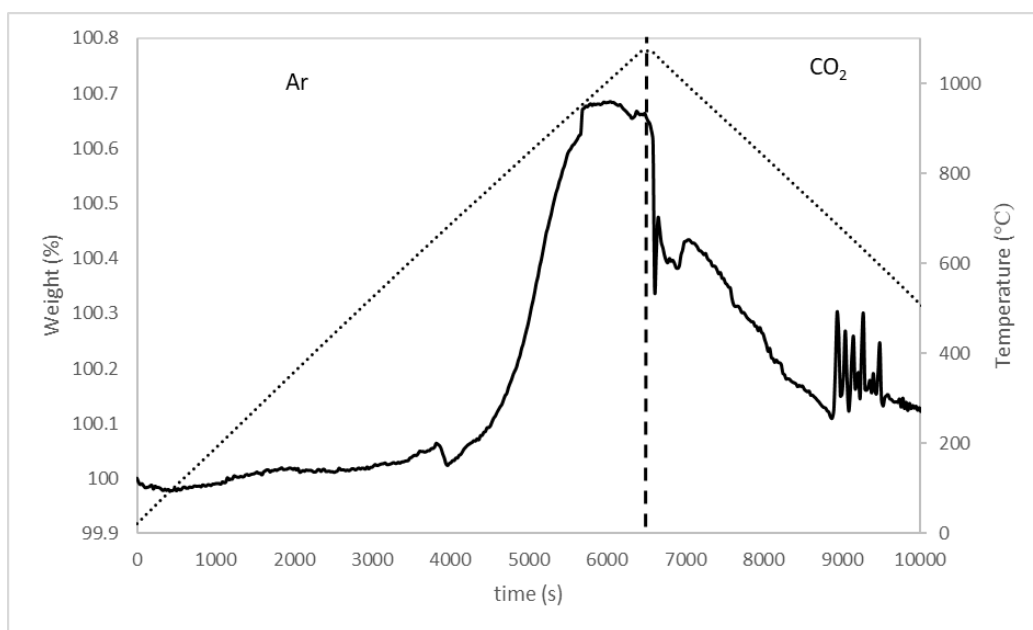


Figure 5.34. Cyclic oxygen exchange of CeFeO_3 based on weight change during heating under Ar flow to 1100 °C and cooling under CO_2 flow to 500 °C (solid and dotted lines represent weight change and temperature respectively).

Thermal Stability of $\text{Sr}_{0.6}\text{Ce}_{0.4}\text{Fe}_{0.7}\text{Co}_{0.3}\text{O}_3$ (SCFC-6473): Red/ox performance of SCFC-6473 was tested by heating under Ar atmosphere and cooling down under CO_2 atmosphere. Cyclic tests were performed by using fresh SCFC-6473. The red/ox pair was heated to 1100 °C with a heating rate of 10 °C/min under argon flow. Then, the material was cooled to 800 °C with 10 °C/min under CO_2 flow. Consecutive cycles were repeated several times. The red/ox cycle performance was given in Figure 5.35. Weight change of SCFC-6473 and temperature were shown by solid line and dashed line respectively.

Oxygen equivalent to 1.2 wt.% of the initial weight was evolved during the first thermal decomposition period in the temperature range of 350 to 1100 °C. 0.5 wt.% of the initial weight was regained during the following reoxidation step. The amount of oxygen exchanged between thermal decomposition and reoxidation was decreased to 47% as the cycle number increases. The adverse effect of temperature on the red/ox performance of SCFC-6473 was also investigated.

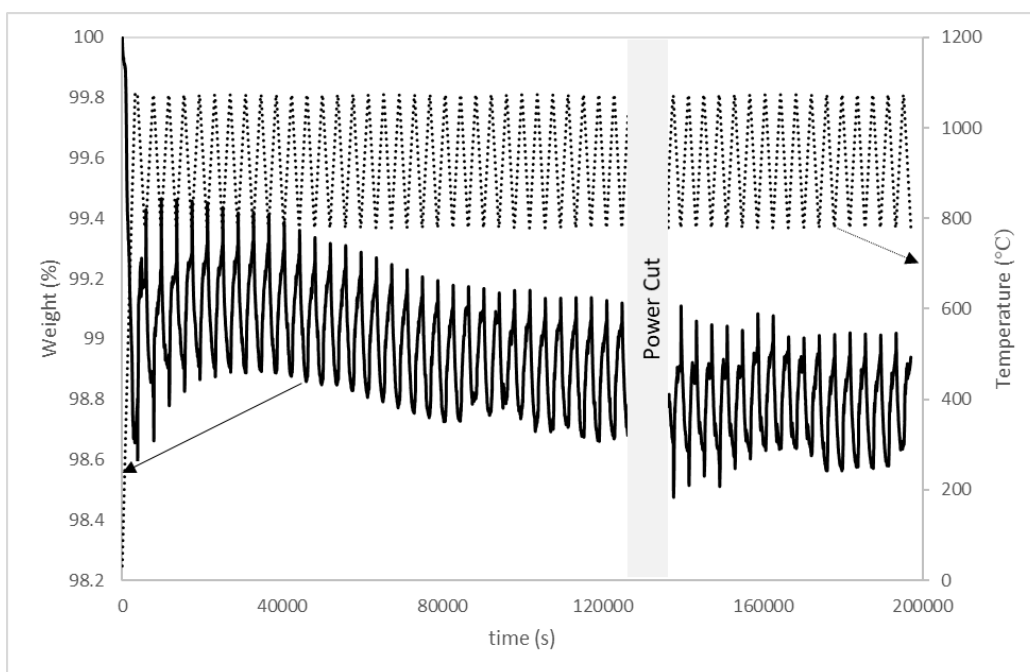


Figure 5.35. Cyclic oxygen exchange of SCFC-6473 based on weight change during heating under Ar flow to 1100 °C and cooling under CO₂ flow to 800 °C (solid and dotted lines represent weight change and temperature respectively)

Additional TGA experiment was conducted by decreasing thermal decomposition temperature from 1100 °C to 950 °C. The remaining operational parameters were kept same. The red/ox cycle performance of SCFC-6473 between 800 and 950 °C was given in Figure 5.36. Weight change of SCFC-6473 and temperature were shown by solid line and dashed line respectively.

Oxygen equivalent to 1.1 wt.% of the initial weight was evolved during the first thermal decomposition period in the temperature range of 350 to 950 °C. 0.4 wt.% of the initial weight was regained during the following reoxidation step. The amount of oxygen exchanged between thermal decomposition and reoxidation did not change during the 50 cycles. The final weight of each cycle decreased from 98.8% to 98.4%. By comparing the results shown in Figure 5.35 and Figure 5.36, the thermal decomposition temperatures has a negative effect on the oxygen exchange performance of SCFC-6473. The selection of the lower temperature limit of

reoxidation was tested by decreasing the temperature to 400 °C during the reoxidation steps.

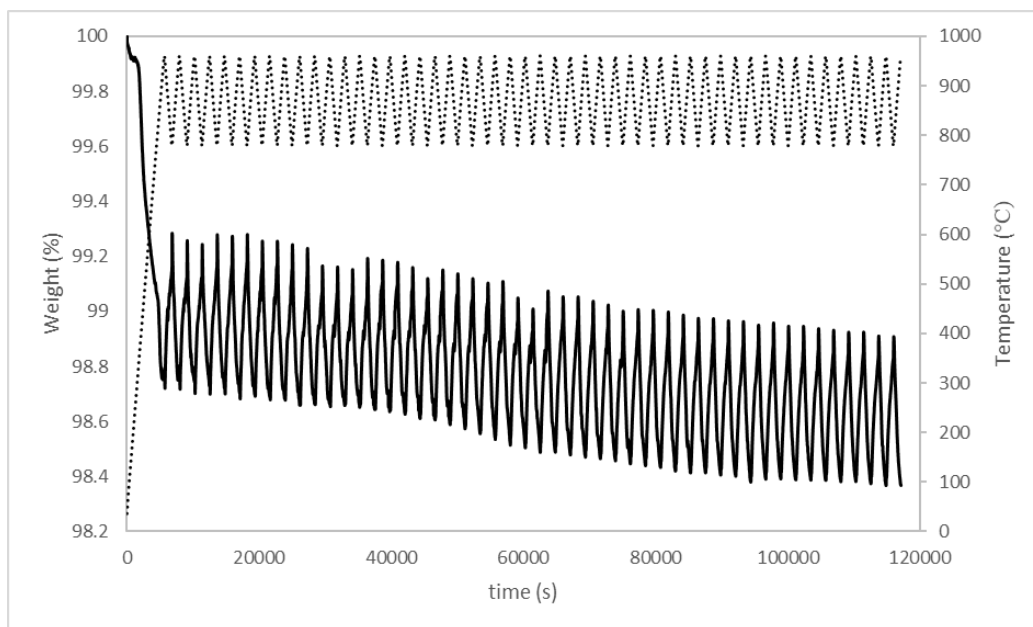


Figure 5.36. Cyclic oxygen exchange of SCFC-6473 based on weight change during heating under Ar flow to 950 °C and cooling under CO₂ flow to 800 °C (solid and dotted lines represent weight change and temperature respectively)

The selection of temperature during reoxidation steps was also studied by decreasing reoxidation temperature from 800 °C to 400 °C. The remaining operational parameters were kept same with the parameters chosen in Figure 5.35. The red/ox cycle performance of SCFC-6473 between 400 and 1100 °C was given in Figure 5.37. Weight change of SCFC-6473 and temperature were shown by solid line and dashed line respectively.

Oxygen equivalent to 1.2 wt.% of the initial weight was evolved during the first thermal decomposition period in the temperature range of 350 to 1100 °C. 1.0 wt.% of the initial weight was regained during the following reoxidation step. The amount of oxygen exchanged between thermal decomposition and reoxidation did not change during five cycles. The final weight of each cycle increased from 98.3% to 98.4%. As the gas flow changed from oxidizing to reducing environment, adsorbed

oxygen was immediately released from SCFC-6473 and continued up to 1100 °C. By comparing the results shown in Figure 5.35 and Figure 5.37, the extent of oxygen exchange of SCFC-6473 is depended on the operational temperatures.

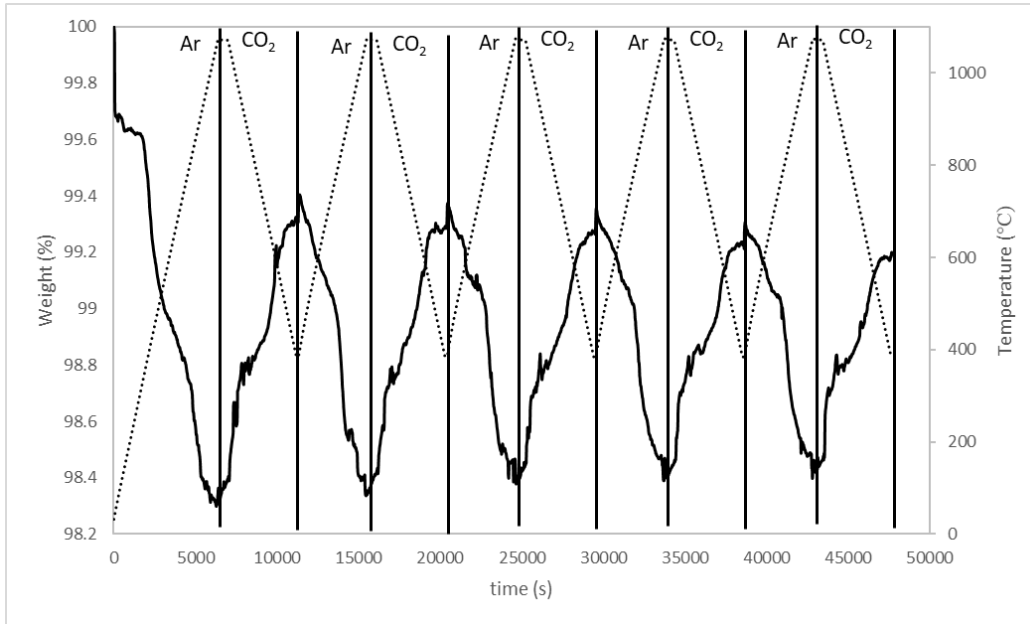
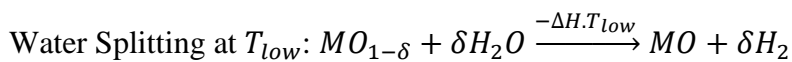
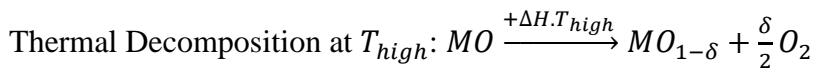


Figure 5.37. Cyclic oxygen exchange of SCFC-6473 based on weight change during heating under N₂ flow to 1100 °C and cooling under CO₂ flow to 400 °C (solid and dotted lines represent weight change and temperature respectively)

5.2 Two-Step Thermochemical Water Splitting Cycles

Having studied the oxygen exchange properties of red/ox materials, the performance of the synthesized materials was studied for two-step thermochemical water splitting cycles. The desired reaction steps were given as,



5.2.1 The Performance of Co_3O_4 and 1.84% Pt- Co_3O_4 doped Monolith during Temperature Programmed Thermal Decomposition (TPtD) and Water Splitting (TPWS)

77mg Co_3O_4 and 70.6mg 1.84%Pt- Co_3O_4 were doped into different monoliths. The rate of thermal decomposition was enhanced by Pt addition as shown in Figure 5.38. $12.7\text{cm}^3/\text{g}$ and $29.7\text{cm}^3/\text{g}$ O_2 was released for Co_3O_4 doped monolith and 1.84%Pt- Co_3O_4 doped monolith respectively. The oxygen release performance of these materials was estimated 20% and 51% of available Co_3O_4 was thermally decomposed during TPtD for Co_3O_4 doped monolith and 1.84%Pt- Co_3O_4 doped monolith respectively. These percentages were low when compared to bulk Co_3O_4 reduction since previous experiments shows that the amount of desorbed oxygen was exactly same with the reduction mechanism of $\text{Co}_3\text{O}_4 \rightarrow 3\text{CoO} + 0.5\text{O}_2$.

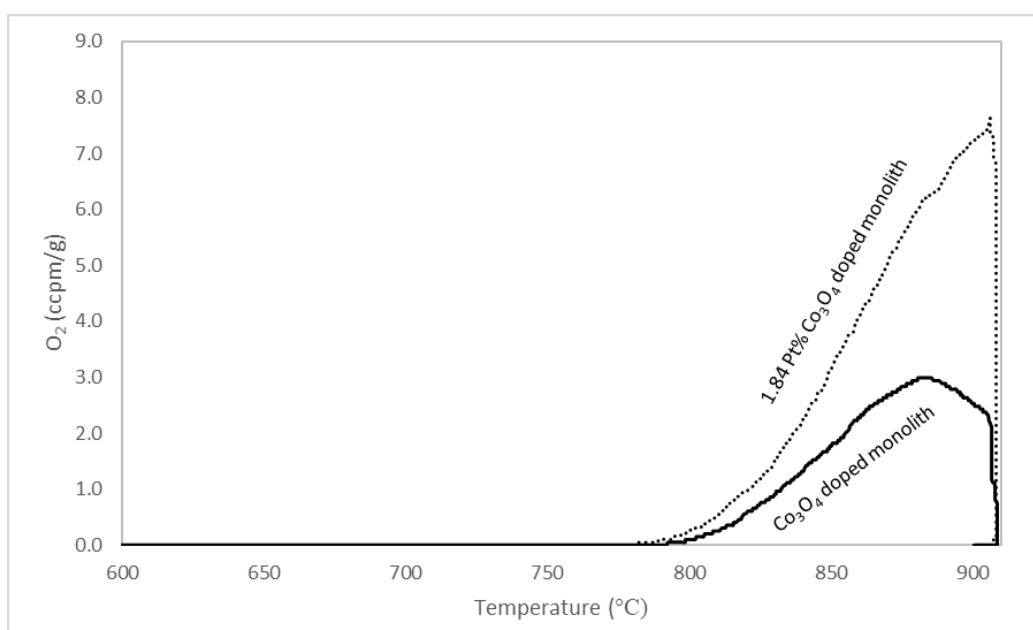


Figure 5.38. O_2 evolution profile during thermal decomposition for Co_3O_4 and 1.84 Pt% Co_3O_4 doped monoliths

Water splitting reaction was carried out after thermal reduction experiment. Hydrogen production could not be observed as given Figure 5.39. The obtained signal was close to noise.

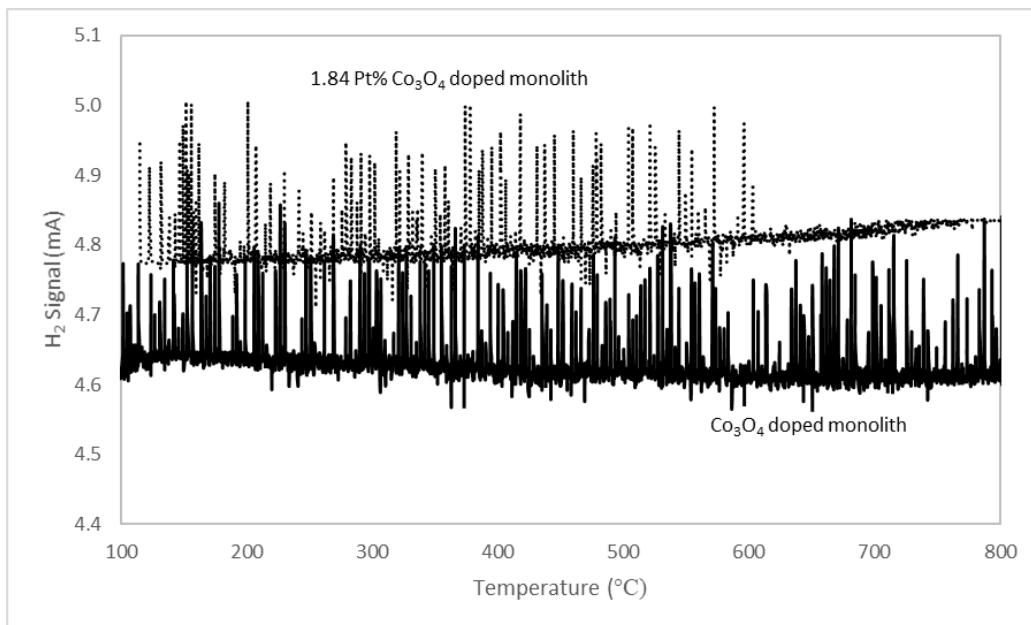


Figure 5.39. H₂ production profile by TPWS for Co₃O₄ and 1.84 Pt% Co₃O₄ doped monoliths

5.2.2 The Performance of 1% Pd-CeO₂ during TPtD and TPWS

Case 1: TPtD up to 900 °C and TPWS at 800 °C

The oxygen desorption profile of 100mg of 1%Pd-CeO₂ was shown in Figure 5.40. The obtained rectangular oxygen signal indicates the lowest detection limit of sensor. Therefore, the amount of desorbed O₂ could not be calculated. After thermal reduction, material was cooled down to 800 °C for WS. Flows were changed so that humidified Ar at 20 °C passed through reactor. The hydrogen production was achieved as shown in Figure 5.41. The obtained signal was clear but still close to noise.

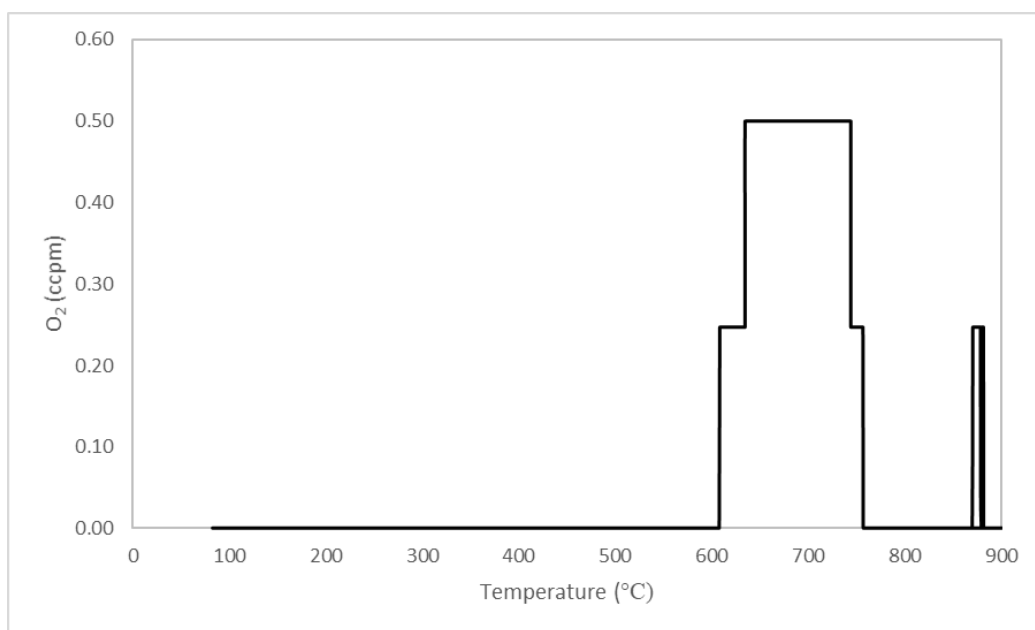


Figure 5.40. Oxygen releasing profile of 1% Pd-CeO₂ up to 900 °C (1st cycle)

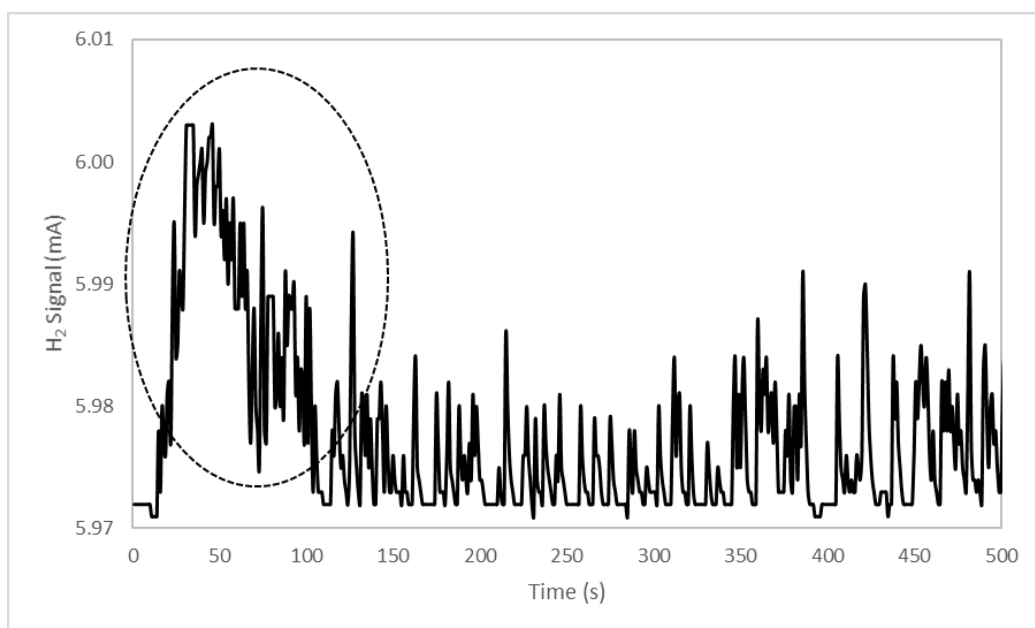


Figure 5.41. Hydrogen production profile from reduced 1% Pd-CeO₂ at 800 °C (1st cycle)

After water splitting experiment, material was heated up to 900 °C for TPtD. During this second cycle, no oxygen desorption and hydrogen production was detected as seen in Figure 5.42. The material was reactivated by increasing the temperature to 1150 °C.

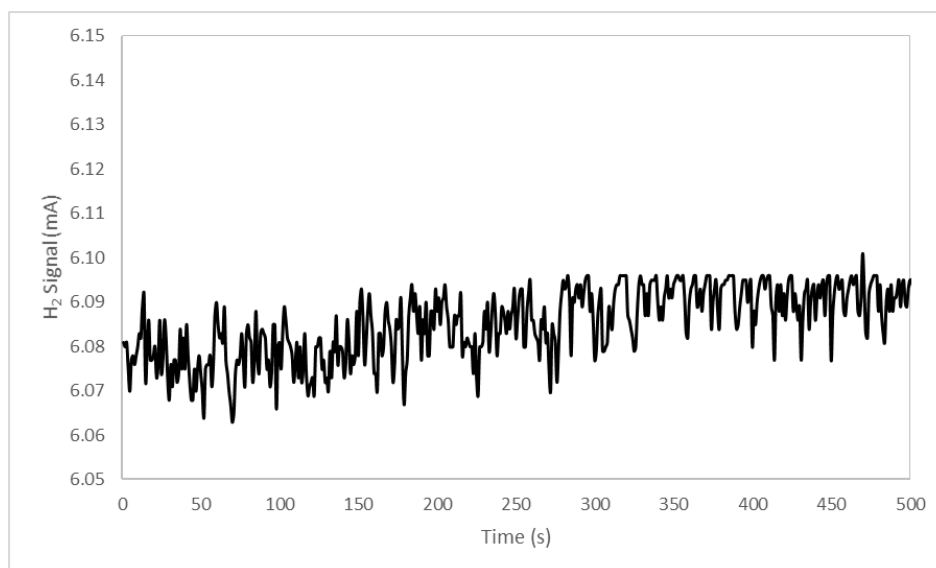


Figure 5.42. Hydrogen production profile from reduced 1% Pd-CeO₂ at 800 °C (2nd cycle)

Case 2: TPtD up to 1150 °C and TPWS at 800 °C

The residue of Case 1 was heated from 800 °C to 1150 °C. New desorption band around 1150 °C was given in Figure 5.43. The oxygen signal obtained for thermal reduction was so low that the O₂ analyzer was operating at its lowest detection limit. Therefore, the amount of desorbed O₂ was not calculated. After thermal decomposition, material was cooled down to 800 °C and water splitting experiment was performed. Hydrogen production profile was Figure 5.44. The obtained signal was clear but still close to noise. After the 1st cycle, similar experimental procedure was followed to see the performance of 2nd cycle. Oxygen desorption and water splitting profiles were given Figure 5.45 and Figure 5.46 respectively. Similar hydrogen and oxygen production behaviors were observed with the 1st cycle.

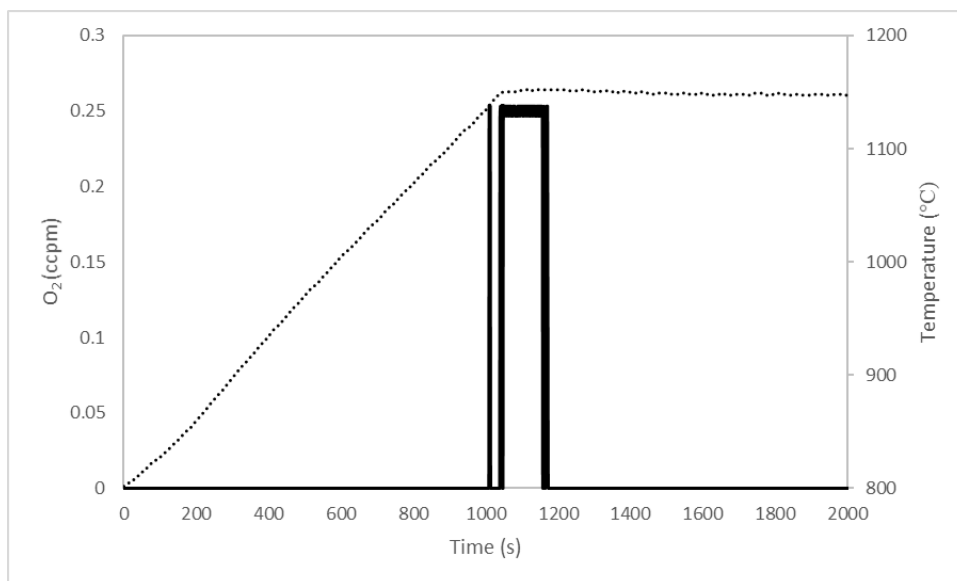


Figure 5.43. Oxygen releasing profile of 1% Pd-CeO₂ up to 1150 °C during 1st cycle (solid and dotted lines represent weight change and temperature respectively)

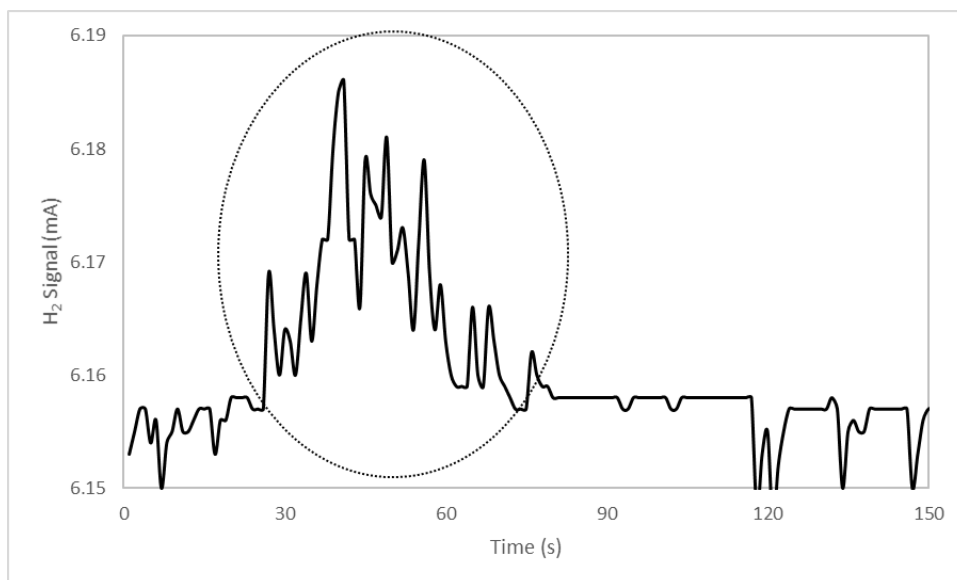


Figure 5.44. Hydrogen production profile at 800 °C from reduced 1% Pd-CeO₂ at 1150 °C during 1st cycle

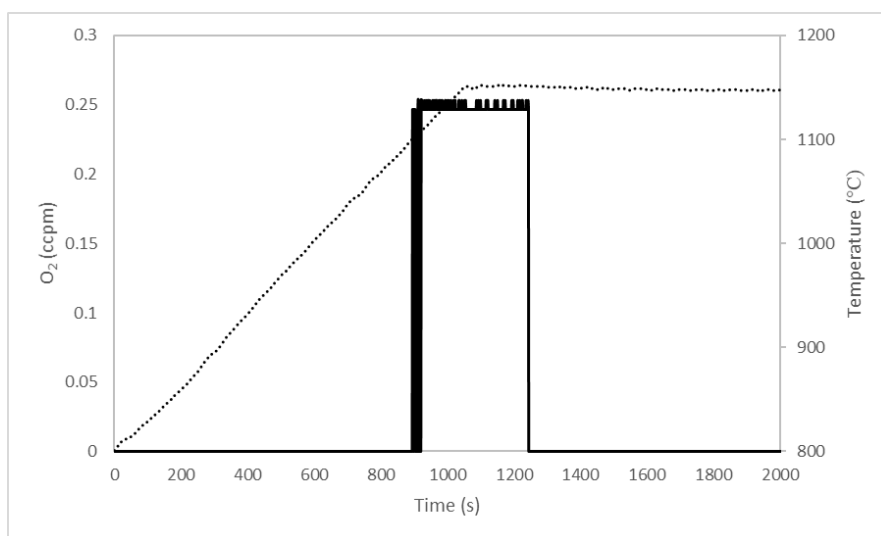


Figure 5.45. Oxygen releasing profile of 1% Pd-CeO₂ up to 1150 °C during 2nd cycle (solid and dotted lines represent weight change and temperature respectively)

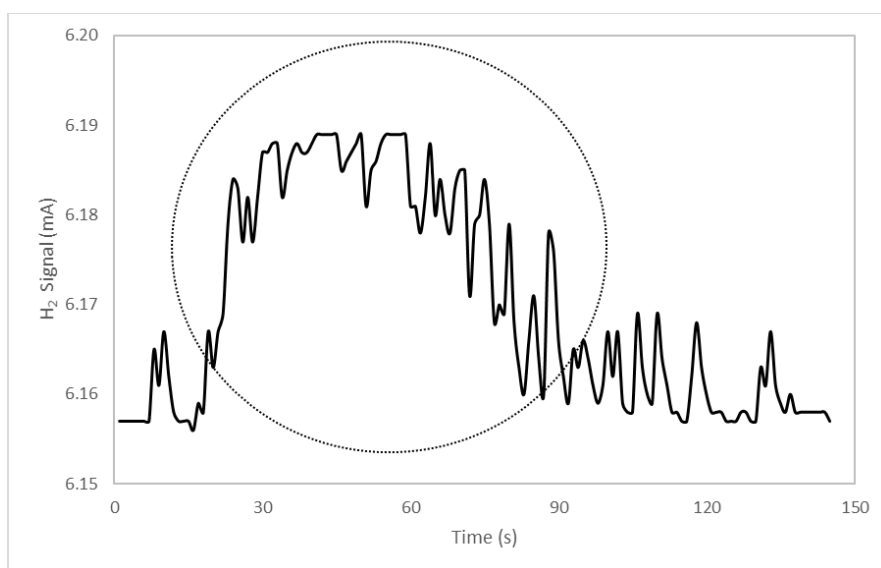


Figure 5.46. Hydrogen production profile at 800 °C from reduced 1% Pd-CeO₂ at 1150 °C during 2nd cycle

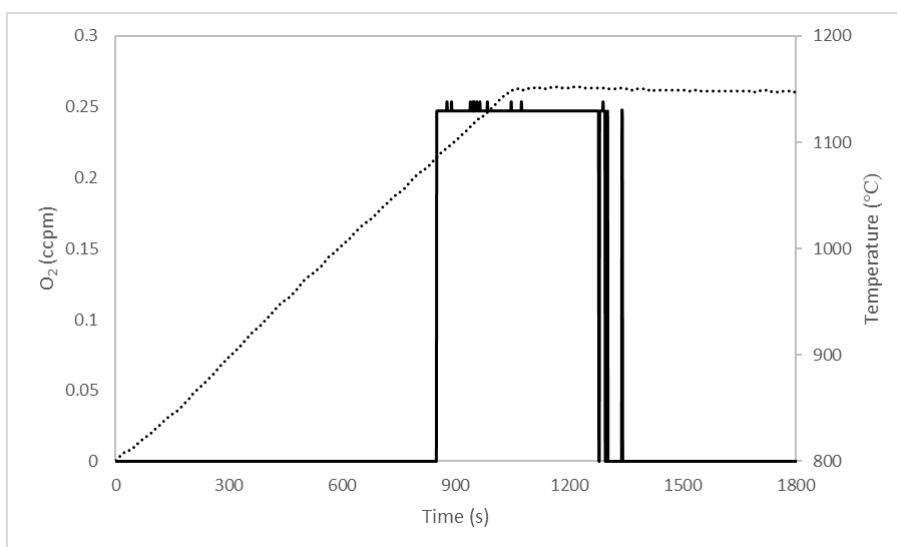


Figure 5.47. Oxygen releasing profile of 1% Pd-CeO₂ up to 1150 °C during 3rd cycle (solid and dotted lines represent weight change and temperature respectively)

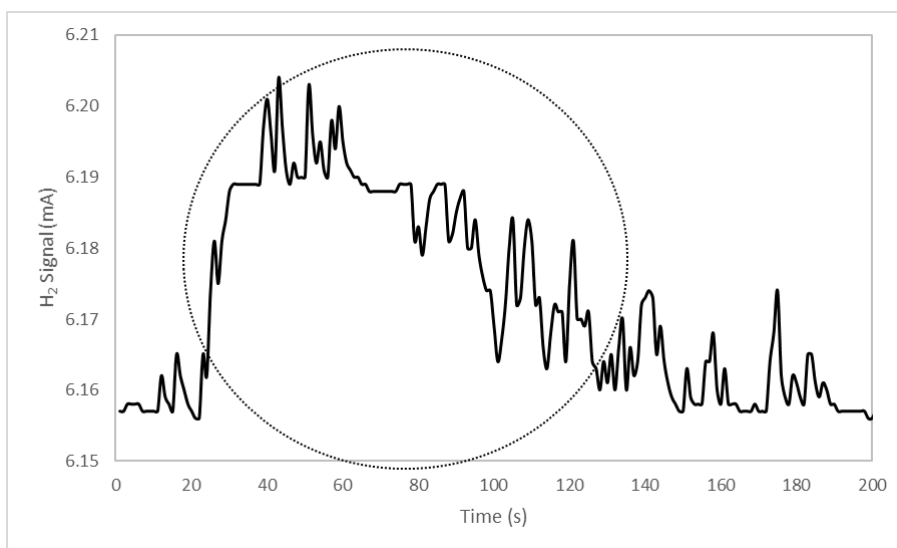


Figure 5.48. Hydrogen production profile at 800 °C from reduced 1% Pd-CeO₂ at 1150 °C during 3rd cycle

After the 2nd cycle, similar experimental procedure was followed to see the performance of 3rd cycle. Oxygen desorption and water splitting profiles were given Figure 5.47 and Figure 5.48 respectively. Similar hydrogen and oxygen production behaviors were observed with the 1st and 2nd cycles. Hydrogen production profiles were compared for three cycles as seen in Figure 5.49. As the cycle number increases, the amount of hydrogen production increases with a parallel increase with desorbed oxygen. By knowing the error coming from the operation oxygen sensor at its lowest detection limit, the amount of oxygen desorption was calculated as 0.54 cm³, 1.38 cm³ and 1.84 cm³ for 1st, 2nd and 3rd cycles respectively.

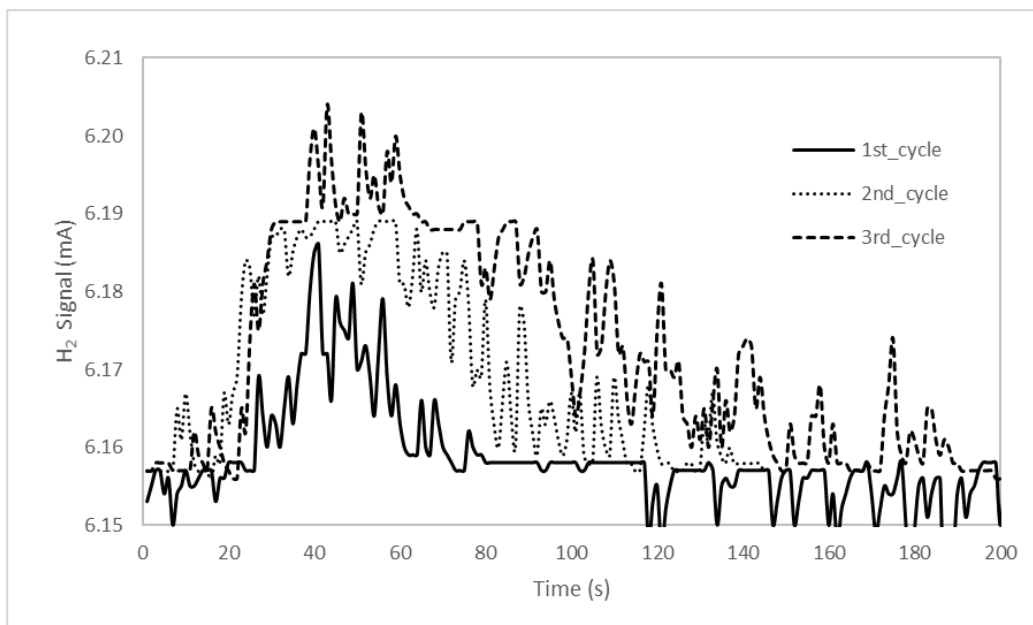


Figure 5.49. Comparison of hydrogen production profiles of 1% Pd-CeO₂ for 3 cycles

Case 3: TPtD up to 1150 °C and TPWS at 1000-500 °C

The loaded material was heated up to 1150 °C and cooled down to 1000 °C, 900 °C, 800 °C, 700 °C, 600 °C and 500 °C respectively as given in Figure 5.50. After final TPWS experiment at 500 °C, material was heated up to 1150 °C and reoxidized by

water at 1000 °C in order to compare the final and initial performances. The material lost its activity as the cycle number increases due to high temperature reduction.

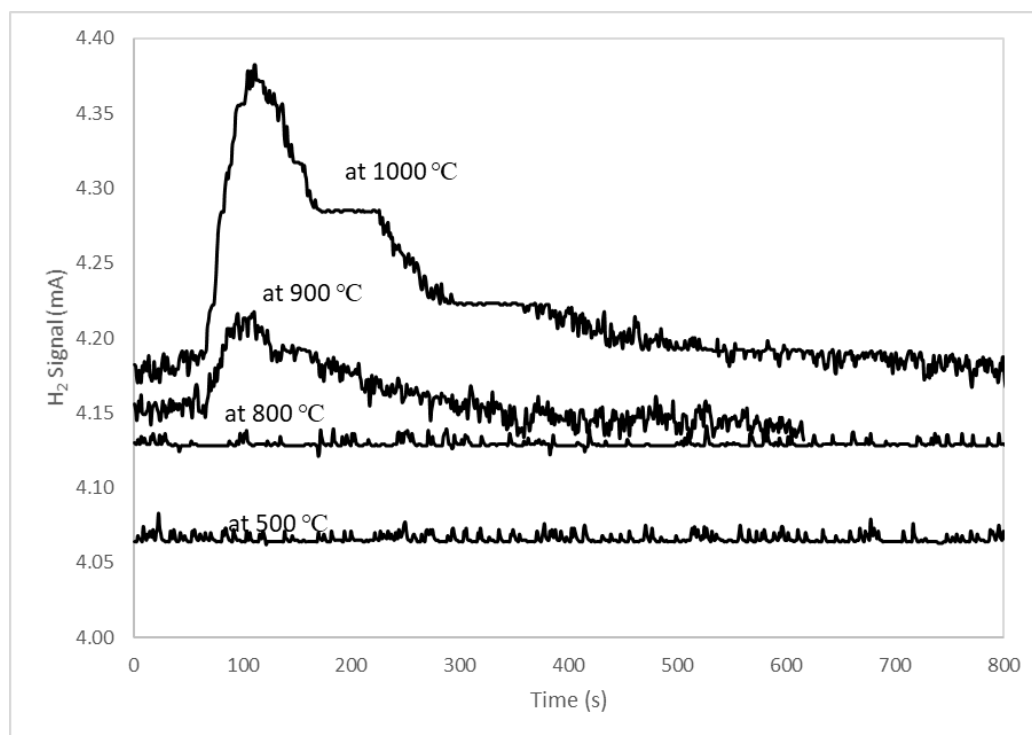


Figure 5.50. Hydrogen production profiles between 1000 to 500 °C (Thermal decomposition experiments performed at 1150 °C)

5.2.3 The Performance of SCFM (6473) during TPtD and TPWS

Preliminary experiments performed by SCFM (6473) shows that the thermally reduced red/ox pair interacts with quartz reactor. This interaction causes complete activation loss. Therefore, material was introduced into reactor by using SS316 and ceramic cartridges. During experiments, 200mg red/ox pair is initially loaded into cartridges.

SCFM (6473) was thermally decomposed up to 1250 °C by using SS316 cartridge. During decomposition no oxygen desorption was detected due to possible oxidation of the steel cartridge. It is known that the oxidation resistance of 316stainless steel

is up to 800 °C and the scale on the cartridge can be seen in Figure 5.51. The volume shrink also indicates the oxygen desorption.



Figure 5.51. 316 stainless steel cartridge with SCFM (6473) after experiment

The hydrogen production profile of SCFM (6473) was shown in Figure 5.52. Two similar hydrogen production profiles were observed for consecutive 2 cycles. The reaction time was kept 60min for the 1st cycle and 20min for 2nd cycle. 52.5mL/g MO_x H₂ production was calculated for the first cycle and the hydrogen produced at first 20min was estimated as 32mL H₂/g and 34mL H₂/gr for first and second cycle respectively. This shows that 61% of hydrogen was produced in the first 20mins. The signal obtained by H₂ detector was also confirmed by GC-TCD and MS equipments as shown in Figure 5.53.

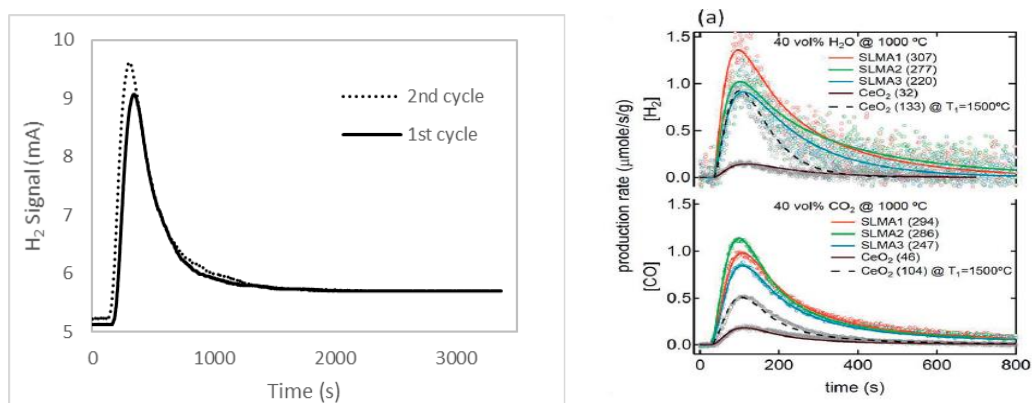


Figure 5.52. Hydrogen evolution profiles of SCFM (6473) for two cycles (left) and production profile from McDaniel *et al.* [38] (right)

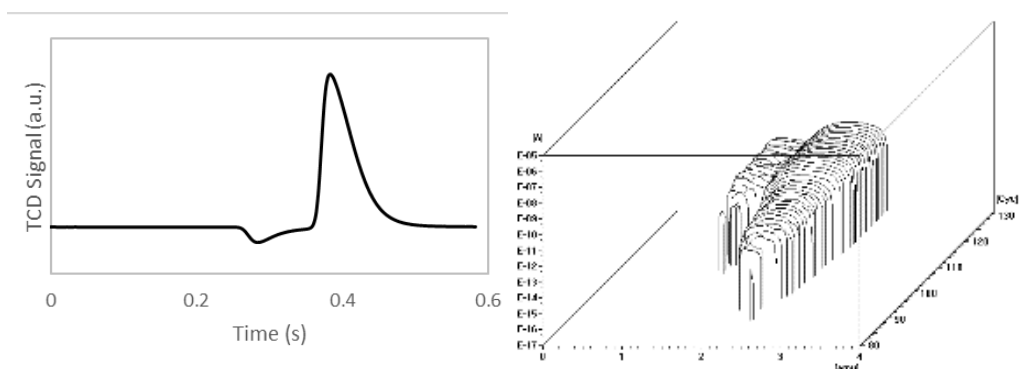


Figure 5.53. Hydrogen signal detected by GC-TCD (left) and MS (right) of SCFM (6473)

In order to detect oxygen evolution during thermal decomposition, this experiment was repeated by changing the cartridge from 316SS to ceramic. During thermal reduction, oxygen evolution starts after 1040 °C and reaches its maxima at 1200 °C as seen in Figure 5.54. However, reduced material could not be oxidized during the water splitting. The activity loss of the material was explained by the photos taken after experiment as shown in Figure 5.55. All reduced material interacted with the ceramic and almost no free red/ox material remained in the cartridge.

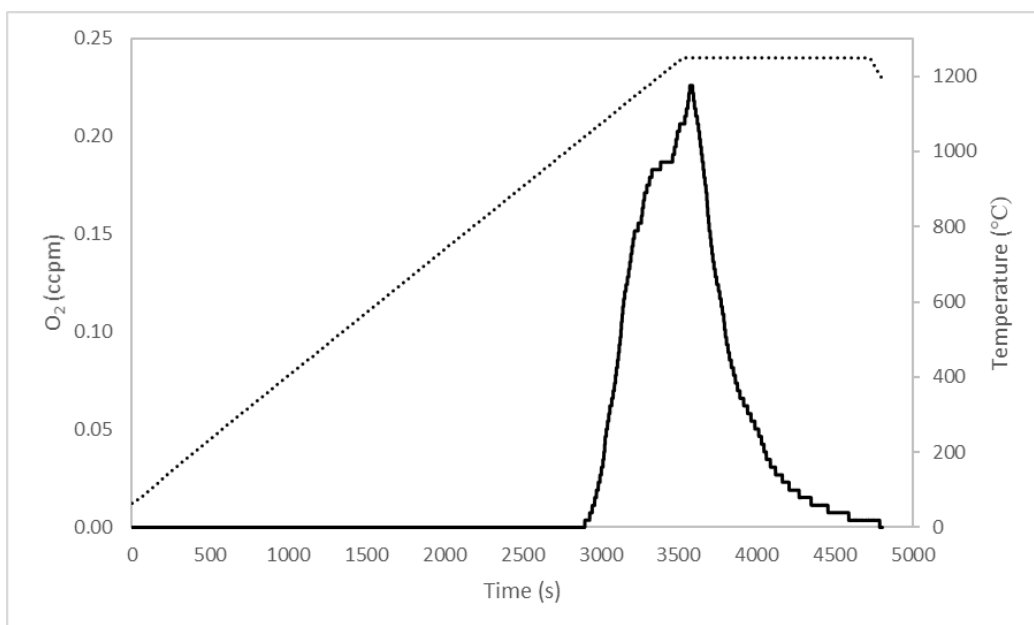


Figure 5.54. O₂ evolution profile of SCFM (6473)



Figure 5.55. Ceramic cartridge before and after experiment of SCFM (6473)

5.2.4 The Performance of Pb at Molten State

The red/ox pairs for thermochemical processes are expected to have moderate or low operational temperatures, high thermal stability, and excellent cyclic performance and high overall efficiencies. Some examples for such materials such as 1700°C for ZnO [321], 1500°C for SnO₂ [89], 2000°C for CeO₂ [322] and 1200°C for Fe₃O₄ [323] were investigated during two-step solar thermochemical water splitting cycles. Aforementioned materials require high-temperature operation during thermal decomposition step. Therefore, mixed metal oxides such as spinel oxides [324] and perovskites [325] were investigated to increase the oxygen evolution rate at lower temperatures and to improve structural stability. Nevertheless, the reported temperature needed for the O₂-releasing step is still higher than 1200 °C. At such high temperatures, the processes lose feasibility due to the limitations imposed by the materials of construction as well as due to the thermal losses. Therefore, materials that can release oxygen at lower temperatures must be sought.

In an effort to find a material with lower temperatures for the reduction excursion, oxides of Pb are investigated. Pb is a favorable candidate with a low melting point (hence storing energy as latent heat) and a cascade of oxidation states [326], [327]. Earlier studies for oxidative coupling of CH₄ [328], carbon black oxidation [329] and soot oxidation [330] revealed the ease with which Pb can accept and donate its oxygen. This mostly stems from the fact that atomic structure of Pb allows a cascade

of compounds with “partial” oxidation states. Furthermore, the high volatility of Pb and PbO facilitates the migration and mobility of these species.

The saturation vapor pressure of lead and lead monoxide were given in Figure 5.56 as a function of temperature. The data are used to estimate the amounts of Pb or PbO that can be volatilized and carried away in a flow reactor. Furthermore, the data were used to estimate the chemical equilibria for the water splitting reaction.

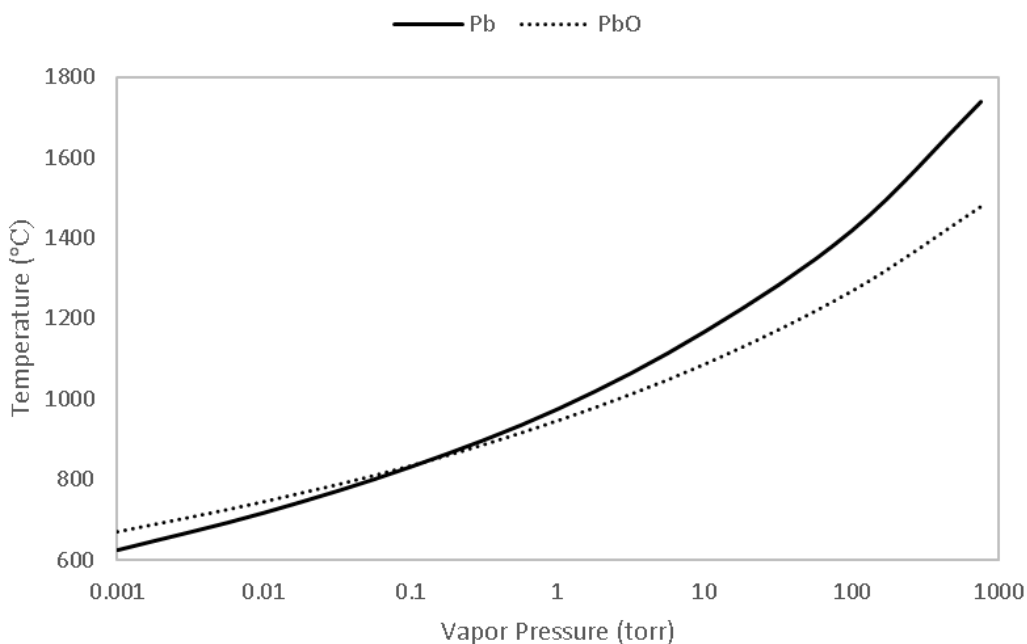


Figure 5.56. The volatility of lead and lead monoxide at high temperatures plotted based on the data obtained from [331]

The thermodynamic driving force for H₂O splitting was reported in Figure 5.57 (a). The degree of Pb oxidation is controlled by the water composition. The thermodynamic estimations revealed that water splitting over lead is favorable at the ratios of $P_{H_2O}/P_{H_2} \gg 1$. The temperature favors the stability regions for PbO_x with a certain drawback which is the loss of intermediate oxidation steps such as Pb₃O₄ and Pb₂O₃.

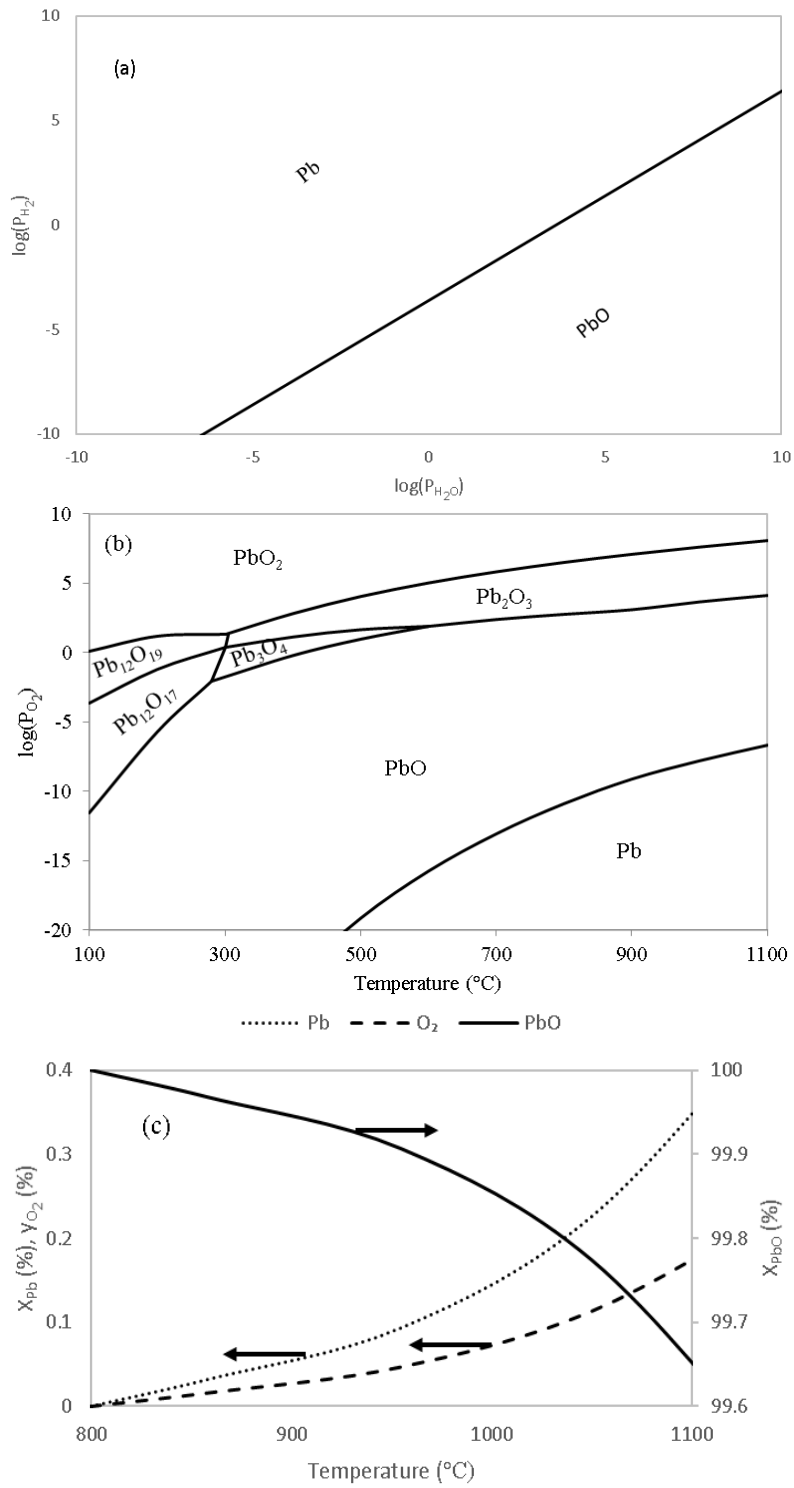


Figure 5.57. Predominance diagram of Pb exposed to H_2O/H_2 at 1000 $^{\circ}C$ and (b) oxygen atmosphere; (c) equilibrium composition during thermal decomposition of PbO at 1 atm

The cyclic operation potential of this oxidation mechanism is also studied in terms of thermal decomposition behavior of formed lead oxide forms. Starting from the higher oxidation state, the decomposition of PbO_2 can follow a complex reaction pathway, Figure 5.57. The predominance diagram on lead oxides was calculated as described in Chapter 3 and shown in Figure 5.57 (b). The oxide forms other than PbO can decompose at relatively high oxygen partial pressures. PbO is the most stable compound indicating that PbO exists in the temperature range of 100 to 1000 °C under relatively low oxygen partial pressures.

Equilibrium conversion during thermal decomposition was also calculated and shown in Figure 5.57 (c). PbO was found as the dominant oxide form of the lead during the water splitting calculations. Oxygen started to evolve around 900 °C. This temperature is very close to the melting point of PbO . The rate of thermal decomposition was increased with respect to the reaction temperature. The equilibrium conversion values of the decomposition reaction from PbO to Pb was estimated as 0.06% at 900 °C while 0.35% at 1100 °C. It turns out that this is the most prohibitive step of the solar thermochemical water splitting reaction.

Hydrogen Production in Lab Scale: Hydrogen production using molten Pb was first demonstrated in a semi-batch reactor configuration; solid Pb was placed in a stainless-steel boat, which was located inside a quartz tube, as described in detail in the experimental part. Prior to the exposure to water, lead was reduced under 5% H_2 - Ar flow up to 500 °C. Then, adsorbed hydrogen on the sample was removed by heating under an inert (Ar) flow up to 550 °C. The system was cooled under inert flow. Water was supplied to the system by bubbling argon flow through a wash bottle, where water was kept at room temperature, corresponding to a water vapor pressure of around 2.6 kPa at saturation. The effluent gases were analyzed by a Teledyne thermal conductivity (XTC-2000 calibrated to 0-5% H_2 in Ar) detector designed for hydrogen analysis. Before the gases were sent to the detector, unconverted water was removed by passing the gases through a U tube placed in an ice bath. Evolving hydrogen gas concentration as a function of temperature was shown in Figure 5.58. Considering the slight baseline shift, water splitting has started

after 300 °C with a maxima around 500 °C. The diffusion barrier formed on the surface of the lead and the decrease in the available Pb sites at the surface were possible causes of the decreasing hydrogen production rate after 500 °C.

The second cycle could not be performed due to the difficulty in lead oxide decomposition as discussed before. The oxygen signal could not be detected. The second excursion of water did not produce any hydrogen, indicating the inability to decompose PbO under the conditions used in this experiment.

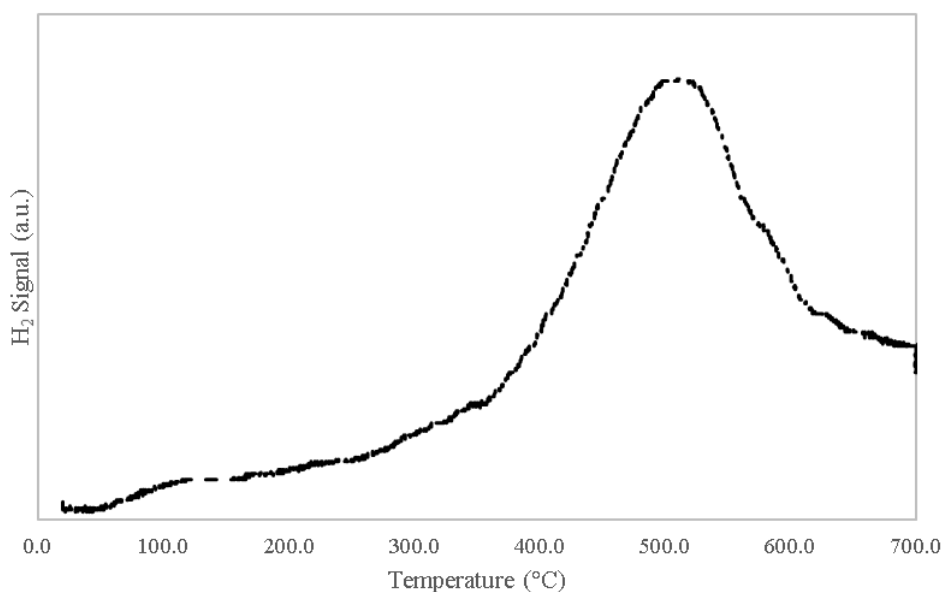


Figure 5.58. Hydrogen production rate during water splitting

Equilibrium limitations for water splitting over lead were calculated and the results are given in Figure 5.59. A close examination of Figure 5.57 (a) reveal that at atmospheric water pressures, the amount of hydrogen production can be as low as 10^{-2} atmospheres under the conditions that Pb and PbO are both in the solid state. But when the volatility of Pb and PbO are taken into consideration, the results become more favorable. At atmospheric pressure, lead starts to be oxidized by water around 500 °C. The reaction temperature favors the rate of hydrogen production. The equilibrium conversion at 1000 °C was estimated as 0.095%. The dominant lead oxide was found as PbO. Higher oxidation states of Pb (Pb_3O_4 , PbO_2 , Pb_2O_3 , etc.)

are not observed in the calculations due to their unstable behavior at the studied reaction conditions as shown in Figure 5.57.

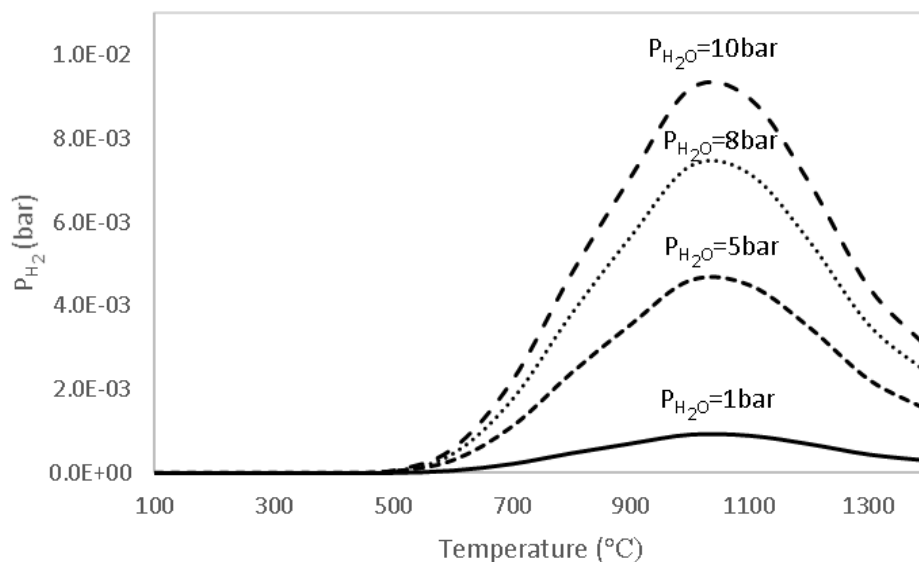


Figure 5.59. Estimated equilibrium conversions of H_2 under different water vapor pressures, 1, 5, 8 and 10 bar. Pb and PbO are considered to be in vapor form.

Despite the similarity between the behavior of hydrogen evolution, the points of maxima differed between the estimated (Figure 5.59) and experimentally measured (Figure 5.58) curves. One must bear in mind that the temperatures were measured externally during the experiments. Furthermore, early decline of the temperature could be attributed to the formation of a surface oxide layer, that imposed a mass transfer barrier to the contact of water with molten lead, which will be discussed in detail in the last section.

Hydrogen Production in the Bench Scale: In order to overcome the barriers formed by a surface oxide layer, a molten bath bubbling reactor was constructed. The molten bath bubbling reactor was loaded up to 2kg Pb. A sparger with 1/4inch tubing is used to disperse the gases and to increase the contact area between reactive gas (wet argon) and lead. The effluent gases were analyzed using a home-made low-cost gas analyzer described in Ogulgonen *et al.* [278]. The hydrogen production profile in arbitrary units (right scale) was plotted in the same graphs with the equilibrium

conversions (left scale) for comparison (Figure 5.60). Hydrogen production commenced around 600 °C.

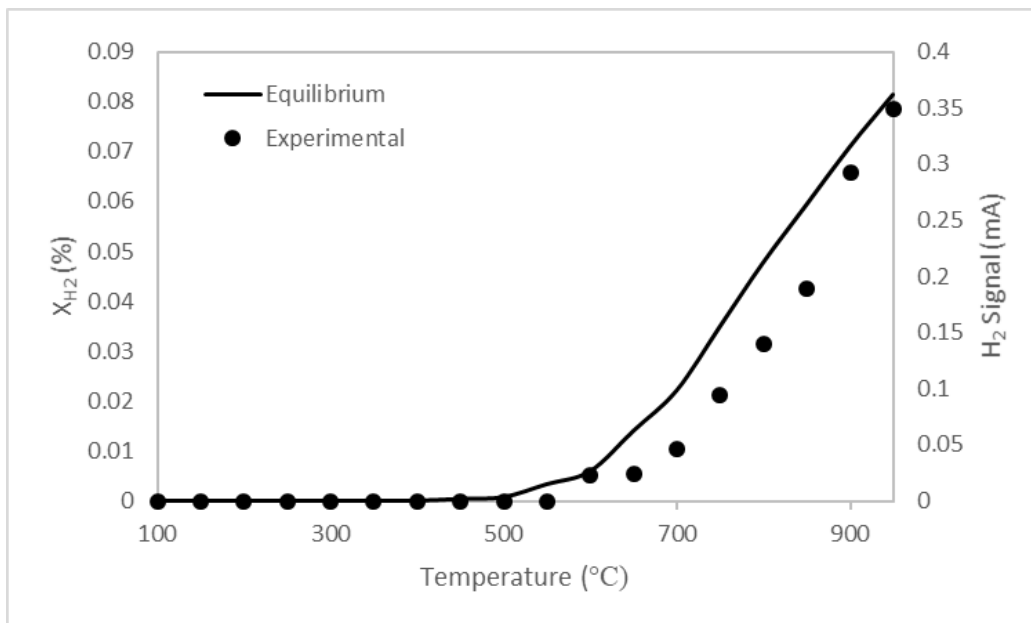


Figure 5.60. The deviation of hydrogen production (symbols) from the thermodynamic equilibrium values (line)

Oxygen evolution during the thermal decomposition of PbO_x was carried out right after the water splitting experiment performed in surface sweep reactor. The reactor was heated to 950 °C under the inert atmosphere during thermal decomposition experiment. The effluent stream was monitored by mass spectrometry and the results are shown in Figure 5.61. Lead has various oxidation states that can give flexibility in oxygen evolution control. Starting from PbO to PbO_2 , the intermediate stages have certain stability regions depending on the temperature and partial pressure of oxygen. These regions show the oxygen exchange capability of the lead under the specified operational conditions such as $PbO_2 \xrightarrow{150\text{ }^\circ\text{C}} PbO_{1.98} \xrightarrow{200\text{ }^\circ\text{C}} PbO_{1.965} \xrightarrow{270\text{ }^\circ\text{C}} PbO_{1.952} \xrightarrow{293\text{ }^\circ\text{C}} PbO_{1.74} \xrightarrow{343\text{ }^\circ\text{C}} PbO_{1.568} \xrightarrow{384\text{ }^\circ\text{C}} PbO_{1.34}$ [327]. As the temperature increase to 800 °C, thermal reduction of PbO is the only stable oxide. But the caution must be exercised: Under an operating temperature of 1000 °C, the vapor pressure of Pb and

PbO is close to 0.1 kPa. At these vapor pressure levels, it is possible to carry away 16mg Pb per hour from the reactor under 100ccpm effluent flow.

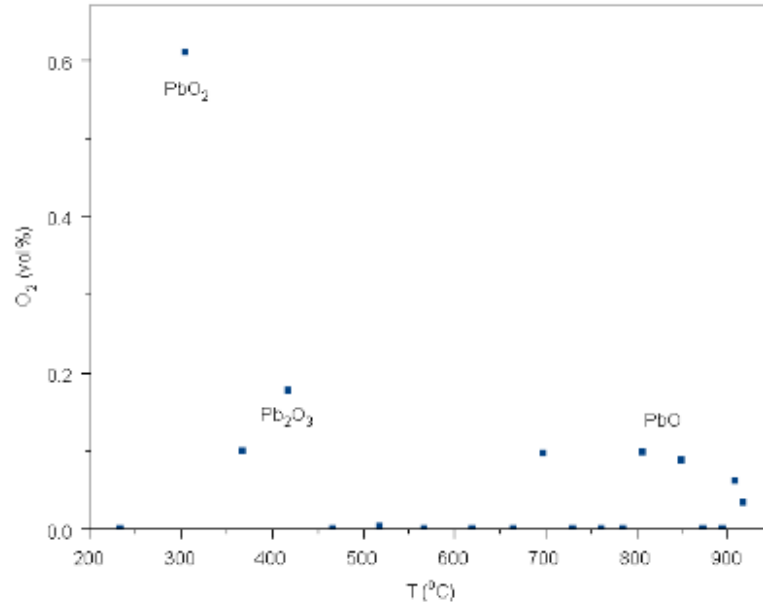


Figure 5.61. The oxygen composition in the effluent stream during thermal decomposition

A reaction-diffusion model for flat geometry was selected for the estimation of the relationship between molten metal bed height and the reaction time required for total oxidation during water splitting as given in Figure 5.62. PbO_x scale was expected to form a layer at the top due to the differences in the density Pb (11.34 g/cm³) and PbO (9.53 g/cm³). The thickness of this layer increases as the water splitting and/or carbon dioxide reaction proceeds. This behavior causes a diffusion barrier that controls the reaction extent. The reaction barriers can be written as follows:

Resistances = Gas Film Mass Transfer + PbO_x Layer Diffusion + Reaction Controlled Region

$$-\frac{1}{S_{ex}} \frac{dN_{Pb}}{dt} = \frac{1}{S_{ex}} \frac{dN_{CO/H_2}}{dt} = \frac{C_{O_2}}{\frac{1}{k_g} + \frac{L}{2D_{eff}} + \frac{1}{k''}} \quad \text{Eq. 30}$$

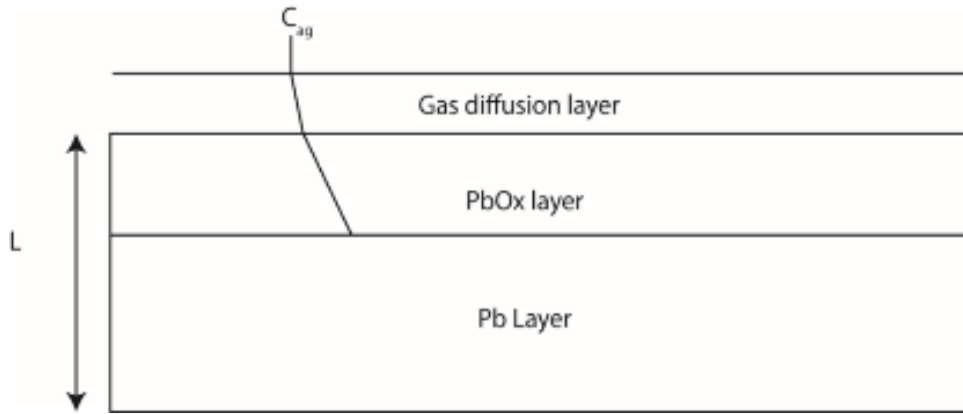


Figure 5.62. Shrinking core model for plate geometry for this experiment

Barbara and Thompson demonstrated that the oxidation of lead is controlled by anion diffusion even if the ionic radii of the Pb^{2+} and O^{2-} ions are almost identical [332]. Water splitting, and carbon dioxide reduction occurred at the surface and the further reaction was controlled by the O^{2-} diffusion through the PbO_x layer. Nozaki et al. also offered a similar oxygen diffusion controlled mechanism [333]. After performing necessary simplifications, the thickness of the oxide layer can be estimated from

$$\frac{\delta^2}{2D_{O^{2-},PbO}} + \frac{\delta}{k_1} = \widehat{V}_{PbO} C_{O^{2-}_o} t \quad \text{Eq. 31}$$

By assuming the O^{2-} diffusion is the rate-limiting step ($k_1 \gg D_{O^{2-},PbO}$), the equation becomes for

$$\frac{\delta^2}{2D_{AD}} = \widehat{V}_D D_{AD} t \quad \text{Eq. 32}$$

The diffusion constant of oxygen in PbO layer was considered to be very similar to the oxygen diffusion in Pb as

$$D_{AD} = 9.65 \cdot 10^{-5} \exp(-20083/RT) \quad [334] \quad \text{Eq. 33}$$

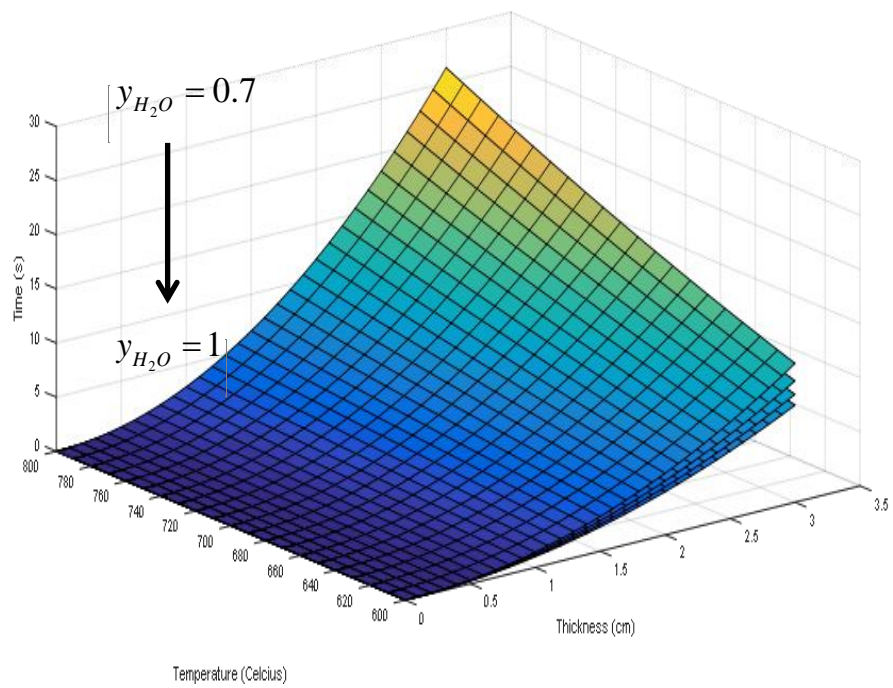
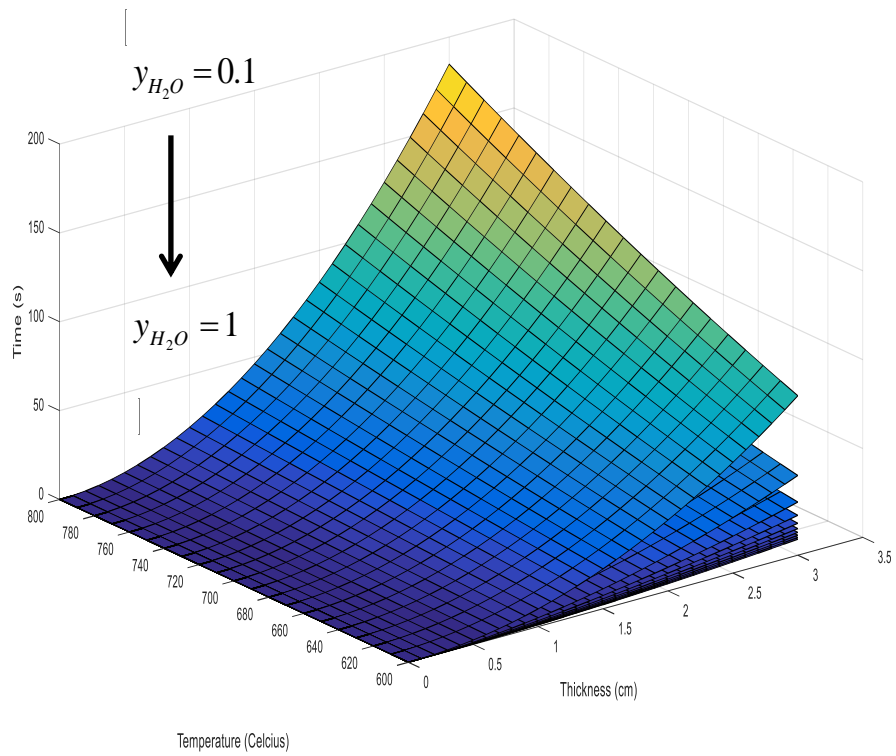


Figure 5.63. The growth of PbO_x layer as a function of time, temperature and y_{H_2O}

The estimated thickness of PbO layer was shown in Figure 5.63. The time required for the oxidation of 3cm of Pb was calculated as 5 seconds at 600 °C with $y_{H_2} = 1$. The increase in the temperature has an adverse effect on the operational time due to the decrease in the diffusion constant. Increasing water composition in the reactant flow decreases the required reaction time for a specific conversion.

5.3 Discussions on Hydrogen Production by Two-Step Thermochemical Water Splitting Processes

Red/Ox metal oxides have been extensively studied over two decades in terms of storage of solar energy in chemical bounds. For this manner, thermochemical process is a proven technology during demonstration of solar energy storage based on oxidation state. Heat as a driving force is used for reducing the red/ox pair; that is, energy is transferred to chemical bounds so that metal oxygen bound is broken. Therefore, reduced metal oxide starts to store energy. This stored energy comes off during the reoxidation of reduced material. This transfer mechanism has to overcome thermodynamic, transport and kinetic barriers not necessarily in that given order.

Solar energy, the most abundant renewable energy source, is utilized during thermochemical applications. The magnitude of solar energy should be sufficient to sustain red/ox reaction at a certain level. The selection of this level is directly related to the reduction extent of metal oxide. Generally, temperatures higher than 1200 °C are enough for breaking of metal-oxygen bound for solar thermochemical processes. The requirement of these temperature levels are obtained by concentrating solar energy into a small area in order to obtain high energy fluxes. High solar concentration ratios are obtained by increasing the concentrator sizes. However, concentrating solar energy has a certain drawback coming from reradiation losses. Our previous studies demonstrated the application of 70cm OD parabolic dishes to thermochemical [335] and reforming process[279]. The reactor temperatures were easily reached 800 °C and sustained the energy requirement of ongoing reactions.

Having known the limits of our experimental capability, an investigation on suitable red/ox material for two step thermochemical processes was carried out in terms of thermodynamics. All metals were examined in terms of their potential towards oxidation and reduction. The examination was carried out in terms of Ellingham diagrams. The analysis were concluded with grouping at metals in certain groups as oxygen desorption, water splitting and solid state oxygen diffusion assistant. In the first group, metal oxides having high tendency to desorb and adsorb oxygen from mainly air was listed. Metals in water splitting group can dissociate water in order to fill their oxygen imbalances. Final group consists of metals having strong metal oxygen bond. These metal oxides have a strong ability for oxygen diffusion.

As a starting material Co_3O_4 was selected as a model compound for understanding the oxygen exchange mechanism from a red/ox pair. Conducted TPx experiments revealed that Co_3O_4 can thermally decomposed to CoO after $800\text{ }^\circ\text{C}$. TG analysis also confirmed the stoichiometric reduction; that is, $\text{Co}_3\text{O}_4 \rightarrow 3\text{CoO} + 1/2\text{O}_2$. Further reduction to Co requires reducing environment such as hydrogen. The oxygen evolution rate were tried to promoted by addition of platinum and increasing surface area. Although platinum addition had a certain effect on H_2 -reduction and reoxidation performances, the thermal decomposition of Co_3O_4 did not change significantly.

Having evaluated the oxygen exchange potential of Co_3O_4 , two step thermochemical water splitting reaction was carried out. Co_3O_4 was thermally decomposed and tried to oxidize under water vapor – argon flow. The effluent gas stream was analyzed by H_2 -TC detector. During the analysis, hydrogen signal was in the range of S/N ratio during the water splitting step even if the Co_3O_4 was completely decomposed to CoO . Thereafter, Co_3O_4 was completely reduced to Co under H_2 environment. The reduced Co was then used for water splitting. The resulting hydrogen evolution confirms the transformation Co to CoO . Further oxidation was inhibited by the thermodynamics. Therefore, Co_3O_4 is a poor hydrogen production material due to the lattice oxygen in the form of CoO after the first decomposition step. The

produced hydrogen by $3CoO + H_2O \rightarrow Co_3O_4 + H_2$ and/or $Co + H_2O \rightarrow CoO + H_2$ is consumed by the products Co_3O_4 and CoO by the reverse reactions as $CoO + H_2 \rightarrow Co + H_2O$ and $Co_3O_4 + H_2 \rightarrow 3CoO + H_2O$.

Despite the fact that Co_3O_4/CoO red/ox pair can be used very effectively as a heat storage material[336], the regeneration of the material was only possible in air. With the outcomes from thermodynamic analysis, cobalt was mixed with a water splitting assistant, cerium. The atomic ratio was arranged in such a way that they formed a perovskite form. $CeCoO_3$ was analyzed with a similar procedure with Co_3O_4 . Oxygen exchange characteristics were significantly enhanced comparing to Co_3O_4 and CeO_2 . New material shows higher desorption rates at lower temperatures with increasing thermal stability. Nevertheless, the water splitting performance was found to be limited with cobalt reduction. Cobalt atom was changed to iron atom which present under the two columns named as oxygen desorption and water splitting. New material became $CeFeO_3$ in the perovskite form. This material was thermally reduced and reoxidized by water several times. The resulting hydrogen production was found as 11 mmol $H_2/mol MO_x$.

Having conducted analysis with single and bimetallic red/ox pair, more complex red/ox pairs were also studied. From the set of analysis, $Sr_{0.6}Ce_{0.4}Fe_{0.7}Mn_{0.3}O_3$ (SCFM 6473) showed an extraordinary performance on hydrogen production. 52.5 mL $H_2/g MO_x$ was produced during two step thermochemical cycle between 1250 °C to 800 °C. The produced hydrogen has almost double the values reported in the literature. Nevertheless, high amounts of material were needed to be imposed to solar reactor due to the molecular weight of red/ox material (212.18 g/mol). In addition, reduced SCFM-6473 so reactive that it should be preserved in the reactor without conducting any oxygen source; that is, the experiments performed on quartz reactor reveals low hydrogen production since reduced red/ox pair deactivated by SiO_2 .

The transport of oxygen in the crystal framework requires bond making and bond breaking events, which are subject to the same barriers that drive the thermodynamic limitations as well. The crystal structure of the oxide as well as the particle size

determines the transport limitations of the oxygen during the chemical looping process. Small particles provide high surface areas. But, small particles are metastable states of the matter. High temperature processes can cause aggregation of the particles. Once aggregated, the diameter of the particle increase. As a result, related diffusive processes have to overcome longer distances for the transport requiring longer times for thermochemical reduction. The kinetic barriers are also prone to the same oxygen-metal bond energies as the activation barrier of the desorption reactions. Thus, it has crucial importance to achieve required high decomposition temperatures. However, today, obtaining and maintaining high temperatures for the reduction step are still a continuing issue for solar thermochemical hydrogen production system. Although the efficient solar collector designs address this problem, achieving high reduction temperatures required for the red/ox material to fully decompose and release its oxygen in the reactor are challenging and unattainable.

5.4 Reforming Tests

After the investigation of hydrogen production limit in two step thermochemical water splitting processes, conventional hydrogen production technology, methane reforming, was studied by the information obtained in oxygen exchange properties of the red/ox materials. For this purpose, Ni, as reference catalyst, was studied. Hydrogen yield and coke deposition were examined by using alumina support and CeCoO_3 which is the one of the outputs of this thesis. During the analysis, $\text{Ni-Al}_2\text{O}_3$ was studied under lean methane reforming conditions as reference catalyst.

5.4.1 Ni- Al_2O_3 as Reference Case

The synthesis procedure of 15% $\text{Ni-Al}_2\text{O}_3$ was given in Chapter 2. 15% $\text{Ni-Al}_2\text{O}_3$ was reduced up to 700 °C with a heating rate of 10 °C/min. After the reduction, reactor was swept with pure argon flow. The reactor was heated to reaction

temperature (800 °C) under the same flow. Steam methane reforming reaction was performed under the flow of 2.7 % CH₄, 2.7 % H₂O balance Ar at 800 °C. Methane conversion and product gas conversion were given in Figure 5.64. Hydrogen yield reached to 3.0 while with 100% CH₄ conversion was obtained around the 80th minute of the reaction.

After completing the steam methane reaction, the inlet flow was changed to argon at 800 °C. The methane and water reactant gas mixture were removed from the reactor. Thereafter, reactor was cooled down to room temperature naturally. The spent catalysts were stored for further analysis. The amount of carbon deposited on 15wt.% Ni-Al₂O₃ sample was determined by using thermal gravimetric analysis. The change in the weight of the catalysts under oxidizing environment was given in Figure 5.65. The combustion of carbon deposited on the catalysts would result a decrease in weight due to the material loss. However, a weight gain (2.1%) was observed during the TGA. During the oxidation of spent catalysts, two competing reaction occurred simultaneously such as coke combustion (weight loss) and oxidation of reduced nickel (weight gain). Depending on the amount of coke deposited, TGA curves can show a profile representing an increasing or a decreasing trend. In our case, 4% increase in the weight was expected during the oxidation of reduced nickel particles. The observed 2.1% increase gives a hint of ~1.9% of coke was deposited on the spent Ni-Al₂O₃ catalysts. SEM/EDS analysis shows the weight concentration of the atoms as follows: 42.02%, 40.31%, 15.05% and 2.62 for O, Al, Ni, and C atoms respectively. 2.62% C amount is consistent with ~1.9% unaccounted weight in TGA.

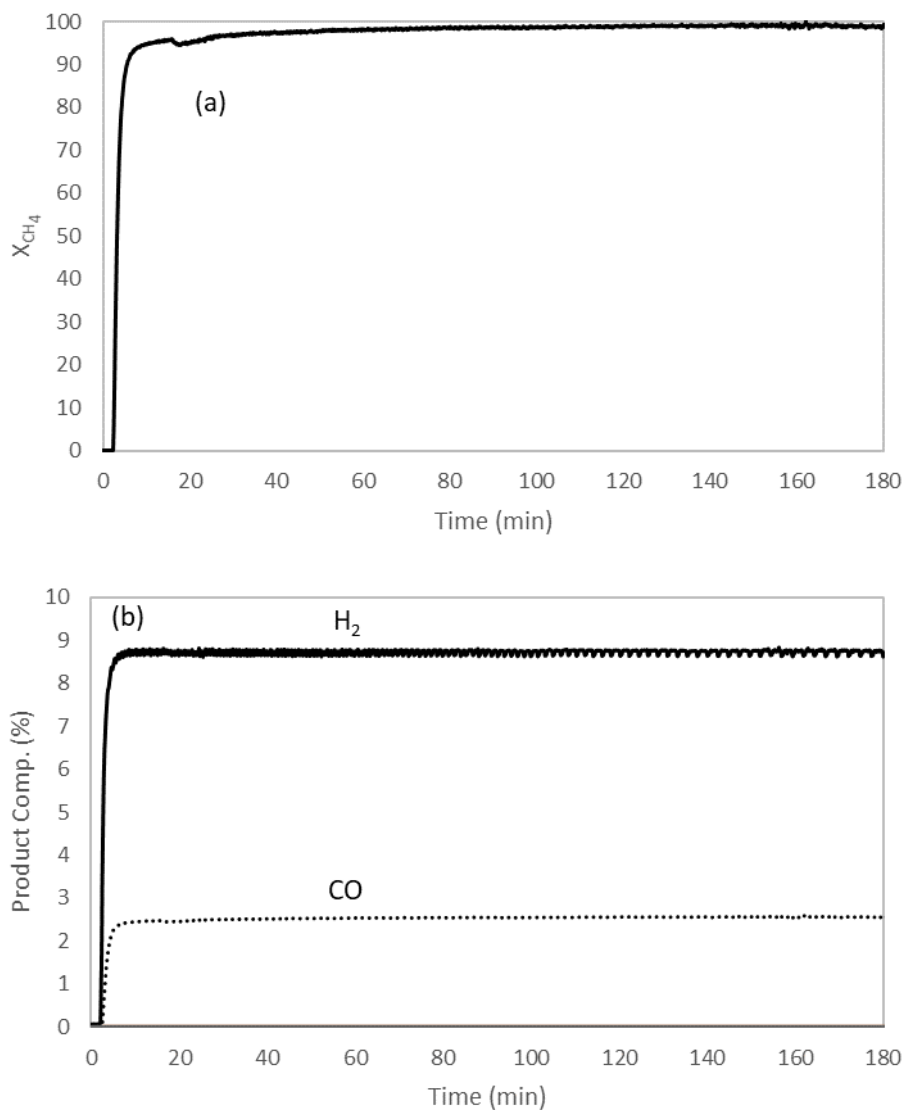


Figure 5.64. Methane conversion (a) and syngas composition (b) during the steam methane reforming reaction over 15 wt.% Ni/Al₂O₃ powdered catalyst in a lab scale reactor.

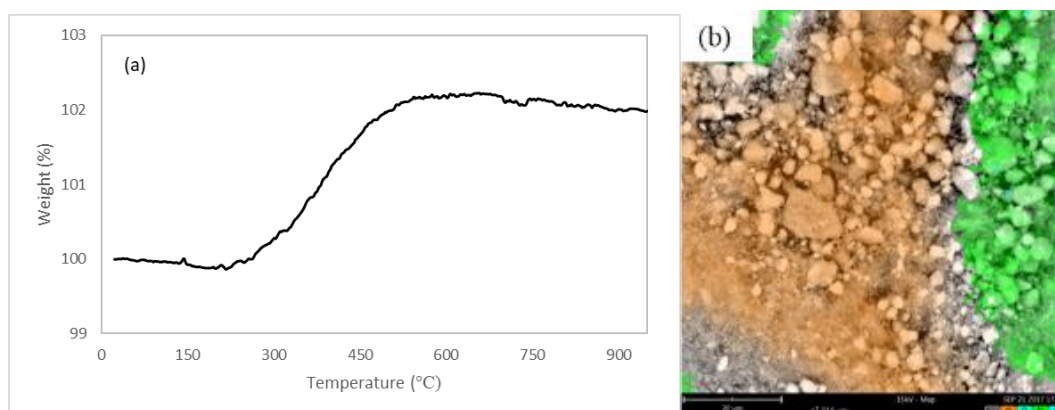


Figure 5.65. TGA curve (a) and SEM image with combined EDS mapping (b) of 15wt. % Ni-Al₂O₃ after being used in SMR reaction at 800 °C

5.4.2 The Effect of CeCoO₃ as Catalyst and Support

All catalysts (15% Ni-Al₂O₃, CeCoO₃ and 5% Ni-CeCoO₃) were reduced up to 700 °C. After the reduction process, residuals gases were swept under argon flow. The reactor was heated to reaction temperature (800 °C) under the same flow. Steam methane reforming reaction performed under the flow of 2.7 % CH₄, 2.7 % H₂O balance Ar at 800 °C. The H₂, CO and CO₂ signals were plotted in Figure 5.66. Initial hydrogen production rate was found same for Ni-Al₂O₃ and Ni-CeCoO₃ samples. For the Ni-Al₂O₃ catalyst, hydrogen production rate falls at 18min and reached its initial value at 27min. Hydrogen signal gradually increased after a small peak for CeCoO₃.

Reforming reaction catalyzed by Ni-CeCoO₃ followed a similar hydrogen profile at the initial period. A small decline followed by gradual increase was observed as the reaction proceeded. Similar signal behavior was also found in terms of CO₂ production rate. The magnitude of CO signal was found in the order of Ni-CeCoO₃>CeCoO₃>Ni-Al₂O₃. The increase in CO signal can be explained by the contribution of water gas shift reaction ($CO + H_2O \leftrightarrow CO_2 + H_2$) catalyzed by CeCoO₃ as support.

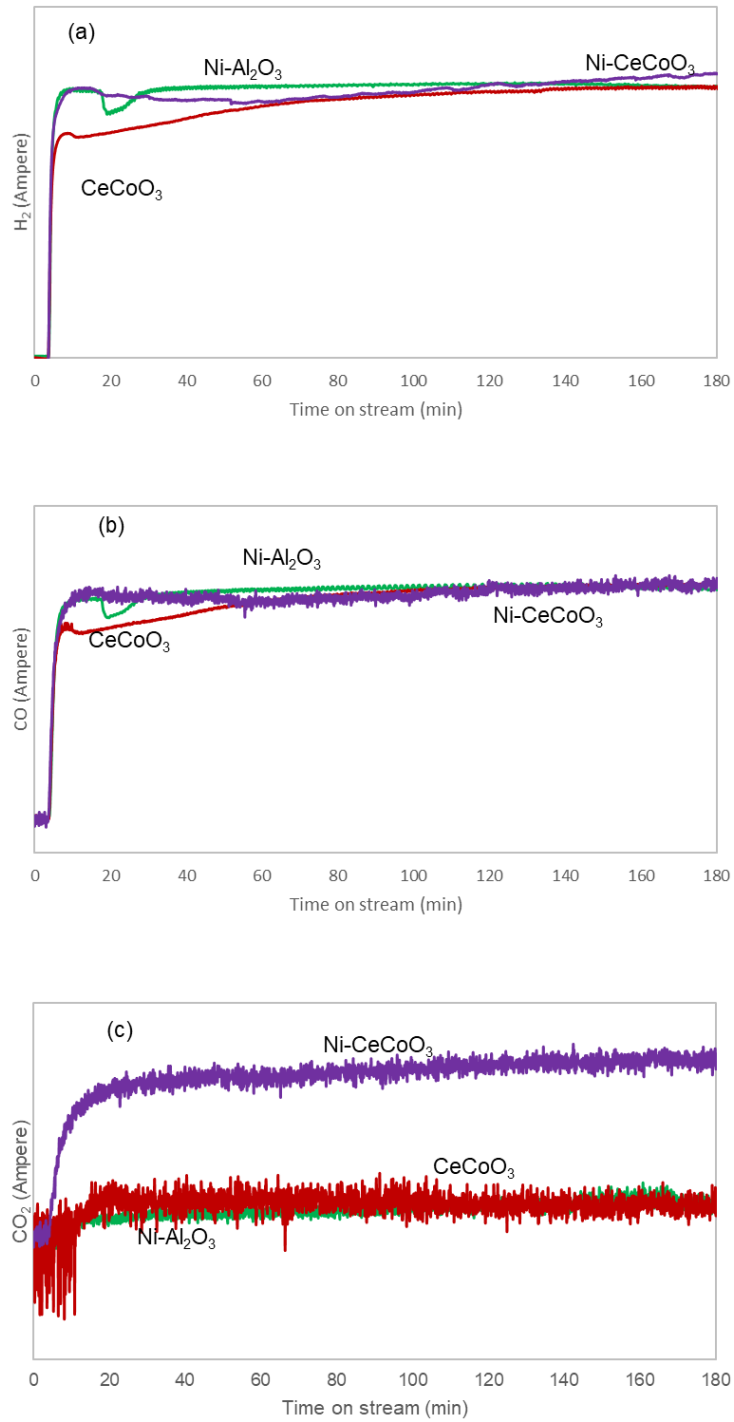


Figure 5.66. Hydrogen (a), carbon dioxide (b) and carbon monoxide (c) signals collected during the steam methane reforming reaction

Following the completion of reforming reaction, reactor was swept under argon flow. After removing of residual product gases, reactor was cooled down naturally under same flow. The amount of coke deposited on the spent catalysts was analyzed by TGA. The weight change during oxidation of coke under dry air flow was given in Figure 5.67.

During the oxidation of spent catalysts, two competing mechanisms, coke oxidation (weight loss) and oxidation of reduced components (weight gain), were expected in the studied conditions [279]. A positive gain in TGA profiles (Figure 5.67) was observed for Ni-Al₂O₃, CeCoO₃ and Ni-CeCoO₃ as 2.1 wt. %, 8.6 wt. % and 8.3wt. % respectively. These observed values were compared with the theoretical estimations conducted under the assumption of all reduced atoms were oxidized in the absence of carbon. It was found that the observed weight gain signals hint the amount of coke deposition as 1.9 wt. %, 0.1 wt. % and 0.12 wt. % for Ni-Al₂O₃, CeCoO₃ and Ni-CeCoO₃ respectively. The presence of reducible oxide as support decreased the presence of coke at the surface probably due to the oxidation of deposited coke with the available lattice oxygen. The nickel presence increased the reforming rate, therefore, a small increase in the coke amount was detected for the CeCoO₃ and Ni-CeCoO₃ case.

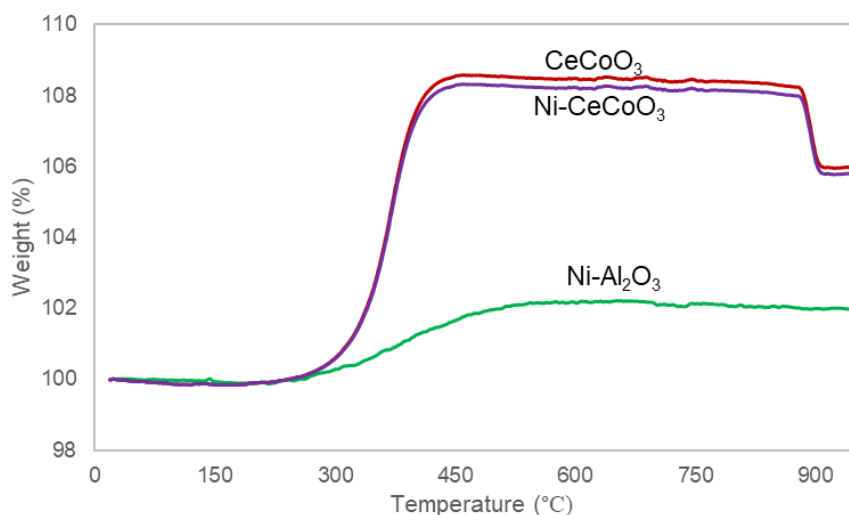


Figure 5.67. The TGA profile of spent catalysis after SMR reaction at 800 °C

Coke formation cannot be inhibited but be limited in certain rates due to thermodynamics [217]. Whisker type carbon is mainly observed in methane reforming processes. Coke formation mechanism starts with the adsorption of hydrocarbon or coke on the catalyst. Carbon diffuses through the catalyst and starts nucleation. At the end of the process, carbon fibers forms with catalyst at the tip [337]. High mechanical strength and insulation properties of Whisker type of carbon results with catalyst fragmentation, reactor failure, heat transfer problems and pressure drop problems. The thermal cameras and pressure monitoring systems generally used for online tracking reactor conditions in industry. Reactor tubes shows a trend towards failure are blinded so that process is tried to sustain in a certain level until maintenance schedule.

Problems related to endothermicity of the overall reaction and coke formation was addressed in the scope of this thesis. Energy requirement will be discussed at the end of section mainly. In this part, coke formation problem was studied with the findings of material research. Nickel was selected as reference catalyst during reforming experiments. After the validation of reaction setup, CeCoO_3 and Ni doped CeCoO_3 were studied in terms of deposited coke. CeCoO_3 was selected due to its oxygen exchange capability. Competing CO and H_2 formations were observed for CeCoO_3 and Ni/ CeCoO_3 comparing to Ni/ Al_2O_3 . CO_2 formation was found higher for CeCoO_3 due to its oxidation potential. Post experimental TG analysis revealed the amount of coke deposition as 1.9 wt. %, 0.1 wt. % and 0.12 wt. % for Ni- Al_2O_3 , CeCoO_3 and Ni- CeCoO_3 respectively. The presence of reducible oxide as support decreased the presence of coke at the surface probably due to the oxidation of deposited coke with the available lattice oxygen.

Having performed steady state reforming reaction, reforming reaction was carried out under cyclic conditions. The theory behind the cyclic conditions to remove deposited coke on a cyclic reforming period and produce hydrogen rich stream during steam treating. The mechanism was inspired from the working principle of two-step thermochemical cycles. Ni- Al_2O_3 as reference catalyst showed a steady decline performance as the cycle number increases. CeCoO_3 exhibited higher

performance when compared to Ni-Al₂O₃. During reforming, some of methane was oxidized by the lattice oxygen in the CeCoO₃. As the consumption rate decreases due to the lack of available oxygen sites in the lattice, methane conversion starts to decrease and reaches a steady level. During the water splitting period, immediate increase in hydrogen was observed since reduced CeCoO₃ started to split water. Formed coke is also oxidized by water since CO signal was also observed in this step. During the splitting period, random hydrogen peaks were also detected due to our inability to send water to reactor in continuous water. These proof of principle experiments concluded that reducible supports, CeCoO₃ in this study, has a potential for coke removal during process by increasing the steam to methane ratio. Byproduct of this process is hydrogen containing stream which produce an additional hydrogen to overall production.

5.4.3 Steam Methane Reforming (SMR) Performance on Cyclic Conditions

Steam methane reforming reaction carried out at steady state. Having evaluated the CeCoO₃ performance on steam methane reforming at steady state, the oxygen exchange properties of CeCoO₃ were also investigated under cyclic conditions. The object of this section is to increase the hydrogen yield per methane by using two step thermochemical process. The desired reaction mechanism was given as

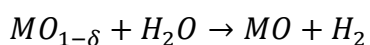
Step 1: Reaction with CH₄

Methane Oxidation: $CH_4 + MO \rightarrow MO_{1-\delta} + CO_x + H_2O_y$ whereas $x = 0,1,2$, $y = 0,1$ and $\delta = x + y$

Steam Methane Reforming: $CH_4 + H_2O \xrightarrow{MO, MO_{1-\delta}} CO + 3H_2$

Dry Methane Reforming: $CH_4 + CO_2 \xrightarrow{MO, MO_{1-\delta}} 2CO + 2H_2$

Step 2: Water Splitting



13wt. % Ni-Al₂O₃ as Reference Catalyst: 13 wt.% Ni-Al₂O₃ (100mg) was loaded into 60cm long (6mm OD) quartz reactor. Prior to the reforming, 13 wt.% Ni-Al₂O₃ was reduced under 10% H₂-Ar atmosphere up to 1000 °C. After the reduction of 13 wt.% Ni-Al₂O₃, the material was cooled down to 800 °C. SMR reaction was performed by alternating gas flows from reducing to oxidizing environment. Gas flows were changed with the timer controlled 4-way ball valves. Reducing experiment was conducted under the flow of 1% CH₄-Ar. The reactor was heated to 1000 °C with a heating rate of 20 °C/min and dwell at 1000 °C for 20min. After that, gas flow was changed to 10% H₂O-Ar for the oxidizing experiment. Water was supplied by injecting liquid water at 20 °C to reactant gas line with a rate of 0.6 mL/h. The reactor was cooled to 800 °C with a cooling rate of 20 °C/min and dwell at 800 °C for 20min. Several cycles were conducted during the experiment. Product gases were passed through a silica gel trap to capture water of reaction before QME 200 MS. During the analysis, hydrogen, methane, water, carbon monoxide, carbon dioxide, oxygen, and argon signals were monitored from mass to charge ratios 2, 15, 18, 28, 44, 32 and 40 respectively. Hydrogen, methane, carbon monoxide, carbon dioxide, and temperature signals were shown as black, red, green, gray lines and blue respectively. Reaction environment was labeled on the corresponding illustration.

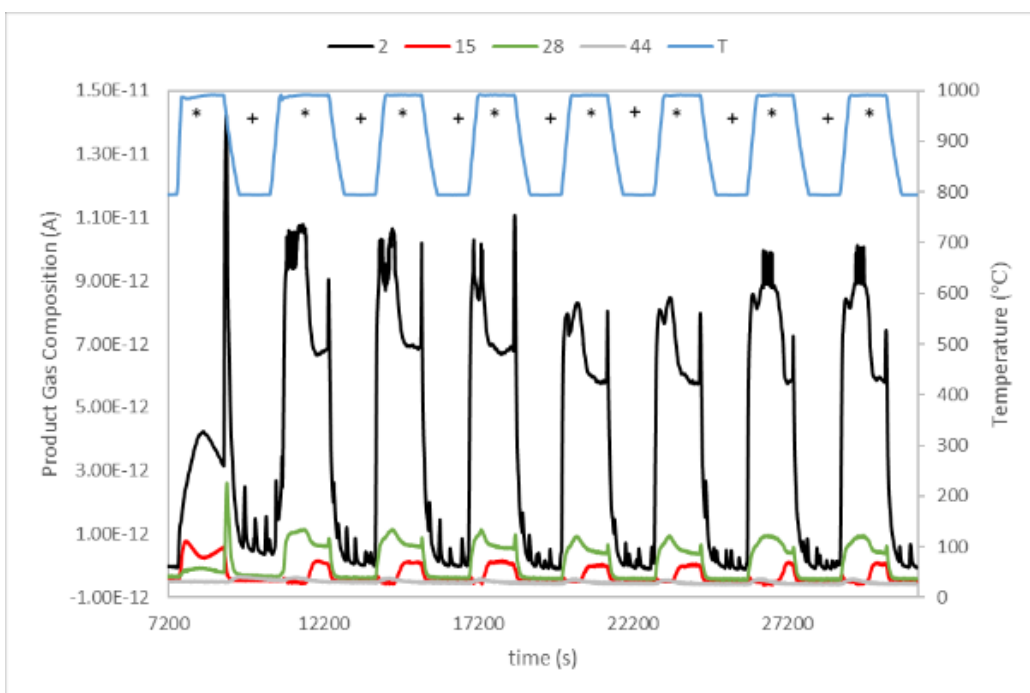


Figure 5.68. Cyclic reduction (*) and oxidation (+) performance of 13 wt.% Ni-Al₂O₃ which reoxidized by water at 800 °C (Reducing was performed under 1% CH₄-Ar from 800 to 1000 °C with a heating rate of 20 °C/min and dwelling at 1000 °C for 20min. Oxidizing was conducted under 10% H₂O-Ar from 1000 to 800 °C with a cooling rate of 20 °C/min and dwelling at 800 °C for 20min.)

Cyclic reducing and reoxidation experiments were performed over reduced 13 wt.% Ni-Al₂O₃. Product gas analysis was shown in Figure 5.68. Except for the first cycle, almost all CH₄ was converted to CO, CO₂, and H₂ during the first 10min of reduction step. After that, CH₄ conversion decreased. Discontinuous hydrogen signals were observed as H₂O passed through 13 wt.% Ni-Al₂O₃. The overall reaction behavior was conserved during the consecutive cycles.

CeCoO₃ as New Catalyst: CeCoO₃ (100mg) was loaded into 60cm long (6mm OD) quartz reactor. Prior to the reforming, CeCoO₃ was reduced under 10% H₂-Ar atmosphere up to 1000 °C. After the reduction of CeCoO₃; the material was cooled down to 800 °C and reoxidized by H₂O-Ar mixture (10% H₂O). Water was supplied by injecting liquid water at 20 °C to reactant gas line with a rate of 0.6 mL/h. SMR

reaction was performed by alternating gas flows from reducing to oxidizing environment. Gas flows were changed with the timer controlled 4-way ball valves. Reducing experiment was performed under the flow of 1% CH₄-Ar. The reactor was heated to 1000 °C with a heating rate of 20 °C/min and dwell at 1000 °C for 5min. After that, gas flow was changed to 10% H₂O-Ar for the oxidizing experiment. The reactor was cooled down to 800 °C with a cooling rate of 20 °C/min and dwell at 800 °C for 5min. Several cycles were conducted during the experiment. Product gases were passed through a silica gel trap to capture water of reaction before QME 200 MS. During the analysis, hydrogen, methane, water, carbon monoxide, carbon dioxide, oxygen, and argon signals were monitored from mass to charge ratios 2, 15, 18, 28, 44, 32 and 40 respectively. Hydrogen, methane, carbon monoxide, carbon dioxide, and temperature signals were shown as black, red, green, gray lines and blue respectively. Reaction environment was labeled on the corresponding illustration.

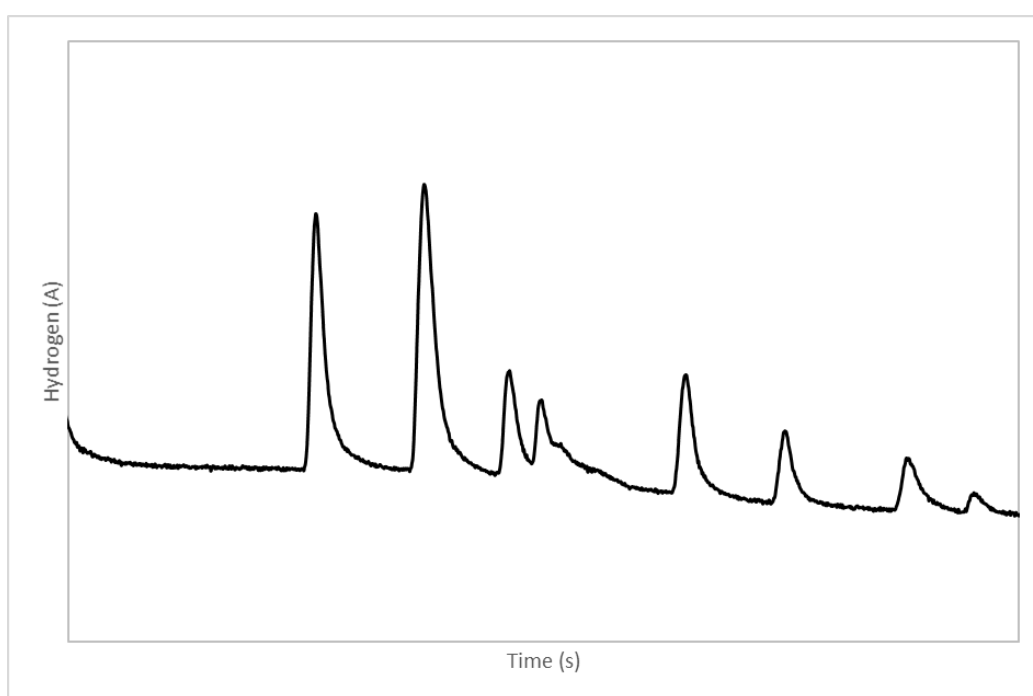


Figure 5.69. Hydrogen production rate during reoxidation of reduced CeCoO₃ under the flow 10% H₂O-Ar at 800 °C

Reduced CeCoO_3 under hydrogen environment was reoxidized under H_2O -Ar flow at $800\text{ }^\circ\text{C}$ as illustrated in Figure 5.69. Distinct hydrogen signals were monitored during the reoxidation. After reoxidation by 10% H_2O -Ar, cyclic oxidation and reduction experiments were performed. The product gas analysis was shown in Figure 5.70. During the reduction, almost all CH_4 was converted to CO , CO_2 , and H_2 . During the change in the reactant gas from reducing to oxidizing a sharp H_2 signal was observed. Discontinuous hydrogen signals were found as H_2O passed through the reduced CeCoO_3 . The overall reaction behavior was conserved during the consecutive cycles.

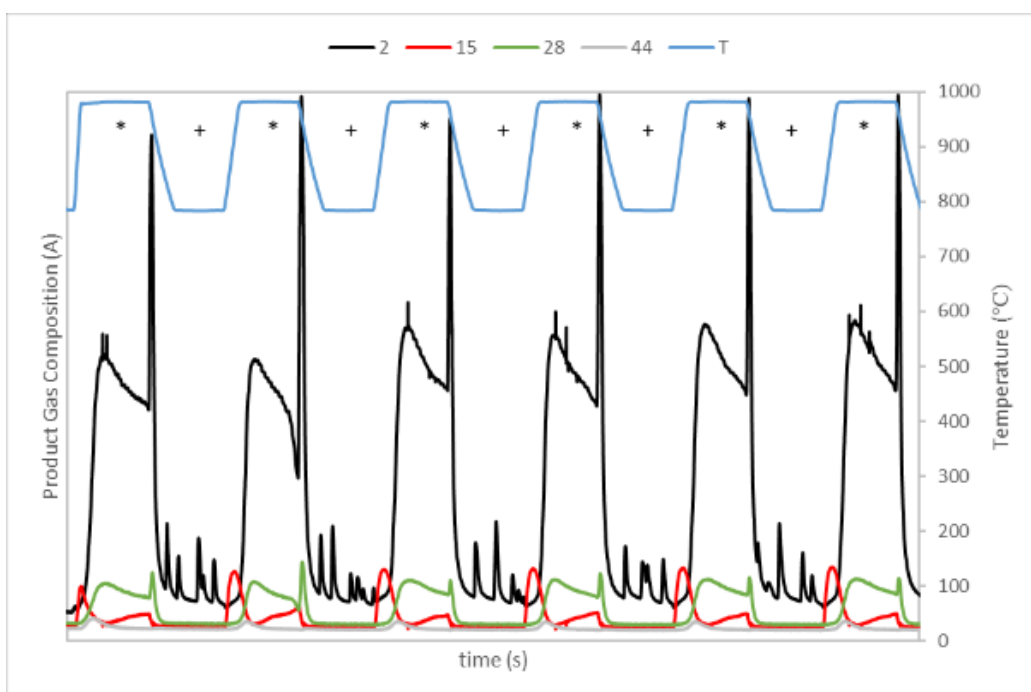


Figure 5.70. Cyclic reduction (*) and oxidation (+) performance of CeCoO_3 which reoxidized by water at $800\text{ }^\circ\text{C}$ (Reducing was performed under 1% CH_4 -Ar from 800 to $1000\text{ }^\circ\text{C}$ with a heating rate of $20\text{ }^\circ\text{C}/\text{min}$ and dwelling at $1000\text{ }^\circ\text{C}$ for 5min. Oxidizing was conducted under 10% H_2O -Ar from 1000 to $800\text{ }^\circ\text{C}$ with a cooling rate of $20\text{ }^\circ\text{C}/\text{min}$ and dwelling at $800\text{ }^\circ\text{C}$ for 5min.

5.5 Pilot Plant Test

5.5.1 Characterization of Energy Utilized by Solar Concentration Plant

Determination of Focus: 70cm OD parabolic dishes were obtained from local market (Ozturk Ayna Ltd.) The size and shape of focus were determined by wood test. A rectangular wood was placed at the focus of the dish to heat and burn the wood. The focal point was determined by visual inspection.

The focus of the parabolic dishes was determined by simple wood test. A rectangular wood was assembled on the parabolic dishes. The shape and the size of the focus were measured under three different cases as given in Table 5.7. The distance of between the wood and the mirror was changed in the first two cases. In the third case, the arrangement of two parabolic dishes was changed so that their focuses were coincide at a certain distance. The wood was placed at this combined focus for observing the combination effect of two solar flux coming from identical parabolic dishes.

Table 5.7 The conditions for parabolic dishes-focus test

Case No	Mirror No	The distance between mirror and wood (cm)	Average solar irradiation (W/m ²)	Ambient Temp. (°C)
1	1	60	955	32
2	1	57	970	30
3	2	Combined focus of two dishes	1061	26

The traces of solar irradiation on wood was shown in Figure 5.71. The focus shape was found as triangle indicating imperfections during the manufacturing of parabolic dishes. The focus size was getting smaller when the distance between wood and the mirror was increased from 57cm to 60cm. Focus was getting larger with a further increase in the distance. The behavior of focus size with respect to distance reveals that focus of the parabolic dishes is 60cm away from the center of the mirror. For the third case, the effect of two identical solar flux on focus size and shape was investigated. In a perfect mirror, an ellipsoidal shape was expected during the focus combining. However, the shape of the focus was changed from triangle to hourglass due to radiation scattering and mentioned imperfections on the parabolic dishes.

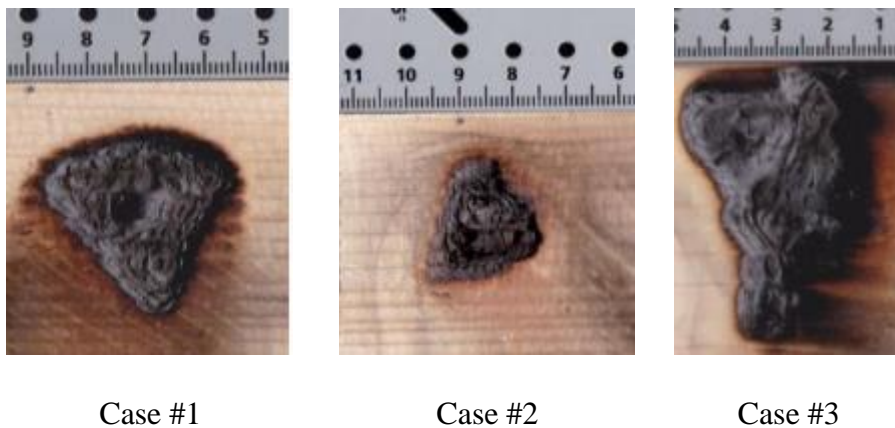


Figure 5.71. The shape and the size of the focus of parabolic dishes

Concentrated Solar Power: Gas Heating: The amount of solar energy that be concentrated via 70cm (OD) parabolic dishes was determined by heating air passing through a spiral 1/4" OD 316SS tubing (Figure 5.72). The back of the spiral tubing was insulated. The flow rate of air was adjusted in the range of 5-30L/min by rotameter. The inlet and outlet temperatures of air were measured by J-type thermocouples with respect to solar irradiation.



Figure 5.72. The determination of concentrated Solar energy

For the stationary flux measurements, a 316 SS disk (32mm in diameter 10mm height) was used. The disk was drilled from 4 positions starting from centre. The holes were just 1mm behind the front surface. K-type thermocouples were inserted for temperature measurements in radial coordinates. The disk was insulated from back and lateral area. The concentrated solar radiation was applied for recording temperature variations during heating. After the heating period, disk was removed from the focus to obtain cooling trend. The heating and cooling trend of SS disk was modelled according to energy balance stated as

$$\rho V C_p \frac{dT}{dt} = Q_{in} - A_{rad} \sigma \varepsilon (T^4 - T_a^4) - A_{conv} h (T - T_a) \quad \text{Eq. 34}$$

By introducing to physical parameters.

$$28.0 \frac{dT}{dt} = Q_{in} - 2.8 \cdot 10^{-11} (T^4 - T_a^4) - 1.86 \cdot 10^{-2} (T - T_a) \quad \text{Eq. 35}$$

The energy supplied by parabolic dishes is determined by measurement of solar radiation per square meter and then knowing the concentration ratio of parabolic dishes. These data are processed in enhanced mathematical models for the estimation of the solar power concentrated on a certain object. During real time experiments, knowing the exact solar flux is very difficult since the variations in the amount of absorbed heat highly depends on the heat losses (mainly radiation and convection). In this section, the solar flux estimations were conducted under two different cases, flow and stationary.

In the flow scenario, the concentrated solar energy was focused on the spiral tubing on a typical day. The change in the air temperature with respect to solar irradiation was plotted on Figure 5.73 (a). Due to intermittent nature of solar energy, the heat transferred to the air varies depending on the solar irradiation. The time gap between the loss in irradiation and its response to the air temperature at the outlet was explained by the heat storage of the setup. The heat transfer from solar radiation to air is controlled by the air velocity affecting the heat transfer coefficient. During the trials for obtaining best heating flux, different focus positions were tried for all directions. The deformation on spiral tubing caused by solar concentration was shown in Figure 5.73 (b). The color variations on SS tubing indicates that the temperatures at the surface of the tubing can be reached temperatures higher than 800 °C. However, only limited amount of this energy was transferred to air due to convectional and radiational losses. The solar power utilized during the air heating was estimated as 10.1 W, 15.1 W, and 22.7W for air flow rates 5 L/min, 10 L/min and 15 L/min respectively. The maximum heat flux that can be achieved in this system was calculated as 120 kW/m². In this system, total solar flux than can be achieved in a black body is around 1600 kW/m². The efficiency of the system (ratio of utilized solar flux to total flux) is calculated as 7.5%.

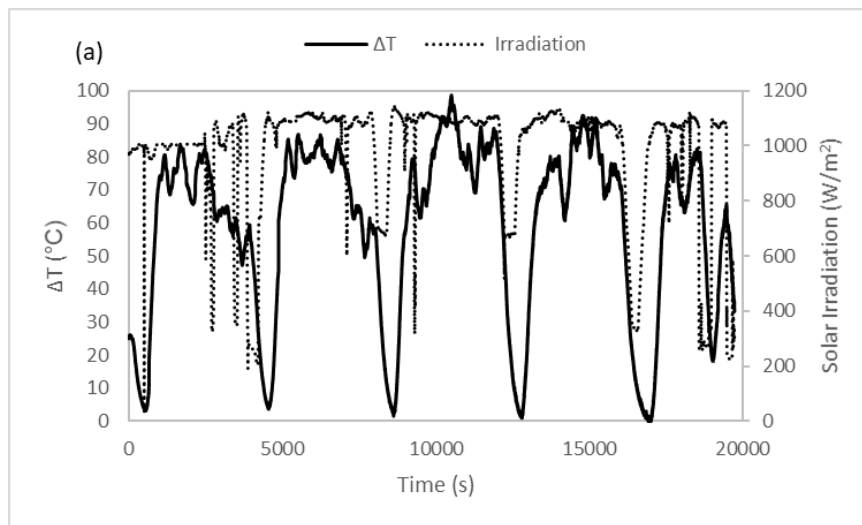


Figure 5.73. The variation of air temperature with respect to solar irradiation (a) and the spiral tubing after the air heating experiments (b)

A steel disk was heated under the solar radiation for stationary case experiments (Figure 5.74). The recorded temperature from the four thermocouples positioned behind the disk shows that the radial temperature distribution did not change considerably (3-7%). Therefore, mean temperature was taken into account for the estimations of solar flux coming to surface of the disk. The temperature of the center (recorded 1mm below the surface) of the disk reached to 660 °C within the 700s after the focus position. After reaching plateau during heating, disk was removed from the focus so that cooling trend was recorded. During cooling, it took 2000s to reach to ambient conditions. The mathematical model used for the prediction of the SS disk temperature overlapped the experimental results indicating high goodness of fit. With this model, net power absorbed or dissipated from the solar disk was estimated as given in Figure 5.74. At the initial period, 160W was absorbed by SS disk. As the temperature increases, radiational and convective losses became dominant so that it reaches a steady state at 660 °C. Following the off-focus position, heat absorbed by the SS disk was dissipated with rate of 165W.

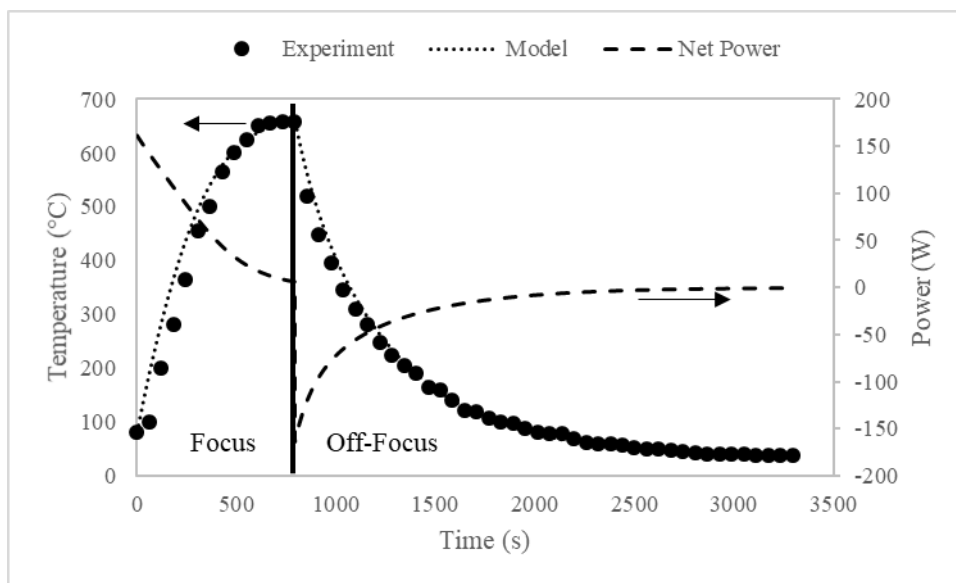


Figure 5.74. Mean temperature measurements and net power estimations during heating and cooling periods of SS disk

Concentrated Solar Energy Utilization: One of the constraints of using solar thermal cycles is the requirement of very high temperatures under steady conditions [338] dictated by the red/ox behavior of the selected oxide. These high temperatures can be achieved by intense focusing, but at the expense of high thermal losses [339]. The limits of temperature by using smaller mirrors was investigated in this study and the measured temperatures across an inert mullite monolith is shown in Figure 5.75. As can be seen, at the back of a blank monolith, temperatures of 700 °C could be easily achieved in a single mirror of 70 cm diameter. The temperature gradient between the illuminated side and the dark side of mullite monolith was around 100 °C ensuring a local temperature of around 800 °C. The range of applicability of Pb/PbO pair will be investigated for this purpose.

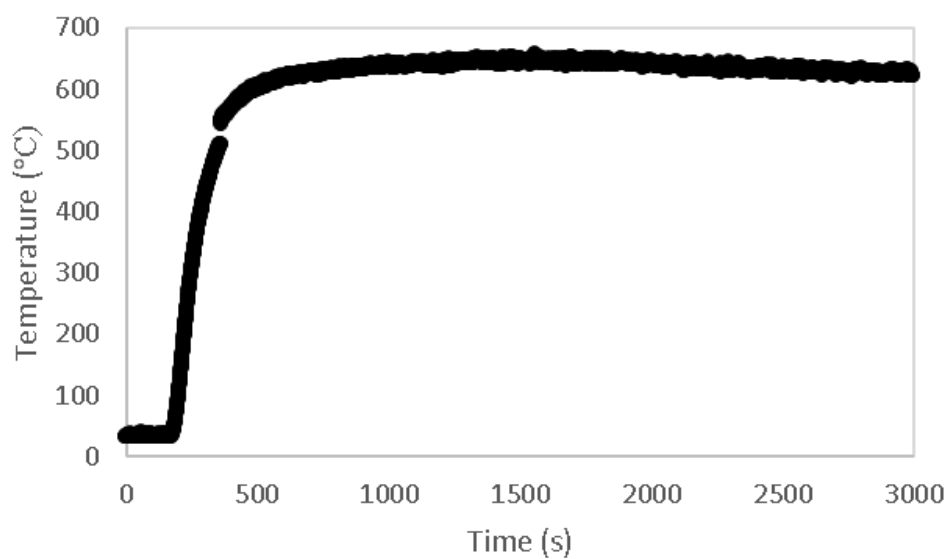


Figure 5.75. The temperature-time diagram measured inside the reactor across a mullite monolith.

5.5.2 Steam Methane Reforming at Pilot Scale

Following the characterization of solar energy utilization by the pilot plant, steam methane reforming reaction was performed by 12.8% Ni-mullite (Figure 5.76). Due to the limited in-house capabilities and the long distance between the utilities and the reactor-dish assembly, water had to be fed through a peristaltic pump with a long feeding line (>10m). Water was fed “in excess”. Since steam generation was taking place in the frontal zone of the solar powered domain, fluctuations of the steam amount were inevitable in the present design. The monolith temperature profiles are shown in Figure 5.77 and Figure 5.78, along with solar irradiation and methane conversion observed during the pilot plant test performed under solar irradiation. It must be noted that, day 1 was sunny with cloudy patches, particularly later in the day, resulting in a shorter run. Day 2 was a sunny day averaging backside monolith temperature of 330°C. The dip in the temperature at ~140min was due to a tower located 10 m away from the reactor-dish assembly; its shadow falling around 4 pm in summer seasons for approximately 15 min long.



Figure 5.76. Solar reactor during the reforming operation

The overall temperature trends of the Day 1 (Figure 5.77) and Day 2 (Figure 5.78) were found to be similar. Conversion levels also show some similarity due to the endothermic nature of SMR reaction. There was an initial period of around 60min of consistently rising conversion levels, likely the amount of time it takes for water to saturate the entire system as well as other processes such as catalyst activation. The water was fed by injection in liquid form at a distance approximately 12m away from the reactor itself. Once saturation conditions were met, liquid water also reached the reactor. Instantaneous evaporation of water resulted in an expansion due to phase change. Our inability to control a steady steam flow rate resulted in fluctuations in steam to methane ratio, hence fluctuations in the conversion as seen in Figure 5.77 and Figure 5.78. These events were accompanied by temperature drops due to the latent heat of vaporization of water.

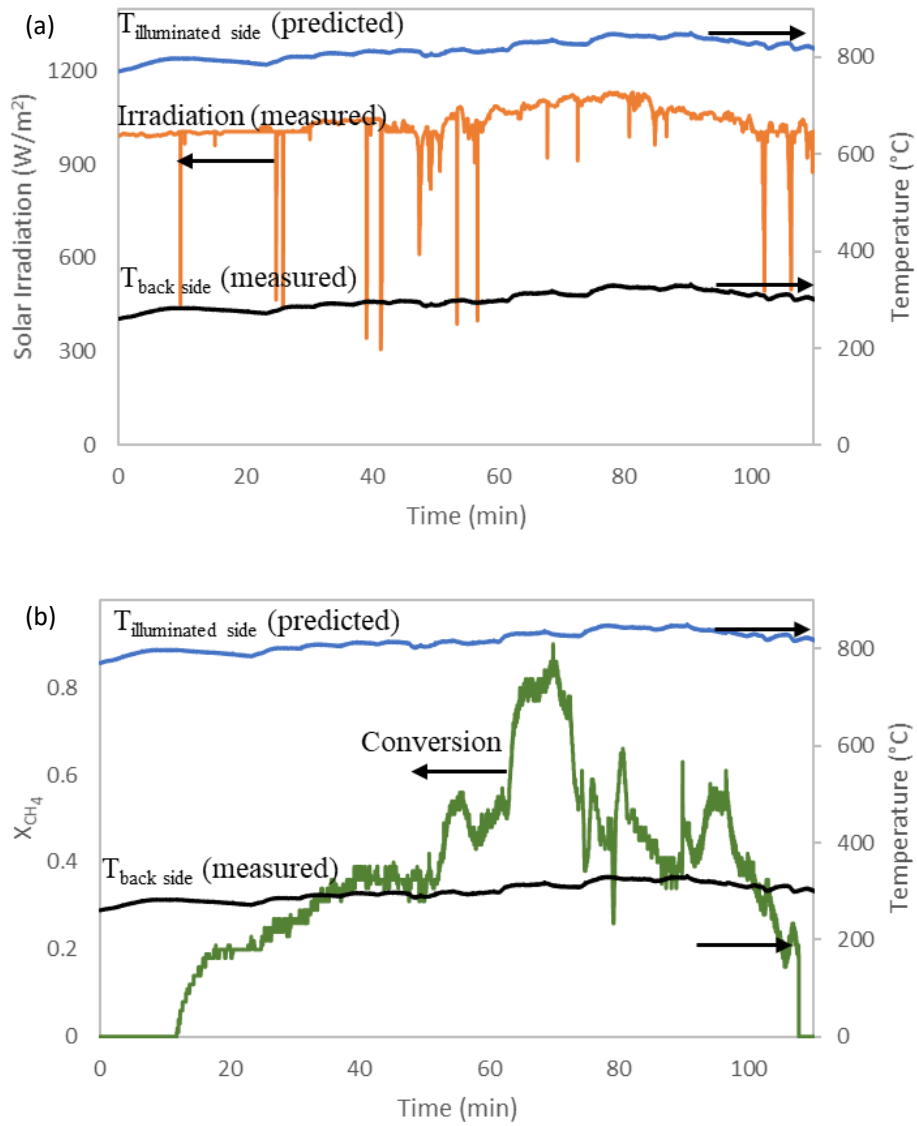


Figure 5.77. Solar irradiation and temperature profiles (a) and methane conversion (b) during solar steam methane reforming catalyzed by 12.8% Ni-mullite (Day 1)

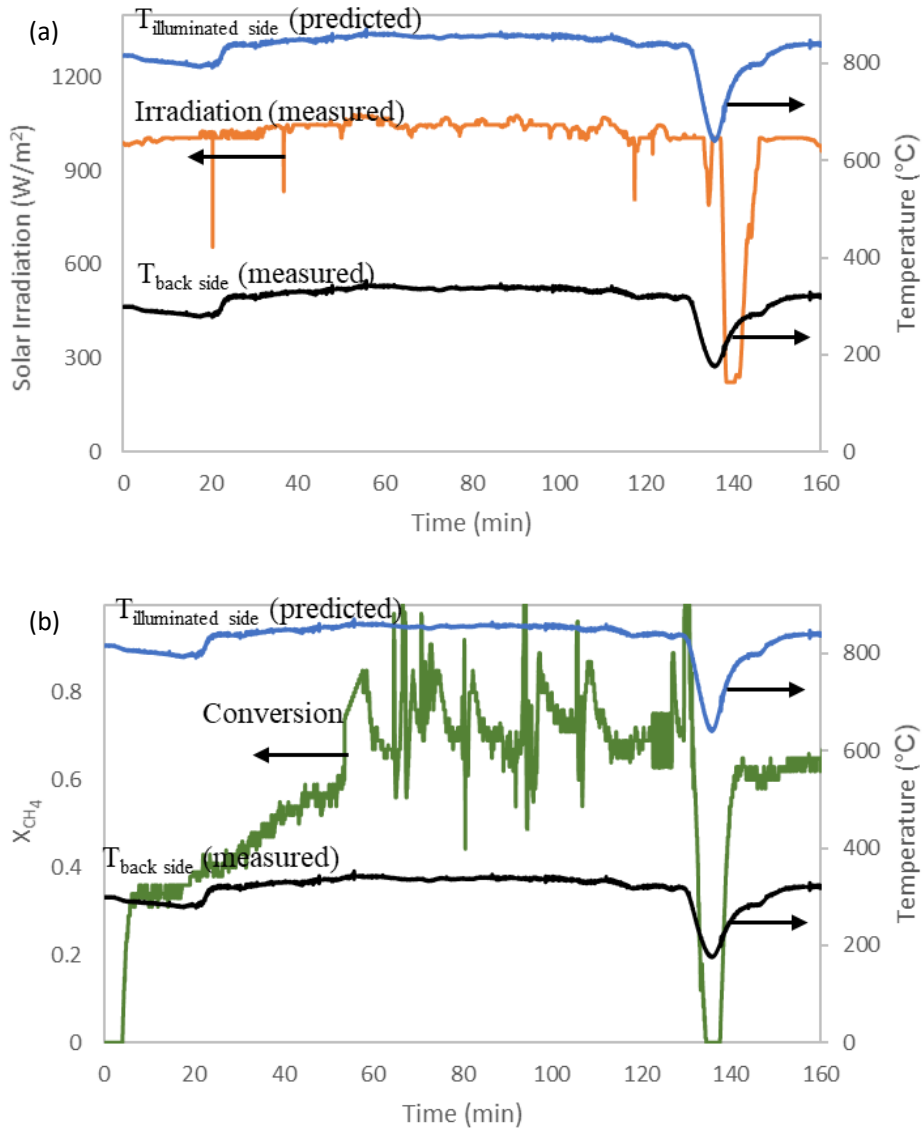


Figure 5.78. Solar irradiation and temperature profiles (a) and methane conversion (b) during solar steam methane reforming catalyzed by 12.8% Ni-mullite (Day 2)

1.0 wt. % Pd/CeO₂/mullite (CeO₂: Mullite 20:80) monolith was also tested in the solar pilot plant. The feeding strategy was the same as Ni coated monolith experiments. Figure 5.79, Figure 5.80 and Figure 5.81 show the profiles of monolith temperature, solar irradiation and methane conversion observed during the pilot plant test performed under solar irradiation. Day 3 (Figure 5.81) has the highest achieved monolith temperatures followed by day 2 (Figure 5.80) and day 1 (Figure 5.79). All three days contained intermittent cloud coverages whereas only day 2 (Figure 5.80) and 3 (Figure 5.81) attained the completion of the experimental procedure. Day 1 (Figure 5.79) had to be stopped early due to complete and consistent cloud presence, eliminating any possibility of the reactions going forward indicating that the solar irradiation directly drives the reaction temperature and eventually the extent of reaction.

Pd catalyst did not show the slow increase in conversion as Ni catalyst, the activity on Pd containing catalyst climbed to its eventual level much more rapidly. The fluctuations in the conversion profiles are attributed to the fluctuations in steam generation.

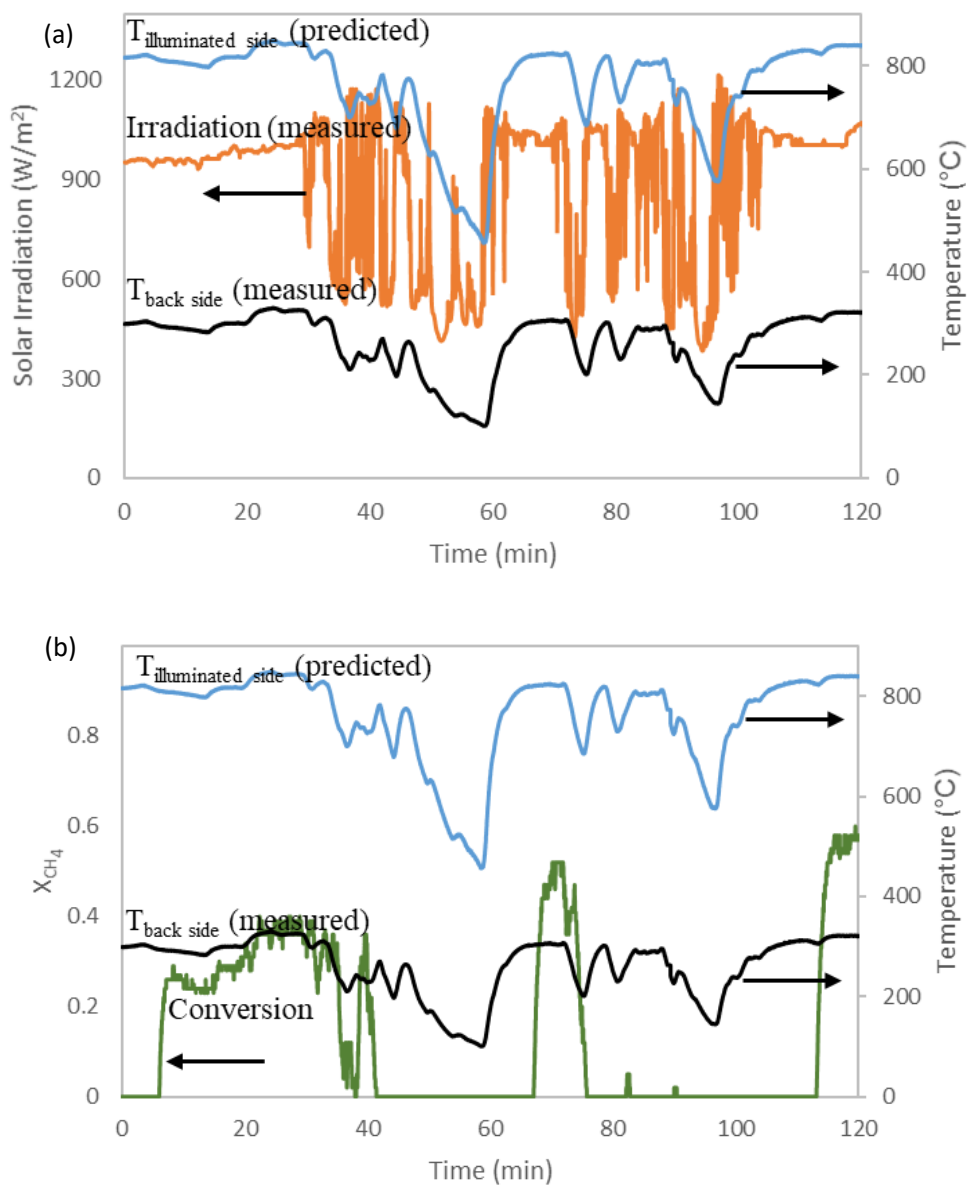


Figure 5.79. Solar irradiation and temperature profiles (a) and methane conversion (b) during solar steam methane reforming catalyzed by 1.0 wt. % Pd/CeO₂/mullite (CeO₂: Mullite 20:80) (Day 1)

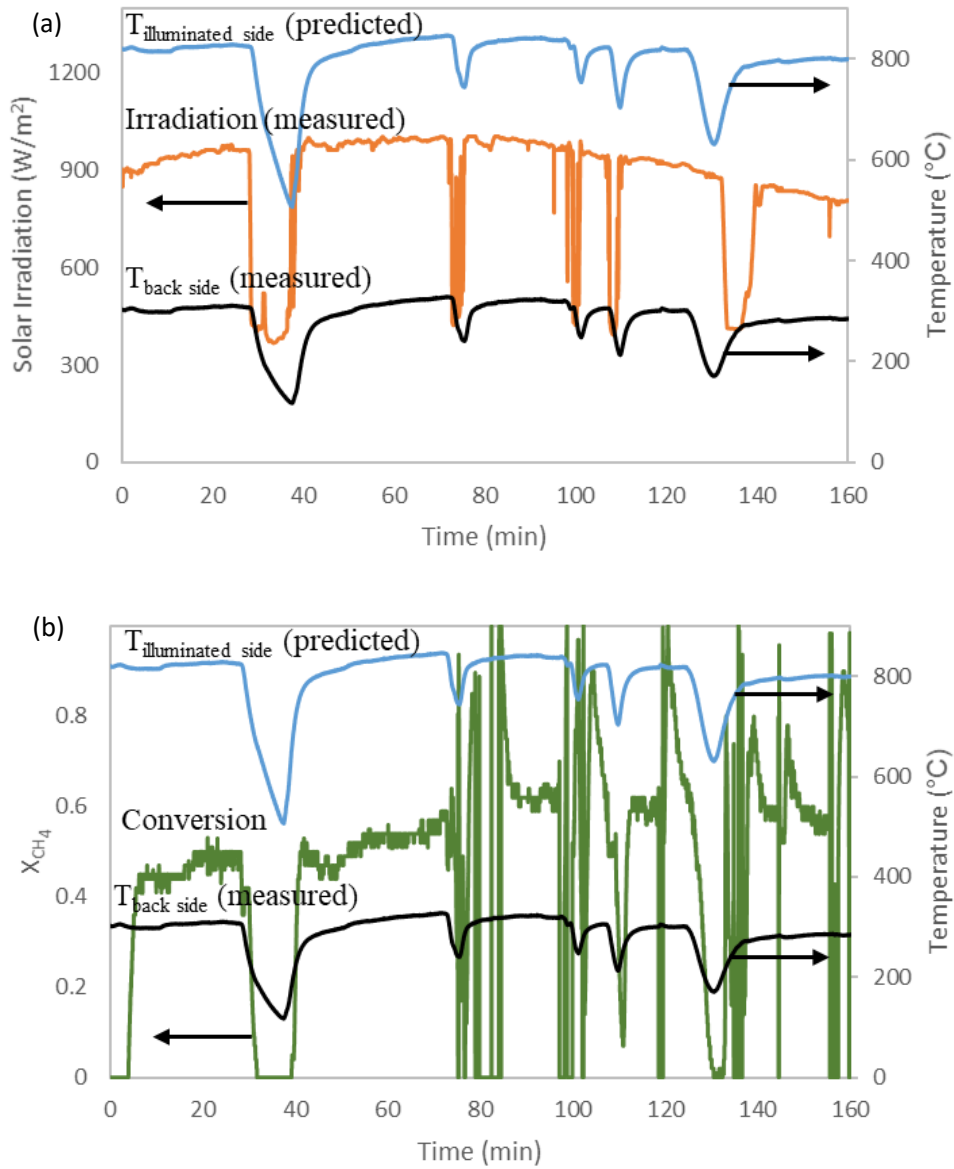


Figure 5.80. Solar irradiation and temperature profiles (a) and methane conversion (b) during solar steam methane reforming catalyzed by 1.0 wt. % Pd/CeO₂/mullite (CeO₂: Mullite 20:80) (Day 2)

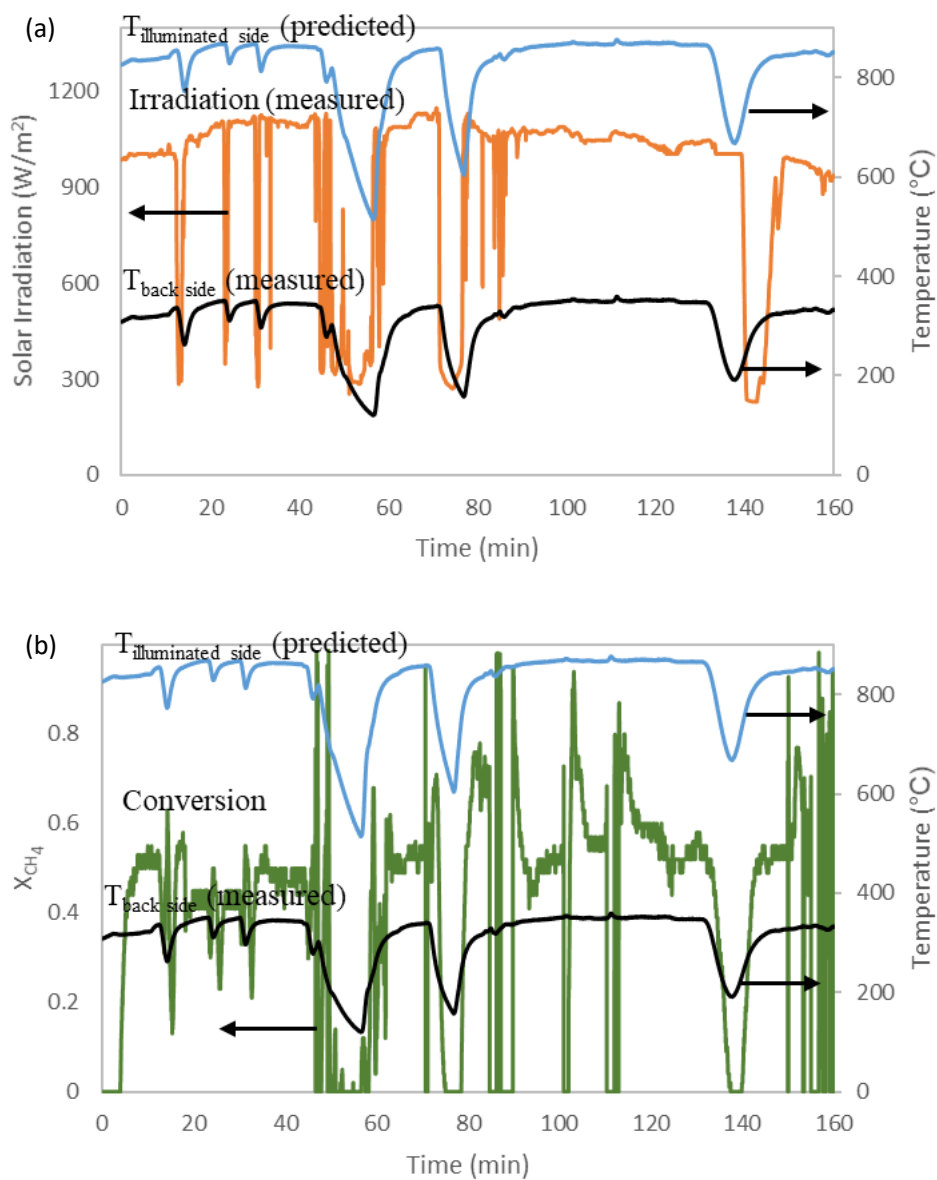


Figure 5.81. Solar irradiation and temperature profiles (a) and methane conversion (b) during solar steam methane reforming catalyzed by 1.0 wt. % Pd/CeO₂/mullite (CeO₂: Mullite 20:80) (Day 3)

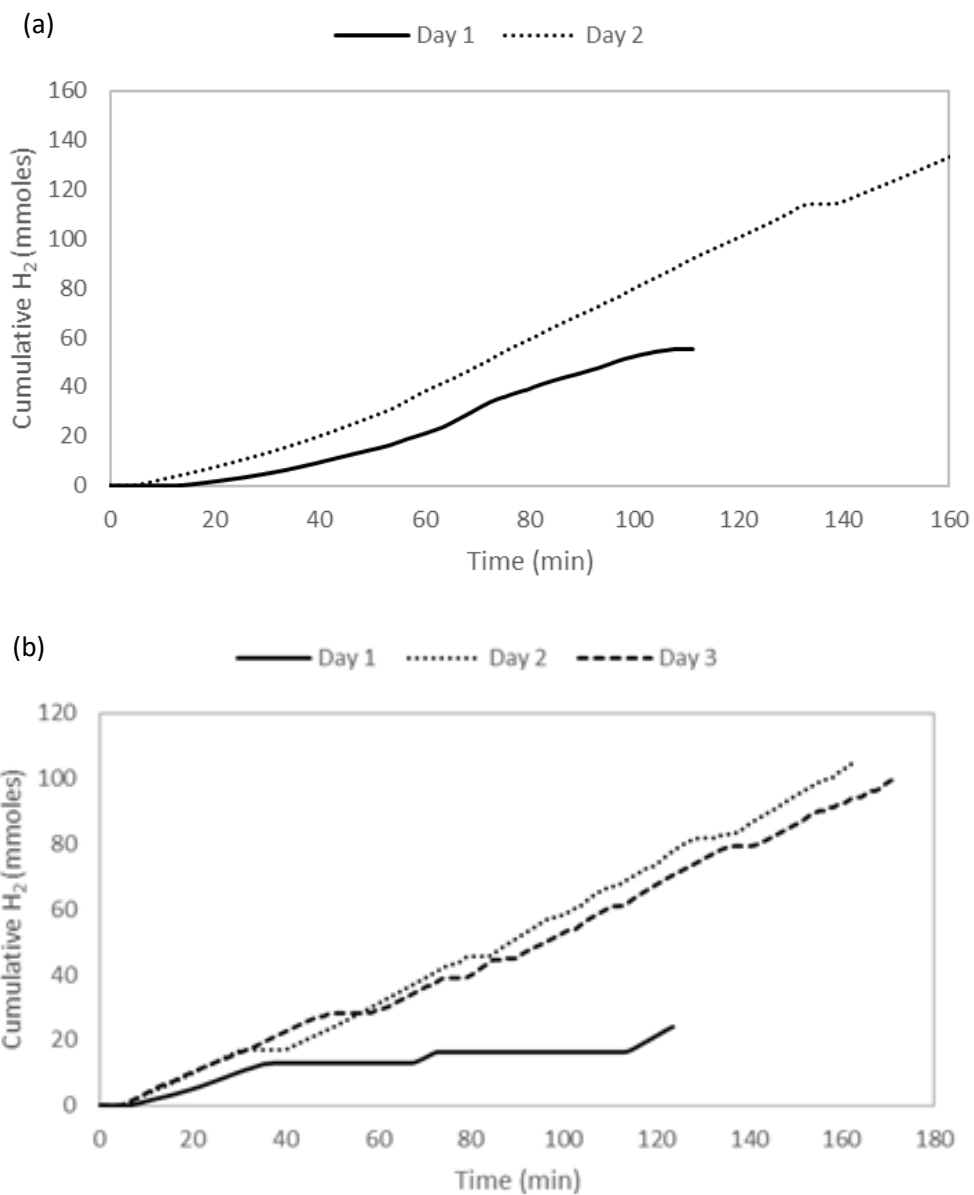


Figure 5.82. Cumulative hydrogen production for (a) 12.8% Ni-mullite and (b) 1.0 wt. % Pd/CeO₂/mullite (CeO₂: Mullite 20:80) during pilot plant tests

The overall quantitative analysis of the hydrogen production amounts was given in Figure 5.82. For the Ni coated monolith, day 1 produces 0.11 mols of H₂ in about 110mins with another 0.28 mols in 165 minutes in day 2. Difference was driven by temperature and the associated lower conversion levels. For the Pd loaded monolith, the first day production was very low – only around 0.05 mols in 125mins due to the failing sunlight. The latter two days were somewhat similar, around 0.20 mols with the final day, producing slightly less than the first day.

After the field tests, the appearances of 12.8% Ni-mullite and 1.0 wt.% Pd/CeO₂/mullite (CeO₂: Mullite 20:80) were shown in Figure 5.83. Coke deposition on the surface of the catalysts (black regions) is apparent at the end of field test. In addition to reforming reaction, both monoliths also facilitate the thermal cracking of CH₄. Visual observations states that the degree of coke deposition was higher for Pd-catalysts. For the Pd loaded monolith, a molten region was also observable indicating that local temperature reached to melting point of mullite, 1700 °C. This is attributed to the catalytic combustion of CH₄ prior to cracking/SMR reactions. In the presence of reducible oxides, such as Pd/CeO₂ possessing lattice oxygen, methane combustion utilizing lattice oxygen is a distinct possibility. Furthermore, dissolved oxygen in the feed water also provides additional medium for direct oxidation. Independent from the source, the trace amounts of residual O₂ in the system can take localized temperatures to very high levels. Considering the water feeding strategy and the nature of the reactor system in this study, there could be a possible runaway reaction of methane oxidation due to the trace amounts of oxygen present in the reactor or the dissolved oxygen in feed water.

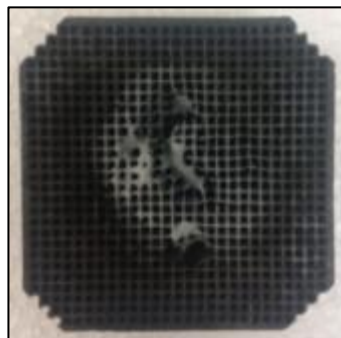
In this experiment, direct response of this drastic change in the temperature of the surface exposed to concentrate solar radiation, could not be monitored by the thermocouple since thermocouple is located in the back of the monolith, 10mm away from the surface. The main reason for the significant difference between the measured vs front face monolith temperatures is caused by the low thermal conductivity (6 W m⁻¹ K⁻¹) of mullite. It was also noted that this melting has

happened in different locations. These likely correspond to the different focal points at the beginning of the experiment each day.



(a) Ni Loaded Monolith

After the second day of reaction



(b) Pd Loaded Monolith

After the third day of reaction

Figure 5.83. Monolith pictures after the continuous SMR experiments performed at pilot scale plant

The amount of coke deposition was analyzed by TGA and SEM/EDS. For the TGA, a channel of the monolith was taken from a black colored region. The TGA curves in oxidizing environment was given in Figure 5.84. Weight gain profile of Ni-catalysts was found similar with the data represented in Figure 5.65. Conducted material balance indicated that 3.5% increase in weight of Ni-mullite representing the oxidation of nickel atoms. TGA also reveals that no significant carbon was deposited on Pd catalysts. The conflict between the visual observations (Figure 5.83) and the TGA results (Figure 5.84) was explained by the inadequate sample selection. It is well known that sample size selection is critical for the demonstration of overall sample. Therefore, surface analysis was conducted for determining the degree of coke deposition. Samples taken from different parts of the 1.0 wt. % Pd/CeO₂/mullite (CeO₂: Mullite 20:80) such as inside the channel, channel edge and molten region were analyzed by SEM/EDS tool. The images were given in Figure 5.85. Performed EDS analysis were presented in Table 5.8. Carbon was not detected in the edges or

inside the channels. On the other hand, SEM analysis performed on the molten region indicates 14 wt.% of carbon.

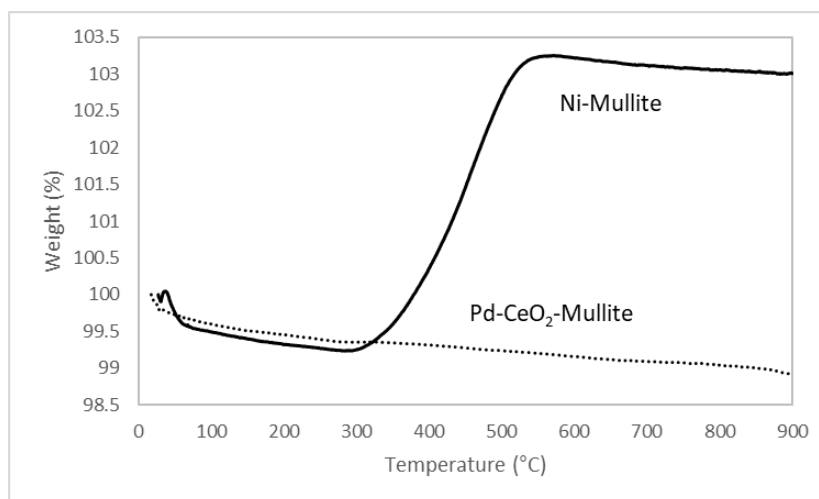


Figure 5.84. TGA curves of 12.8% Ni-mullite and 1.0 wt. % Pd/CeO₂/mullite (CeO₂: Mullite 20:80) after field SMR tests

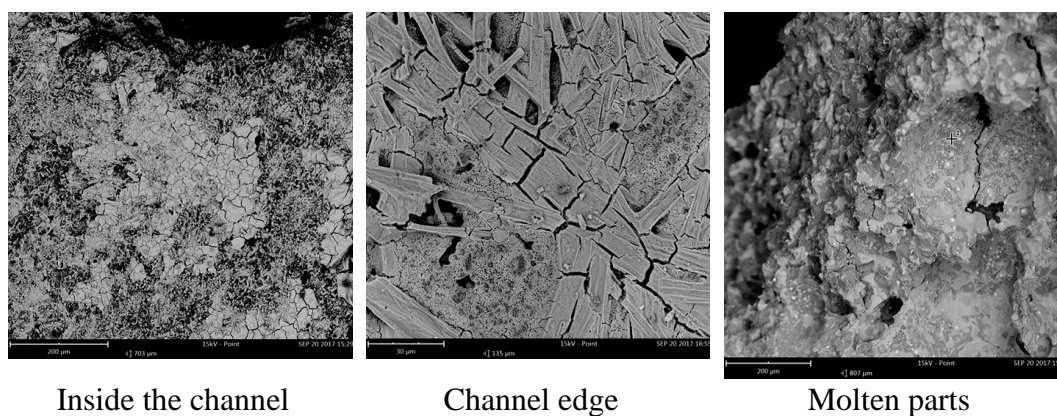


Figure 5.85. SEM images of 1.0 wt. % Pd/CeO₂/mullite (CeO₂: Mullite 20:80) after field SMR tests

Table 5.8 EDS map analysis of 1.0 wt. % Pd/CeO₂/mullite (CeO₂: Mullite 20:80) after field SMR tests

Atoms	Weight Concentration (%)		
	Inside the channel	Channel edge	Molten parts
Ce	73.70	69.80	13.12
O	12.89	17.42	34.26
Pd	7.24	7.38	-
Al	4.46	4.49	31.65
Si	1.70	0.90	6.93
C	-	-	14.04

5.6 Discussions on Solar Integrated Methane Reforming Process

Steam reforming provides a more favorable route, supported by both kinetics and thermodynamics of the overall reaction. Appreciable amounts of hydrogen production by direct water splitting is only possible after 2000 °C. However, hydrogen production by steam reforming, regardless of the catalyst, has favorable equilibrium conversions at much lower temperatures, as shown in Figure 5.86.

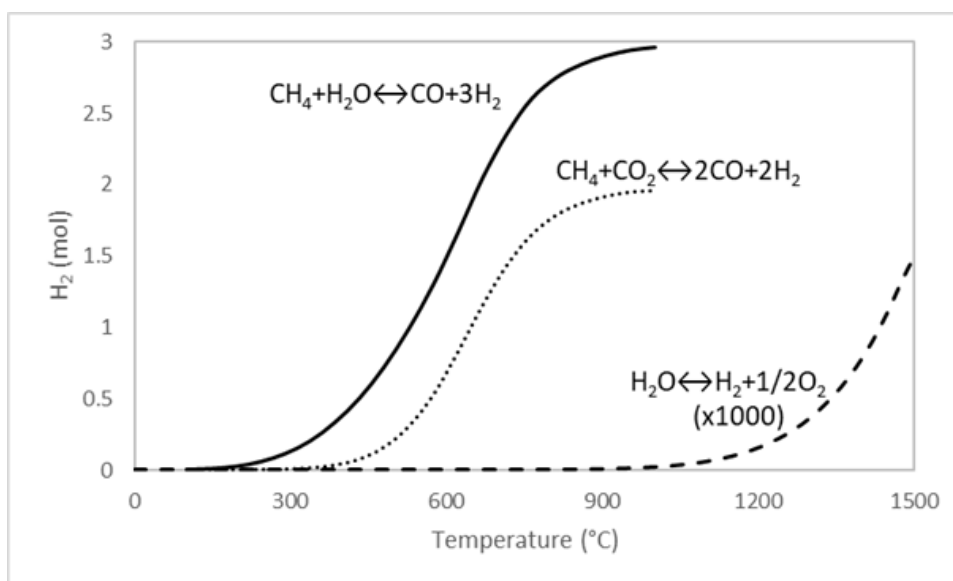


Figure 5.86. Equilibrium hydrogen production for direct water splitting, steam methane reforming and dry reforming of methane

Nickel is generally used during methane reforming process even if there are some demonstrations related to ruthenium, cobalt and group 8 metals. The last metals show high activity in terms of kinetic considerations but they are not preferred in industry due to cost considerations. In addition, all stated metals show relatively good activity to sustain a feasible reforming operation. Therefore, the catalytic activity is not a main factor for the design of such plants. In industrial application, effectiveness factor of catalysts is limited ($\approx 10\%$) with the heat and mass transfer limitations [217]. The observed rates show a rough linearity with the surface area of the catalyst. Therefore, catalysts are coated or doped on structural materials such as cylinder, sphere, monolith, foam [340].

Having conducted the reforming experiments at lab scale, pilot scale demonstration was performed under solar irradiation. Therefore, problems related to sustaining reaction energy was addressed. For this purpose, Ni, and Pd-Ce doped mullite monolith was mainly studied. The reforming reaction was carried out using solar energy in terms of heat. Performed experiments revealed that 70cm OD parabolic dish can sustain reforming reaction around 800 °C on a sunny day. Nevertheless,

reaction temperature could not be controlled due to the intermittent nature of the solar energy. Therefore, minimum 500 °C was measured on a typical day with clouds indicating a decrease around 300 °C from desired operational temperature. Such a loss is undesired for the commercialization of solar reformers.

CHAPTER 6

OPTIMIZATION

6.1 Process Simulations for Solar Energy Integration to SMR Process

6.1.1 Base Simulations for SMR and ATR Process

Autothermal reforming (ATR) is an alternative hydrogen production method which supplies the required energy by partial combustion reaction. The products of combustion as CO_2 and H_2O were internally used for methane reforming. Unlike SMR process, dry (CO_2) and steam (H_2O) methane reforming reactions are performed simultaneously in ATR process.

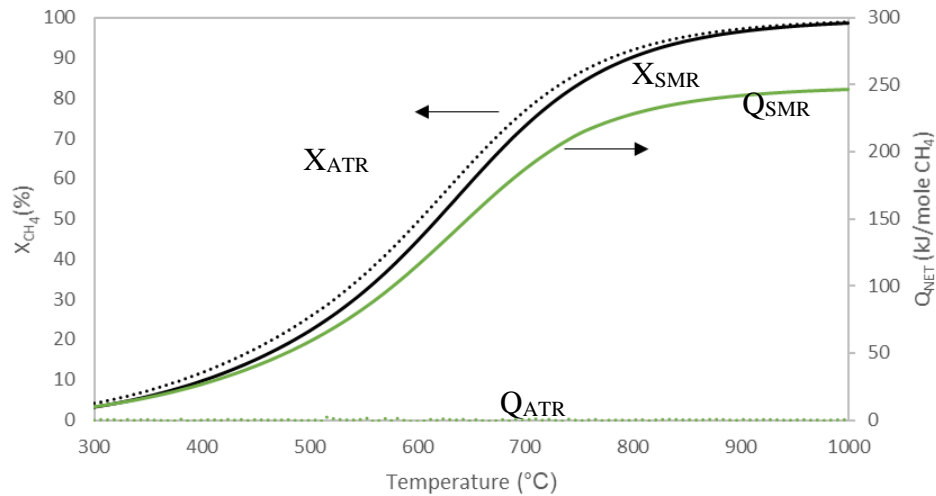


Figure 6.1. Performance of SMR and ATR processes in terms of CH_4 conversion and overall energy requirement

The conversion of methane with respect to temperature for SMR and ATR processes was given in Figure 6.1. The overall conversion reaches to 95% around 900 °C for both processes. The methane conversion in ATR is slightly higher than that of SMR

due to the additional CH₄ consumption in the combustor. Heat flow profiles of SMR and ATR processes were also demonstrated in Figure 6.1. Self-sustaining operation of ATR results with a net zero energy demand ($Q_{ATR}=0$). However, SMR process needs 240kJ/mol CH₄ to reach 95% methane conversion at 900 °C for the studied block diagram (Figure 3.16).

In conventional systems, the energy requirement of SMR reaction is supplied by methane combustion in the tubular reforming reactors [341]. In these reformers, the hot flue stream coming from methane and air combustion heats the reformer tubes from outside for sustaining reaction at a certain level. Therefore, the SMR simulation was improved by additional methane combustion to keep reformer at isothermal conditions. In this modified configuration, the performances of SMR and ATR were compared in terms of CH₄ fed and CO₂ emissions for 1 mol H₂ production (Figure 6.2). The consumption of methane per mol H₂ production was found to be slightly lower for SMR case. The methane requirement does not change significantly after 800 °C for both cases. In terms of CO₂ emissions, the ATR offers a significant advantage over SMR due to the dry reforming capability of ATR. The CO₂ emissions for SMR and ATR processes are found as 97 mmol and 3.8 mmol CO₂ per mol H₂ produced at 900 °C. The gap is considerable in terms of environmental regulations.

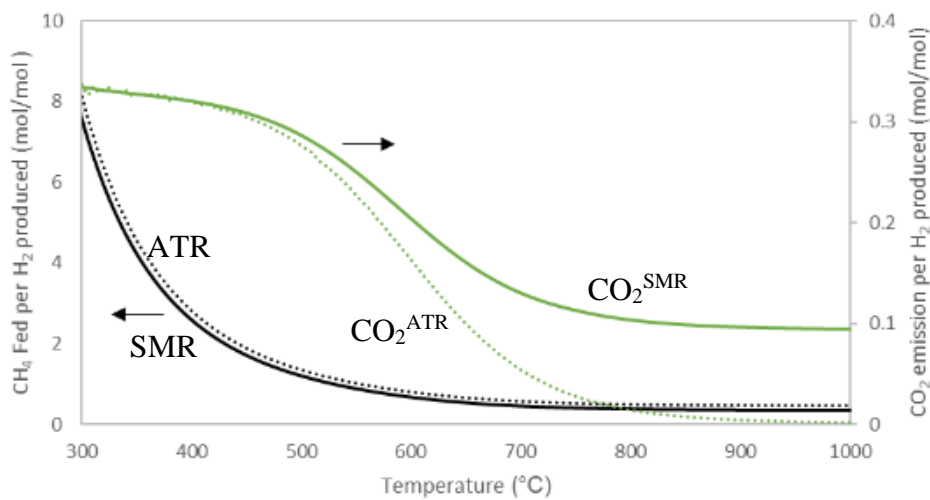
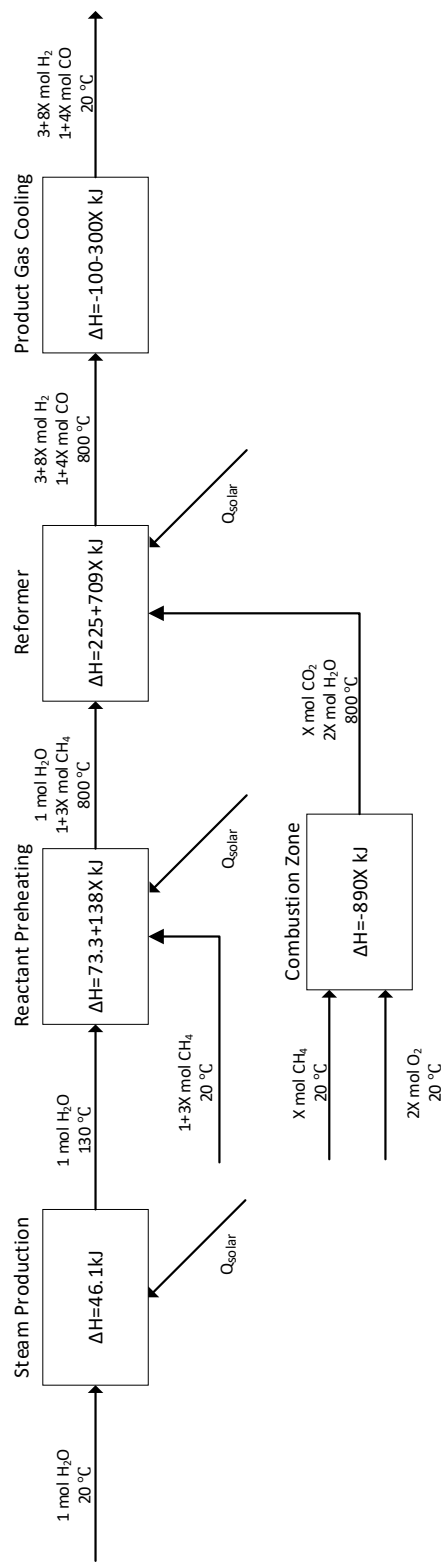


Figure 6.2. Methane requirement and CO₂ emission of SMR and ATR processes based on 1 mol H₂ production

6.1.2 Hybrid Solar-ATR Process Simulations

Solar energy can be embedded to methane reforming process in terms of heat. The heat demand of endothermic operations is met with the solar irradiation. In ideal case, Q1, Q2, and Q3 can be replaced by Q_{solar} during the solar energy integration to steam reforming (Figure 3.16 and Figure 3.17). Q4 can be used as additional energy production or can be utilized by heat exchanger networks. However, 100% integration of solar energy to steam methane reforming would result with unsteady state operations due to the intermittent nature of solar energy. In addition, process will be shut down during the night operations or during seasonal changes. In order to overcome this challenge, the operation of ATR process was modified. For a sunny day operation, assuming the presence of enough solar energy to run the reforming reaction (Q_{rxn}), energy demand of SMR was sustained from Q_{solar} which is distributed to Q1, Q2 and Q3. Therefore, combustor would not be in operation mode. For a cloudy day or seasonal change when solar irradiation reduces significantly ($Q_{rxn} > Q_{solar}$), the combustor will be operated in such a way that the energy gap due to the solar energy loss will be covered by the methane combustion. For the final case, night operation ($Q_{rxn} > Q_{solar} = 0$), the overall process will behave like conventional ATR. The overall material and energy balance of the system was given in Figure 6.3.



$$\Delta H_{\text{overall}} = Q_{\text{solar}} + 343X - 247 \text{ (kJ)}$$

$$2.2 \ll \text{Hydrogen Yield} \ll 3$$

Figure 6.3. Overall material and energy balance of the modified ATR system

The effect of solar energy integration to reforming process was analyzed by increasing solar energy ratio with respect to overall process energy demand. Simulations were carried out between 800-1000 °C in order to be consistent with the conventional reformers. Solar energy contribution was found by dividing different solar irradiations to energy demand of SMR process (Figure 6.1). Therefore, when the solar energy contribution is equal to zero, process behaves as ATR while $Q_{\text{solar}}/Q_{\text{process}}=100\%$ indicates the SMR is in the operation. The second case differs from the analysis mentioned in Figure 6.2 in such a way that the energy needed for the process is supplied from Q_{solar} not from combustion of methane. The amount of CH_4 in the feed stream (Figure 6.4) decreases about 28% for all reformer temperatures when solar contribution is changing from 0 to 100%. CO_2 emissions were calculated as 13.7, 3.7 and 1.2 mmol $\text{CO}_2/\text{mol H}_2$ at temperatures 800 °C, 900 °C and 1000 °C respectively when $Q_{\text{solar}}/Q_{\text{process}}$ is equal to 0. With the contribution of solar energy ($Q_{\text{solar}}/Q_{\text{process}}=100\%$), CO_2 emissions decreased to 9.4. These values are decreased to 9.4, 2.5, 0.8 mmol $\text{CO}_2/\text{mol H}_2$ at temperatures 800 °C, 900 °C and 1000 °C respectively. High CH_4 consumption and CO_2 emissions was observed during the reforming operation at 800 °C due to the low conversion governed by operating conditions.

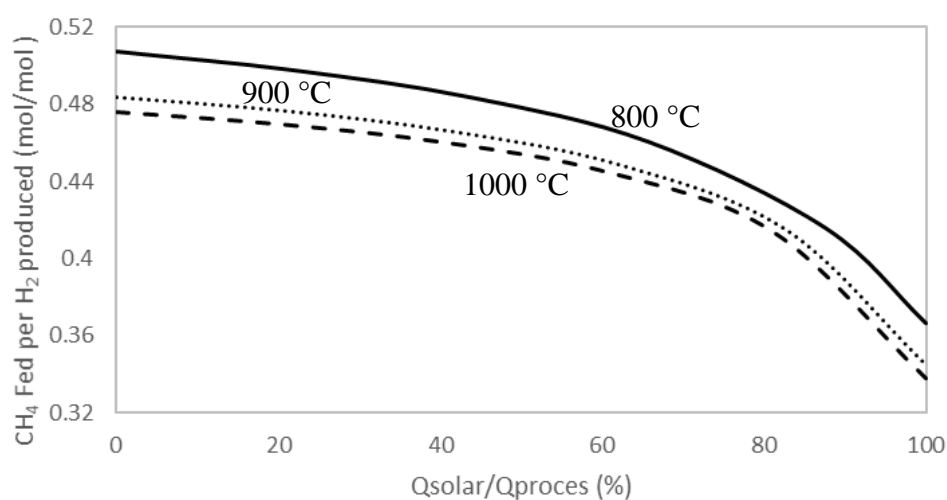


Figure 6.4. CH_4 requirement for producing 1 mol of H_2 under different solar energy contributions

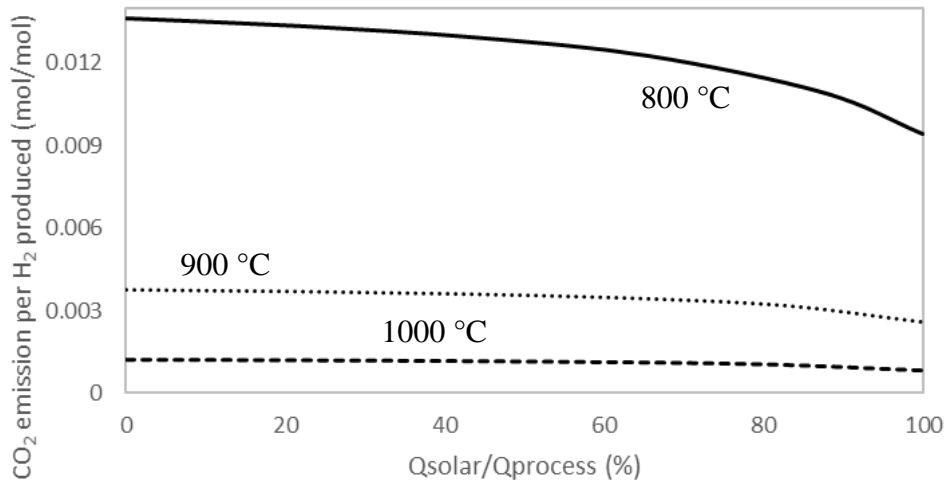


Figure 6.5. CO₂ emission based on 1 mol of H₂ under different solar energy contributions

6.1.3 Application of Hybrid Reforming Process to Real Case Example

Following the theoretical simulations mentioned above, the performance of solar energy integration was investigated for real case examples. The answer behind the question of “What would be the result if the experiments were carried out by using hybrid process?” were sought. Temperature profiles and conversions obtained during Ni-Mullite (Day 2) and Pd/CeO₂/mullite (Day 3) were taken as inputs for simulations [279]. Reforming operation was assumed to be performed at 900 °C. The CH₄ feed was taken as 8sccm in order to be consistent with experiments conditions. Excess water condition was not taken into the consideration and the H₂O to CH₄ ratio was assumed as 1 for the simplification purpose. In addition, the all incapacibilities of pilot plant were ignored.

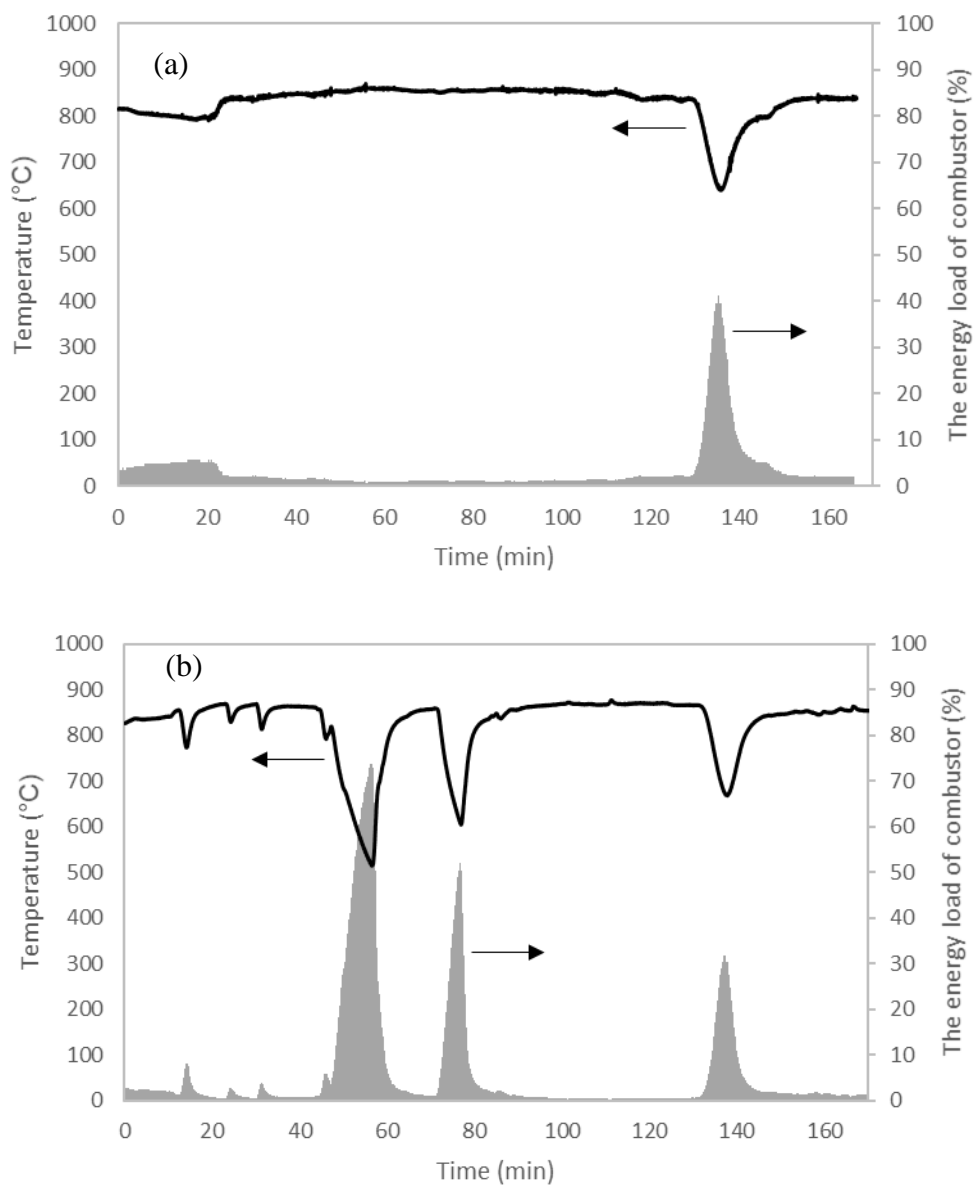


Figure 6.6. The heat load of combustor in hybrid reforming process during solar embed methane reforming process (Ni-mullite-Day 2 (a) and Pd/CeO₂/mullite-Day 3 (b))

The intermittent nature of solar energy is the main challenge for solar based applications. This fact gains more importance for methane reforming process mainly due to the high endothermicity of the reactions and thermodynamic favorability of coke formation at lower temperatures. The experiments performed under pilot plant test conditions revealed that solar irradiation has a direct effect on the reactor temperature, which in turn influences the product gas compositions [279]. The suggested hybrid reforming system offers a solution for recovering non-controllable energy loss coming from the sun. The load of combustor is defined as the ratio energy supplied by combustor to overall energy requirement of hybrid process to run reforming operations. The contribution of combustor during the sudden solar irradiation losses was given in Figure 6.6. Combustor supplied energy to hybrid process in order to keep reformer temperature at 900 °C since maximum recorded temperature was 875 °C during the stated experiments. For the Ni-mullite temperature profile, the combustor introduced 40% of the overall energy demand of the process due to solar irradiation loss around 130min. The load combustor was varied from 1% to 73% due to the cloudy conditions of Pd/CeO₂/mullite scenario.

The share of solar energy on the equilibrium methane conversion was shown in Figure 6.7. Minimum conversions were calculated as 54% and 24% from the temperature profiles of Ni-mullite and Pd/CeO₂/mullite respectively. These conversions were increased to 97% (the equilibrium conversion at 900 °C under the studied conditions) by the incoming energy from combustor. Therefore, the shares of the heat sources (Solar: Combustor) became 59:41 and 27:73 for the worst-case scenario. Energy consumption and the methane conversions follow similar trends due to the energy demanding behavior of reforming reaction.

The amount of consumed methane per one mol hydrogen production was given in Figure 6.8. Methane consumption was found to be in the range of 0-100% for $Q_{\text{solar}}/Q_{\text{process}}$. In the studied time domain, methane was steadily consumed in order to keep reformer temperature at 900 °C (maximum recorded temperature was 875 °C in the experiment). During the loss of solar irradiation, combustor was activated, and the methane consumption increased gradually.

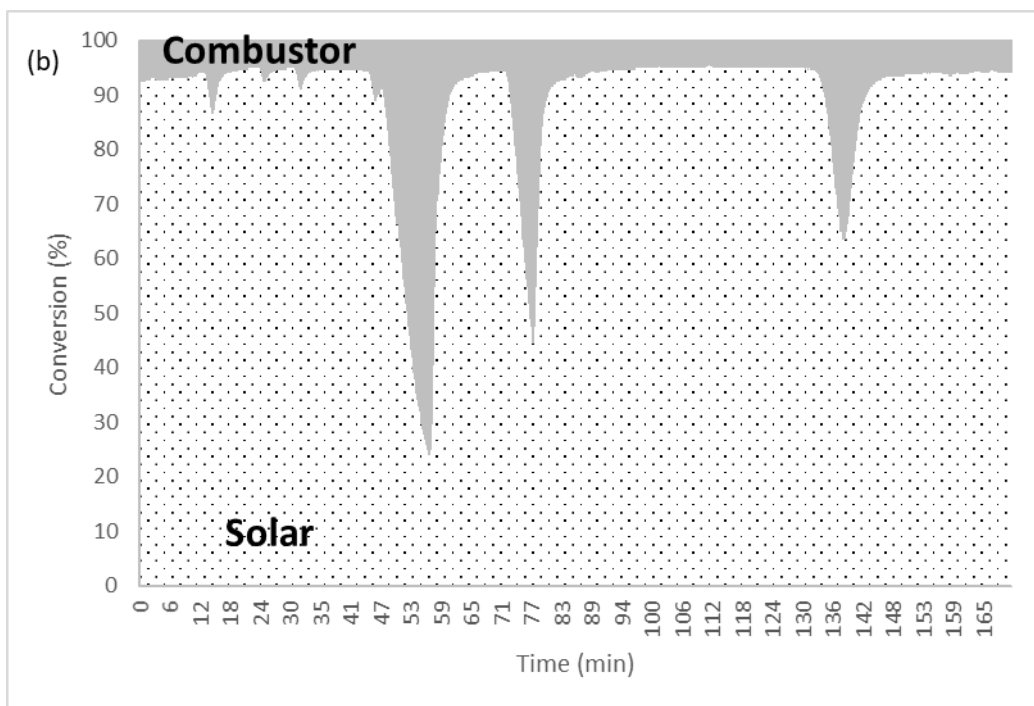
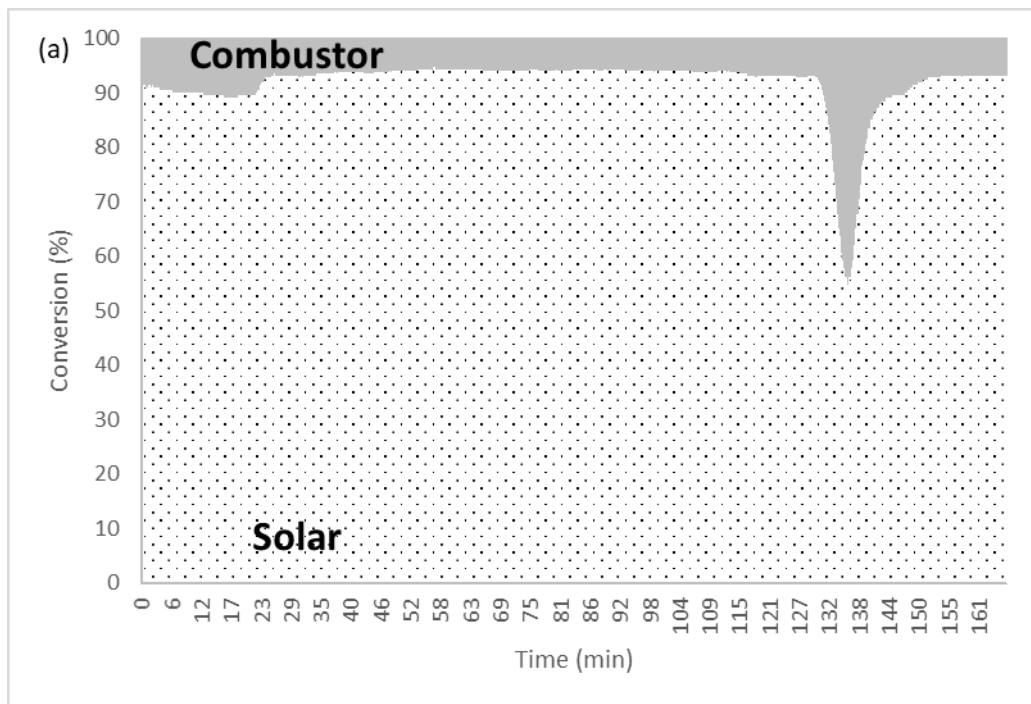


Figure 6.7. The solar energy contribution to methane conversion during solar embed methane reforming process (Ni-mullite-Day 2 (a) and Pd/CeO₂/mullite-Day 3 (b))

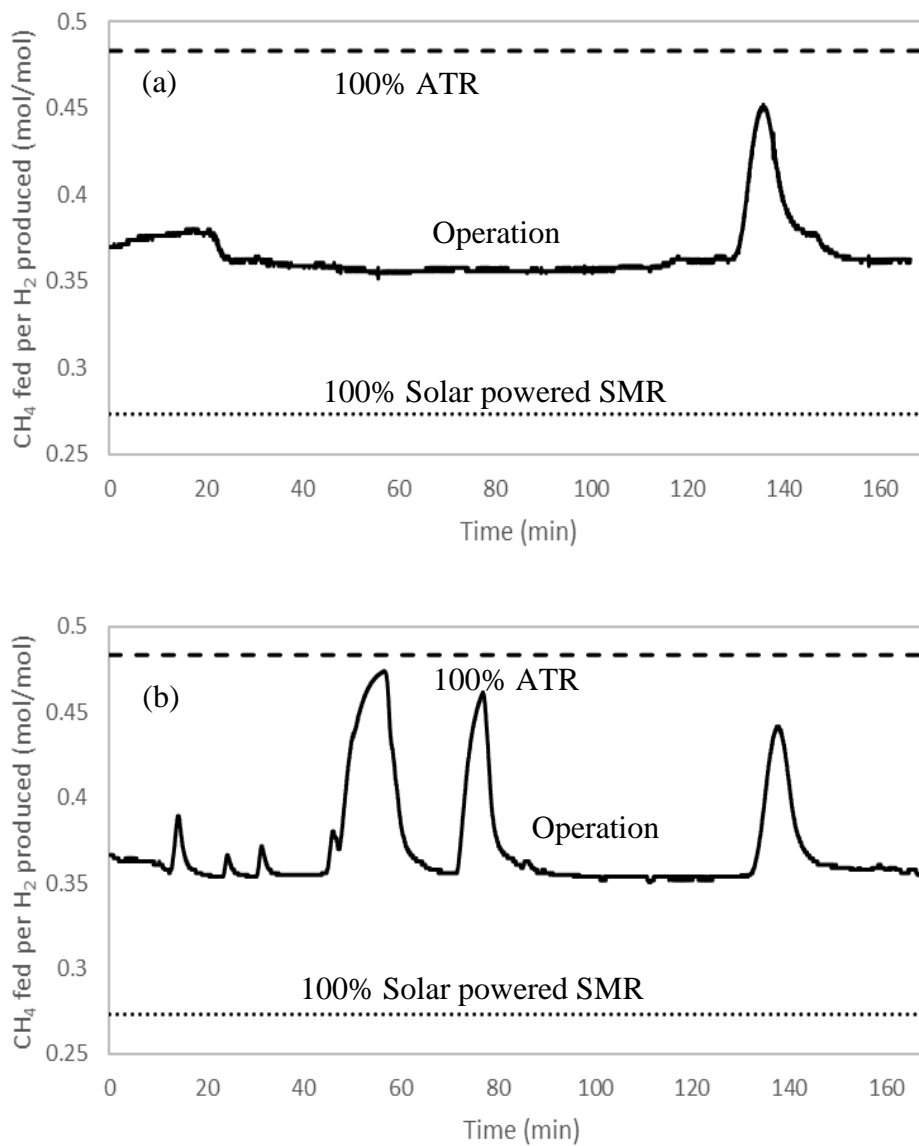


Figure 6.8. The CH₄ consumption for producing 1 mol H₂ during solar embed methane reforming process (Ni-mullite-Day 2 (a) and Pd/CeO₂/mullite-Day 3 (b))

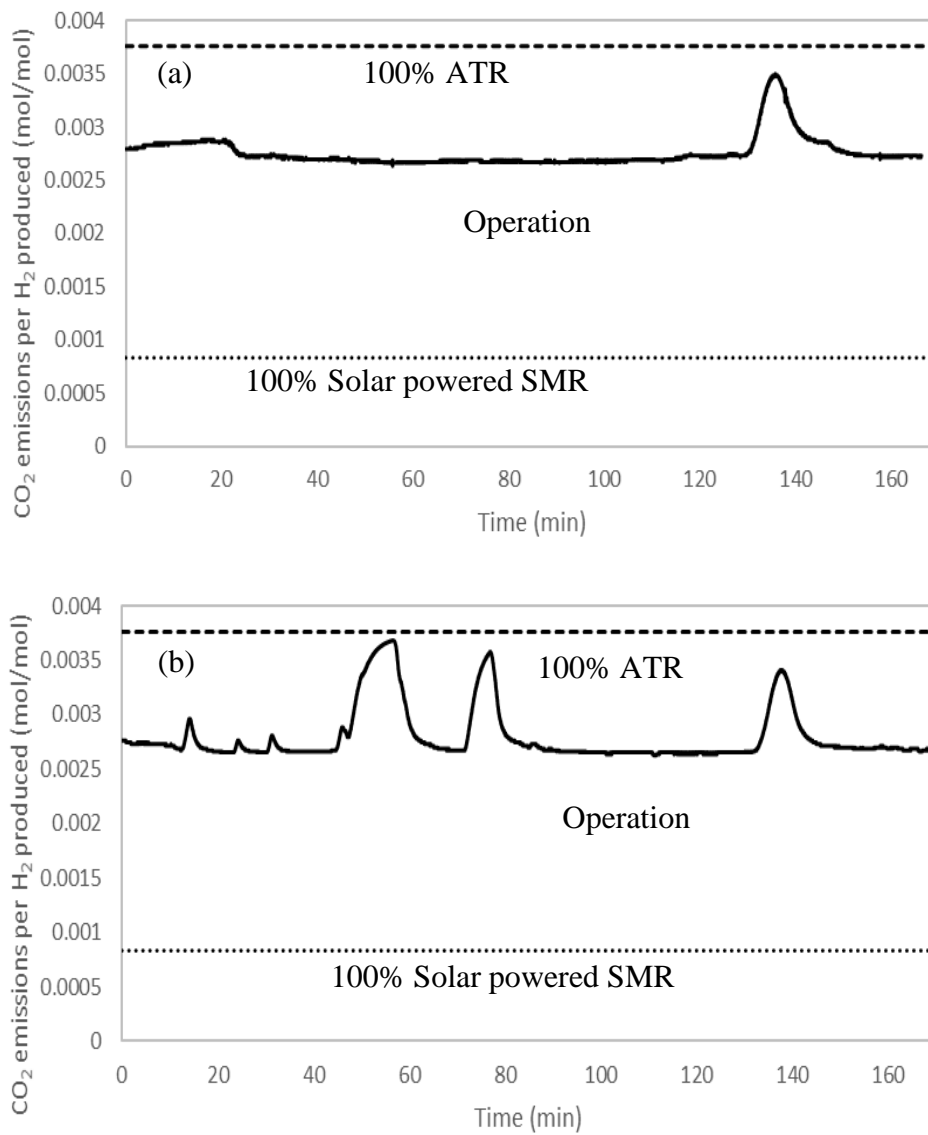


Figure 6.9. The CO₂ emissions for producing 1 mol H₂ during solar embed methane reforming process (Ni-mullite-Day 2 (a) and Pd/CeO₂/mullite-Day 3 (b))

The enhancement of CO₂ emissions was shown in Figure 6.9. Integration of solar energy to reforming process, CO₂ emissions were always lower than the $Q_{\text{solar}}/Q_{\text{process}}=0$ (ATR operation) case. The theoretical emission is also much lower than the conventional SMR operation (Figure 6.2).

Experimental H₂ production [279] were compared with the cases ATR ($Q_{\text{solar}}/Q_{\text{process}}=0$) and for hybrid system (solar embed methane reforming) in Figure 6.10. The predicted production profile for $Q_{\text{solar}}/Q_{\text{process}}=100\%$ was found to be very close to hybrid system. This is due to the yield difference between steam methane reforming ($Q_{\text{solar}}/Q_{\text{process}}=100\%$, H₂/CH₄=3) and dry reforming of methane (DRM, H₂/CH₄=2) reactions. In hybrid system, the solar irradiation losses were compensated with the energy coming from the combustor. The CO₂ in the effluent stream was used during the dry reforming of methane so produces 2 mol of hydrogen was produced. On the other hand, 3 mols of hydrogen were produced when all reaction energy was sustained from the solar energy. Even though the loss of reaction rate during radiational losses were recovered by the hydrogen yield theoretically, the catalytical properties are lost in an irreversible way in real case due the favorability of coke formation at low temperatures. Hydrogen production profiles of Ni-mullite (Day 2) and Pd/CeO₂/mullite (Day 3)) were found to be very similar to predicted profiles of $Q_{\text{solar}}/Q_{\text{process}}=100\%$ and $Q_{\text{solar}}/Q_{\text{process}}=0\%$ cases.

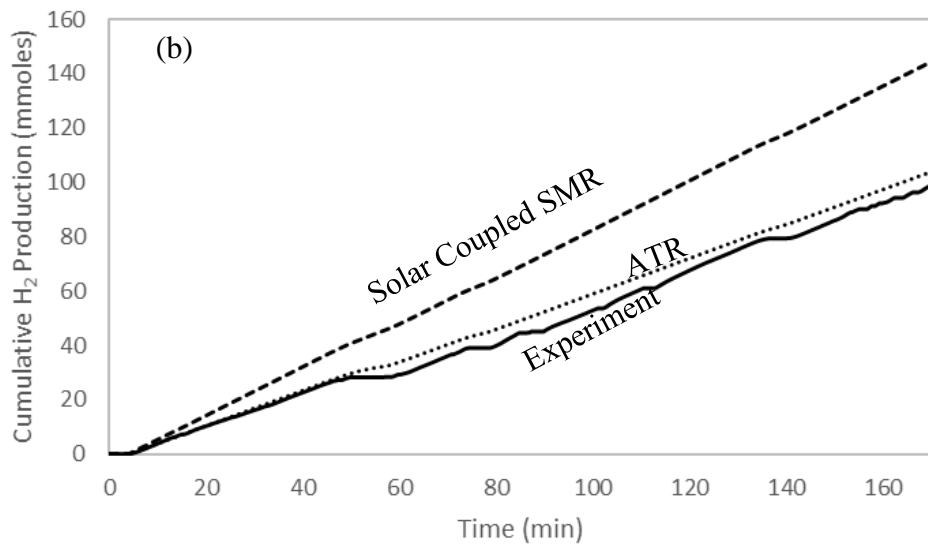
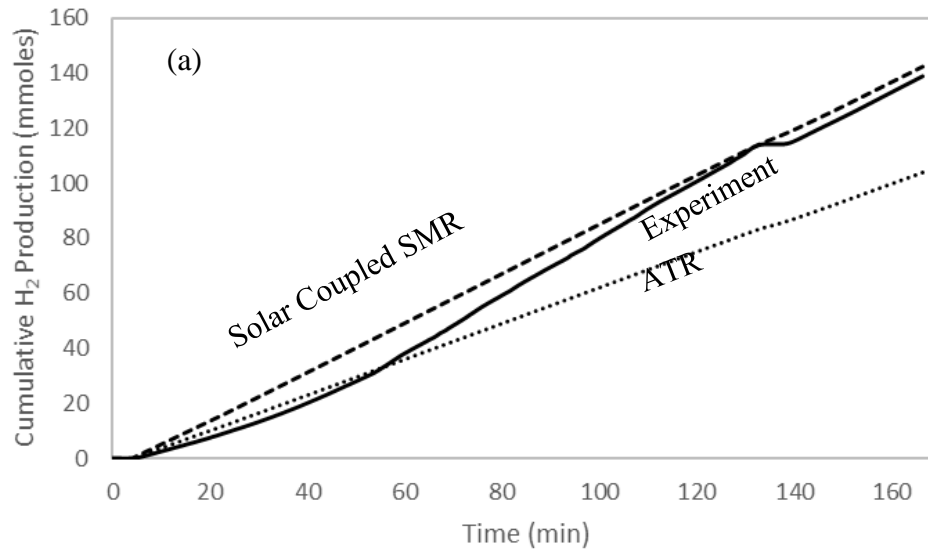


Figure 6.10. The cumulative H₂ production during solar embed methane reforming process (Ni-mullite-Day 2 (a) and Pd/CeO₂/mullite-Day 3 (b))

6.2 The Design of Sustainable Hydrogen Production Plant

In the scope of this thesis, a sustainable route for hydrogen production was addressed in the perspective of thermochemical and reforming processes. With the outcomes of the theoretical and experimental studies, sustainability in hydrogen production was created offering a unique hybrid process. This process aimed to integrate solar energy to reforming technology. In this area, several demonstrations were completed in terms of solar reformers [209,211,215,249,250]. With the focus on intermittent nature of solar energy, the developed process mainly solves the problems related to heat transfer. Solar energy is highly dependent on atmospheric events, seasonal changes, geographic position, and day-night transition. These events change the incoming solar irradiation causing a drawback towards solar energy utilization. Reforming process and thermochemical processes are heat driven processes. Therefore, heat flux should be kept in a certain level in order to sustain the reaction rate in a certain level. Conducted pilot plant experiments revealed that even if it is a summer time where solar energy utilization have a maxima, clouds prevents the incoming solar irradiation so that control over the reactor can be lost. The effect of energy loss towards heat driven reactions such as reforming is solved by integration of a combustion zone into the solar reformer. The process flow diagram describing the reforming section was described in Figure 6.3. Considering the block diagram, 1 mol methane can be converted to 3mols of hydrogen with an energy input (around 245kJ) from solar energy (energy requirement needed for oxygen separation from air was ignored during this calculation). The proposed process operates like autothermal process under certain situations such as night operations. Under this circumstance, the required energy is supplied from combusting some of the feed methane with oxygen. 2.2 mols of hydrogen can be produced from 1 mol of methane. Those two edges were considered as the limits of the operations. The hydrogen yield (hydrogen produced per methane consumed) was calculated by considering solar energy contribution to proposed block diagram as given in Figure 6.11. The products of methane combustion (CO_2 and H_2O) contributes to dry reforming as well as steam

reforming. Therefore, hydrogen yield increases with respect to the ratio of solar energy in the total energy requirement.

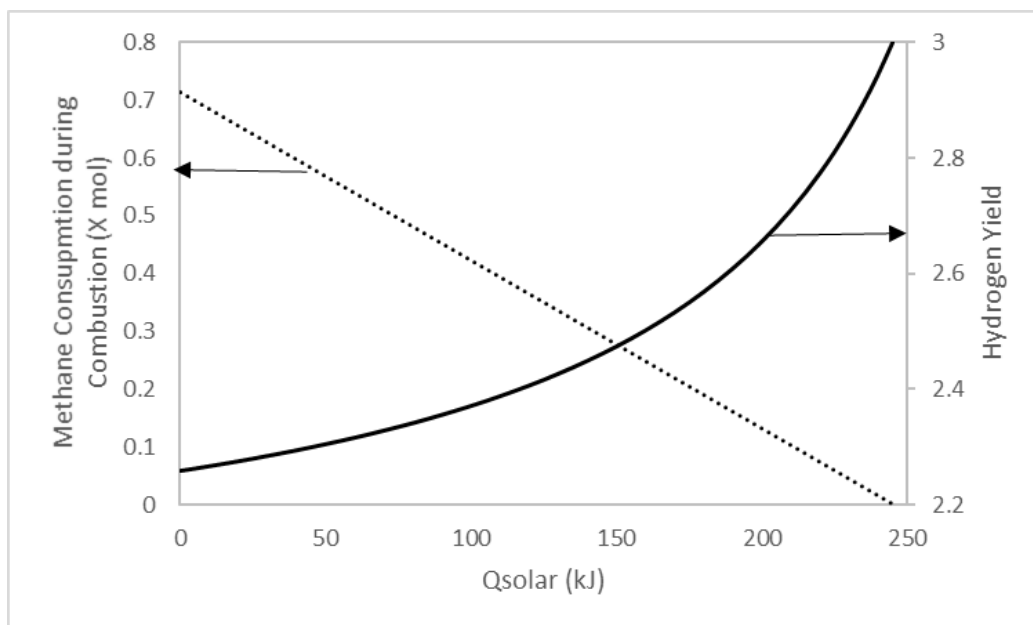


Figure 6.11. The effect of solar energy contribution on hydrogen yield

The proposed block diagram has an additional advantage in terms of compensation of intermittence of solar energy. This is done by activating the methane combustion during changes in the solar irradiation. The control parameter, the reactor temperature, is kept at a certain level by manipulating the methane/oxygen feed to the combustion zone. The solar irradiation is measured as disturbance to the system. The overall process is controlled by specialized algorithm. The artificial intelligence will be integrated to the algorithm so that proactive steps will be taken in order to minimize the effect of disturbances to the system. The algorithm mainly measures the reactor temperature profile and calculates the online energy demand as given in Figure 6.12. The output of this algorithm will set the energy capacity and the frequency of the combustion zone. Therefore, this algorithm will maximize the utilization of solar energy into hydrogen production no matter where the plant location is and no matter what the time is.

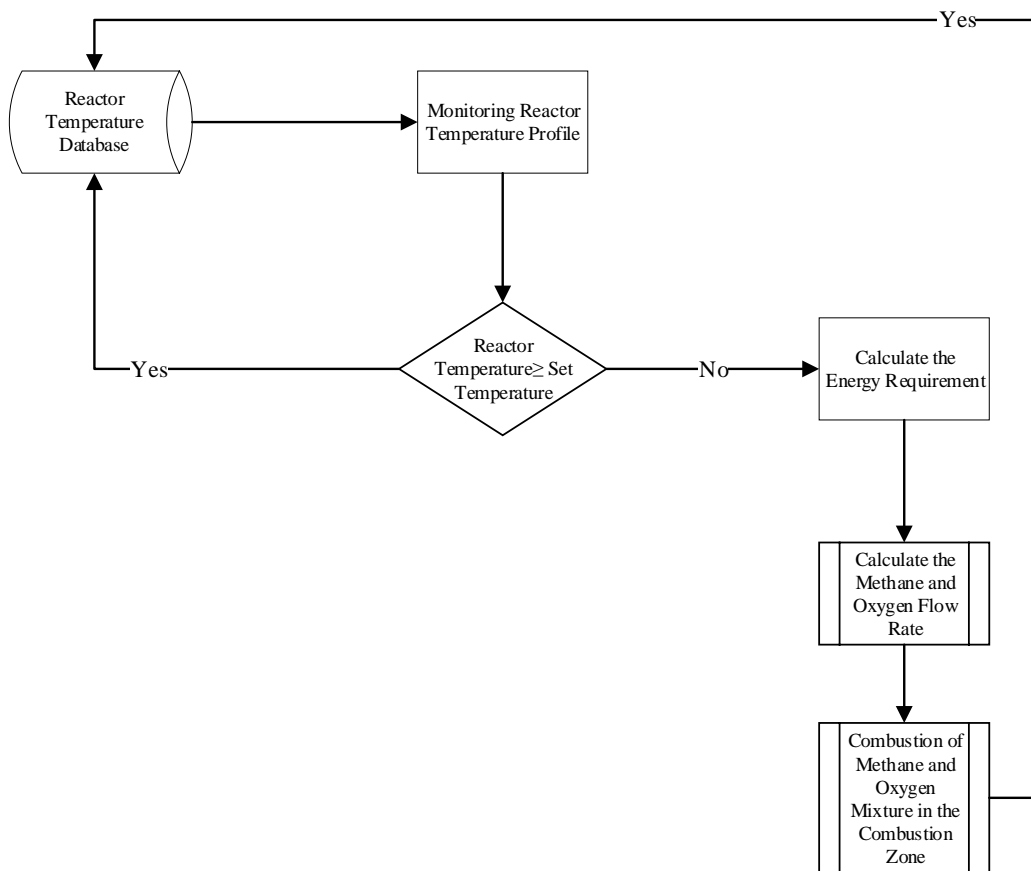


Figure 6.12. Main control algorithm for reactor temperature control

The oxygen requirement of combustion zone will be sustained from solar integrated oxygen plant. This plant uses reducible oxides for separation of oxygen from air. The working principle of thermochemical cycles and performances of some reducible oxides were given in the previous sections. In the proposed production plant, concentrated oxygen coming from looping reactors is pressurized, and stored in pressurized tanks. Oxygen plant will be operated depending on the solar irradiation and the pressure of oxygen storage tanks as given in Figure 6.13.

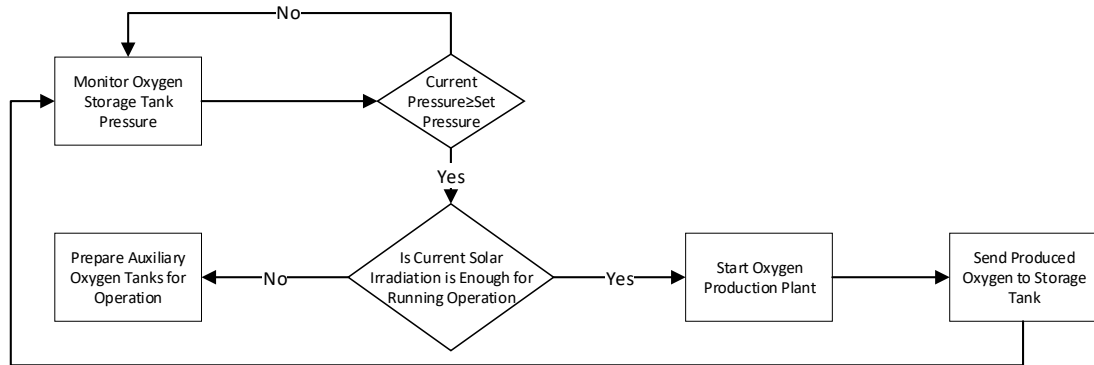


Figure 6.13. Main control algorithm for oxygen plant start-up

The steam requirement of reformer is produced from solar integrated steam generation plant. Plant design should satisfy the steam requirement on a sunny day alone. During intermittence, conventional boiler starts to operate to keep steam quality on a certain level as shown in Figure 6.14. Steam pressure will be sustained at operational levels by adjusting the load water pumps.

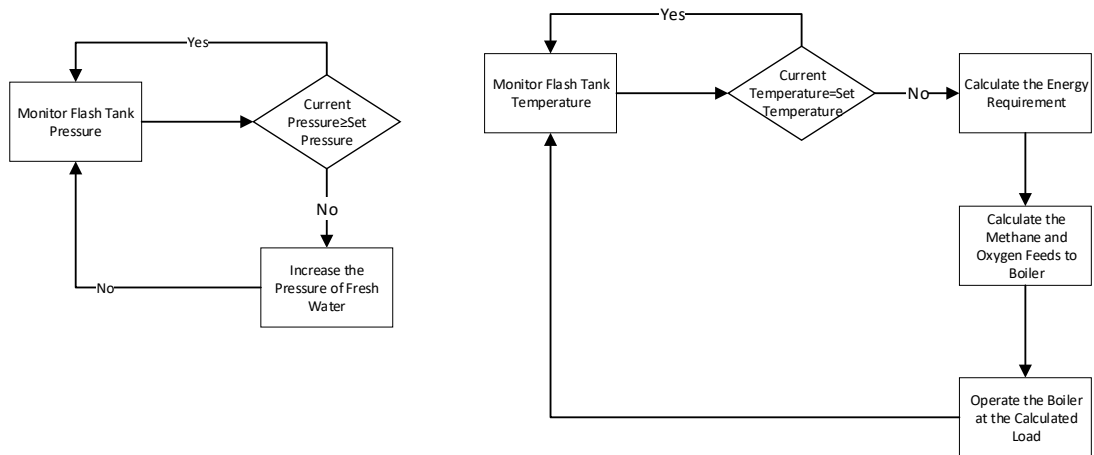


Figure 6.14. Main control algorithm for steam production plant

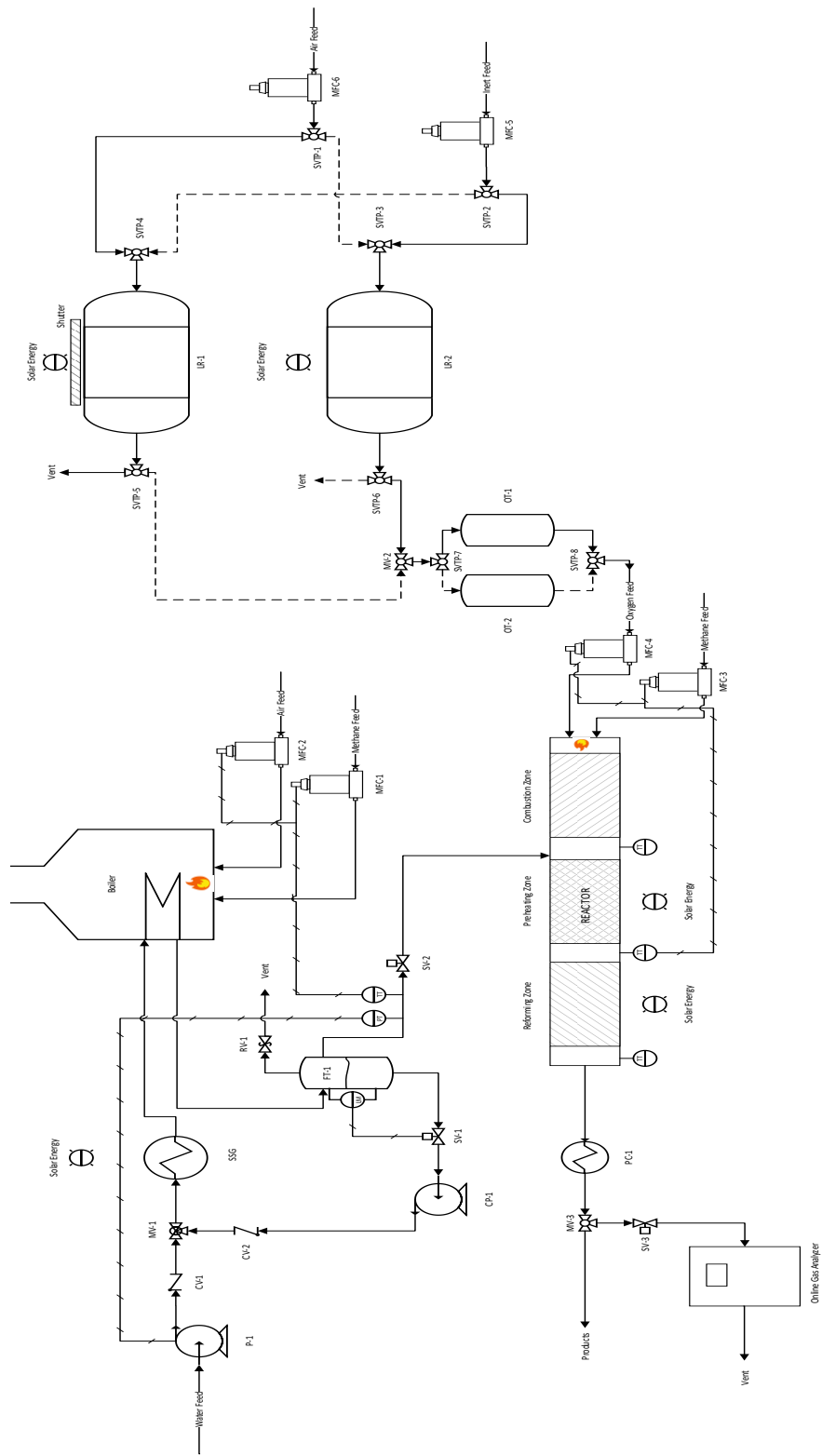


Figure 6.15. Process flow diagram for the solar integrated hybrid methane reformer

Having evaluated the benefits of solar integration to reforming technology and the solutions for the drawbacks of intermittent nature of solar energy, the sustainable hydrogen production plant with the integration of reducible oxides was proposed as shown in Figure 6.15. During the design period of the plant, the continuous hydrogen production with maximizing energy efficiency was mainly addressed for the removal commercialization barrier in front for solar thermal processes. In the proposed process, the limits of hydrogen production were determined just after the reforming. The rest can be utilized depending on the downstream processes such as the integration of water gas shift reactor. The feed streams of the overall process are methane, water and air.

The operation of solar steam generation and solar reforming sections in the proposed systems is given in Figure 6.16. For the steam generation section, fresh water is pumped to the system with P-1. The working load of this pump is mainly controlled by the pressure transmitter at the outlet of flash tank (FT-1). The fresh water is mixed with the circulated water coming from FT-1 and then passes through the solar steam generator (SSG). Depending on the available solar irradiation, the temperature of water is increased to a certain level. If the temperature of water is not meet the requirements of reforming section, boiler starts to operate at a certain load. The boiler combusts the methane and air in order to supply additional heat for steam productions. The steam is then expanded in FT-1 so that vapor and liquid is separated. Vapor phase is sent to the reforming section. Liquid phase, on the other hand, is recirculated to the mixing valve MV-1. Liquid level in the flash tank is controlled with an internal level control loop.

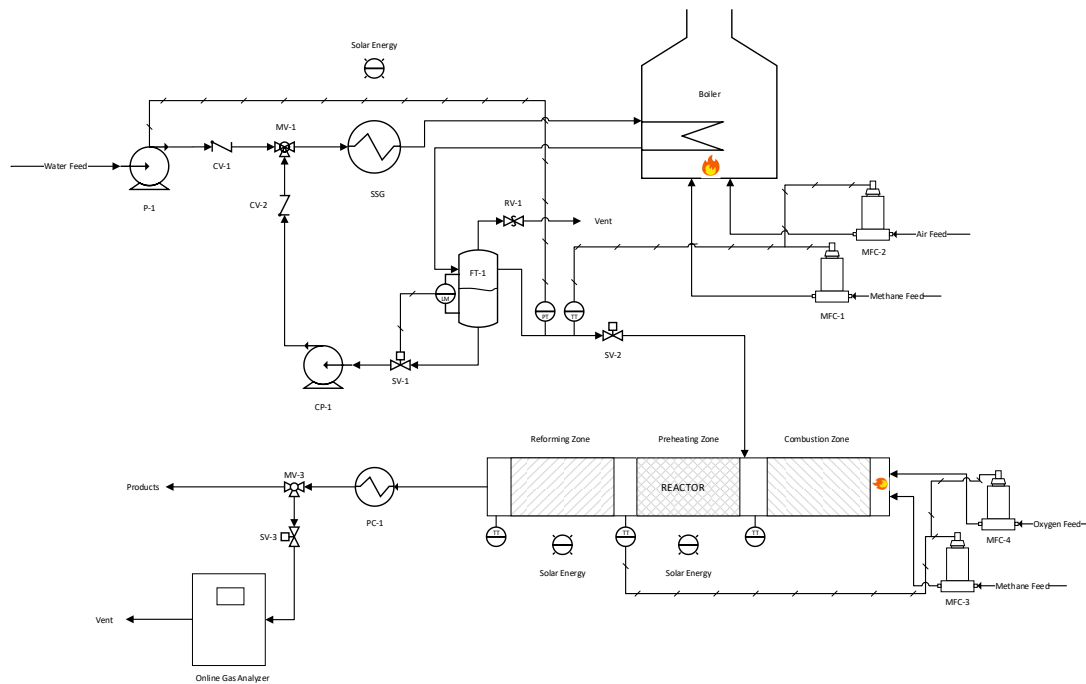


Figure 6.16. Solar steam generation and solar reforming section of proposed process

Solar reformer is divided into three sections such as combustion zone, preheating zone, and reforming zone (Figure 6.16). The main control parameter is the temperature of the outlet of preheating zone since it directly controls the efficiency of reforming reaction. In a sunny day, steam generated from solar steam generation plant is mixed with methane right before the preheating zone. Solar irradiation is then increased the reactant gas mixture to reaction temperature. The preheated gas enters the reforming section. The products are sent to product cooling exchanger (PC-1). The cooled products pass through a mixing valve (MV-3). The online gas analyzer takes sample for calculation of reforming performance. Combustion zone is activated mainly tracking the temperature at the outlet of preheating zone. Depending on the intermittence in the solar energy, the preheating zone temperature starts to decrease. The lack of energy is then sustained by the combustion of methane and oxygen in the combustion zone. The temperature at the outlet of reformer is monitored for the reforming efficiency in terms of heat.

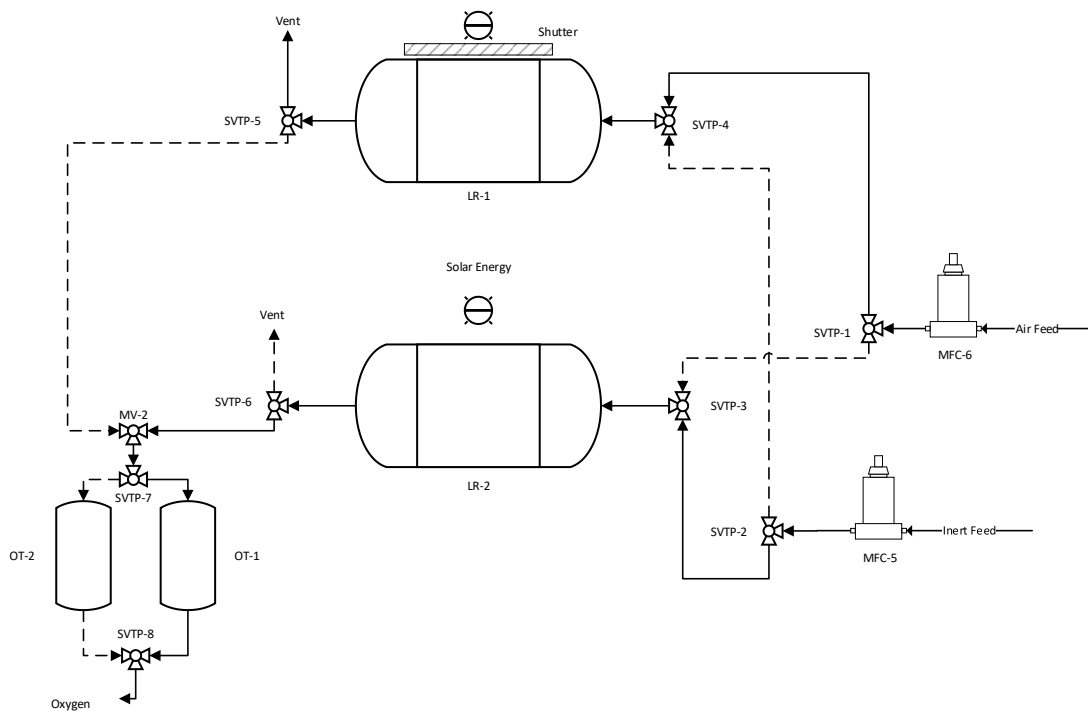


Figure 6.17. Solar integrated oxygen generation plant section of proposed process

The oxygen requirement of the system is sustained from solar integrated oxygen generation plant (Figure 6.17). This plant uses the principle of thermochemical looping process. Reducible oxides such as Co_3O_4 , CeCoO_3 is planned to use in the proposed plant due to their high potential described in previous section. Reducible oxide is fixed in the looping reactors (LR-1 and LR-2). The operation is handled by changing the flows. Mainly two flows are used in the system, oxidizing and inert. Steam is planned to use in the current system due to condensation at the outlet. Gases like N_2 and Ar can also be used for sweeping purpose but the generated oxygen will be diluted. Vacuum is another alternative imposing energy penalty coming from vacuum and pressurization. During the operation, reducible oxides is thermally decomposed under solar irradiation. Thereafter, solar energy is cut by the help of shutter. The reduced oxide is then reoxidized by air. The generated oxygen is then stored in the oxygen storage tanks for the use in the combustion zone. An auxiliary oxygen tank is also used for storing additional oxygen in the case of long-term solar energy losses. Process control algorithm for coke was given in Appendix E.

CHAPTER 7

SUMMARY

A sustainable hydrogen production process development using solar energy was addressed in the scope of this thesis. The integration of solar energy into both two-step thermochemical process and methane reforming process were compared. In the first phase of the study, the feasibility of solar thermochemical process was investigated. The feasibility is strongly related to the reaction step where oxygen removal from the red/ox material can be carried out. As a result, thermodynamics were used as main aid for the searching of new red/ox couples. Performed thermodynamic analysis revealed that the design of a red/ox material is dependent on the careful selection of metals missions such as the use of $\text{Co}^{3+,4+}$ for increasing the oxygen adsorption activity from air while the use of Co^{2+} for adsorbing oxygen from water. The bi-metallic interactivity was also investigated for the CeFe_2O_4 , MnMoO_4 etc. The thermodynamic driving force could not be found satisfactory for the application in two-step thermochemical cycles. Therefore, the perspective was switch to perovskites showing new potential in the area of oxygen exchange.

Having conducted the thermodynamics analysis, the knowledge of metal selection was mixed with the perovskite technology. New oxygen carriers in the thermochemical water splitting literatures as CeCoO_3 , and CeFeO_3 were proposed. CeCoO_3 showed a significant improvement on oxygen transfer from air. Thereafter, metal sites in the perovskites increased with new materials such as $\text{Sr}_{0.6}\text{Ce}_{0.4}\text{Fe}_{0.7}\text{Mn}_{0.3}\text{O}_3$. Maximum hydrogen production was obtained as 52.5 mL/g $\text{Sr}_{0.6}\text{Ce}_{0.4}\text{Fe}_{0.7}\text{Mn}_{0.3}\text{O}_3$ ($T_{\text{high}}=1250\text{ }^\circ\text{C}$) which doubled the literature values given in Table 1.2. However, the solar thermochemical hydrogen production with the oxides is inhibited by the presence of oxygen in the material. This was demonstrated through $\text{Co}_3\text{O}_4 \rightarrow \text{CoO} \rightarrow \text{Co}$ reaction network. In addition, the oxygen exchange rates from a red/ox pair is mainly controlled by the heat and mass transfer limitations even if

new materials still have a potential to increase overall hydrogen amount. Energy penalty coming from the temperature difference between thermal decomposition and water splitting steps is another parameter for overall process feasibility. The overall energy efficiency is low since energy needed for operation is higher than the energy value of hydrogen as product. Under the circumstances that solar thermochemical processes are not favorable, methane reforming reaction was investigated using solar thermal energy.

Ni/Al₂O₃ was selected as reference catalyst and the performance of CeCoO₃ and Ni/CeCoO₃ was studied under steam methane reforming conditions. Having known that steam methane reforming is a highly endothermic process, the new catalysts are investigated in terms of coke deposition. Under direct solar irradiation, temperature fluctuations are expected due to the intermittent nature of solar energy. During the temperature fluctuations, temperature of the reactor will drop and enhances the coke formation on the catalyst. The experiments performed under same conditions revealed that the presence of reducible oxides in the lattice limits the coke formation; in other words, coke deposited on the catalysts reacts with the lattice oxygen and forms CO and CO₂.

Solar energy utilization on methane reforming was also demonstrated at pilot scale under solar irradiation. Even if satisfactory results were observed under solar irradiation, the vulnerability towards intermittent nature of solar energy was also seen during the operation. The temperature of the reactor decreased to 500 °C which was so low to sustain the reaction rate during cloud passing. Therefore, ATR combined with solar thermal SMR is proposed. The experimental data collected on solar reactor, solar heat storage and air separation/solar O₂ production were consolidated with the concept of ATR to develop a process that will overcome the limitations imposed by the intermittency of solar irradiation. The simplified flow diagram was shown in Figure 7.1. Theoretical simulations were performed by using ASPEN Plus software. In the proposed hybrid process, solar energy utilization was taken as a primary focus. The developed process control algorithms were unique in terms of maximization of the system energy efficiency. Steam and oxygen were

mainly produced from solar energy and stored in tanks for sustaining the demand of reformer. The uniqueness of reformer comes from its operation orientated subdivisions such as combustion zone, preheating zone and reforming zone. The proposed process supported by simulations has a significant potential for the commercialization of solar driven hydrogen production. The operation of this system in real case scenarios were left as a future subject.

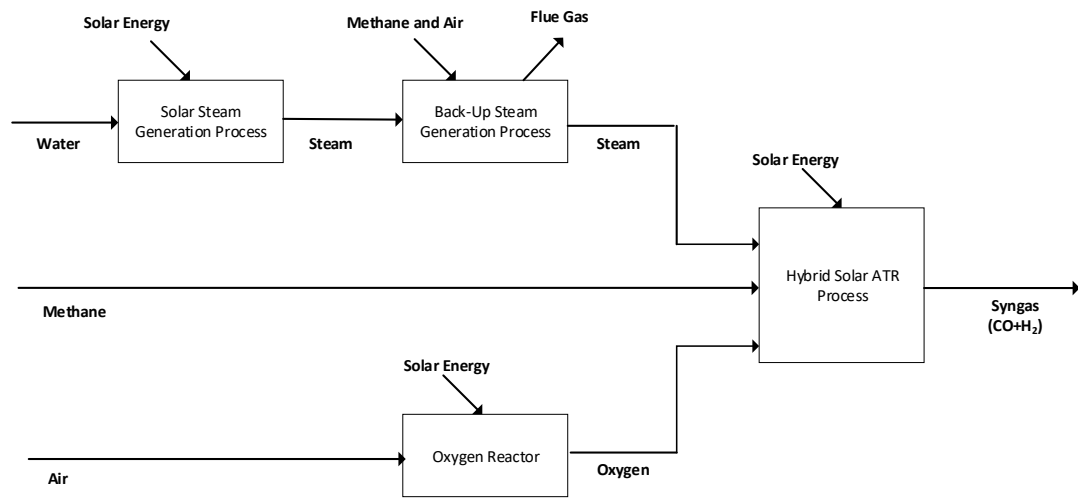


Figure 7.1. Block diagram of hybrid solar ATR process

CHAPTER 8

CONCLUSION

In the foreseeable future, the promises of the solar thermochemical process in terms of hydrogen production may not materialize due to substantial thermodynamic and kinetic barriers as revealed by the experimental and theoretical studies in the scope of this thesis. However, SMR with solar thermal energy is feasible if the intermittency problems causing temperature fluctuations are overcome. Therefore, the main outcome of this thesis becomes the proposed hybrid solar methane reforming process which gives a flexibility for application areas such as urban area, country side and industry. The final product of the process was limited with syngas. Further treatment of syngas was left to the end user due to the huge variety of application areas such as synthetic fuels, fuel cell. The proposed process is also applicable to any other energy intensive processes other than methane reforming such as cracking, pyrolysis. To sum up, increasing the share of renewable sources on the energy intensive processes step by step is a practical solution during the technological shift from fossil fuels to renewable sources. The commercial demonstrations of hybrid processes, mixing renewable and fossil energy sources, as proposed by the scope of this thesis will contribute the efforts to sustain the world energy demand in a more reliable way.

REFERENCES

- [1] International Historical Statistics. London: Palgrave Macmillan UK; 2013. doi:10.1057/9781137305688.
- [2] Hawks J, Hunley K, Lee SH, Wolpoff M. Population bottlenecks and Pleistocene human evolution. *Mol Biol Evol* 2000;17:2–22. doi:10.1093/oxfordjournals.molbev.a026233.
- [3] Smil V. *Energy Transitions. Power Density* 2019. doi:10.7551/mitpress/10046.003.0010.
- [4] Fossil fuel energy consumption (% of total) | Data n.d. <https://data.worldbank.org/indicator/EG.USE.COMM.FO.ZS> (accessed February 24, 2020).
- [5] What countries are the top producers and consumers of oil? - FAQ - U.S. Energy Information Administration (EIA) n.d. <https://www.eia.gov/tools/faqs/faq.php?id=709&t=6> (accessed February 24, 2020).
- [6] Venn F. *The oil crisis*. Longman; 2002.
- [7] Kathea Energy solar-peak - Kathea Energy n.d. <http://katheaenergy.co.za/tesla-powerwall/solar-peak/> (accessed March 3, 2020).
- [8] ISO 13600:1997(en), Technical energy systems — Basic concepts n.d. <https://www.iso.org/obp/ui/#iso:std:iso:13600:ed-1:v1:en> (accessed July 8, 2016).
- [9] Mazloomi K, Gomes C. Hydrogen as an energy carrier: Prospects and challenges. *Renew Sustain Energy Rev* 2012;16:3024–33. doi:10.1016/j.rser.2012.02.028.
- [10] Hydrogen Generation Market worth 152.09 Billion USD by 2021 n.d. <http://www.marketsandmarkets.com/PressReleases/hydrogen.asp> (accessed July 8, 2016).
- [11] Rostrup-Nielsen JR, Rostrup-Nielsen T. Large-scale hydrogen production. *Cattech* 2002;6:150–159.
- [12] Yadav D, Banerjee R. A review of solar thermochemical processes. *Renew Sustain Energy Rev* 2016;54:497–532. doi:10.1016/j.rser.2015.10.026.
- [13] Agrafiotis CC, Pagkoura C, Zygianni A, Karagiannakis G, Kostoglou M, Konstandopoulos AG. Hydrogen production via solar-aided water splitting thermochemical cycles: Combustion synthesis and preliminary evaluation of

- spinel redox-pair materials. *Int J Hydrogen Energy* 2012;37:8964–80. doi:10.1016/j.ijhydene.2012.02.196.
- [14] Davenport TC, Yang C-K, Kucharczyk CJ, Ignatowich MJ, Haile SM. Implications of Exceptional Material Kinetics on Thermochemical Fuel Production Rates. *Energy Technol* 2016;4:764–70. doi:10.1002/ente.201500506.
- [15] Bork AH, Kubicek M, Struzik M, Rupp JLM. Perovskite $\text{La}_{0.6}\text{Sr}_{0.4}\text{Cr}_{1-x}\text{Co}_x\text{O}_{3-\delta}$ solid solutions for solar-thermochemical fuel production: strategies to lower the operation temperature. *J Mater Chem A* 2015;3:15546–57. doi:10.1039/C5TA02519B.
- [16] Ganzoury MA, Fateen S-EK, El Sheltawy ST, Radwan AM, Allam NK. Thermodynamic and efficiency analysis of solar thermochemical water splitting using Ce–Zr mixtures. *Sol Energy* 2016;135:154–62. doi:10.1016/j.solener.2016.05.053.
- [17] Dey S, Naidu BS, Govindaraj A, Rao CNR. Noteworthy performance of $\text{La}_{1-x}\text{Ca}_x\text{MnO}_3$ perovskites in generating H_2 and CO by the thermochemical splitting of H_2O and CO_2 . *Phys Chem Chem Phys* 2014;17:122–5. doi:10.1039/C4CP04578E.
- [18] Bulfin B, Call F, Lange M, Lübben O, Sattler C, Pitz-Paal R, et al. Thermodynamics of CeO_2 Thermochemical Fuel Production. *Energy & Fuels* 2015;29:1001–9. doi:10.1021/ef5019912.
- [19] Weidenkaff A, Reller AW, Wokaun A, Steinfeld A. Thermogravimetric analysis of the ZnO/Zn water splitting cycle. *Thermochim Acta* 2000;359:69–75. doi:10.1016/S0040-6031(00)00508-6.
- [20] Daza YA, Maiti D, Kent RA, Bhethanabotla VR, Kuhn JN. Isothermal reverse water gas shift chemical looping on $\text{La}_{0.75}\text{Sr}_{0.25}\text{Co}_{(1-Y)}\text{FeYO}_3$ perovskite-type oxides. *Catal Today* 2015;258:691–8. doi:10.1016/j.cattod.2014.12.037.
- [21] Säck J-P, Breuer S, Cotelli P, Houaijia A, Lange M, Wullenkord M, et al. High temperature hydrogen production: Design of a 750KW demonstration plant for a two step thermochemical cycle. *Sol Energy* 2016;135:232–41. doi:10.1016/j.solener.2016.05.059.
- [22] Charvin P, Abanades S, Beche E, Lemont F, Flamant G. Hydrogen production from mixed cerium oxides via three-step water-splitting cycles. *Solid State Ionics* 2009;180:1003–10. doi:10.1016/j.ssi.2009.03.015.
- [23] Singh AK, AuYeung NJ, Randhir K, Mishra R, Allen KM, Petrasch J, et al. Thermal Reduction of Iron Oxide under Reduced Pressure and Implications on Thermal Conversion Efficiency for Solar Thermochemical Fuel Production. *Ind Eng Chem Res* 2015;54:6793–803. doi:10.1021/ie504402x.
- [24] Takacs M, Hoes M, Caduff M, Cooper T, Scheffe JR, Steinfeld A. Oxygen

- nonstoichiometry, defect equilibria, and thermodynamic characterization of LaMnO₃ perovskites with Ca/Sr A-site and Al B-site doping. *Acta Mater* 2016;103:700–10. doi:10.1016/j.actamat.2015.10.026.
- [25] Gokon N, Sagawa S, Kodama T. Comparative study of activity of cerium oxide at thermal reduction temperatures of 1300–1550 °C for solar thermochemical two-step water-splitting cycle. *Int J Hydrogen Energy* 2013;38:14402–14. doi:10.1016/j.ijhydene.2013.08.108.
- [26] Gokon N, Suda T, Kodama T. Thermochemical reactivity of 5–15mol% Fe, Co, Ni, Mn-doped cerium oxides in two-step water-splitting cycle for solar hydrogen production. *Thermochim Acta* 2015;617:179–90. doi:10.1016/j.tca.2015.08.036.
- [27] Chueh WC, Falter C, Abbott M, Scipio D, Furler P, Haile SM, et al. High-Flux Solar-Driven Thermochemical Dissociation of CO₂ and H₂O Using Nonstoichiometric Ceria. *Science* (80-) 2010;330:1797–801. doi:10.1126/science.1197834.
- [28] Meng Q-L, Lee C, Kaneko H, Tamaura Y. Solar thermochemical process for hydrogen production via two-step water splitting cycle based on Ce_{1-x}Pr_xO_{2-δ} redox reaction. *Thermochim Acta* 2012;532:134–8. doi:10.1016/j.tca.2011.01.028.
- [29] Bonk A, Maier AC, Schlupp MVF, Burnat D, Remhof A, Delmelle R, et al. The effect of dopants on the redox performance, microstructure and phase formation of ceria. *J Power Sources* 2015;300:261–71. doi:10.1016/j.jpowsour.2015.09.073.
- [30] Venstrom LJ, Petkovich N, Rudisill S, Stein A, Davidson JH. The Effects of Morphology on the Oxidation of Ceria by Water and Carbon Dioxide. *J Sol Energy Eng* 2011;134:011005–011005–8. doi:10.1115/1.4005119.
- [31] Kodama T, Nakamuro Y, Mizuno T. A Two-Step Thermochemical Water Splitting by Iron-Oxide on Stabilized Zirconia. *J Sol Energy Eng* 2004;128:3–7. doi:10.1115/1.1878852.
- [32] Song L, Kang HW, Park S Bin. Thermally stable iron based redox catalysts for the thermo-chemical hydrogen generation from water. *Energy* 2012;42:313–20. doi:10.1016/j.energy.2012.03.051.
- [33] Dey S, Naidu BS, Rao CNR. Beneficial effects of substituting trivalent ions in the B-site of La_{0.5}Sr_{0.5}Mn_{1-x}A_xO₃ (A = Al, Ga, Sc) on the thermochemical generation of CO and H₂ from CO₂ and H₂O. *Dalt Trans* 2016;45:2430–5. doi:10.1039/C5DT04822B.
- [34] Rao CNR, Dey S. Generation of H₂ and CO by solar thermochemical splitting of H₂O and CO₂ by employing metal oxides. *J Solid State Chem* 2016;242:107–15. doi:10.1016/j.jssc.2015.12.018.

- [35] Deml AM, Stevanović V, Muhich CL, Musgrave CB, O'Hayre R. Oxide enthalpy of formation and band gap energy as accurate descriptors of oxygen vacancy formation energetics. *Energy Environ Sci* 2014;7:1996–2004. doi:10.1039/C3EE43874K.
- [36] Tsvetkov N, Lu Q, Yildiz B. Improved electrochemical stability at the surface of La(0.8)Sr(0.2)CoO₃ achieved by surface chemical modification. *Faraday Discuss* 2015;182:257–69. doi:10.1039/c5fd00023h.
- [37] Dey S, Naidu BS, Rao CNR. Ln_{0.5}A_{0.5}MnO₃ (Ln=Lanthanide, A= Ca, Sr) Perovskites Exhibiting Remarkable Performance in the Thermochemical Generation of CO and H₂ from CO₂ and H₂O. *Chem – A Eur J* 2015;21:7077–81. doi:10.1002/chem.201500442.
- [38] McDaniel AH, Ambrosini A, Coker EN, Miller JE, Chueh WC, O'Hayre R, et al. Nonstoichiometric Perovskite Oxides for Solar Thermochemical H₂ and CO Production. *Energy Procedia* 2014;49:2009–18. doi:10.1016/j.egypro.2014.03.213.
- [39] McDaniel AH, Miller EC, Arifin D, Ambrosini A, Coker EN, O'Hayre R, et al. Sr- and Mn-doped LaAlO₃- δ for solar thermochemical H₂ and CO production. *Energy Environ Sci* 2013;6:2424–8. doi:10.1039/C3EE41372A.
- [40] Evdou A, Nalbandian L, Zaspalis VT. Perovskite membrane reactor for continuous and isothermal redox hydrogen production from the dissociation of water. *J Memb Sci* 2008;325:704–11. doi:10.1016/j.memsci.2008.08.042.
- [41] Scheffe JR, McDaniel AH, Allendorf MD, Weimer AW. Kinetics and mechanism of solar-thermochemical H₂ production by oxidation of a cobalt ferrite–zirconia composite. *Energy Environ Sci* 2013;6:963–73. doi:10.1039/C3EE23568H.
- [42] Amar VS, Puszynski JA, Shende R V. H₂ generation from thermochemical water-splitting using yttria stabilized NiFe₂O₄ core-shell nanoparticles. *J Renew Sustain Energy* 2015;7:023113. doi:10.1063/1.4915312.
- [43] Muhich CL, Ehrhart BD, Witte VA, Miller SL, Coker EN, Musgrave CB, et al. Predicting the solar thermochemical water splitting ability and reaction mechanism of metal oxides: a case study of the hercynite family of water splitting cycles. *Energy Environ Sci* 2015;8:3687–99. doi:10.1039/C5EE01979F.
- [44] Gokon N, Takahashi S, Yamamoto H, Kodama T. Thermochemical two-step water-splitting reactor with internally circulating fluidized bed for thermal reduction of ferrite particles. *Int J Hydrogen Energy* 2008;33:2189–99. doi:10.1016/j.ijhydene.2008.02.044.
- [45] Fresno F, Fernández-Saavedra R, Belén Gómez-Mancebo M, Vidal A, Sánchez M, Isabel Rucandio M, et al. Solar hydrogen production by two-step

- thermochemical cycles: Evaluation of the activity of commercial ferrites. *Int J Hydrogen Energy* 2009;34:2918–24. doi:10.1016/j.ijhydene.2009.02.020.
- [46] Miller JE, Allendorf MD, Diver RB, Evans LR, Siegel NP, Stuecker JN. Metal oxide composites and structures for ultra-high temperature solar thermochemical cycles. *J Mater Sci* 2008;43:4714–28. doi:10.1007/s10853-007-2354-7.
- [47] Inoue M, Hasegawa N, Uehara R, Gokon N, Kaneko H, Tamaura Y. Solar hydrogen generation with H₂O/ZnO/MnFe₂O₄ system. *Sol Energy* 2004;76:309–15. doi:10.1016/j.solener.2003.08.033.
- [48] Le Gal A, Abanades S. Catalytic investigation of ceria-zirconia solid solutions for solar hydrogen production. *Int J Hydrogen Energy* 2011;36:4739–48. doi:10.1016/j.ijhydene.2011.01.078.
- [49] Kaneko H, Miura T, Ishihara H, Taku S, Yokoyama T, Nakajima H, et al. Reactive ceramics of CeO₂–MO_x (M=Mn, Fe, Ni, Cu) for H₂ generation by two-step water splitting using concentrated solar thermal energy. *Energy* 2007;32:656–63. doi:10.1016/j.energy.2006.05.002.
- [50] Zhang Y, Zhu Q, Lin X, Xu Z, Liu J, Wang Z, et al. A novel thermochemical cycle for the dissociation of CO₂ and H₂O using sustainable energy sources. *Appl Energy* 2013;108:1–7. doi:10.1016/j.apenergy.2013.03.019.
- [51] Seo K, Lim T, Mills EM, Kim S, Ju S. Hydrogen generation enhanced by nano-forest structures. *RSC Adv* 2016;6:12953–8. doi:10.1039/C5RA26226G.
- [52] Roberts SJ, Dodson JJ, Carpinone PL, Hagelin-Weaver HE. Evaluation of nanoparticle zirconia supports in the thermochemical water splitting cycle over iron oxides. *Int J Hydrogen Energy* 2015;40:15972–84. doi:10.1016/j.ijhydene.2015.09.109.
- [53] Gokon N, Suda T, Kodama T. Oxygen and hydrogen productivities and repeatable reactivity of 30-mol%-Fe-, Co-, Ni-, Mn-doped CeO₂– δ for thermochemical two-step water-splitting cycle. *Energy* 2015;90:1280–9. doi:10.1016/j.energy.2015.06.085.
- [54] Lin F, Wokaun A, Alxneit I. Rh-doped Ceria: Solar Organics From H₂O, CO₂ and Sunlight? *Energy Procedia* 2015;69:1790–9. doi:10.1016/j.egypro.2015.03.151.
- [55] Lorentzou S, Karagiannakis G, Dimitrakis D, Pagkoura C, Zygogianni A, Konstandopoulos AG. Thermochemical Redox Cycles over Ce-based Oxides. *Energy Procedia* 2015;69:1800–9. doi:10.1016/j.egypro.2015.03.152.
- [56] Scheffe JR, Li J, Weimer AW. A spinel ferrite/hercynite water-splitting redox cycle. *Int J Hydrogen Energy* 2010;35:3333–40. doi:10.1016/j.ijhydene.2010.01.140.

- [57] Le Gal A, Abanades S, Flamant G. CO₂ and H₂O Splitting for Thermochemical Production of Solar Fuels Using Nonstoichiometric Ceria and Ceria/Zirconia Solid Solutions. *Energy & Fuels* 2011;25:4836–45. doi:10.1021/ef200972r.
- [58] Kostoglou M, Lorentzou S. ScienceDirect Improved kinetic model for water splitting thermochemical cycles using Nickel Ferrite. *Int J Hydrogen Energy* 2014;39:6317–27. doi:10.1016/j.ijhydene.2014.01.121.
- [59] Yang C-K, Yamazaki Y, Aydin A, Haile SM. Thermodynamic and kinetic assessments of strontium-doped lanthanum manganite perovskites for two-step thermochemical water splitting. *J Mater Chem A* 2014;2:13612–23. doi:10.1039/C4TA02694B.
- [60] Demont A, Abanades S, Beche E. Investigation of Perovskite Structures as Oxygen-Exchange Redox Materials for Hydrogen Production from Thermochemical Two-Step Water-Splitting Cycles. *J Phys Chem C* 2014;118:12682–92. doi:10.1021/jp5034849.
- [61] Monazam ER, Breault RW, Siriwardane R, Richards G, Carpenter S. Kinetics of the reduction of hematite (Fe₂O₃) by methane (CH₄) during chemical looping combustion: A global mechanism. *Chem Eng J* 2013;232:478–87. doi:10.1016/j.cej.2013.07.091.
- [62] Abad A, Mattisson T, Lyngfelt A, Rydén M. Chemical-looping combustion in a 300W continuously operating reactor system using a manganese-based oxygen carrier. *Fuel* 2006;85:1174–85. doi:10.1016/j.fuel.2005.11.014.
- [63] Johansson M, Mattisson T, Lyngfelt A. Investigation of Mn₃O₄ With Stabilized ZrO₂ for Chemical-Looping Combustion. *Chem Eng Res Des* 2006;84:807–18. doi:10.1205/cherd.05206.
- [64] Agrafiotis C, Roeb M, Konstandopoulos AG, Nalbandian L, Zaspalis VT, Sattler C, et al. Solar water splitting for hydrogen production with monolithic reactors. *Sol Energy* 2005;79:409–21. doi:10.1016/j.solener.2005.02.026.
- [65] Fend T, Hoffschmidt B, Pitz-Paal R, Reutter O, Rietbrock P. Porous materials as open volumetric solar receivers: Experimental determination of thermophysical and heat transfer properties. *Energy* 2004;29:823–33. doi:10.1016/S0360-5442(03)00188-9.
- [66] Furler P, Scheffe J, Gorbar M, Moes L, Vogt U, Steinfeld A. Solar Thermochemical CO₂ Splitting Utilizing a Reticulated Porous Ceria Redox System. *Energy & Fuels* 2012;26:7051–9. doi:10.1021/ef3013757.
- [67] Kodama T, Gokon N. Thermochemical Cycles for High-Temperature Solar Hydrogen Production. *Chem Rev* 2007;107:4048–77. doi:10.1021/cr050188a.
- [68] Beghi GE. A decade of research on thermochemical hydrogen at the joint

- research centre, ISPRA. *Int J Hydrogen Energy* 1986;11:761–771.
- [69] Norman J, Jr JR. Process for the thermochemical production of hydrogen. US Pat ... 1978.
- [70] Goldstein S, Borgard JM, Vitart X. Upper bound and best estimate of the efficiency of the iodine sulphur cycle. *Int J Hydrogen Energy* 2005. doi:10.1016/j.ijhydene.2004.06.005.
- [71] Schultz KR. Use of the modular helium reactor. World Nucl. Assoc. Annu. Symp., London, UK: 2003.
- [72] Roeb M, Noglik A, Rietbrock P-M, Mohr S, de Oliveira L, Sattler C, et al. HYTHEC: Development of a dedicated solar receiver-reactor for the decomposition of sulphuric acid 2005.
- [73] Le Duigou A, Borgard J-M, Larousse B, Doizi D, Allen R, Ewan BC, et al. HYTHEC: An EC funded search for a long term massive hydrogen production route using solar and nuclear technologies. *Int J Hydrogen Energy* 2007;32:1516–29. doi:10.1016/j.ijhydene.2006.10.047.
- [74] Parisi M, Giaconia A, Sau S, Spadoni A, Caputo G, Tarquini P. Bunsen reaction and hydriodic phase purification in the sulfureiodine process: An experimental investigation. *Int J Hydrogen Energy* 2011;36:2007–13. doi:10.1016/j.ijhydene.2010.11.039.
- [75] Russ B. Sulfur Iodine Process Summary for the Hydrogen Technology Down-Selection 2009.
- [76] Corgnale C, Summers WA. Solar hydrogen production by the Hybrid Sulfur process. *Int J Hydrogen Energy* 2011;36:11604–19. doi:10.1016/j.ijhydene.2011.05.173.
- [77] Hinkley JT, O'Brien JA, Fell CJ, Lindquist S-E, O'Brien JA, Fell CJ, et al. Prospects for solar only operation of the hybrid sulphur cycle for hydrogen production. *Int J Hydrogen Energy* 2011;36:11596–603. doi:10.1016/j.ijhydene.2011.06.048.
- [78] Steimke J, J. Characterization Testing of H₂O-SO₂ Electrolyzer at Ambient Pressure. Aiken, SC: pubinfo; 2005. doi:10.2172/890186.
- [79] Gorenssek MB, Summers WA. Hybrid sulfur flowsheets using PEM electrolysis and a bayonet decomposition reactor. *Int J Hydrogen Energy* 2008;34:4097–114. doi:10.1016/j.ijhydene.2008.06.049.
- [80] Summers WA, Gorenssek MB. Nuclear Hydrogen Production Based on the Hybrid Sulfur Thermochemical Process 2006.
- [81] Brecher L, Wu C. Electrolytic decomposition of water, 1975.
- [82] Method for producing hydrogen and sulphuric acid 2008.

- [83] Takai T, Kubo S, Nakagiri T, Inagaki Y. Lab-scale water-splitting hydrogen production test of modified hybrid sulfur process working at around 550 °C 2011. doi:10.1016/j.ijhydene.2011.01.081.
- [84] Dokiya M, Kotera Y. Hybrid cycle with electrolysis using Cu-Cl system. *Int J Hydrogen Energy* 1976;1:117–21. doi:10.1016/0360-3199(76)90064-1.
- [85] Masin JG, Lewis MA. Development of the Low Temperature Hybrid Cu-Cl Thermochemical Cycle n.d.
- [86] Steinfeld A. Solar thermochemical production of hydrogen—a review. *Sol Energy* 2005;78:603–15. doi:10.1016/j.solener.2003.12.012.
- [87] Loutzenhiser PG, Meier A, Steinfeld A. Review of the Two-Step H₂O/CO₂-Splitting Solar Thermochemical Cycle Based on Zn/ZnO Redox Reactions. *Materials (Basel)* 2010;3:4922–38. doi:10.3390/ma3114922.
- [88] Ambriz JJ, Ducarroir M, Sibieude F. Preparation of cadmium by thermal dissociation of cadmium oxide using solar energy. *Int J Hydrogen Energy* 1982;7:143–53. doi:10.1016/0360-3199(82)90141-0.
- [89] Abanades S, Charvin P, Lemont F, Flamant G. Novel two-step SnO₂/SnO water-splitting cycle for solar thermochemical production of hydrogen. *Int J Hydrogen Energy* 2008;33:6021–30. doi:10.1016/j.ijhydene.2008.05.042.
- [90] Abanades S. CO₂ and H₂O reduction by solar thermochemical looping using SnO₂/SnO redox reactions: Thermogravimetric analysis. *Int J Hydrogen Energy* 2012;37:8223–31. doi:10.1016/j.ijhydene.2012.02.158.
- [91] Steinfeld A, Palumbo R. SOLAR THERMOCHEMICAL PROCESS TECHNOLOGY 2001;15:237–56.
- [92] Haueter P, Moeller S, Palumbo R, Steinfeld A. THE PRODUCTION OF ZINC BY THERMAL DISSOCIATION OF ZINC OXIDE—SOLAR CHEMICAL REACTOR DESIGN. *Sol Energy* 1999;67:1–3.
- [93] Nakamura T. Hydrogen production from water utilizing solar heat at high temperatures. *Sol Energy* 1977;19:467–75. doi:10.1016/0038-092X(77)90102-5.
- [94] Chueh WC, Haile SM. A thermochemical study of ceria: exploiting an old material for new modes of energy conversion and CO₂ mitigation. *Philos Trans A Math Phys Eng Sci* 2010;368:3269–94. doi:10.1098/rsta.2010.0114.
- [95] Kuhn M, Bishop SR, Rupp JLM, Tuller HL. Structural characterization and oxygen nonstoichiometry of ceria-zirconia (Ce_{1-x}Zr_xO_{2-δ}) solid solutions. *Acta Mater* 2013;61:4277–88. doi:10.1016/J.ACTAMAT.2013.04.001.
- [96] Siegel N, Diver R, Miller JE, Garino T, Livers S. Reactive Structures for Two-Step Thermochemical Cycles Based on Non-Volatile Metal Oxides. *ASME 2009 3rd Int. Conf. Energy Sustain.* Vol. 2, ASME; 2009, p. 431–7.

doi:10.1115/ES2009-90093.

- [97] Gokon N, Suda T, Kodama T. Thermochemical reactivity of 5–15 mol% Fe, Co, Ni, Mn-doped cerium oxides in two-step water-splitting cycle for solar hydrogen production. *Thermochim Acta* 2015;617:179–90. doi:10.1016/J.TCA.2015.08.036.
- [98] Jiang Q, Tong J, Zhou G, Jiang Z, Li Z, Li C. Thermochemical CO₂ splitting reaction with supported $\text{La}_x\text{A}_{1-x}\text{Fe}_y\text{B}_{1-y}\text{O}_3$ (A = Sr, Ce, B = Co, Mn; $0 \leq x, y \leq 1$) perovskite oxides. *Sol Energy* 2014;103:425–37. doi:10.1016/j.solener.2014.02.033.
- [99] Charvin P, Abanades S, Flamant G, Lemort F. Two-step water splitting thermochemical cycle based on iron oxide redox pair for solar hydrogen production. *Energy* 2007;32:1124–33. doi:10.1016/j.energy.2006.07.023.
- [100] Takacs M, Scheffe JR, Steinfeld A. Oxygen nonstoichiometry and thermodynamic characterization of Zr doped ceria in the 1573–1773 K temperature range. *Phys Chem Chem Phys* 2015;17:7813–22. doi:10.1039/C4CP04916K.
- [101] Rhodes NR, Bobek MM, Allen KM, Hahn DW. Investigation of long term reactive stability of ceria for use in solar thermochemical cycles. *Energy* 2015;89:924–31. doi:10.1016/j.energy.2015.06.041.
- [102] Fresno F, Yoshida T, Gokon N, Fernández-Saavedra R, Kodama T. Comparative study of the activity of nickel ferrites for solar hydrogen production by two-step thermochemical cycles. *Int J Hydrogen Energy* 2010;35:8503–10. doi:10.1016/j.ijhydene.2010.05.032.
- [103] Meng Q-L, Lee C, Kaneko H, Tamaura Y. Solar thermochemical process for hydrogen production via two-step water splitting cycle based on $\text{Ce}_{1-x}\text{Pr}_x\text{O}_{2-\delta}$ redox reaction. *Thermochim Acta* 2012;532:134–8. doi:10.1016/j.tca.2011.01.028.
- [104] Kaneko H, Tamaura Y. Reactivity and XAFS study on $(1-x)\text{CeO}_2-x\text{NiO}$ ($x = 0.025-0.3$) system in the two-step water-splitting reaction for solar H₂ production. *J Phys Chem Solids* n.d.;70:1008–14. doi:10.1016/j.jpccs.2009.05.015.
- [105] Jiang Q, Zhou G, Jiang Z, Li C. Thermochemical CO₂ splitting reaction with $\text{Ce}_x\text{M}_{1-x}\text{O}_{2-\delta}$ (M = Ti⁴⁺, Sn⁴⁺, Hf⁴⁺, Zr⁴⁺, La³⁺, Y³⁺ and Sm³⁺) solid solutions. *Sol Energy* 2014;99:55–66. doi:10.1016/j.solener.2013.10.021.
- [106] McAlpin JG, Surendranath Y, Dincă M, Stich TA, Stoian SA, Casey WH, et al. EPR Evidence for Co(IV) Species Produced During Water Oxidation at Neutral pH. *J Am Chem Soc* 2010;132:6882–3. doi:10.1021/ja1013344.
- [107] Tüysüz H, Hwang YJ, Khan SB, Asiri AM, Yang P. Mesoporous Co₃O₄ as an electrocatalyst for water oxidation. *Nano Res* 2013;6:47–54.

doi:10.1007/s12274-012-0280-8.

- [108] Bai C, Wei S, Deng D, Lin X, Zheng M, Dong Q. A nitrogen-doped nano carbon dodecahedron with Co@Co₃O₄ implants as a bi-functional electrocatalyst for efficient overall water splitting. *J Mater Chem A* 2017;5:9533–6. doi:10.1039/C7TA01708A.
- [109] Jiao F, Frei H. Nanostructured Cobalt Oxide Clusters in Mesoporous Silica as Efficient Oxygen-Evolving Catalysts. *Angew Chemie Int Ed* 2009;48:1841–4. doi:10.1002/anie.200805534.
- [110] Liao M, Feng J, Luo W, Wang Z, Zhang J, Li Z, et al. Co₃O₄ Nanoparticles as Robust Water Oxidation Catalysts Towards Remarkably Enhanced Photostability of a Ta₃N₅ Photoanode. *Adv Funct Mater* 2012;22:3066–74. doi:10.1002/adfm.201102966.
- [111] Navrotsky A, Ma C, Lilova K, Birkner N. Nanophase Transition Metal Oxides Show Large Thermodynamically Driven Shifts in Oxidation-Reduction Equilibria. *Science* (80-) 2010;330:199–201. doi:10.1126/science.1195875.
- [112] Esswein AJ, McMurdo MJ, Ross PN, Bell AT, Tilley TD. Size-Dependent Activity of Co₃O₄ Nanoparticle Anodes for Alkaline Water Electrolysis. *J Phys Chem C* 2009;113:15068–72. doi:10.1021/jp904022e.
- [113] Zhang H, Ling T, Du X-W. Gas-Phase Cation Exchange toward Porous Single-Crystal CoO Nanorods for Catalytic Hydrogen Production. *Chem Mater* 2015;27:352–7. doi:10.1021/cm504076n.
- [114] Liang Y, Li Y, Wang H, Zhou J, Wang J, Regier T, et al. Co₃O₄ nanocrystals on graphene as a synergistic catalyst for oxygen reduction reaction. *Nat Mater* 2011;10:780–6. doi:10.1038/nmat3087.
- [115] Wang H-Y, Hung S-F, Chen H-Y, Chan T-S, Chen HM, Liu B. In Operando Identification of Geometrical-Site-Dependent Water Oxidation Activity of Spinel Co₃O₄. *J Am Chem Soc* 2016;138:36–9. doi:10.1021/jacs.5b10525.
- [116] Lundberg M. Model calculations on some feasible two-step water splitting processes. *Int J Hydrogen Energy* 1993;18:369–76. doi:10.1016/0360-3199(93)90214-U.
- [117] Kodama T, Kondoh Y, Yamamoto R, Andou H, Satou N. Thermochemical hydrogen production by a redox system of ZrO₂-supported Co(II)-ferrite. *Sol Energy* 2005;78:623–31. doi:10.1016/j.solener.2004.04.008.
- [118] Perkins C, Lichty PR, Weimer AW. Thermal ZnO dissociation in a rapid aerosol reactor as part of a solar hydrogen production cycle. *Int J Hydrogen Energy* 2008;33:499–510. doi:10.1016/j.ijhydene.2007.10.021.
- [119] Gstoehl D, Brambilla A, Schunk LO, Steinfeld A. A quenching apparatus for the gaseous products of the solar thermal dissociation of ZnO. *J Mater Sci*

2008;43:4729–36. doi:10.1007/s10853-007-2351-x.

- [120] Berman A, Epstein M. The kinetics of hydrogen production in the oxidation of liquid zinc with water vapor. *Int J Hydrogen Energy* 2000;25:957–67. doi:10.1016/S0360-3199(00)00015-X.
- [121] Loutzenhiser PG, Elena Gálvez M, Hischier I, Graf A, Steinfeld A. CO₂ splitting in an aerosol flow reactor via the two-step Zn/ZnO solar thermochemical cycle. *Chem Eng Sci* 2010;65:1855–64. doi:10.1016/j.ces.2009.11.025.
- [122] Wegner K, Ly HC, Weiss RJ, Pratsinis SE, Steinfeld A. In situ formation and hydrolysis of Zn nanoparticles for H₂ production by the 2-step ZnO/Zn water-splitting thermochemical cycle. *Int J Hydrogen Energy* 2006;31:55–61. doi:10.1016/j.ijhydene.2005.03.006.
- [123] Abu Hamed T, Venstrom L, Alshare A, Brühlhart M, Davidson JH. Study of a Quench Device for the Synthesis and Hydrolysis of Zn Nanoparticles: Modeling and Experiments. *J Sol Energy Eng* 2009;131:031018. doi:10.1115/1.3142825.
- [124] Mü Ller R, Haerberling P, Palumbo RD. Further advances toward the development of a direct heating solar thermal chemical reactor for the thermal dissociation of ZnO(s) 2005. doi:10.1016/j.solener.2005.04.015.
- [125] Palumbo R, Keunecke M, Mö Ller S, Steinfeld A. Reflections on the design of solar thermal chemical reactors: thoughts in transformation. *Energy* 2004;29:727–44. doi:10.1016/S0360-5442(03)00180-4.
- [126] Koepf E, Alxneit I, Wieckert C, Meier A. A review of high temperature solar driven reactor technology: 25 years of experience in research and development at the Paul Scherrer Institute. *Appl Energy* 2017;188:620–51. doi:10.1016/j.apenergy.2016.11.088.
- [127] Steinfeld A. Solar hydrogen production via a two-step water-splitting thermochemical cycle based on Zn/ZnO redox reactions. *Int J Hydrogen Energy* 2002;27:611–9. doi:10.1016/S0360-3199(01)00177-X.
- [128] Abanades S. CO₂ and H₂O reduction by solar thermochemical looping using SnO₂/SnO redox reactions: Thermogravimetric analysis 2012. doi:10.1016/j.ijhydene.2012.02.158.
- [129] Charvin P, Abanades S, Lemont F, Flamant G. Experimental study of SnO₂/SnO/Sn thermochemical systems for solar production of hydrogen. *AIChE J* 2008;54:2759–67. doi:10.1002/aic.11584.
- [130] Levêque G, Abanades S, Jumas J-C, Olivier-Fourcade J. Characterization of Two-Step Tin-Based Redox System for Thermochemical Fuel Production from Solar-Driven CO₂ and H₂O Splitting Cycle. *Ind Eng Chem Res* 2014;53:5668–77. doi:10.1021/ie500206u.

- [131] Gokon N, Mizuno T, Nakamuro Y, Kodama T. Iron-Containing Yttria-Stabilized Zirconia System For Two-Step Thermochemical Water Splitting. *J Sol Energy Eng* 2007;130:11016–8. doi:10.1115/1.2807197.
- [132] Sibieude F, Ducarroir M, Tofighi A, Ambriz J. High temperature experiments with a solar furnace: The decomposition of Fe₃O₄, Mn₃O₄, CdO. *Int J Hydrogen Energy* 1982;7:79–88. doi:10.1016/0360-3199(82)90209-9.
- [133] Kodama T, Gokon N, Yamamoto R. Thermochemical two-step water splitting by ZrO₂-supported Ni_xFe_{3-x}O₄ for solar hydrogen production. *Sol Energy* 2008;82:73–9. doi:10.1016/j.solener.2007.03.005.
- [134] Darken LS, Gurry RW. The System Iron—Oxygen. II. Equilibrium and Thermodynamics of Liquid Oxide and Other Phases. *J Am Chem Soc* 1946;68:798–816. doi:10.1021/ja01209a030.
- [135] Coker EN, Ambrosini A, Rodriguez MA, Miller JE. Ferrite-YSZ composites for solar thermochemical production of synthetic fuels: in operando characterization of CO₂ reduction. *J Mater Chem* 2011;21:10767. doi:10.1039/c1jm11053e.
- [136] Gokon N, Takahashi S, Yamamoto H, Kodama T. New Solar Water-Splitting Reactor With Ferrite Particles in an Internally Circulating Fluidized Bed. *J Sol Energy Eng* 2009;131:11007–9. doi:10.1115/1.3027511.
- [137] Ehrensberger K, Kuhn P, Shklover V, Oswald HR. Temporary phase segregation processes during the oxidation of (Fe_{0.7}Mn_{0.3})_{0.99}O in N₂□H₂O atmosphere. *Solid State Ionics* 1996;90:75–81. doi:10.1016/S0167-2738(96)00376-1.
- [138] Ehrensberger K, Frei A, Kuhn P, Oswald HR, Hug P. Comparative experimental investigations of the water-splitting reaction with iron oxide Fe_{1-y}O and iron manganese oxides (Fe_{1-x}Mn_x)_{1-y}O. *Solid State Ionics* 1995. doi:10.1016/0167-2738(95)00019-3.
- [139] Hutchings K, Wilson M, Larsen P, Cutler R. Kinetic and thermodynamic considerations for oxygen absorption/desorption using cobalt oxide. *Solid State Ionics* 2006;177:45–51. doi:10.1016/j.ssi.2005.10.005.
- [140] Tsuji M, Togawa T, Wada Y, Sano T, Tamaura Y. Kinetic study of the formation of cation-excess magnetite. *J Chem Soc Faraday Trans* 1995;91:1533. doi:10.1039/ft9959101533.
- [141] Tamaura Y, Kojima M, Sano T, Ueda Y, Hasegawa N, Tsuji M. Thermodynamic evaluation of water splitting by a cation-excessive (Ni, Mn) ferrite. *Int J Hydrogen Energy* 1998;23:1185–91. doi:10.1016/S0360-3199(98)00007-X.
- [142] Gokon N, Mataga T, Kondo N, Kodama T. Thermochemical two-step water splitting by internally circulating fluidized bed of NiFe₂O₄ particles:

- Successive reaction of thermal-reduction and water-decomposition steps. *Int J Hydrogen Energy* 2011;36:4757–67. doi:10.1016/j.ijhydene.2011.01.076.
- [143] Miller JE, McDaniel AH, Allendorf MD. Considerations in the Design of Materials for Solar-Driven Fuel Production Using Metal-Oxide Thermochemical Cycles. *Adv Energy Mater* 2014;4:1300469. doi:10.1002/aenm.201300469.
- [144] Agrafiotis C, Zygogianni A, Pagkoura C, Kostoglou M, Konstandopoulos AG. Hydrogen production via solar-aided water splitting thermochemical cycles with nickel ferrite: Experiments and modeling. *AIChE J* 2013;59:1213–25. doi:10.1002/aic.13882.
- [145] Gokon N, Hasegawa T, Takahashi S, Kodama T. Thermochemical two-step water-splitting for hydrogen production using Fe-YSZ particles and a ceramic foam device. *Energy* 2008;33:1407–16. doi:10.1016/j.energy.2008.04.011.
- [146] Allendorf MD, Diver RB, Siegel NP, Miller JE. Two-Step Water Splitting Using Mixed-Metal Ferrites: Thermodynamic Analysis and Characterization of Synthesized Materials. *Energy & Fuels* 2008;22:4115–24. doi:10.1021/ef8005004.
- [147] Jung I-H, Decterov SA, Pelton AD, Kim H-M, Kang Y-B. Thermodynamic evaluation and modeling of the Fe–Co–O system. *Acta Mater* 2004;52:507–19. doi:10.1016/J.ACTAMAT.2003.09.034.
- [148] Scheffe JR, Steinfeld A. Oxygen exchange materials for solar thermochemical splitting of H₂O and CO₂: a review. *Mater Today* 2014;17:341–8. doi:10.1016/j.mattod.2014.04.025.
- [149] Arifin D, Aston VJ, Liang X, McDaniel AH, Weimer AW. CoFe₂O₄ on a porous Al₂O₃ nanostructure for solar thermochemical CO₂ splitting. *Energy Environ Sci* 2012;5:9438. doi:10.1039/c2ee22090c.
- [150] Hao Y, Yang C-K, Haile SM. High-temperature isothermal chemical cycling for solar-driven fuel production. *Phys Chem Chem Phys* 2013;15:17084. doi:10.1039/c3cp53270d.
- [151] Bader R, Venstrom LJ, Davidson JH, Lipiński W. Thermodynamic Analysis of Isothermal Redox Cycling of Ceria for Solar Fuel Production. *Energy & Fuels* 2013;27:5533–44. doi:10.1021/ef400132d.
- [152] Abanades S, Flamant G. Thermochemical hydrogen production from a two-step solar-driven water-splitting cycle based on cerium oxides. *Sol Energy* 2006;80:1611–23. doi:10.1016/j.solener.2005.12.005.
- [153] Abanades S, Legal A, Cordier A, Peraudeau G, Flamant G, Julbe A. Investigation of reactive cerium-based oxides for H₂ production by thermochemical two-step water-splitting. *J Mater Sci* 2010;45:4163–73. doi:10.1007/s10853-010-4506-4.

- [154] Kaneko H, Ishihara H, Taku S, Naganuma Y, Hasegawa N, Tamaura Y. Cerium ion redox system in $\text{CeO}_2\text{-xFe}_2\text{O}_3$ solid solution at high temperatures (1,273–1,673 K) in the two-step water-splitting reaction for solar H_2 generation. *J Mater Sci* 2008;43:3153–61. doi:10.1007/s10853-008-2499-z.
- [155] Liu Y, Wen C, Guo Y, Lu G, Wang Y. Modulated CO Oxidation Activity of M-Doped Ceria (M = Cu, Ti, Zr, and Tb): Role of the Pauling Electronegativity of M. *J Phys Chem C* 2010;114:9889–97. doi:10.1021/jp101939v.
- [156] Call F, Roeb M, Schmücker M, Sattler C, Pitz-Paal R. Ceria Doped with Zirconium and Lanthanide Oxides to Enhance Solar Thermochemical Production of Fuels. *J Phys Chem C* 2015;119:6929–38. doi:10.1021/jp508959y.
- [157] Kaneko H, Taku S, Tamaura Y. Reduction reactivity of $\text{CeO}_2\text{-ZrO}_2$ oxide under high O_2 partial pressure in two-step water splitting process. *Sol Energy* 2011;85:2321–30. doi:10.1016/j.solener.2011.06.019.
- [158] Le Gal A, Abanades S. Dopant Incorporation in Ceria for Enhanced Water-Splitting Activity during Solar Thermochemical Hydrogen Generation. *J Phys Chem C* 2012;116:13516–23. doi:10.1021/jp302146c.
- [159] Gabriele Balducci *,†, M. Saiful Islam ‡, Jan Kašpar †, Paolo Fornasiero † and, Graziani† M. Bulk Reduction and Oxygen Migration in the Ceria-Based Oxides 2000. doi:10.1021/CM991089E.
- [160] Zhou G, Shah PR, Kim T, Fornasiero P, Gorte RJ. Oxidation entropies and enthalpies of ceria–zirconia solid solutions. *Catal Today* 2007;123:86–93. doi:10.1016/J.CATTOD.2007.01.013.
- [161] Evdou A, Zaspalis V, Nalbandian L. $\text{La}_{1-x}\text{Sr}_x\text{FeO}_3$ perovskites as redox materials for application in a membrane reactor for simultaneous production of pure hydrogen and synthesis gas. *Fuel* 2009;89:1265–73. doi:10.1016/j.fuel.2009.09.028.
- [162] and MAP, Fierro* JLG. Chemical Structures and Performance of Perovskite Oxides 2001. doi:10.1021/CR980129F.
- [163] Goldschmidt VM. Die Gesetze der Krystallochemie. *Naturwissenschaften* 1926;14:477–85. doi:10.1007/BF01507527.
- [164] Goodenough JB. Electronic and ionic transport properties and other physical aspects of perovskites. *Reports Prog Phys* 2004;67:1915–93. doi:10.1088/0034-4885/67/11/R01.
- [165] Richter J, Holtappels P, Graule T, Nakamura T, Gauckler LJ. Materials design for perovskite SOFC cathodes. *Monatshefte Für Chemie - Chem Mon* 2009;140:985–99. doi:10.1007/s00706-009-0153-3.

- [166] Mizusaki J, Mori N, Takai H, Yonemura Y, Minamiue H, Tagawa H, et al. Oxygen nonstoichiometry and defect equilibrium in the perovskite-type oxides $\text{La}_{1-x}\text{Sr}_x\text{MnO}_{3+\delta}$. *Solid State Ionics* 2000;129:163–77. doi:10.1016/S0167-2738(99)00323-9.
- [167] Van Roosmalen JAM, Cordfunke EHP, Helmholtz RB, Zandbergen HW. The defect chemistry of $\text{LaMnO}_{3\pm\delta}$. 2. structural aspects of $\text{LaMnO}_{3+\delta}$. *J Solid State Chem* 1994;110:100–5. doi:10.1006/jssc.1994.1141.
- [168] De Souza RA, Maier J. A computational study of cation defects in LaGaO_3 . *Phys Chem Chem Phys* 2003;5:740–8. doi:10.1039/b209062g.
- [169] De Souza RA, Islam MS, Ivers-Tiffée E. Formation and migration of cation defects in the perovskite oxide LaMnO_3 . *J Mater Chem* 1999;9:1621–7. doi:10.1039/a901512d.
- [170] Jones A, Islam MS. Atomic-scale insight into LaFeO_3 perovskite: Defect nanoclusters and ion migration. *J Phys Chem C* 2008;112:4455–62. doi:10.1021/jp710463x.
- [171] Battle PD, Bennett JE, Sloan J, Tilley RJD, Vente JF. A-site cation-vacancy ordering in $\text{Sr}(1-3x/2)\text{La}(x)\text{TiO}_3$: A study by HRTEM. *J Solid State Chem* 2000;149:360–9. doi:10.1006/jssc.1999.8546.
- [172] Abe M, Uchino K. X-ray study of the deficient perovskite $\text{La}_{2-3}\text{TiO}_3$. *Mater Res Bull* 1974;9:147–55. doi:10.1016/0025-5408(74)90194-9.
- [173] Royer S, Duprez D, Can F, Courtois X, Batiot-Dupeyrat C, Laassiri S, et al. Perovskites as Substitutes of Noble Metals for Heterogeneous Catalysis: Dream or Reality. *Chem Rev* 2014;114:10292–368. doi:10.1021/cr500032a.
- [174] Rager T. Re-evaluation of the efficiency of a ceria-based thermochemical cycle for solar fuel generation. *Chem Commun* 2012;48:10520–2. doi:10.1039/C2CC34617F.
- [175] Ovenstone J, White JS, Mixture ST. Phase transitions and phase decomposition of $\text{La}_{1-x}\text{Sr}_x\text{CoO}_{3-\delta}$ in low oxygen partial pressures. *J Power Sources* 2008;181:56–61. doi:10.1016/j.jpowsour.2008.03.033.
- [176] Caignaert V, Nguyen N, Hervieu M, Raveau B. $\text{Sr}_2\text{Mn}_2\text{O}_5$, an oxygen-defect perovskite with Mn(III) in square pyramidal coordination. *Mater Res Bull* 1985;20:479–84. doi:10.1016/0025-5408(85)90101-1.
- [177] Alonso JA, MartinezLope MJ, GarciaMunoz JL, FernandezDiaz MT. A structural and magnetic study of the defect perovskite $\text{LaNiO}_{2.5}$ from high-resolution neutron diffraction data. *J Physics-Condensed Matter* 1997;9:6417–26. doi:10.1088/0953-8984/9/30/010.
- [178] Er-Rakho L, Michel C, Raveau B. $\text{La}_{8-x}\text{Sr}_x\text{Cu}_8\text{O}_{20}$: An oxygen-deficient perovskite built of CuO_6 , CuO_5 , and CuO_4 polyhedra. *J Solid State Chem*

1988;73:514–9. doi:10.1016/0022-4596(88)90138-7.

- [179] Stølen S, Bakken E, Mohn CE. Oxygen-deficient perovskites: linking structure, energetics and ion transport. *Phys Chem Chem Phys* 2006;8:429–47. doi:10.1039/B512271F.
- [180] Shao Z, Halle SM. A high-performance cathode for the next generation of solid-oxide fuel cells. *Nature* 2004;431:170–3. doi:10.1038/nature02863.
- [181] Harvey AS, Litterst FJ, Yang Z, Rupp JLM, Infortuna A, Gauckler LJ. Oxidation states of Co and Fe in $\text{Ba}_{1-x}\text{Sr}_x\text{Co}_{1-y}\text{Fe}_y\text{O}_{3-\delta}$ ($x, y = 0.2\text{--}0.8$) and oxygen desorption in the temperature range 300–1273 K. *Phys Chem Chem Phys* 2009;11:3090. doi:10.1039/b819414a.
- [182] McIntosh S, Vente JF, Haije WG, Blank DHA, Bouwmeester HJM. Oxygen stoichiometry and chemical expansion of $\text{Ba}_{0.5}\text{Sr}_{0.5}\text{Co}_{0.8}\text{Fe}_{0.2}\text{O}_{3-\delta}$ measured by in situ neutron diffraction. *Chem Mater* 2006;18:2187–93. doi:10.1021/cm052763x.
- [183] Švarcová S, Wiik K, Tolchard J, Bouwmeester HJM, Grande T. Structural instability of cubic perovskite $\text{Ba}_x\text{Sr}_{1-x}\text{Co}_1\text{Fe}_y\text{O}_{3-\delta}$. *Solid State Ionics* 2008;178:1787–91. doi:10.1016/j.ssi.2007.11.031.
- [184] Ovenstone J, Jung J-I, White JS, Edwards DD, Misture ST. Phase stability of BSCF in low oxygen partial pressures. *J Solid State Chem* 2008;181:576–86. doi:10.1016/j.jssc.2008.01.010.
- [185] Panlener RJ, Blumenthal RN, Garnier JE. A thermodynamic study of nonstoichiometric cerium dioxide. *J Phys Chem Solids* 1975;36:1213–22. doi:10.1016/0022-3697(75)90192-4.
- [186] Demont A, Abanades S. High redox activity of Sr-substituted lanthanum manganite perovskites for two-step thermochemical dissociation of CO_2 . *RSC Adv* 2014;4:54885–91. doi:10.1039/C4RA10578H.
- [187] Evdou A, Zaspalis V, Nalbandian L. $\text{La}_{1-x}\text{Sr}_x\text{MnO}_{3-\delta}$ perovskites as redox materials for the production of high purity hydrogen. *Int J Hydrogen Energy* 2008;33:5554–62. doi:10.1016/j.ijhydene.2008.06.036.
- [188] Nalbandian L, Evdou A, Zaspalis V. $\text{La}_{1-x}\text{Sr}_x\text{MO}_3$ ($M = \text{Mn, Fe}$) perovskites as materials for thermochemical hydrogen production in conventional and membrane reactors. *Int J Hydrogen Energy* 2009;34:7162–72. doi:10.1016/j.ijhydene.2009.06.076.
- [189] Demont A, Abanades S. Solar thermochemical conversion of CO_2 into fuel via two-step redox cycling of non-stoichiometric Mn-containing perovskite oxides. *J Mater Chem A* 2015;3:3536–46. doi:10.1039/C4TA06655C.
- [190] Bork AH, Kubicek M, Struzik M, Rupp JLM. Perovskite $\text{La}_{0.6}\text{Sr}_{0.4}\text{Cr}_{1-x}\text{Co}_x\text{O}_{3-\delta}$ solid solutions for solar-thermochemical fuel production:

- strategies to lower the operation temperature. *J Mater Chem A* 2015;3:15546–57. doi:10.1039/C5TA02519B.
- [191] Zheng K, Klimkiewicz A, Świerczek K, Malik A, Ariga Y, Tominaga T, et al. Chemical diffusion and surface exchange in selected Ln–Ba–Sr–Co–Fe perovskite-type oxides. *J Alloys Compd* 2014;645:357–60. doi:10.1016/j.jallcom.2014.12.110.
- [192] Falkenstein A, Mueller DN, De Souza RA, Martin M. Chemical relaxation experiments on mixed conducting oxides with large stoichiometry deviations. *Solid State Ionics* 2015;280:66–73. doi:10.1016/j.ssi.2015.07.023.
- [193] Sjøgaard M, Bieberle-Hütter A, Hendriksen PV, Mogensen M, Tuller HL. Oxygen incorporation in porous thin films of strontium doped lanthanum ferrite. *J Electroceramics* 2011;27:134–42. doi:10.1007/s10832-011-9658-3.
- [194] Bucher E, Gspan C, Hofer F, Sitte W. Sulphur poisoning of the SOFC cathode material $\text{La}_{0.6}\text{Sr}_{0.4}\text{CoO}_{3-\delta}$. *Solid State Ionics* 2013;238:15–23. doi:10.1016/j.ssi.2013.03.007.
- [195] Preis W, Bucher E, Sitte W. Oxygen exchange kinetics of $\text{La}_{0.4}\text{Sr}_{0.6}\text{FeO}_{3-\delta}$ by simultaneous application of conductivity relaxation and carrier gas coulometry. *Solid State Ionics*, vol. 175, Elsevier; 2004, p. 393–7. doi:10.1016/j.ssi.2003.12.045.
- [196] Kubicek M, Bork Ac AH, Rupp JLM. Perovskite oxides – a review on a versatile material class for solar-to-fuel conversion processes n.d. doi:10.1039/c7ta00987a.
- [197] Rostrup-Nielsen JR. New aspects of syngas production and use. *Catal Today* 2000;63:159–64. doi:10.1016/S0920-5861(00)00455-7.
- [198] Iulianelli A, Liguori S, Wilcox J, Basile A. Advances on methane steam reforming to produce hydrogen through membrane reactors technology: A review. *Catal Rev* 2016;58:1–35. doi:10.1080/01614940.2015.1099882.
- [199] Dry ME. The Fischer–Tropsch process: 1950–2000. *Catal Today* 2002;71:227–41. doi:10.1016/S0920-5861(01)00453-9.
- [200] Leckel D. Diesel Production from Fischer–Tropsch: The Past, the Present, and New Concepts. *Energy & Fuels* 2009;23:2342–58. doi:10.1021/ef900064c.
- [201] Sharma S, Ghoshal SK. Hydrogen the future transportation fuel: From production to applications. *Renew Sustain Energy Rev* 2015;43:1151–8. doi:10.1016/J.RSER.2014.11.093.
- [202] Caballero A, Pérez PJ. Methane as raw material in synthetic chemistry: the final frontier. *Chem Soc Rev* 2013;42:8809. doi:10.1039/c3cs60120j.
- [203] Haldor Topsoe. SynCORTM - Autothermal Reformer (ATR) 2019.

<https://www.topsoe.com/products/equipment/syncortm-autothermal-reformer-atr> (accessed February 11, 2019).

- [204] Rostrup-Nielsen JR, Sehested J, Nørskov JK. Hydrogen and synthesis gas by steam- and CO₂ reforming. *Adv Catal* 2002;47:65–139. doi:10.1016/S0360-0564(02)47006-X.
- [205] Mueller-Langer F, Tzimas E, Kaltschmitt M, Peteves S. Techno-economic assessment of hydrogen production processes for the hydrogen economy for the short and medium term. *Int J Hydrogen Energy* 2007;32:3797–810. doi:10.1016/J.IJHYDENE.2007.05.027.
- [206] Böhmer M, Langnickel U, Sanchez M. Solar steam reforming of methane. *Sol Energy Mater* 1991;24:441–8. doi:10.1016/0165-1633(91)90081-U.
- [207] Berman A, Karn RK, Epstein M. Steam reforming of methane on a Ru/Al₂O₃ catalyst promoted with Mn oxides for solar hydrogen production. *Green Chem* 2007;9:626. doi:10.1039/b613708n.
- [208] De Maria G, Tiberio CA, D'Alessio L, Piccirilli M, Coffari E, Paolucci M. Thermochemical conversion of solar energy by steam reforming of methane. *Energy* 1986;11:805–10. doi:10.1016/0360-5442(86)90019-8.
- [209] Muir JF, Hogan RE, Skocypec RD, Buck R. Solar reforming of methane in a direct absorption catalytic reactor on a parabolic dish: I—Test and analysis 1994;52. doi:10.1016/0038-092X(94)90654-8.
- [210] Agrafiotis C, von Storch H, Roeb M, Sattler C. Solar thermal reforming of methane feedstocks for hydrogen and syngas production—A review. *Renew Sustain Energy Rev* 2014;29:656–82. doi:10.1016/J.RSER.2013.08.050.
- [211] Sheu EJ, Mokheimer EMA, Ghoniem AF. A review of solar methane reforming systems. *Int J Hydrogen Energy* 2015;40:12929–55. doi:10.1016/J.IJHYDENE.2015.08.005.
- [212] Levitan R, Rosin H, Levy M. Chemical reactions in a solar furnace—direct heating of the reactor in a tubular receiver. *Sol Energy* 1989;42:267–272.
- [213] Kodama T, Ohtake H, Matsumoto S, Aoki A, Shimizu T, Kitayama Y. Thermochemical methane reforming using a reactive WO₃/W redox system. *Energy* 2000;25:411–25. doi:10.1016/S0360-5442(99)00084-5.
- [214] Tamme R, Buck R, Epstein M, Fisher U, Sugarmen C. Solar Upgrading of Fuels for Generation of Electricity. *J Sol Energy Eng* 2001;123:160. doi:10.1115/1.1353177.
- [215] Kodama T. High-temperature solar chemistry for converting solar heat to chemical fuels. *Prog Energy Combust Sci* 2003;29:567–97. doi:10.1016/S0360-1285(03)00059-5.
- [216] Buck R, Muir JF, Hogan RE. Carbon dioxide reforming of methane in a solar

- volumetric receiver/reactor: the CAESAR project. *Sol Energy Mater* 1991;24:449–63. doi:10.1016/0165-1633(91)90082-V.
- [217] Rostrup-Nielsen JR, Sehested J, Nørskov JK. Hydrogen and synthesis gas by steam- and CO₂ reforming. *Adv Catal* 2002;47:65–139. doi:10.1016/S0360-0564(02)47006-X.
- [218] Sehested J. Four challenges for nickel steam-reforming catalysts. *Catal Today* 2006;111:103–10. doi:10.1016/J.CATTOD.2005.10.002.
- [219] Amjad U-E-S, Vita A, Galletti C, Pino L, Specchia S. Comparative Study on Steam and Oxidative Steam Reforming of Methane with Noble Metal Catalysts. *Ind Eng Chem Res* 2013;52:15428–36. doi:10.1021/ie400679h.
- [220] Jang BW-L, Nelson RM, Spivey JJ, Ocal M, Oukaci R, Marcelin G. Catalytic oxidation of methane over hexaaluminates and hexaaluminate-supported Pd catalysts. *Catal Today* 1999;47:103–13. doi:10.1016/S0920-5861(98)00288-0.
- [221] McCarty JG, Gusman M, Lowe DM, Hildenbrand DL, Lau KN. Stability of supported metal and supported metal oxide combustion catalysts. *Catal Today* 1999;47:5–17. doi:10.1016/S0920-5861(98)00279-X.
- [222] Fujimoto K, Ribeiro FH, Avalos-Borja M, Iglesia E. Structure and Reactivity of PdO_x/ZrO₂ Catalysts for Methane Oxidation at Low Temperatures. *J Catal* 1998;179:431–42. doi:10.1006/JCAT.1998.2178.
- [223] Miller JB, Malatpure M. Pd catalysts for total oxidation of methane: Support effects. *Appl Catal A Gen* 2015;495:54–62. doi:10.1016/J.APCATA.2015.01.044.
- [224] Feio LSF, Hori CE, Damyanova S, Noronha FB, Cassinelli WH, Marques CMP, et al. The effect of ceria content on the properties of Pd/CeO₂/Al₂O₃ catalysts for steam reforming of methane. *Appl Catal A Gen* 2007;316:107–16. doi:10.1016/J.APCATA.2006.09.032.
- [225] Cassinelli WH, Damyanova S, Parizotto NV, Zanchet D, Bueno JMC, Marques CMP. Study of the properties of supported Pd catalysts for steam and autothermal reforming of methane. *Appl Catal A Gen* 2014;475:256–69. doi:10.1016/J.APCATA.2014.01.006.
- [226] Tong J, Matsumura Y, Suda H, Haraya K. Thin and dense Pd/CeO₂/MPSS composite membrane for hydrogen separation and steam reforming of methane. *Sep Purif Technol* 2005;46:1–10. doi:10.1016/J.SEPPUR.2005.03.011.
- [227] Craciun R, Shereck B, Gorte RJ. Kinetic studies of methane steam reforming on ceria-supported Pd. *Catal Letters* 1998;51:149–53. doi:10.1023/A:1019022009310.

- [228] Mortola VB, Damyanova S, Zanchet D, Bueno JMC. Surface and structural features of Pt/CeO₂-La₂O₃-Al₂O₃ catalysts for partial oxidation and steam reforming of methane. *Appl Catal B Environ* 2011;107:221–36. doi:10.1016/J.APCATB.2011.07.012.
- [229] Farrauto RJ, Hobson MC, Kennelly T, Waterman EM. Catalytic chemistry of supported palladium for combustion of methane. *Appl Catal A Gen* 1992;81:227–237.
- [230] Aasberg-Petersen K, Christensen TS, Dybkjaer I, Sehested J, Østberg M, Coertzen RM, et al. Synthesis gas production for FT synthesis. *Stud Surf Sci Catal* 2004;152:258–405. doi:10.1016/S0167-2991(04)80461-0.
- [231] Aasberg-Petersen K, Bak Hansen J-H, Christensen T., Dybkjaer I, Christensen PS, Stub Nielsen C, et al. Technologies for large-scale gas conversion. *Appl Catal A Gen* 2001;221:379–87. doi:10.1016/S0926-860X(01)00811-0.
- [232] Wang F, Wang G. Performance and cold spot effect of methanol steam reforming for hydrogen production in micro-reactor. *Int J Hydrogen Energy* 2016;41:16835–41. doi:10.1016/J.IJHYDENE.2016.07.083.
- [233] Zheng T, Zhou W, Yu W, Ke Y, Liu Y, Liu R, et al. Methanol steam reforming performance optimisation of cylindrical microreactor for hydrogen production utilising error backpropagation and genetic algorithm. *Chem Eng J* 2019;357:641–54. doi:10.1016/J.CEJ.2018.09.129.
- [234] Chen J, Yan L, Song W, Xu D. Methane steam reforming thermally coupled with catalytic combustion in catalytic microreactors for hydrogen production. *Int J Hydrogen Energy* 2017;42:664–80. doi:10.1016/J.IJHYDENE.2016.12.114.
- [235] Won JY, Jun HK, Jeon MK. Performance of microchannel reactor combined with combustor for methanol steam reforming. *Catal Today* 2006;111:158–63. doi:10.1016/J.CATTOD.2005.11.004.
- [236] Casanovas A, Saint-Gerons M, Griffon F, Llorca J. Autothermal generation of hydrogen from ethanol in a microreactor. *Int J Hydrogen Energy* 2008;33:1827–33. doi:10.1016/J.IJHYDENE.2008.01.018.
- [237] Kim T. Micro methanol reformer combined with a catalytic combustor for a PEM fuel cell. *Int J Hydrogen Energy* 2009;34:6790–8. doi:10.1016/J.IJHYDENE.2009.06.024.
- [238] Izquierdo U, Barrio VL, Cambra JF, Requies J, Güemez MB, Arias PL, et al. Hydrogen production from methane and natural gas steam reforming in conventional and microreactor reaction systems. *Int J Hydrogen Energy* 2012;37:7026–33. doi:10.1016/J.IJHYDENE.2011.11.048.
- [239] Men Y, Gnaser H, Zapf R, Hessel V, Ziegler C, Kolb G. Steam reforming of

- methanol over Cu/CeO₂/γ-Al₂O₃ catalysts in a microchannel reactor. *Appl Catal A Gen* 2004;277:83–90. doi:10.1016/J.APCATA.2004.08.035.
- [240] Ledesma C, López E, Trifonov T, Rodríguez Á, Llorca J. Catalytic reforming of dimethyl ether in microchannels. *Catal Today* 2019;323:209–15. doi:10.1016/J.CATTOD.2018.03.011.
- [241] Delparish A, Avci AK. Modeling of intensified glycerol steam reforming in a heat-exchange integrated microchannel reactor. *Catal Today* 2018;299:328–38. doi:10.1016/J.CATTOD.2017.03.029.
- [242] Delparish A, Koc S, Caglayan BS, Avci AK. Oxidative steam reforming of glycerol to synthesis gas in a microchannel reactor. *Catal Today* 2019;323:200–8. doi:10.1016/J.CATTOD.2018.03.047.
- [243] Zhou W, Ke Y, Wang Q, Wan S, Lin J, Zhang J, et al. Development of cylindrical laminated methanol steam reforming microreactor with cascading metal foams as catalyst support. *Fuel* 2017;191:46–53. doi:10.1016/J.FUEL.2016.11.058.
- [244] Venvik HJ, Yang J. Catalysis in microstructured reactors: Short review on small-scale syngas production and further conversion into methanol, DME and Fischer-Tropsch products. *Catal Today* 2017;285:135–46. doi:10.1016/J.CATTOD.2017.02.014.
- [245] Levent M, J. Gunn D, Ali El-Bousiffi M. Production of hydrogen-rich gases from steam reforming of methane in an automatic catalytic microreactor. *Int J Hydrogen Energy* 2003;28:945–59. doi:10.1016/S0360-3199(02)00195-7.
- [246] Tian J, Ke Y, Kong G, Tan M, Wang Y, Lin J, et al. A novel structured PdZnAl/Cu fiber catalyst for methanol steam reforming in microreactor. *Renew Energy* 2017;113:30–42. doi:10.1016/J.RENENE.2017.04.070.
- [247] Teixeira ACSC, Giudici R. Deactivation of steam reforming catalysts by sintering: experiments and simulation. *Chem Eng Sci* 1999;54:3609–18. doi:10.1016/S0009-2509(98)00516-8.
- [248] Buck R, Muir JF, Hogan RE. Carbon dioxide reforming of methane in a solar volumetric receiver/reactor: the CAESAR project. *Sol Energy Mater* 1991;24:449–63. doi:10.1016/0165-1633(91)90082-V.
- [249] Skocypec RD, Hogan RE, Muir JF. Solar reforming of methane in a direct absorption catalytic reactor on a parabolic dish: II—Modeling and analysis. *Sol Energy* 1994;52:479–90. doi:10.1016/0038-092X(94)90655-6.
- [250] Möller S, Kaucic D, Sattler C. Hydrogen Production by Solar Reforming of Natural Gas: A Comparison Study of Two Possible Process Configurations. *J Sol Energy Eng* 2006;128:16–23. doi:10.1115/1.2164447.
- [251] Electricity from Renewable Resources. Washington, D.C.: National

Academies Press; 2010. doi:10.17226/12619.

- [252] Valades-Pelayo PJ, Romero-Paredes H, Arancibia-Bulnes CA, Villafán-Vidales HI. Geometric optimization of a solar cubic-cavity multi-tubular thermochemical reactor using a Monte Carlo-finite element radiative transfer model. *Appl Therm Eng* 2016;98:575–81. doi:10.1016/J.APPLTHERMALENG.2016.01.002.
- [253] Venstrom LJ, De Smith RM, Bala Chandran R, Boman DB, Krenzke PT, Davidson JH. Applicability of an Equilibrium Model To Predict the Conversion of CO₂ to CO via the Reduction and Oxidation of a Fixed Bed of Cerium Dioxide. *Energy & Fuels* 2015;29:8168–77. doi:10.1021/acs.energyfuels.5b01865.
- [254] Steinfeld A, Brack M, Meier A, Weidenkaff A, Wuillemin D. A solar chemical reactor for co-production of zinc and synthesis gas. *Energy* 1998;23:803–14. doi:10.1016/S0360-5442(98)00026-7.
- [255] Ermanoski I, Siegel NP, Stechel EB. A New Reactor Concept for Efficient Solar-Thermochemical Fuel Production. *J Sol Energy Eng* 2013;135:31002–10. doi:10.1115/1.4023356.
- [256] Diver RB, Miller JE, Allendorf MD, Siegel NP, Hogan RE. Solar Thermochemical Water-Splitting Ferrite-Cycle Heat Engines. *J Sol Energy Eng* 2008;130:41001–8. doi:10.1115/1.2969781.
- [257] Z'Graggen A, Haueter P, Maag G, Vidal A, Romero M, Steinfeld A. Hydrogen production by steam-gasification of petroleum coke using concentrated solar power—III. Reactor experimentation with slurry feeding. *Int J Hydrogen Energy* 2007;32:992–6. doi:10.1016/J.IJHYDENE.2006.10.001.
- [258] Z'Graggen A, Steinfeld A. Hydrogen production by steam-gasification of carbonaceous materials using concentrated solar energy – V. Reactor modeling, optimization, and scale-up. *Int J Hydrogen Energy* 2008;33:5484–92. doi:10.1016/J.IJHYDENE.2008.07.047.
- [259] Piatkowski N, Steinfeld A. Solar gasification of carbonaceous waste feedstocks in a packed-bed reactor-Dynamic modeling and experimental validation. *AIChE J* 2011;57:3522–33. doi:10.1002/aic.12545.
- [260] Yuan C, Jarrett C, Chueh W, Kawajiri Y, Henry A. A new solar fuels reactor concept based on a liquid metal heat transfer fluid: Reactor design and efficiency estimation. *Sol Energy* 2015;122:547–61. doi:10.1016/j.solener.2015.08.019.
- [261] Marxer D, Furler P, Takacs M, Steinfeld A. Solar thermochemical splitting of CO₂ into separate streams of CO and O₂ with high selectivity, stability, conversion, and efficiency. *Energy Environ Sci* 2017;10:1142–9.

doi:10.1039/C6EE03776C.

- [262] Tamaura Y, Steinfeld A, Kuhn P, Ehrensberger K. Production of solar hydrogen by a novel, 2-step, water-splitting thermochemical cycle. *Energy* 1995;20:325–30. doi:10.1016/0360-5442(94)00099-O.
- [263] Pregger T, Graf D, Krewitt W, Sattler C, Roeb M, Moeller S. Prospects of solar thermal hydrogen production processes. *Int J Hydrogen Energy* 2009;34:4256–67. doi:10.1016/j.ijhydene.2009.03.025.
- [264] Roeb M, Sattler C, Klüser R, Monnerie N, de Oliveira L, Konstandopoulos AG, et al. Solar Hydrogen Production by a Two-Step Cycle Based on Mixed Iron Oxides. *J Sol Energy Eng* 2006;128:125. doi:10.1115/1.2183804.
- [265] Roeb M, Neises M, Säck J-P, Rietbrock P, Monnerie N, Dersch J, et al. Operational strategy of a two-step thermochemical process for solar hydrogen production. *Int J Hydrogen Energy* 2009;34:4537–45. doi:10.1016/j.ijhydene.2008.08.049.
- [266] Roeb M, Säck J-P-P, Rietbrock P, Prah C, Schreiber H, Neises M, et al. Test operation of a 100kW pilot plant for solar hydrogen production from water on a solar tower. *Sol Energy* 2011;85:634–44. doi:10.1016/j.solener.2010.04.014.
- [267] Gokon N, Yamamoto H, Kondo N, Kodama T. Internally Circulating Fluidized Bed Reactor Using m-ZrO₂ Supported NiFe₂O₄ Particles for Thermochemical Two-Step Water Splitting. *J Sol Energy Eng* 2010;132:21102–10. doi:10.1115/1.4001154.
- [268] Gokon N, Mizuno T, Takahashi S, Kodama T. A Two-Step Water Splitting With Ferrite Particles and Its New Reactor Concept Using an Internally Circulating Fluidized-Bed. *Sol. Energy*, vol. 2006, ASME; 2006, p. 205–14. doi:10.1115/ISEC2006-99063.
- [269] Gokon N, Kodama T, Nagasaki A, Sakai K, Hatamachi T. Ferrite-Loaded Ceramic Foam Devices Prepared by Spin-Coating Method for a Solar Two-Step Thermochemical Cycle. *ASME 2009 3rd Int. Conf. Energy Sustain. Vol. 2*, ASME; 2009, p. 439–49. doi:10.1115/ES2009-90172.
- [270] Gokon N, Yamamoto H, Kondo N, Kodama T. Internally Circulating Fluidized Bed Reactor Using m-ZrO₂ Supported NiFe₂O₄ Particles for Thermochemical Two-Step Water Splitting. *J Sol Energy Eng* 2010;132:021102. doi:10.1115/1.4001154.
- [271] Kaneko H, Miura T, Ishihara H, Yokoyama T, Chen M, Tamaura Y. Solar Rotary Reactor for Continuous H₂ Production Using Two-Step Water Splitting Process. *WHEC* 2006;16:13–6.
- [272] Kaneko H, Lee C, Ishikawa Y, Hosogoe K, Tamaura Y. Solar H₂ Production with Tokyo Tech Rotary-Type Solar Reactor to Be Tested Using Solar

- Concentration System at Csiro in Australia. *Es2009 Proc Asme 3rd Int Conf Energy Sustain Vol 2* 2009:491–6. doi:10.1115/ES2009-90420.
- [273] Kaneko H, Miura T, Fuse A, Ishihara H, Taku S, Fukuzumi H, et al. Rotary-Type Solar Reactor for Solar Hydrogen Production with Two-step Water Splitting Process n.d. doi:10.1021/ef060581z.
- [274] Tamaura Y, Kaneko H, Naganuma Y, Taku S, Ouchi K, Hasegawa N. Simultaneous Production of H₂ AND O₂ WITH ROTARY-TYPE SOLAR REACTOR (TOKYO TECH MODEL) FOR SOLAR HYBRID FUEL. *ASME 2008 2nd Int. Conf. Energy Sustain. Vol. 2*, ASME; 2008, p. 403–8. doi:10.1115/ES2008-54282.
- [275] Diver RB, Miller JE, Siegel NP, Moss TA. Testing of a CR5 Solar Thermochemical Heat Engine Prototype. *ASME 2010 4th Int. Conf. Energy Sustain. Vol. 2*, ASME; 2010, p. 97–104. doi:10.1115/ES2010-90093.
- [276] Miller JE, Allendorf MD, Ambrosini A, Coker EN, Diver RB. J, Ermanoski I, et al. Development and assessment of solar-thermal-activated fuel production. Phase 1, summary. Albuquerque, NM, and Livermore, CA (United States): Sandia National Laboratories; 2012. doi:10.2172/1055617.
- [277] Barin I, Wiley InterScience (Online service). Thermochemical data of pure substances. n.d.
- [278] Ogulgonen CG, Calisan A, Uner D, Kincal S. A Low Cost, Continuous H₂-CH₄ Sensor Assembly. In: Dincer I, Midilli A, Yurdakul H, Aydin K, editors. *3rd Int. Hydrog. Technol. Congr.*, Alanya: National Hydrogen Association; 2018, p. 167–9.
- [279] Calisan A, Ogulgonen CG, Yilmaz A, Uner D, Kincal S. Steam Methane Reforming Over Structured Reactors Under Concentrated Solar Irradiation (Accepted Manuscript). *Int J Hydrogen Energy* 2019;Accepted.
- [280] Bilgen E, Ducarroir M, Foex M, Sibieude F, Trombe F. Use of solar energy for direct and two-step water decomposition cycles. *Int J Hydrogen Energy* 1977;2:251–7. doi:10.1016/0360-3199(77)90021-0.
- [281] Bulfin B, Vieten J, Agrafiotis C, Roeb M, Sattler C. Applications and limitations of two step metal oxide thermochemical redox cycles; a review n.d. doi:10.1039/c7ta05025a.
- [282] Roeb M, Neises M, Monnerie N, Call F, Simon H, Sattler C, et al. Materials-related aspects of thermochemical water and carbon dioxide splitting: A review. *Materials (Basel)* 2012;5:2015–54. doi:10.3390/ma5112015.
- [283] Carrillo AJ, Serrano DP, Pizarro P, Coronado JM. Improving the Thermochemical Energy Storage Performance of the Mn₂O₃/Mn₃O₄ Redox Couple by the Incorporation of Iron. *ChemSusChem* 2015;8:1947–54. doi:10.1002/cssc.201500148.

- [284] Carrillo AJ, Serrano DP, Pizarro P, Coronado JM. Manganese oxide-based thermochemical energy storage: Modulating temperatures of redox cycles by Fe–Cu co-doping. *J Energy Storage* 2016;5:169–76. doi:10.1016/J.EST.2015.12.005.
- [285] Crum J V., Riley BJ, Vienna JD. Binary Phase Diagram of the Manganese Oxide-Iron Oxide System. *J Am Ceram Soc* 2009;92:2378–84. doi:10.1111/j.1551-2916.2009.03230.x.
- [286] Kjellqvist L, Selleby M. Thermodynamic Assessment of the Fe-Mn-O System. *J Phase Equilibria Diffus* 2010;31:113–34. doi:10.1007/s11669-009-9643-6.
- [287] Zinkevich M, Djurovic D, Aldinger F. Thermodynamic modelling of the cerium–oxygen system. *Solid State Ionics* 2006;177:989–1001. doi:10.1016/J.SSI.2006.02.044.
- [288] Edmund J. Cussen †, Jeremy Sloan †,‡, Jaap F. Vente †, Peter D. Battle *,† and, Gibb§ TC. 15R SrMn_{1-x}FexO_{3-δ} (x ≈ 0.1); A New Perovskite Stacking Sequence 1998. doi:10.1021/IC980802J.
- [289] Schmidt M, Campbell S. In situ neutron diffraction study (300–1273 K) of non-stoichiometric strontium ferrite SrFeO_x. *J Phys Chem Solids* 2002;63:2085–92. doi:10.1016/S0022-3697(02)00198-1.
- [290] Vieten J, Bulfin B, Call F, Lange M, Schmücker M, Francke A, et al. Perovskite oxides for application in thermochemical air separation and oxygen storage. *J Mater Chem A* 2016;4:13652–9. doi:10.1039/C6TA04867F.
- [291] Jain A, Hautier G, Ong SP, Moore CJ, Fischer CC, Persson KA, et al. Formation enthalpies by mixing GGA and GGA + U calculations. *Phys Rev B* 2011;84:045115. doi:10.1103/PhysRevB.84.045115.
- [292] Jain A, Ong SP, Hautier G, Chen W, Richards WD, Dacek S, et al. Commentary: The Materials Project: A materials genome approach to accelerating materials innovation. *APL Mater* 2013;1:011002. doi:10.1063/1.4812323.
- [293] Curnan MT, Kitchin JR. Effects of Concentration, Crystal Structure, Magnetism, and Electronic Structure Method on First-Principles Oxygen Vacancy Formation Energy Trends in Perovskites. *J Phys Chem C* 2014;118:28776–90. doi:10.1021/jp507957n.
- [294] Bulfin B, Vieten J, Starr DE, Azarpira A, Zachäus C, Hävecker M, et al. Redox chemistry of CaMnO₃ and Ca_{0.8}Sr_{0.2}MnO₃ oxygen storage perovskites. *J Mater Chem A* 2017;5:7912–9. doi:10.1039/C7TA00822H.
- [295] Ezbiri M, Allen KM, Gálvez ME, Michalsky R, Steinfeld A. Design Principles of Perovskites for Thermochemical Oxygen Separation.

ChemSusChem 2015;8:1966–71. doi:10.1002/cssc.201500239.

- [296] Nagai T, Ito W, Sakon T. Relationship between cation substitution and stability of perovskite structure in SrCoO_{3-δ}-based mixed conductors. *Solid State Ionics* 2007;177:3433–44. doi:10.1016/J.SSI.2006.10.022.
- [297] Bakken E, Stølen S, Norby T, Glenne R, Budd M. Redox energetics of SrFeO_{3-δ} — a coulometric titration study. *Solid State Ionics* 2004;167:367–77. doi:10.1016/J.SSI.2004.01.014.
- [298] Haavik C, Atake T, Kawaji H, Stølen S. On the entropic contribution to the redox energetics of SrFeO_{3-δ}. *Phys Chem Chem Phys* 2001;3:3863–70. doi:10.1039/b104401j.
- [299] Bakken E, Norby T, Stølen S. Nonstoichiometry and reductive decomposition of CaMnO_{3-δ}. *Solid State Ionics* 2005;176:217–23. doi:10.1016/J.SSI.2004.07.001.
- [300] Lisbeth Rørmark †,‡, Anne Beate Mørch ‡, Kjell Wiik †, Svein Stølen ‡ and Tor Grande* †. Enthalpies of Oxidation of CaMnO_{3-δ}, Ca₂MnO_{4-δ} and SrMnO_{3-δ} Deduced Redox Properties 2001. doi:10.1021/CM011050L.
- [301] Pishahang M, Larring Y, McCann M, Bredesen R. Ca_{0.9}Mn_{0.5}Ti_{0.5}O_{3-δ}: A Suitable Oxygen Carrier Material for Fixed-Bed Chemical Looping Combustion under Syngas Conditions. *Ind Eng Chem Res* 2014;53:10549–56. doi:10.1021/ie500928m.
- [302] Rydén M, Lyngfelt A, Mattisson T. CaMn_{0.875}Ti_{0.125}O₃ as oxygen carrier for chemical-looping combustion with oxygen uncoupling (CLOU)—Experiments in a continuously operating fluidized-bed reactor system. *Int J Greenh Gas Control* 2011;5:356–66. doi:10.1016/J.IJGGC.2010.08.004.
- [303] Bevan DJM, Kordis J. Mixed oxides of the type MO₂ (fluorite)—M₂O₃—I oxygen dissociation pressures and phase relationships in the system CeO₂□Ce₂O₃ at high temperatures. *J Inorg Nucl Chem* 1964;26:1509–23. doi:10.1016/0022-1902(64)80038-5.
- [304] Hao Y, Yang C-K, Haile SM. Ceria–Zirconia Solid Solutions (Ce_{1-x}Zr_xO_{2-δ}, x ≤ 0.2) for Solar Thermochemical Water Splitting: A Thermodynamic Study. *Chem Mater* 2014;26:6073–82. doi:10.1021/cm503131p.
- [305] Bonk A, Remhof A, Maier AC, Trottmann M, Schlupp MVF, Battaglia C, et al. Low-Temperature Reducibility of M_xCe_{1-x}O₂ (M = Zr, Hf) under Hydrogen Atmosphere. *J Phys Chem C* 2016;120:118–25. doi:10.1021/acs.jpcc.5b10796.
- [306] Cho WC, Seo MW, Kim SD, Kang KS, Bae KK, Kim CH, et al. Reactivity of iron oxide as an oxygen carrier for chemical-looping hydrogen production. *Int J Hydrogen Energy* 2012;37:16852–63. doi:10.1016/J.IJHYDENE.2012.08.020.

- [307] Le Gal A, Abanades S, Flamant G, ephane Abanades S, Flamant G, Abanades S, et al. CO₂ and H₂O Splitting for Thermochemical Production of Solar Fuels Using Nonstoichiometric Ceria and Ceria/Zirconia Solid Solutions. *Energy & Fuels* 2011;25:4836–45. doi:10.1021/ef200972r.
- [308] Muhich CL, Evanko BW, Weston KC, Lichty P, Liang X, Martinek J, et al. Efficient generation of H₂ by splitting water with an isothermal redox cycle. *Science* 2013;341:540–2. doi:10.1126/science.1239454.
- [309] Steinfeld A, Schubnell M. Optimum aperture size and operating temperature of a solar cavity-receiver. *Sol Energy* 1993;50:19–25. doi:10.1016/0038-092X(93)90004-8.
- [310] Masel RI. Principles of adsorption and reaction on solid surfaces. New York : Wiley, c1996.; 1996.
- [311] Zhu H, Qin Z, Shan W, Shen W, Wang J. Pd/CeO₂–TiO₂ catalyst for CO oxidation at low temperature: a TPR study with H₂ and CO as reducing agents. *J Catal* 2004;225:267–77. doi:10.1016/j.jcat.2004.04.006.
- [312] Markaryan GL, Ikryannikova LN, Muravieva GP, Turakulova AO, Kostyuk BG, Lunina E V, et al. Red–ox properties and phase composition of CeO₂–ZrO₂ and Y₂O₃–CeO₂–ZrO₂ solid solutions. *Colloids Surfaces A Physicochem Eng Asp* 1999;151:435–47. doi:10.1016/S0927-7757(98)00574-3.
- [313] Wimmers OJ, Arnoldy P, Moulijn JA. Determination of the reduction mechanism by temperature-programmed reduction: application to small iron oxide (Fe₂O₃) particles. *J Phys Chem* 1986;90:1331–7. doi:10.1021/j100398a025.
- [314] Fröhlich G, Sachtler WMH. Reduction enhancement of Fe₂O₃ in physical mixtures with Pt/mordenite via Pt migration or ‘hydrogen spillover.’ *J Chem Soc Faraday Trans* 1998;94:1339–46. doi:10.1039/A800200B.
- [315] Liang M, Kang W, Xie K. Comparison of reduction behavior of Fe₂O₃, ZnO and ZnFe₂O₄ by TPR technique. *J Nat Gas Chem* 2009;18:110–3. doi:10.1016/S1003-9953(08)60073-0.
- [316] Ji Y, Zhao Z, Duan A, Jiang G, Liu J. Comparative Study on the Formation and Reduction of Bulk and Al₂O₃-Supported Cobalt Oxides by H₂-TPR Technique. *J Phys Chem C* 2009;113:7186–99. doi:10.1021/jp8107057.
- [317] Bernal S, Blanco G, Gatica JM, Pérez-Omil JA, Pintado JM, Vidal H. Chemical Reactivity of Binary Rare Earth Oxides. In: Adachi G, Imanaka N, Kang ZC, editors., Springer Netherlands; 2004, p. 9–55.
- [318] Liotta LF, Di Carlo G, Pantaleo G, Venezia AM, Deganello G. Co₃O₄/CeO₂ composite oxides for methane emissions abatement: Relationship between Co₃O₄–CeO₂ interaction and catalytic activity. *Appl Catal B Environ*

2006;66:217–27. doi:10.1016/j.apcatb.2006.03.018.

- [319] Chen Y, Liu D, Yang L, Meng M, Zhang J, Zheng L, et al. Ternary composite oxide catalysts CuO/Co₃O₄-CeO₂ with wide temperature-window for the preferential oxidation of CO in H₂-rich stream. *Chem Eng J* 2013;234:88–98. doi:10.1016/j.cej.2013.08.063.
- [320] Monazam ER, Breault RW, Siriwardane R. Kinetics of Magnetite (Fe₃O₄) Oxidation to Hematite (Fe₂O₃) in Air for Chemical Looping Combustion. *Ind Eng Chem Res* 2014;53:13320–8. doi:10.1021/ie501536s.
- [321] Schunk LO, Haeberling P, Wepf S, Wuillemin D, Meier A, Steinfeld A. A Receiver-Reactor for the Solar Thermal Dissociation of Zinc Oxide. *J Sol Energy Eng* 2008;130:21006–9. doi:10.1115/1.2840576.
- [322] Chueh WC, Falter C, Abbott M, Scipio D, Furler P, Haile SM, et al. High-Flux Solar-Driven Thermochemical Dissociation of CO₂ and H₂O Using Nonstoichiometric Ceria. *Science* (80-) 2010;330:1797–801. doi:10.1126/science.1197834.
- [323] Roeb M, Gathmann N, Neises M, Sattler C, Pitz-Paal R. Thermodynamic analysis of two-step solar water splitting with mixed iron oxides. *Int J Energy Res* 2009;33:893–902. doi:10.1002/er.1513.
- [324] Kostoglou M, Lorentzou S, Konstandopoulos AG. Improved kinetic model for water splitting thermochemical cycles using Nickel Ferrite. *Int J Hydrogen Energy* 2014;39:6317–27. doi:10.1016/j.ijhydene.2014.01.121.
- [325] Jiang Q, Tong J, Zhou G, Jiang Z, Li Z, Li C. Thermochemical CO₂ splitting reaction with supported La_xA_{1-x}Fe_yB_{1-y}O₃ (A=Sr, Ce, B=Co, Mn; 0 ≤ x, y ≤ 1) perovskite oxides. *Sol Energy* 2014;103:425–37. doi:10.1016/j.solener.2014.02.033.
- [326] Otto EM. Equilibrium Pressures of Oxygen over Oxides of Lead at Various Temperatures. *J Electrochem Soc* 1966;113:525–7. doi:10.1149/1.2424016.
- [327] Butler G, Copp JL. The thermal decomposition of lead dioxide in air. *J Chem Soc* 1956:725–735.
- [328] Nozaki T, Fujimoto K. Oxide ion transport for selective oxidative coupling of methane with new membrane reactor. *AIChE J* 1994;40:870–7. doi:10.1002/aic.690400513.
- [329] Neeft JPA, Makkee M, Moulijn JA. Catalytic oxidation of carbon black — I. Activity of catalysts and classification of oxidation profiles. *Fuel* 1998;77:111–9. doi:10.1016/S0016-2361(97)00187-7.
- [330] Uner D, Demirkol MK, Dernaika B. A novel catalyst for diesel soot oxidation. *Appl Catal B Environ* 2005;61:334–45. doi:10.1016/J.APCATB.2005.05.011.

- [331] LUXEL corp. Vapor pressure chart 2018. <https://luxel.com/wp-content/uploads/2013/04/Luxel-Vapor-Pressure-Chart.pdf> (accessed April 8, 2018).
- [332] Thompson BA, Strong RL. SELF-DIFFUSION OF OXYGEN IN LEAD OXIDE1. *J Phys Chem* 1963;67:594–7. doi:10.1021/j100797a012.
- [333] Nozaki T, Hashimoto S, Omata K, Fujimoto K. Oxidative coupling of methane with membrane reactors containing lead oxide. *Ind Eng Chem Res* 1993;32:1174–1179.
- [334] Honma S, Sano N, Matsushima Y. Electrochemical Measurement of the Diffusivity of Oxygen in Liquid Lead. *Inst Met Lect Trans*, TL~IA 1930;7:8–10.
- [335] Calisan A, Ogulgonen CG, Kincal S, Uner D. Finding the optimum between volatility and cycle temperatures in solar thermochemical hydrogen production: Pb/PbO pair. *Int J Hydrogen Energy* 2019. doi:10.1016/j.ijhydene.2018.12.189.
- [336] Nekokar N, Pourabdoli M, Ghaderi Hamidi A, Uner D. Effect of mechanical activation on thermal energy storage properties of Co₃O₄/CoO system. *Adv Powder Technol* 2018;29:333–40. doi:10.1016/J.APT.2017.11.020.
- [337] Ay H, Üner D. Dry reforming of methane over CeO₂ supported Ni, Co and Ni–Co catalysts. *Appl Catal B Environ* 2015;179:128–38. doi:10.1016/j.apcatb.2015.05.013.
- [338] Chueh WC, Abbott M, Scipio D, Haile SM. High-flux solar-driven thermochemical dissociation of CO₂ and H₂O using ceria redox reactions. *Science* (80-) 2010;63:2010. doi:10.1126/science.1197834.
- [339] Ozcan H, Dincer I. Energy and exergy analyses of a solar driven Mg–Cl hybrid thermochemical cycle for co-production of power and hydrogen. *Int J Hydrogen Energy* 2014;39:15330–41. doi:10.1016/J.IJHYDENE.2014.07.089.
- [340] Feaviour MR, Bailie JE. WO2005056179A1.pdf. WO/2005/056179, 2005.
- [341] Haldor Topsoe. Convection Reformer HTCR 2019. <https://www.topsoe.com/products/equipment/convection-reformer-htcr> (accessed February 14, 2019).

APPENDICES

A. A Brief Literature Survey on Red/Ox Couples

Table A.1 Literature Survey on Red/Ox Materials

Red/ox Material	Oxygen Desorption Step		Water Splitting Step		Reactor	Important Points	Ref
	T (°C)	O ₂ (mL/g)	T (°C)	H ₂ (ml/g)			
La _{0.9} St _{0.1} MnO _{3-γ}	1400	0.55±0.09	800	0.91±0.04	Fixed bed alumina Tube Reactor; Infrared heater; heating ramp 500 °C/min both cooling and heating	O ₂ production increases with Sr content; Oxygen release rate is independent on Sr-content. It is limited by rate of temperature change; hydrogen production rate decreases at high levels of Sr; H ₂ production could be limited by surface reaction kinetics	[58]
		1.45±0.05		2.89±0.07			
La _{0.8} St _{0.2} MnO _{3-γ}	3.4±0.3	5.68±0.07					
	4.9±0.4	8.9±0.2					

Table A.1 (continued) Literature Survey on Red/Ox Materials

Red/ox Material	Oxygen Desorption Step		Water Splitting Step		Reactor	Important Points	Ref
	T (°C)	O ₂ (mL/g)	T (°C)	H ₂ (mL/g)			
La _{0.6} Ca _{0.4} Mn _{0.6} Al _{0.4} O ₃	1700	6.01	-	-	TGA	Sr replacement with Ca increases oxygen nonstoichiometry; the red/ox couples Mn ⁴⁺ /Mn ³⁺ and Mn ³⁺ /Mn ²⁺ described the chemical defects; Reoxidation by H ₂ O and CO ₂ are less favorable than CeO ₂	[23]
La _{0.6} Ca _{0.4} Mn _{0.6} Al _{0.4} O ₃	1750		-	-			
La _{0.6} Ca _{0.4} Mn _{0.6} Al _{0.4} O ₃	1800		-	-			
La _{0.6} Ca _{0.4} Mn _{0.6} Al _{0.4} O ₃	1900		-	-			
La _{0.6} Ca _{0.4} Mn _{0.6} Al _{0.4} O ₃	1970		-	-			
20 wt % Fe ₃ O ₄ in 8mol% YSZ	1450	-	1200	3 (max)	Fixed bed alumina tube reactor; heating ramp 10 °C/min both cooling and heating;	The dwell time at reduction T increases the reduction extent; that is, the hydrogen production is doubled after 60mins at 1450 °C and reaches to 3mL/g	[22]

Table A.1 (continued) Literature Survey on Red/Ox Materials

Red/ox Material	Oxygen Desorption Step		Water Splitting Step		Reactor	Important Points	Ref
	T (°C)	O ₂ (mL/g)	T (°C)	H ₂ (mL/g)			
10 wt % CoFe ₂ O ₄ in 8mol% YSZ	1350- 1500	-	1200	1.5 (max)	Fixed bed alumina tube reactor; heating ramp 10 °C/min	The hydrogen yield increases 5.5 times as the reduction temperature increases from 1350 to 1500	[22]
CeO ₂	1300	1.69	-	-	TGA; heating rate 50 °C/min	CeO ₂ was thermally reduced to CeO _{1.96} and reoxidized by CO ₂ ; porous structure using SPF-G method was thermally stable over 2000cycles;	[97]
Ce _{0.75} Zr _{0.25} O ₂	1400	5.3	1200	10.4	TGA; heating rate 20 °C/min	synthesized by coprecipitation, Pechini, sol-gel and hydrothermal methods; the best performing by Pechini method due to its porous morphology;; Zr- addition increases the reduction yield from 5% to 20% as compared to CeO ₂ ;	[47]

Table A.1 (continued) Literature Survey on Red/Ox Materials

Red/ox Material	Oxygen Desorption Step		Water Splitting Step		Reactor	Important Points	Ref
	T (°C)	O ₂ (mL/g)	T (°C)	H ₂ (mL/g)			
CeO ₂	1300	1.69	-	-	Quartz chamber with platinum cup for thermal reduction; fixed bed quartz tubular reactor for water splitting; infrared heater; Heating ramp >1300 °C/min	The reduction degree of CeO ₂ is highly dependent on high temperature step; maximum reduction degree was found as CeO _{1.89} ; obtained H ₂ /O ₂ ratios were very close to stoichiometry; the amount of hydrogen production has no dependency on temperature; NiFe ₂ O ₄ /m-ZrO ₂ shows the highest oxygen evolution rate than CeO ₂ ; however, reoxidation is much more slower	[24]
	1350	2.46	-	-			
	1400	4.62	-	-			
	1450	5.22	-	-			
	1500	5.87	-	-			
	1550	7.02	-	-			
	1500	5.1	400	10.0			
	1500	4.9	600	10.0			
NiFe ₂ O ₄	1400	5.1	800	10.2			
		5.3	1000	11.3			
		6.4		11.4			
NiFe ₂ O ₄ /m-	1400	5.0	1000	11.3			
NiFe ₂ O ₄ /c-		3.3		6.4			

Table A.1 (continued) Literature Survey on Red/Ox Materials

Red/ox Material	Oxygen Desorption Step		Water Splitting Step		Reactor	Important Points	Ref
	T (°C)	O ₂ (mL/g)	T (°C)	H ₂ (mL/g)			
CeO ₂	1500	5.2	1150	6.4	Quartz chamber with platinum cup for thermal reduction; fixed bed quartz tubular reactor for water splitting; infrared heater; Heating ramp >1300 °C/min	The oxygen evolution rates are ordered as Ni-CeO ₂ >Mn-CeO ₂ >Co-CeO ₂ >Fe-CeO ₂ while hydrogen production rates are as CeO ₂ >Mn-CeO ₂ >Fe-CeO ₂ >Co-CeO ₂ >Ni-CeO ₂ ; increase in doped content results with a different crystal structures which significantly changes the production rates e.g. formation of Fe ₂ O ₃ , CeFeO _{2-δ} , CeO ₂ and Fe-CeO _{2-δ} .	[99]
5 mol% Fe-CeO ₂		5.9		10.2			
5 mol% Co-CeO ₂		5.3		11.7			
5 mol% Ni- CeO ₂		5.6		11			
5 mol% Mn- CeO ₂		5.9		8.5			
10 mol% Fe-CeO ₂		6.6		11			
10 mol% Co-CeO ₂		4.8		11.1			
10 mol% Ni-CeO ₂		4.8		6.7			
10 mol% Mn-CeO ₂		5.7		6.8			
15 mol% Fe- CeO ₂		6.6		10			
15 mol% Co- CeO ₂		7.3		12			
15 mol% Ni- CeO ₂		5.45		17.2			
15 mol% Mn- CeO ₂		6.4		15.4			

Table A.1 (continued) Literature Survey on Red/Ox Materials

Red/ox Material	Oxygen Desorption		Water Splitting Step		Reactor	Important Points	Ref
	T (°C)	O ₂ (mL/g)	T (°C)	H ₂ (mL/g)			
Ba _{0.5} Sr _{0.5} Co _{0.8} Fe _{0.2} O _{3-δ}	1000	14.4	800	2	TGA; rate 20 °C/min	O ₂ evolution order; La _{0.8} Sr _{0.2} CoO ₃ > Ba _x Sr _{1-x} Co _y Fe _{1-y} O ₃ > La _x Sr _{1-x} Co _y Fe _{1-y} O ₃ > La _x Sr _{1-x} FeO ₃ > La Sr Co O ₄ > La _x Sr _{1-x} MnO ₃ ; This order is dependent on the charge balance of perovskite. The reduction of Co in perovskite shows better performance even if they have the same oxidation state with Fe. the magnitude of driving force disrupts the crystallographic structure as $2(La, Sr)CoO_3 \rightarrow (La, Sr)_2CoO_4 + CoO + 0.5O_2$	[59]
Ba _{0.5} Sr _{0.5} Co _{0.6} Fe _{0.4} O _{3-δ}		14.7	-	-			
Ba _{0.5} Sr _{0.5} Co _{0.2} Fe _{0.8} O _{3-δ}		15.2	-	-			
Ba _{0.25} Sr _{0.75} Co _{0.8} Fe _{0.2} O _{3-δ}		16.8	800	1.8			
La _{0.8} Sr _{0.2} MnO _{3-δ}	1400	2.7	-	-			
La _{0.65} Sr _{0.35} MnO _{3-δ}		4	1050	2.9			
La _{0.5} Sr _{0.5} MnO _{3-δ}		7.2	1000	4.7			
La _{0.6} Sr _{0.4} Co _{0.2} Fe _{0.8} O _{3-δ}	1200	12.1	800	2.2			
La _{0.8} Sr _{0.2} CoO _{3-δ}	1300	10.2	-	-			
La _{0.6} Sr _{0.4} FeO _{3-δ}	1200	17.6	-	-			
LaSrCoO ₄	1300	6.4	800	3.9			
LaSrFeO ₄	1200	1.6	-	-			

Table A.1 (continued) Literature Survey on Red/Ox Materials

Red/ox Material	Oxygen Desorption Step		Water Splitting Step		Reactor	Important Points	Ref
	T (°C)	O ₂ (mL/g)	T (°C)	H ₂ (mL/g)			
CeO ₂	1500	5.7	-	-	Fixed bed alumina tubular reactor; heated by electrical furnace; heating rate 20 °C/min up to 1200 °C and 5 °C/min to 1400 or 1500 °C	doping 4+ cations with smaller radius into ceria increases the oxygen production due to decrease in diffusivity barrier and vacancy formation energy; increase oxygen vacancy by addition of 3+ cations is independent of ionic radius; the reduced materials reoxidized by CO ₂ between 700 and 1100 °C; CO production was doubled for Ce _{0.75} Zr _{0.25} O ₂ as compared to CeO ₂ ; reoxidation of 3+ doped ceria showed lower performance as expected from reduction period	[104]
Ce _{0.8} Ti _{0.2} O ₂	1400	13.2	-	-			
Ce _{0.8} Sn _{0.2} O ₂		11.2	-	-			
Ce _{0.75} Hf _{0.25} O ₂	1500	10.2	-	-			
Ce _{0.75} Zr _{0.25} O ₂		9.2	-	-			
Ce _{0.9} La _{0.1} O _{2-γ}		4.5	-	-			
Ce _{0.85} La _{0.15} O _{2-γ}		3.9	-	-			
Ce _{0.85} Sr _{0.15} O _{2-γ}		3.8	-	-			
Ce _{0.85} Y _{0.15} O _{2-γ}		3.9	-	-			

Table A.1 (continued) Literature Survey on Red/Ox Materials

Red/ox Material	Oxygen Desorption		Water Splitting Step		Reactor	Important Points	Ref
	T (°C)	O ₂ (mL/g)	T (°C)	H ₂ (mL/g)			
LaFeO ₃	>1210	1.3	-	-	Fixed bed tubular reactor; rate for support activity 20 °C/min up to 800 °C and 10 °C/min to 1300 °C; rate of A- and B- site effect 20 °C/min up to 1200 °C and 5 °C/min to 1300 °C;	LaFeO ₃ , LaCoO ₃ and LaMnO ₃ , the reduction mechanism occurs by transformation of Mn ^{2+,3+} to Mn ²⁺ , Co ^{2+,3+} to Co ²⁺ and Fe ^{2+,3+} to Fe ²⁺ ; the change in oxidation state of Fe is thermodynamically less favorable; negligible CO produced by reduced LaFeO ₃ , LaCoO ₃ , LaMnO ₃ , LaFe _{0.7} Co _{0.3} O ₃ and LaFe _{0.7} Mn _{0.3} O ₃ during the reoxidation at 1000 °C; to enhance thermal stability the materials were doped on SiO ₂ ; the enhancement by support was investigated by doping LaFe _{0.7} Co _{0.3} O ₃ to ZrO ₂ , Al ₂ O ₃ and SiO ₂ ; the maximum oxygen evolution rate increases 13 times for SiO ₂	[100]
LaCoO ₃	>800	11.8	-	-			
LaMnO ₃		10.6	-	-			
LaFe _{0.7} Co _{0.3} O ₃		6.4	-	-			
LaFe _{0.7} Mn _{0.3} O ₃		8.5	-	-			
LaFeO ₃ /SiO ₂	800 to 1200	≈2.9	-	-			
SrFeO ₃ /SiO ₂		≈1.6	-	-			
La _{0.7} Sr _{0.3} FeO ₃ /Si		≈6.5	-	-			
La _{0.7} Ce _{0.3} FeO ₃ /S		≈4.8	-	-			
LaFe _{0.9} Co _{0.1} O ₃ /S		≈3.8	-	-			
LaFe _{0.7} Co _{0.3} O ₃ /S		≈5.5	-	-			
LaFe _{0.5} Co _{0.5} O ₃ /S		≈7.1	-	-			
LaFe _{0.7} Mn _{0.3} O ₃ /SiO ₂		≈7.2	-	-			

Table A.1 (continued) Literature Survey on Red/Ox Materials

Red/ox Material	Oxygen Desorption Step		Water Splitting Step		Reactor	Important Points	Ref
	T (°C)	O ₂ (mL/g)	T (°C)	H ₂ (mL/g)			
CeO ₂	1500	2.5	900>	4	Solar cavity reactor	Porous monolith CeO ₂ was tested in pilot scale reactor; Oxygen desorption stage was controlled by diffusion while rapid reoxidation was achieved during water dissociation step; material shows stable production levels over 500cycles; solar to fuel efficiency is around 0.7-0.8%	[26]
Ce ₂ Si ₂ O ₇	1500	26.7	530	41.3	Solar furnace for thermal reduction; special test tube heated by electrical furnace for reoxidation	Three step water splitting reaction was proposed with the following steps thermal reduction, alkali metal activation by molten salts and hydrolysis step; highest reaction rates was obtained for Ce ₂ Si ₂ O ₇ ;	[21]
Ce ₂ Ti ₂ O ₇	1400	24	630	39.7			
CeFeO ₃	1500	24	500	14.4			
CeNbO ₄	700	20	500	19.7			

Table A.1 (continued) Literature Survey on Red/Ox Materials

Red/ox Material	Oxygen Desorption Step		Water Splitting Step		Reactor	Important Points	Ref
	T (°C)	O ₂ (mL/g)	T (°C)	H ₂ (mL/g)			
(1-x)CeO ₂ -xNiO (x=0.025-0.3)	1400	0.8-1.4	1000	1.2-2.5	Alumina tubular reactor	The reduction of Ce ⁴⁺ -Ce ³⁺ enhanced by Ni ²⁺ -Ni; as nickel ratio increases, the oxygen production decreases.	[103]
CeO ₂	1500	≈2.12	750	≈3.3	Quartz tubular reactor; material in platinum cup; infrared heater; heating rate 200 °C/min; cooling rate 1000 °C/min	Oxygen release triggered by Pr content; the produced oxygen amount is directly proportional to reduction of Pr ⁴⁺ to Pr ³⁺ ; Pr ³⁺ could not be activated by water splitting; the repeated cycles were obtained from the red/ox mechanism of Ce ⁴⁺ /Ce ³⁺ ; hydrogen evolution was promoted by addition of Pr up to 10 mol%.	[27]
Ce _{0.95} Pr _{0.05} O _{2-γ}		≈2.1		≈3.8			
Ce _{0.9} Pr _{0.1} O _{2-γ}		≈2.3		≈3.9			
Ce _{0.8} Pr _{0.2} O _{2-γ}		≈1.6		≈2.5			
Ce _{0.7} Pr _{0.3} O _{2-γ}		≈1.0		≈1.7			

Table A.1 (continued) Literature Survey on Red/Ox Materials

Red/ox Material	Oxygen Desorption Step		Water Splitting Step		Reactor	Important Points	Ref
	T (°C)	O ₂ (mL/g)	T (°C)	H ₂ (mL/g)			
	CeO ₂		3.1	-			
Zr _{0.05} Ce _{0.95} O ₂	1500	3.3	-	-			
Zr _{0.1} Ce _{0.9} O ₂	4.1	-	-	-			
Zr _{0.2} Ce _{0.8} O ₂	6	-	-	-			
Hf _{0.05} Ce _{0.95} O ₂	3.4	-	-	-			
Hf _{0.1} Ce _{0.9} O ₂	4.8	-	-	-			
Hf _{0.15} Ce _{0.85} O ₂	5	-	-	-			
Hf _{0.2} Ce _{0.8} O ₂	5.7	-	-	-			
Li _{0.02} Hf _{0.098} Ce _{0.88}	4.3	-	-	-			
Li _{0.06} Hf _{0.094} Ce _{0.84}	4.2	-	-	-			
Li _{0.1} Hf _{0.09} Ce _{0.81} O	4.1	-	-	-			

Table A.1 (continued) Literature Survey on Red/Ox Materials

Red/ox Material	Oxygen Desorption Step		Water Splitting Step		Reactor	Important Points	Ref
	T (°C)	O ₂ (mL/g)	T (°C)	H ₂ (mL/g)			
Commercial CeO ₂	-	-	827	21	Vertical tubular quartz fixed bed reactor; H ₂ O saturated Ar	DS CeO ₂ has the highest surface area followed by 3DOM CeO ₂ ; post results shows that commercial and DS CeO ₂ has the same surface area while t 3DOM CeO ₂ decreased to half; the reactivity increases as commercial, DS and 3DOM CeO ₂ ; morphology has strong effect on kinetics but no	[29]
DS CeO ₂	-	-		20			
3DOM CeO ₂	-	-		20			
C _{0.9} Fe _{2.1} O ₄ / ZrO ₂	1400-1450	4.8-12	900-1300	12-24	Stagnation flow reactor; heated by electrical furnace; heated by electrical furnace	Hydrogen and oxygen yields are found to be similar between cobalt ferrite and magnetite; Reoxidation mechanism was found to be competitive reaction of second order and 1D diffusion; the water dissociation is activated by reduced iron that is dissolved in zirconia	[40]

Table A.1 (continued) Literature Survey on Red/Ox Materials

Red/ox Material	Oxygen Desorption Step		Water Splitting Step		Reactor	Important Points	Ref
	T (°C)	O ₂ (mL/g)	T (°C)	H ₂ (mL/g)			
CoFe ₂ O ₄	1200-1500	-	1000	2.4-33.7	Mullite reaction tube with ZrO ₂ sample holder; heated by electrical furnace; heating rate 20 °C/min;	Tred lowers Fe ₃ O ₄ >CoFe ₂ O ₄ >Fe ₃ O ₄ +5Al ₂ O ₃ >CoFe ₂ O ₄ +5Al ₂ O ₃ ; CoFe ₂ O ₄ is a solid solution of Fe ₃ O ₄ , CoFe ₂ O ₄ and FeCo ₂ O ₄ and as the Tred increases FeO, CoO and Fe ₂ O ₃ are formed until total decomposition of CoFe ₂ O ₄ ; when CoFe ₂ O ₄ supported on alumina, additional species were formed as FeAl ₂ O ₄ , AlFe ₂ O ₄ , CoAl ₂ O ₄ and AlCo ₂ O ₄ ; formation of latter species make the cycle	[55]
CoFe ₂ O ₄ /5Al ₂ O ₃				14.4-24			
20 wt% Fe ₃ O ₄ /YSZ	1400	-	1000	6	Quartz tube with platinum holder; infrared furnace	Fe ²⁺ solubility in YSZ increases the activity; the active red/ox pair is found to be Fe ²⁺ and Fe ³⁺ ; hydrogen production kinetics can be enhanced by the increase in	[30]
25 wt% Fe ₃ O ₄ /YSZ				9.5			

Table A.1 (continued) Literature Survey on Red/Ox Materials

Red/ox Material	Oxygen Desorption		Water Splitting Step		Reactor	Important Points	Ref
	T (°C)	O ₂ (mL/g)	T (°C)	H ₂ (mL/g)			
Fe ₂ O ₃	-	-	700	125(avg.)	Fixed bed quartz reactor	Morphological changes over cycles affect the hydrogen production; 33 mol% Fe-Si _x Al _{1-x} O _y and Fe ₂ O ₃ shows sintering related problems decreasing the red/ox activity due to collapse of pores of Si _x Al _{1-x} O _y	[31]
13% Fe-Si-Al-O	-	-		147(avg.)			
17% Fe-Si-Al-O	-	-		98(avg.)			
20% Fe-Si-Al-O	-	-		152(avg.)			
33% Fe-Si-Al-O	-	-		88(avg.)			
Commercial FeO	-	-	575	38	Tubular fixed bed reactor; heated by vertical electrical furnace; Fe ₂ O ₃ reduced in solar reactor	Fe ₂ O ₃ reduced to FeO _{0.9} which shows high hydrogen production during water splitting; water dissociation step is highly dependent on temperature, reaction, time, particle size and sample composition; the decrease in reaction rate during reoxidation is limited by H ₂ O diffusion through Fe ₃ O ₄ layer; increase in the reduction degree of iron enhances the initial hydrogen	[101]
Fe ₂ O ₃	-	-	700	125(avg.)			

B. The Operating Procedures for Micromeritics Chemisorp 2720

The Operating Procedure of Micromeritics Chemisorp 2720 for TPR Experiments

The TPR experiments were performed by following the steps:

- i. If the sample is present from a previous experiment, follow the step ii directly; if not, put appropriate amount of material into the reaction tube, and connect to reaction chamber.
- ii. Purge the gas lines and reaction tube with pure helium gas until a stable TCD signal is achieved.
- iii. Change the polarity of the TCD signal to negative.
- iv. Change the gas flow to 10% H₂ in Ar and wait for a stable TCD signal to make sure no residual gas is present in the system.
- v. Set the desired temperature and heating rate.
- vi. Start data recording by using software after initiating the heating.
- vii. After reaching the desired temperature, let the system cool down to 400 °C.
- viii. Stop data recording by using software.
- ix. Open the oven where reaction tube is present and start the external fan for forced convective cooling.
- x. Change the gas flow to pure helium when the temperature of the reaction tube reaches 40 °C.
- xi. Disconnect the sample tube and preserve the residual if no sequential experiment is planned otherwise follow the desired procedure.

The Operating Procedure of Micromeritics Chemisorp 2720 for TPO Experiments

The TPO experiments were performed by following the steps:

- i. If the sample is present from a previous experiment, follow the step ii directly; if not put appropriate amount of material into the reaction tube, and connect to reaction chamber.
- ii. Purge the gas lines and reaction tube with pure helium gas until a stable TCD signal is achieved.
- iii. Change the polarity of the TCD signal to positive.
- iv. Change the gas flow to 2% O₂ in He and wait for a stable TCD signal to make sure no residual gas is present in the system.
- v. Set the desired temperature and heating rate.
- vi. Start data recording by using software after initiating the heating.
- vii. After reaching the desired temperature, let the system cool down to 400 °C.
- viii. Stop data recording by using software.
- ix. Open the oven where reaction tube is present and start the external fan for forced convective cooling.
- x. Change the gas flow to pure helium when the temperature of the reaction tube reaches 40 °C.
- xi. Disconnect the sample tube and preserve the residual if no sequential experiment is planned otherwise follow the desired procedure.

The Operating Procedure of Micromeritics Chemisorp 2720 for TPtD Experiments

The TPtD experiments were performed by following the steps:

- i. If the sample is present from a previous experiment, follow the step ii directly; if not put appropriate amount of material into the reaction tube, and connect to reaction chamber.

- ii. Purge the gas lines and reaction tube with pure helium gas until a stable TCD signal is achieved.
- iii. Change the polarity of the TCD signal to negative.
- iv. Set the desired temperature and heating rate.
- v. Start data recording by using software after initiating the heating.
- vi. After reaching the desired temperature, let the system cool down to 400 °C.
- vii. Stop data recording by using software.
- viii. Open the oven where reaction tube is present and start the external fan for forced convective cooling up to 40 °C.
- ix. Disconnect the sample tube and preserve the residual if no sequential experiment is planned otherwise follow the desired procedure.

C. The Operating Procedures for Multi Gas Analyzer

The Operating Procedure of Multi-Gas Analyzer for TPtD Experiments

The TPtD experiments were performed by following the steps:

- i. If the sample is present from a previous experiment, follow the step ii directly; if not, put appropriate amount of material into quartz reactor, and connect to flow lines.
- ii. Set the MFC to 100ccpm Ar actual flow by using MFCS.
- iii. Check the connections of the reactor for any leaking problem by soap
- iv. Insulate the spaces left between oven and reactor.
- v. Power on Multi-Gas Analyzer
- vi. Energize the O₂ detector and wait for a stable signal. When operating in low detection limit, the time required for a stable signal can take approximately 1h.
- vii. Set the heating rate and desired temperature by using built in temperature controller (TC).
- viii. Open the ORDEL data logger software. Data is automatically recorded when the software opened.
- ix. Start the experiment by running the TC.
- x. After reaching the desired temperature, let the system cool down to 400 °C.
- xi. Remove the insulation between oven and reactor.
- xii. Export the experimental data and close the software. If additional experiment is planned, skip this step.
- xiii. Power off the O₂ detector.

- xiv. Wait for cooling down to 40 °C. If additional experiment is planned, skip the steps of xv to xvii and follow the desired operating procedure.
- xv. Turn off the Multi-Gas Analyzer.
- xvi. Stop the gas flow by using MFCS.
- xvii. Detach the connections of the reactor.

The Operating Procedure of Multi-Gas Analyzer for TPO Experiments

The TPtD experiments were performed by following the steps:

- i. If the sample is present from a previous experiment, follow the step ii directly; if not, put appropriate amount of material into quartz reactor, and connect to flow lines.
- ii. Set the MFC to 100ccpm dry air actual flow by using MFCS.
- iii. Check the connections of the reactor for any leaking problem by soap
- iv. Insulate the spaces left between oven and reactor.
- v. Power on Multi-Gas Analyzer
- vi. Energize the O₂ detector and wait for a stable signal. When operating in low detection limit, the time required for a stable signal can take approximately 1h.
- vii. Set the heating rate and desired temperature by using built in TC.
- viii. Open the ORDEL data logger software. Data is automatically recorded when the software opened.
- ix. Start the experiment by running the TC.
- x. After reaching the desired temperature, let the system cool down to 400 °C.
- xi. Remove the insulation between oven and reactor.
- xii. Export the experimental data and close the software. If additional experiment is planned, skip this step.

- xiii. Power off the O₂ detector.
- xiv. Wait for cooling down to 40 °C. If additional experiment is planned, skip the steps of xv to xvii and follow the desired operating procedure.
- xv. Turn off the Multi-Gas Analyzer.
- xvi. Stop the gas flow by using MFCS.
- xvii. Detach the connections of the reactor.

The Operating Procedure of Multi-Gas Analyzer for TPWS Experiments

The TPWS experiments were performed by following the steps:

- i. If the sample is present from a previous experiment, follow the step ii directly; if not, put appropriate amount of material into quartz reactor, and connect to flow lines.
- ii. Set the MFC to 100ccpm Ar actual flow by using MFCS. The sweep gas will be humidified in the wash bottle.
- iii. Check the connections of the reactor for any leaking problem by soap
- iv. Insulate the spaces left between oven and reactor.
- v. Power on Multi-Gas Analyzer
- vi. Energize the H₂ TCT detector and wait for a stable signal.
- vii. Set the heating rate and desired temperature by using built in TC.
- viii. Open the ORDEL data logger software. Data is automatically recorded when the software opened.
- ix. Start the experiment by running the TC.
- x. After reaching the desired temperature, let the system cool down to 400 °C.
- xi. Remove the insulation between oven and reactor.

- xii. Export the experimental data and close the software. If additional experiment is planned, skip this step.
- xiii. Power off the H₂ TCT detector.
- xiv. Wait for cooling down to 40 °C. If additional experiment is planned, skip the steps of xv to xvii and follow the desired operating procedure.
- xv. Turn off the Multi-Gas Analyzer.
- xvi. Stop the gas flow by using MFCS.
- xvii. Detach the connections of the reactor.

The Operating Procedure of Multi-Gas Analyzer for Two Step Thermochemical Water Splitting Experiment

One cycle is defined as thermal decomposition followed by water splitting. The experiments were performed by following the steps:

- i. Put appropriate amount of material into quartz reactor and connect to flow lines.
- ii. Set the MFCs to 100ccpm Ar actual flow by using MFCS. One of the argon MFC will be humidified in the wash bottle. This stream is used for water splitting experiments.
- iii. Check the connections of the reactor for any leaking problem by soap.
- iv. Arrange the flow configurations for TPtD.
- v. Insulate the spaces left between oven and reactor.
- vi. Power on Multi-Gas Analyzer
- vii. Energize the O₂ and wait for a stable signal.
- viii. Set the heating rate and desired temperature by using built in TC.

- ix. Open the ORDEL data logger software. Data is automatically recorded when the software is opened.
- x. Start the experiment by running the TC.
- xi. After reaching the desired temperature, let the system cool down up to 400 °C.
- xii. Remove the insulation between oven and reactor and wait for cooling down to 40 °C.
- xiii. Export the experimental data.
- xiv. Arrange the flow configurations for TPWS.
- xv. Energize H₂ TCT detector and wait for a stable signal.
- xvi. Set the heating rate and desired temperature by using built in TC.
- xvii. Start the experiment by running the TC.
- xviii. After reaching the desired temperature, let the system cool down to 400 °C.
- xix. Remove the insulation between oven and reactor.
- xx. Export the experimental data and close the software.
- xxi. Power off the H₂ TCT detector.
- xxii. Wait for cooling down to 40 °C. If the additional experiments are planned, go to step iv; if not follow the next step.
- xxiii. Turn off the Multi-Gas Analyzer.
- xxiv. Stop the gas flow by using MFCS.
- xxv. Detach the connections of the reactor.

D. Ellingham Diagrams

Ellingham diagrams of the red/ox pairs in the periodic table are shown in Figure D.1 to Figure D.32. Some poisonous metals such as mercury and radioactive metals are discarded during the analysis.

Aluminum and Boron: Relative oxidation strength of aluminum and boron were shown in Figure D.1. In the reference book, the intermediate oxidation state of the aluminum and boron could not be found. Therefore, the oxidation of $Al \rightleftharpoons Al_2O_3$ and $B \rightleftharpoons B_2O_3$ are taken into consideration. It is found that both aluminum and boron are so stable that they can easily oxidized by H_2O between 300 and 1700K. Coke formation is favorable in the studied temperature range. The use of Al_2O_3 as support material instead of looping material is highly recommended due to high oxide stability.

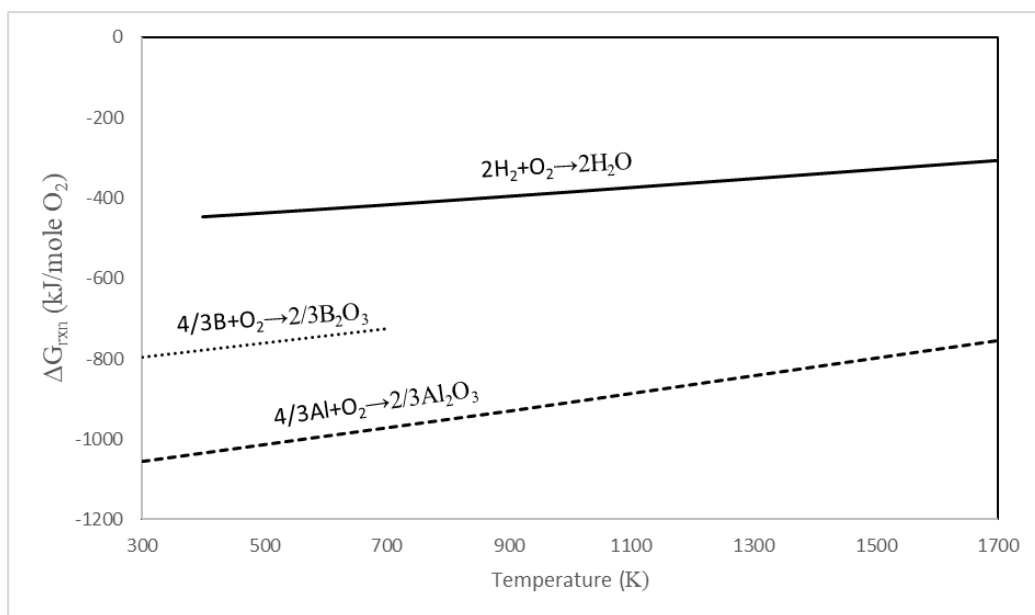


Figure D.1 Ellingham diagram of aluminum and boron

Barium: Relative oxidation strength of barium is given in Figure D.2. The oxidation of $Ba \rightleftharpoons BaO$ and $BaO \rightleftharpoons BaO_2$ are taken into consideration. It is found that barium can be oxidized to BaO by H_2O between 300 and 1700K. Air is needed for further oxidation to BaO_2 . In terms of two step thermochemical cycles, $BaO_2 \rightleftharpoons BaO$ transformation can be used for decreasing the thermal decomposition temperature. Since the relative oxidation strength between $BaO \rightleftharpoons BaO_2$ and $BaO \rightleftharpoons BaO_2$ is high, BaO is the most stable phase in the studied temperature range.

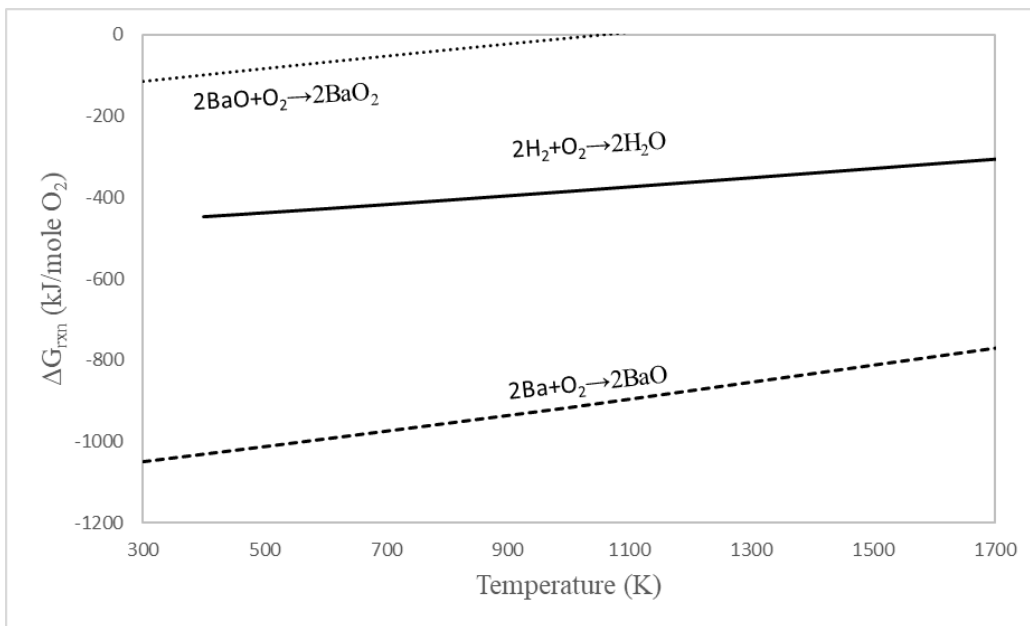


Figure D.2 Ellingham diagram of barium

Beryllium and Bismuth: Relative oxidation strength of beryllium and bismuth is shown in Figure D.3. In the reference book [294], the intermediate oxidation states of bismuth could not be find. Therefore, oxidation of $Bi \rightleftharpoons Bi_2O_3$ is taken into consideration. Bismuth oxidation by H_2O between 300 and 1700K is thermodynamically unfavorable. Partial oxidation can be expected since reaction Gibbs free energy line of $Bi \rightleftharpoons Bi_2O_3$ is close with the lines of H_2O . Beryllium can be oxidized by H_2O . Considering the red/ox thermodynamics, $Bi \rightleftharpoons Bi_2O_3$ transformation can be used for decreasing the thermal decomposition temperature while BeO should be used as support material due to high oxide stability.

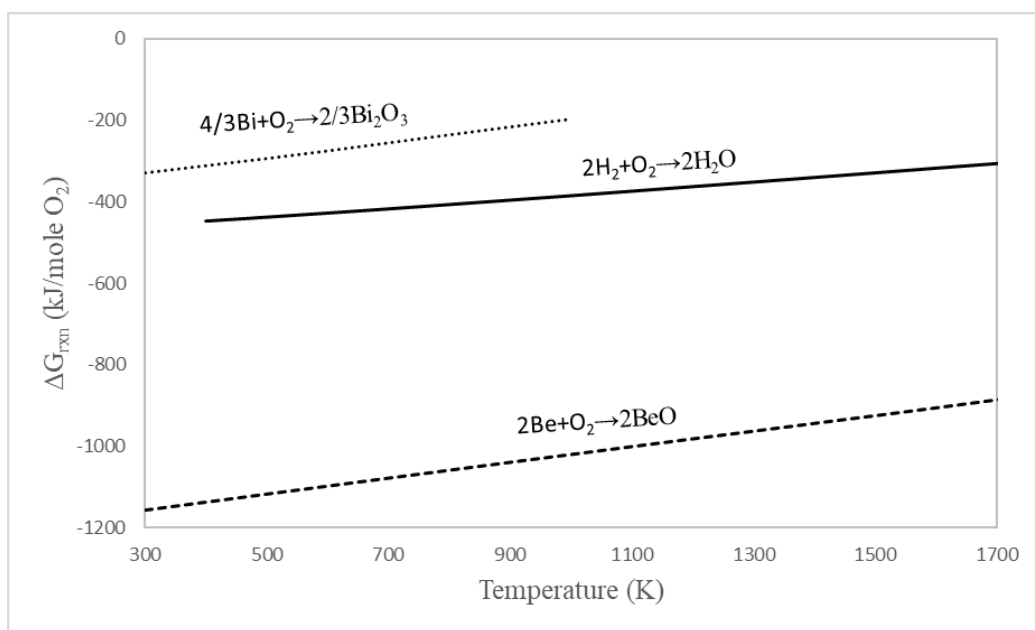


Figure D.3 Ellingham diagram of beryllium and bismuth

Calcium and Cadmium: The favorability of calcium and cadmium towards oxidation is shown in Figure D.4. Calcium oxidation by H_2O is thermodynamically favorable. Reaction Gibbs free energy line of $\text{Cd} \rightleftharpoons \text{CdO}$ is close to the lines of H_2O . The degree of partial oxidation by these oxidation agents is higher than $\text{Bi} \rightleftharpoons \text{Bi}_2\text{O}_3$. $\text{Cd} \rightleftharpoons \text{CdO}$ is expected to be used for thermochemical hydrogen production while CaO should be used as support material due to high oxide stability.

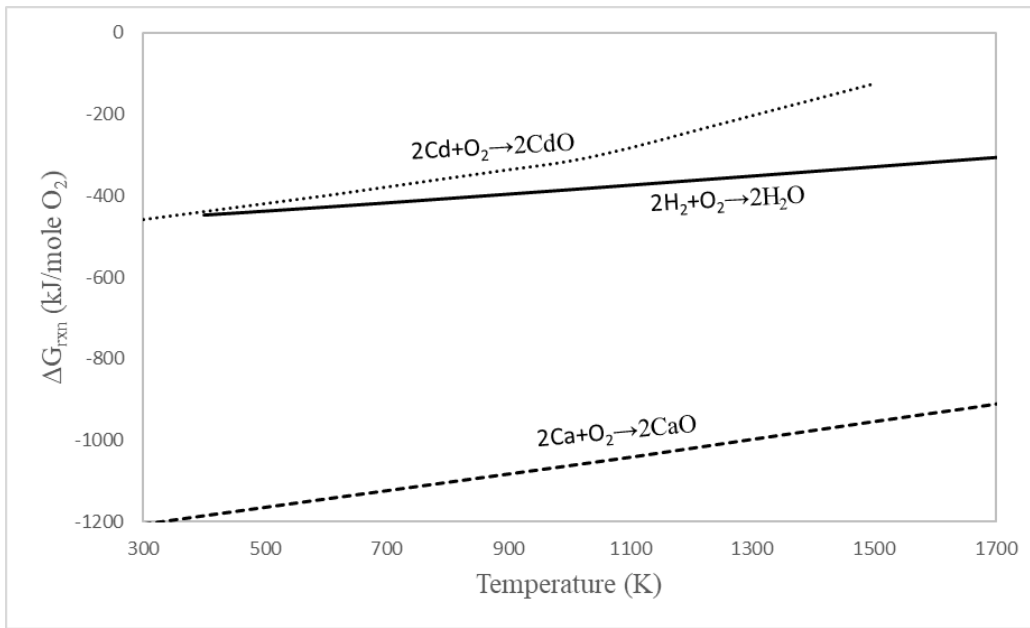


Figure D.4 Ellingham diagram of calcium and cadmium

Cerium: $\text{Ce} \rightleftharpoons \text{Ce}_2\text{O}_3$ and $\text{Ce}_2\text{O}_3 \rightleftharpoons \text{CeO}_2$ oxidation by H_2O is thermodynamically favorable between 300 and 1200K as shown in Figure D.5. The upper temperature range is limited to 1200K since the data in the reference book [294] is available up to 1200K. $\text{Ce}_2\text{O}_3 \rightleftharpoons \text{CeO}_2$ transformation is suitable for water splitting if the oxidation state of cerium is kept between +3 and +4.

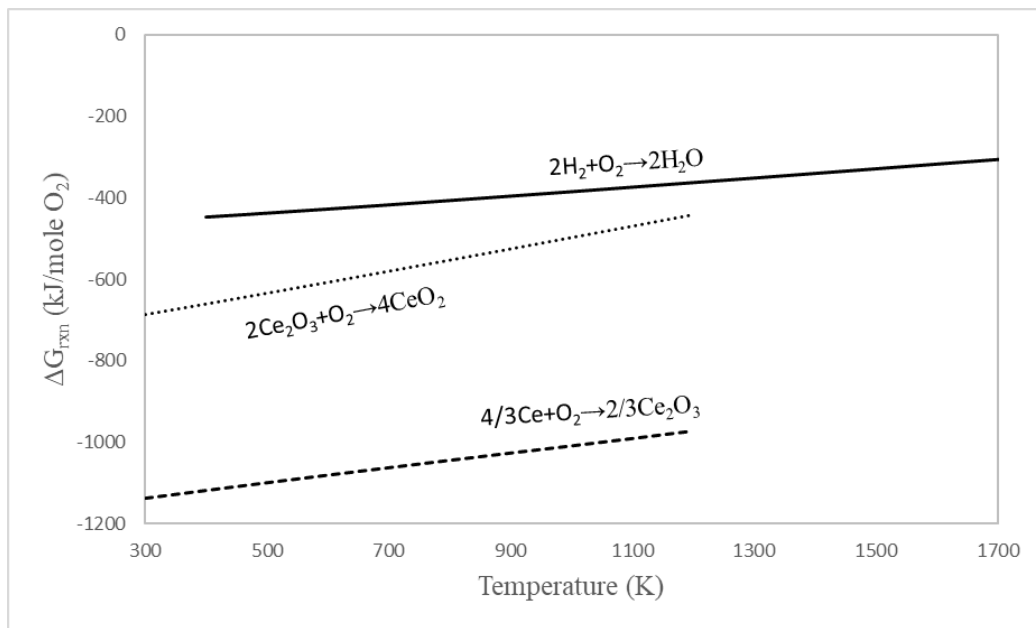


Figure D.5 Ellingham diagram of cerium

Cobalt: Relative oxidation strength of cobalt is shown in Figure D.6. Co_3O_4 can be decomposed thermally around 1200K. Reaction Gibbs free energy line of $\text{Co} \rightleftharpoons \text{CoO}$ is close to the lines of H_2O . The degree of partial oxidation of cobalt is expected. Cobalt and its oxides can be used for decreasing the thermal decomposition temperature as well as water splitting and carbon dioxide splitting by controlling the oxidation state of cobalt.

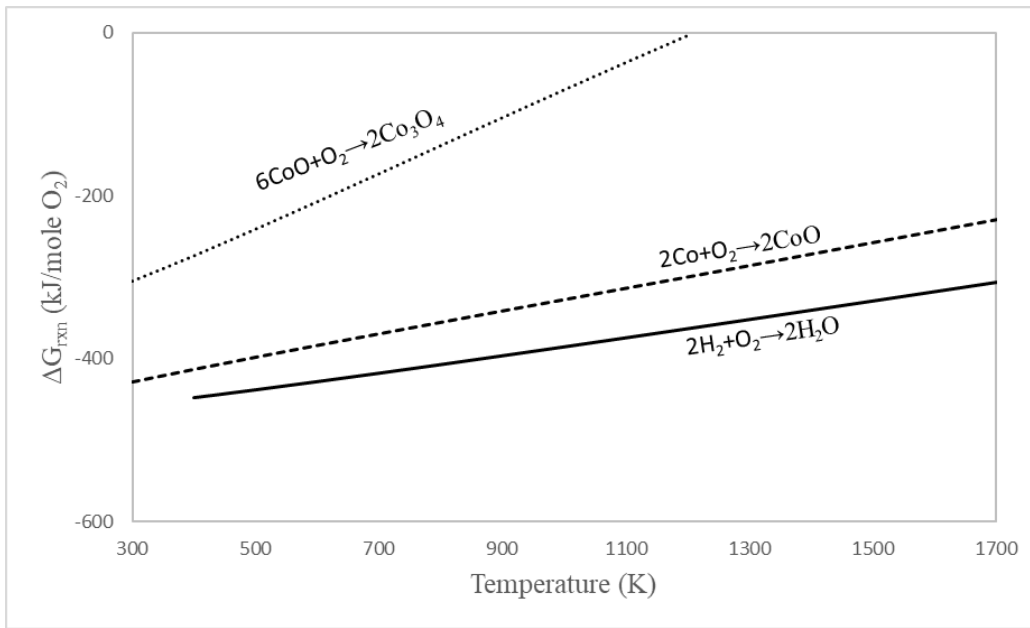


Figure D.6 Ellingham diagram of cobalt

Chromium: $\text{Cr}_2\text{O}_3 \rightleftharpoons \text{CrO}_2$ transformation is suitable for decreasing thermal decomposition step as shown in Figure D.7. The oxidation of chromium to Cr_2O_3 by H_2O between 300 and 1200K is thermodynamically favorable. The oxidation couple, $\text{Cr} \rightleftharpoons \text{Cr}_2\text{O}_3$, is suitable for thermochemical water splitting reaction.

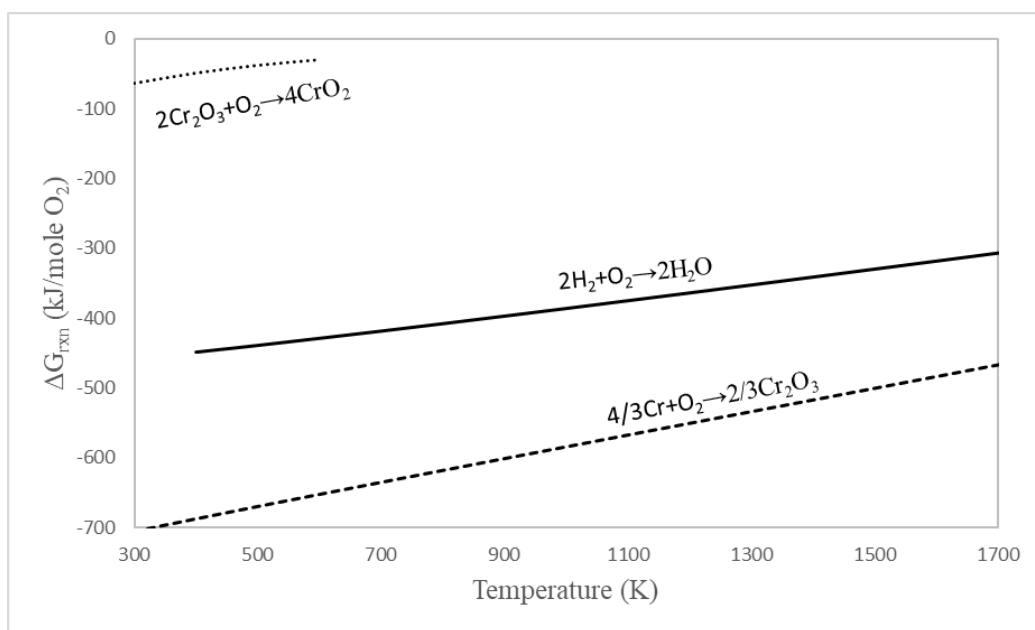


Figure D.7 Ellingham diagram of chromium

Cesium: Relative oxidation strength of cesium is shown in Figure D.8. The upper temperature range is limited to 700K since the data in the reference book [294] is available up to 700K. Therefore, it is hard to say about the suitability of cesium in solar thermal hydrogen production processes.

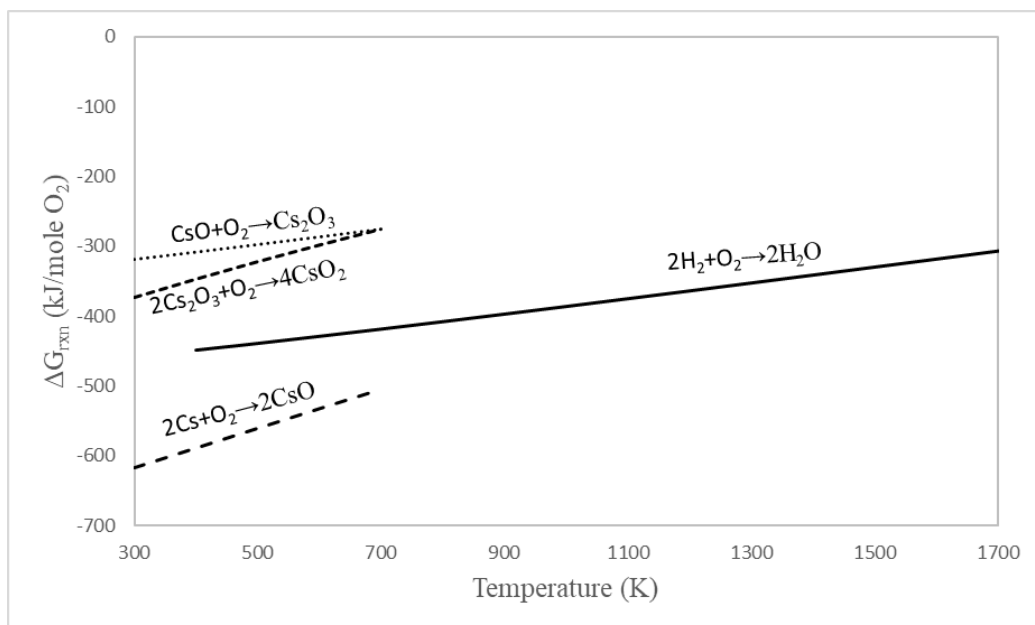


Figure D.8 Ellingham diagram of cesium

Copper: Copper oxidation is not thermodynamically suitable for oxidation by H₂O at the studied temperature as given in Figure D.9. It is strange to see a crossover between $Cu \rightleftharpoons Cu_2O$ and $Cu_2O \rightleftharpoons CuO$. This behavior can be explained as the change in the oxidation stability of the material determines the expected reaction; that is, the thermodynamic oxidation mechanism of copper should be $Cu \rightleftharpoons Cu_2O \rightleftharpoons CuO$ up to 800K. Further increase in temperature limits the reaction of $Cu \rightleftharpoons Cu_2O$ so that the full oxidation of copper should not be expected until all copper oxidized to Cu₂O. Copper and its oxides can be used for decreasing the thermal decomposition temperature.

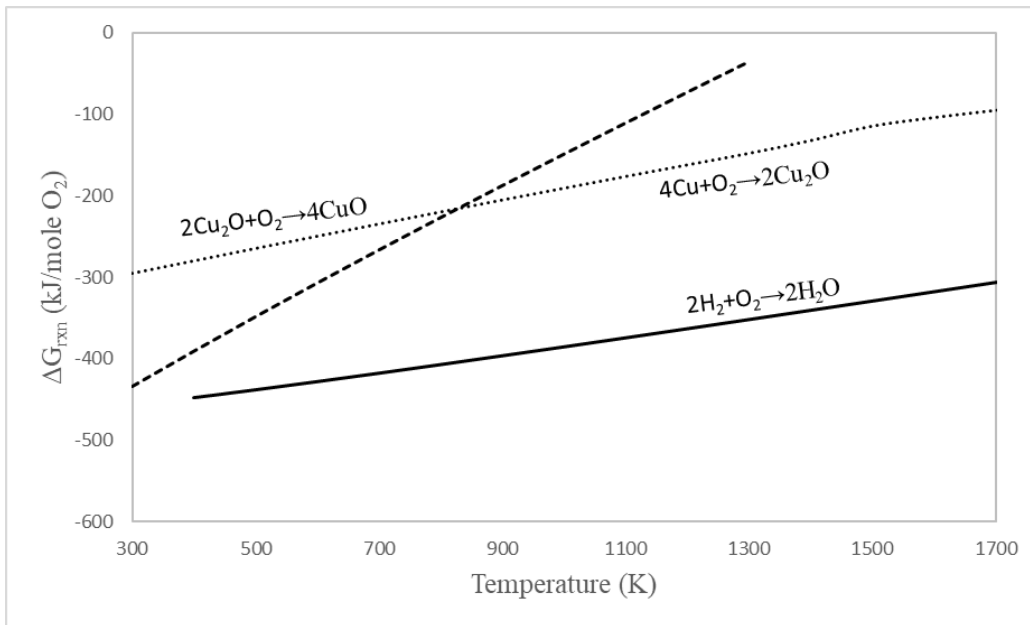


Figure D.9 Ellingham diagram of copper

Gallium and Gadolinium: Thermodynamic favorability towards oxidation of gallium and gadolinium is shown in Figure D.10. In the reference book [294], the intermediate oxidation state of the gallium and gadolinium could not be find. Thus, oxidation of $Ga \rightleftharpoons Ga_2O_3$ and $Gd \rightleftharpoons Gd_2O_3$ is taken into consideration. The oxidation of gallium and gadolinium by H₂O between 300 and 1700K is thermodynamically favorable. $Ga \rightleftharpoons Ga_2O_3$ transformation is suitable for thermochemical processes while Gd₂O₃ should be used as support material due to high oxide stability.

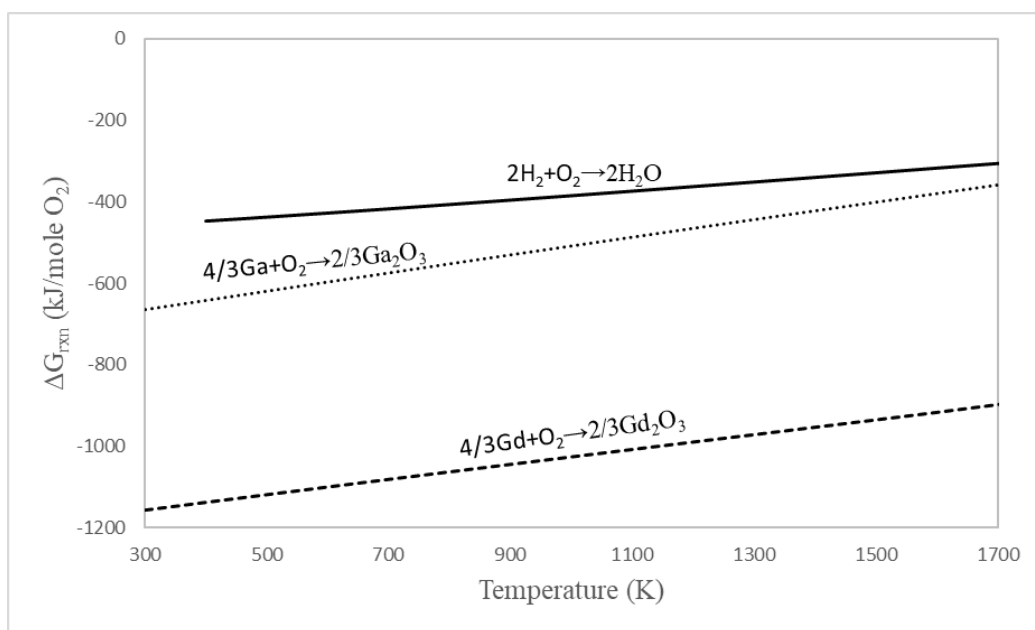


Figure D.10 Ellingham diagram of gallium and gadolinium

Germanium and Hafnium: Relative oxidation strengths of germanium and hafnium are shown in Figure D.11. The oxidation of hafnium is more favorable than germanium at the studied temperature range. Germanium can be used for thermochemical water splitting reaction while HfO_2 should be used as support material due to high oxide stability.

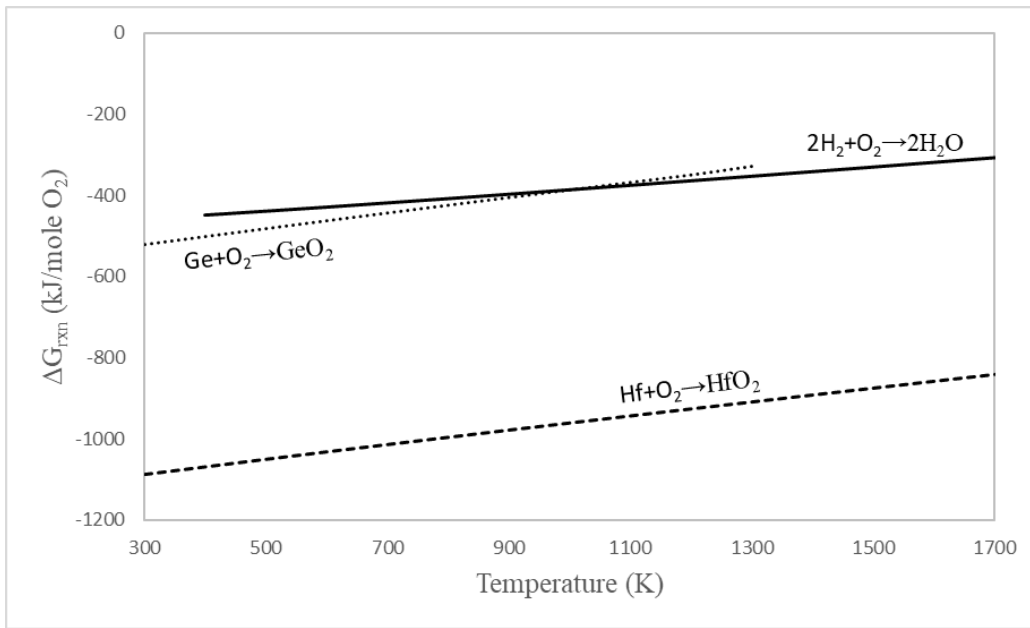


Figure D.11 Ellingham diagram of germanium and hafnium

Holmium, Indium and Iridium: Relative oxidation strength of holmium, indium and iridium is shown in Figure D.12. In the reference book [294], the intermediate oxidation states of holmium, indium, and iridium could not be find. Thus, oxidation of $\text{Ho} \rightleftharpoons \text{Ho}_2\text{O}_3$, $\text{In} \rightleftharpoons \text{In}_2\text{O}_3$, and $\text{Ir} \rightleftharpoons \text{Ir}_2\text{O}_3$ is taken into consideration. The thermodynamic driving force for indium is similar to germanium. IrO_2 can decomposed after 1300K. Holmium oxidation by H_2O is favorable between 300 and 1700K. Iridium can be used for decreasing the thermal decomposition temperature while Ho_2O_3 should be used as support material due to high oxide stability. In addition, indium is suitable for thermochemical water splitting.

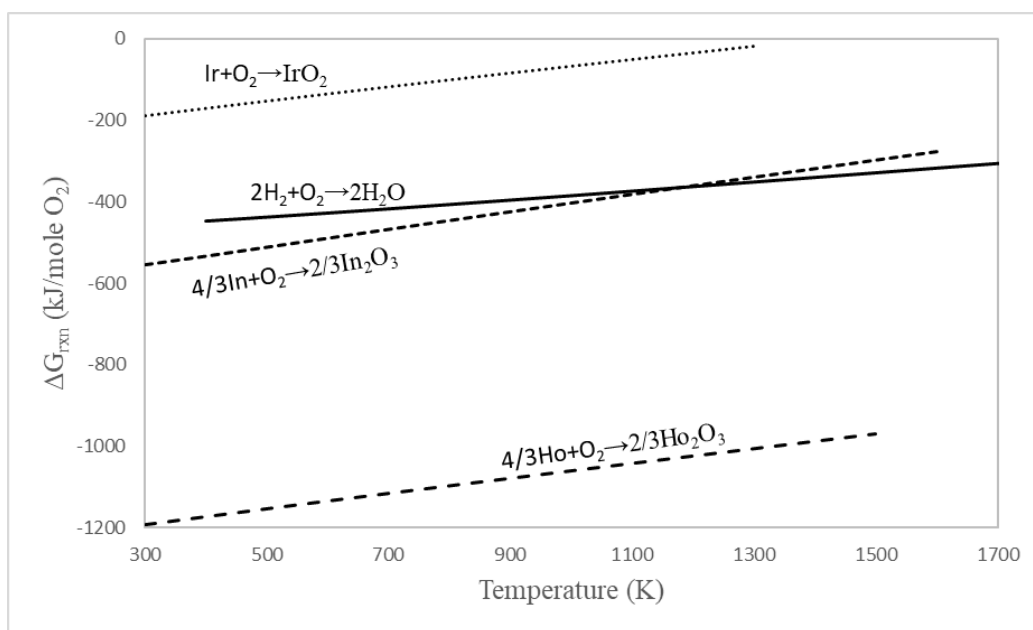


Figure D.12 Ellingham diagram of holmium, indium and iridium

Potassium: The upper temperature range is limited to 600K for $\text{K}_2\text{O}_2 \rightleftharpoons \text{KO}_2$ and $\text{K}_2\text{O} \rightleftharpoons \text{K}_2\text{O}_2$ since the data in the reference book [294] is available up to 600K as shown in Figure D.13. Therefore, it is hard to say about the suitability of these pairs in solar thermal hydrogen production. The oxidation of potassium to K_2O by H_2O is thermodynamically favorable between 300 and 1000K. $\text{K} \rightleftharpoons \text{K}_2\text{O}$ transformation can be used for solar thermal hydrogen production processes.

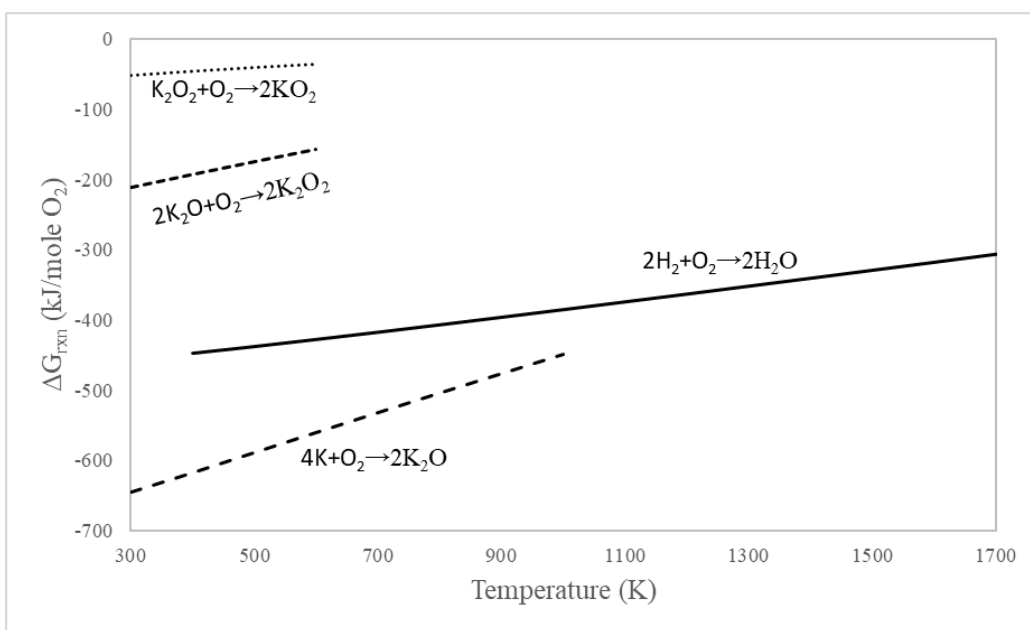


Figure D.13 Ellingham diagram of potassium

Lanthanum and Lutetium: Relative oxidation strength of lanthanum and lutetium is shown in Figure D.14. In the reference book [294], the intermediate oxidation states of lanthanum and lutetium could not be find. Thus, oxidation of $\text{La} \rightleftharpoons \text{La}_2\text{O}_3$ and $\text{Lu} \rightleftharpoons \text{Lu}_2\text{O}_3$ is taken into consideration. Lanthanum and lutetium can be easily oxidized by H_2O in the studied temperature range. La_2O_3 and Lu_2O_3 should be used as support material due to high oxide stability.

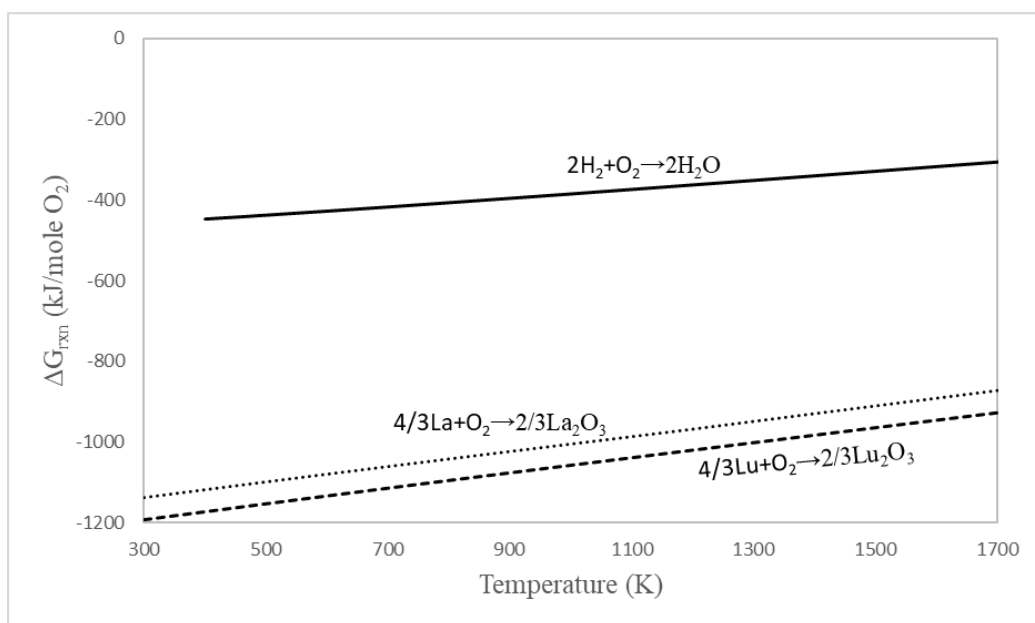


Figure D.14 Ellingham diagram of lanthanum and lutetium

Lithium and Magnesium: Thermodynamic favorability towards oxidation of lithium and magnesium is shown in Figure D.15. Li_2O_2 can be decomposed to very stable oxide, Li_2O , around 400 K. The oxidation of lithium and magnesium by H_2O are thermodynamically favorable. Coke formation is thermodynamically favorable in the presence of both metals. Li_2O and MgO can be used as support material due to high oxide stability.

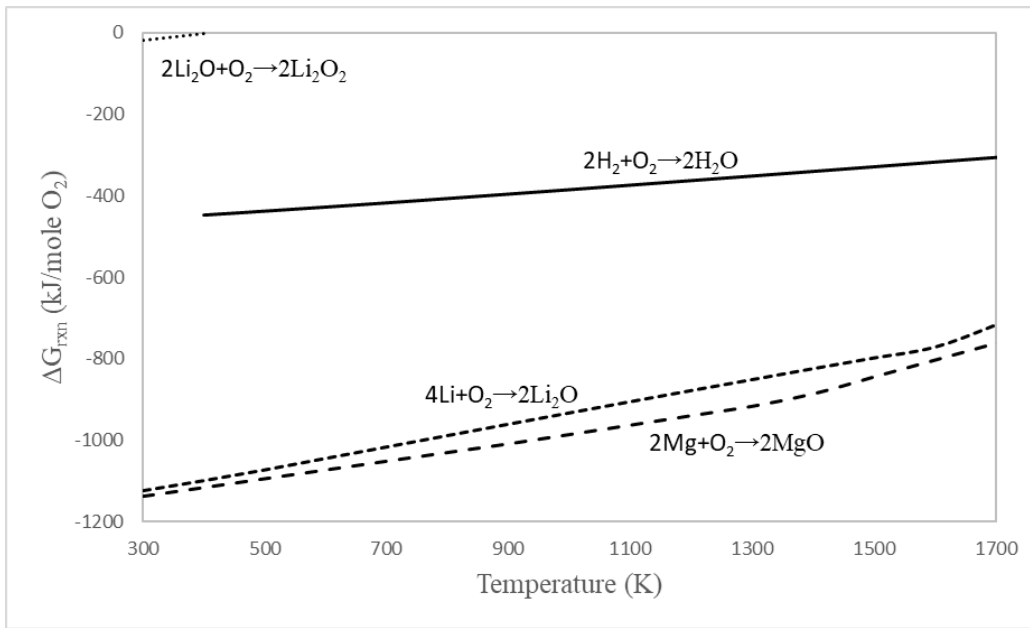


Figure D.15 Ellingham diagram of lithium and magnesium

Manganese: Relative oxidation strength of manganese is shown in Figure D.16. MnO_2 , Mn_2O_3 and Mn_3O_4 can be used for decreasing the thermal decomposition temperature as well as for splitting H_2O depending on the oxidation state of manganese. The manganese can be oxidized by H_2O between 300 and 1700K. Manganese has high thermodynamic potential for decreasing the high temperature step as well as solar thermal hydrogen production.

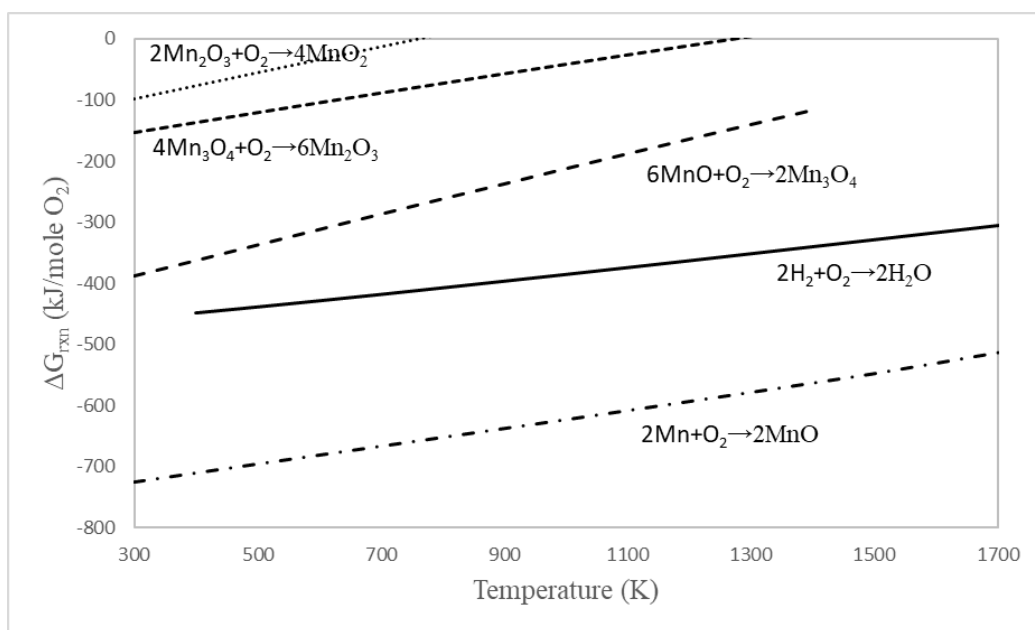


Figure D.16 Ellingham diagram of manganese

Molybdenum: The oxidation of molybdenum to MoO_2 by H_2O is thermodynamically favorable as given in Figure D.17. Further oxidation to MoO_3 can be completed by using air. Thermodynamic driving force towards $\text{MoO}_2 \rightleftharpoons \text{MoO}_3$ transformation has a low potential for decreasing the thermal decomposition temperature. Therefore, $\text{Mo} \rightleftharpoons \text{MoO}_2$ transformation is suitable for thermochemical water splitting processes.

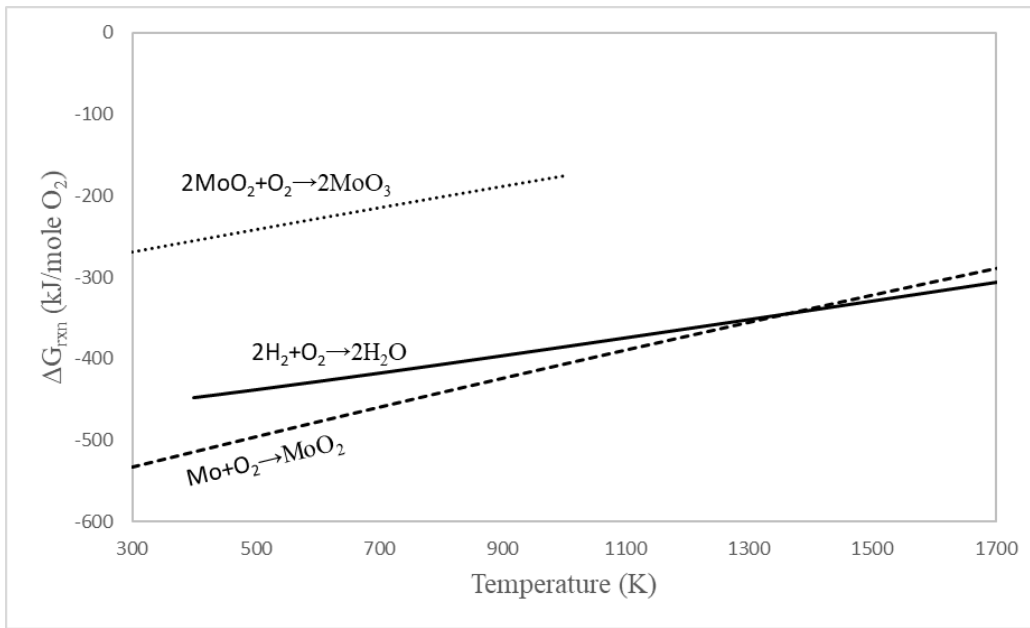


Figure D.17 Ellingham diagram of molybdenum

Sodium: The oxidation of sodium to Na_2O by H_2O is thermodynamically favorable between 300 and 1400K as given in Figure D.18. Further oxidation to Na_2O_2 can be completed by using air. Only $\text{Na} \rightleftharpoons \text{Na}_2\text{O}$ transformation is suitable for solar thermal hydrogen production processes.

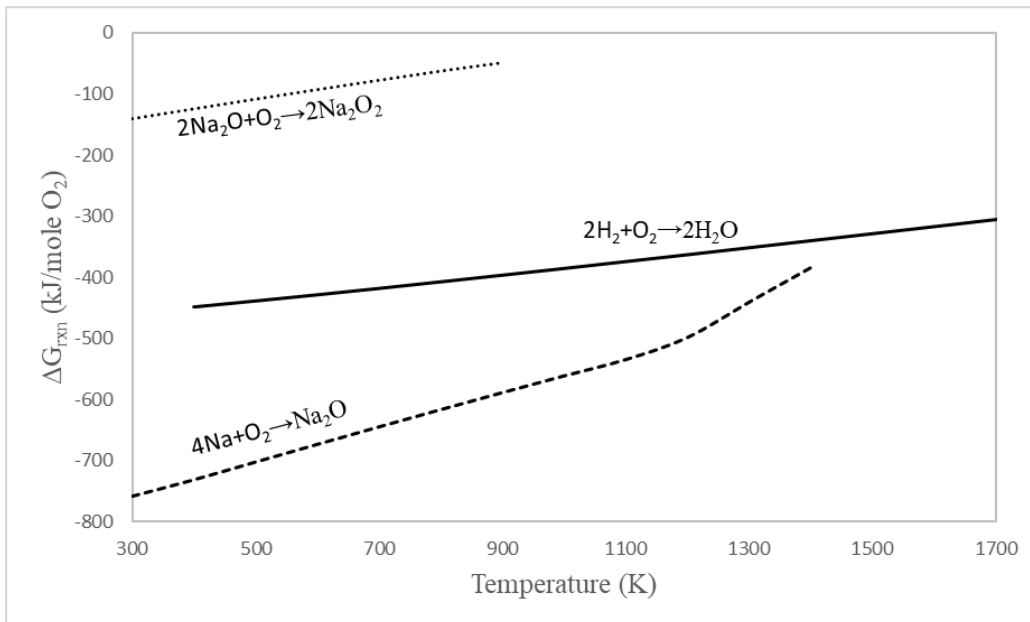


Figure D.18 Ellingham diagram of sodium

Niobium: Relative oxidation strength of niobium is demonstrated in Figure D.19. It is interesting to see that the reaction Gibbs free energy lines of $NbO \rightleftharpoons NbO_2$ and $NbO_2 \rightleftharpoons Nb_2O_5$ overlaps around 1200K. In thermodynamic point of view, these transformations have equal probability to happen; that is, the intermediate oxidation state of NbO_2 cannot be seen during full oxidation of NbO to Nb_2O_5 . The oxidation of $NbO \rightleftharpoons NbO_2$ and $NbO_2 \rightleftharpoons Nb_2O_5$ by H_2O is favorable between 300 and 1700K. further increase in temperature decreases the driving force towards coke formation. Nb to NbO oxidation by H_2O is also favorable. Niobium has a potential in thermochemical water splitting processes.

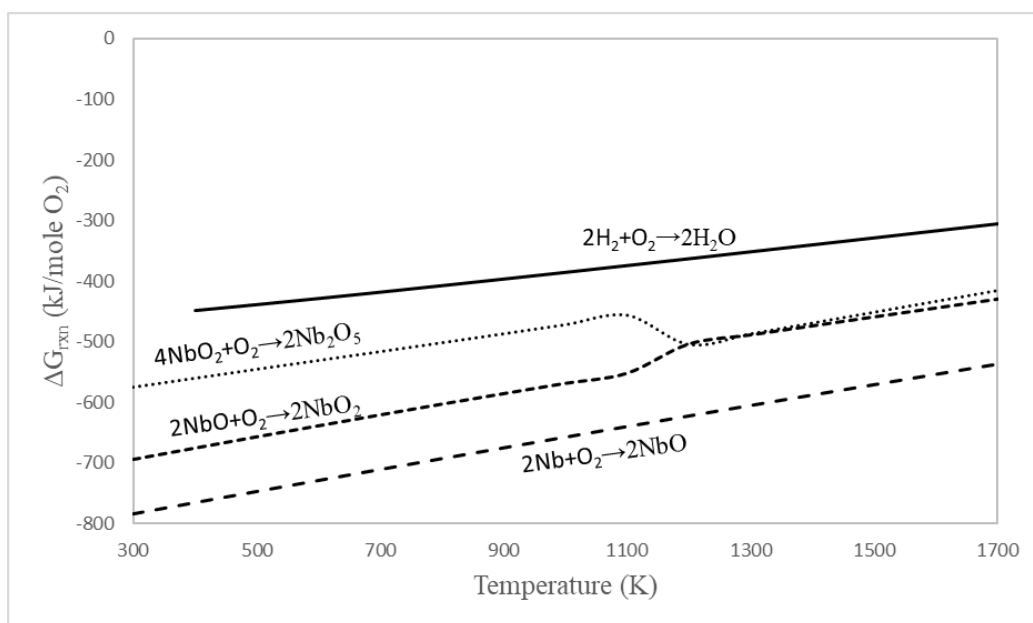


Figure D.19 Ellingham diagram of niobium

Nickel, Neodymium and Osmium: Thermodynamic driving force towards oxidation of nickel, neodymium and osmium is shown in Figure D.20. In the reference book [294], the intermediate oxidation states of neodymium could not be find. Thus, oxidation of $Nd \rightleftharpoons Nd_2O_3$ is taken into consideration. Osmium can be used for decreasing thermal decomposition temperature. The partial oxidation by H_2O can be expected for nickel between 300 and 1700K. Neodymium can be oxidized by H_2O . Osmium should be selected for decreasing the high temperature step of thermochemical processes while nickel can be used as water splitting processes with

low equilibrium conversion. Nd_2O_3 can be used as support material due to high oxide stability.

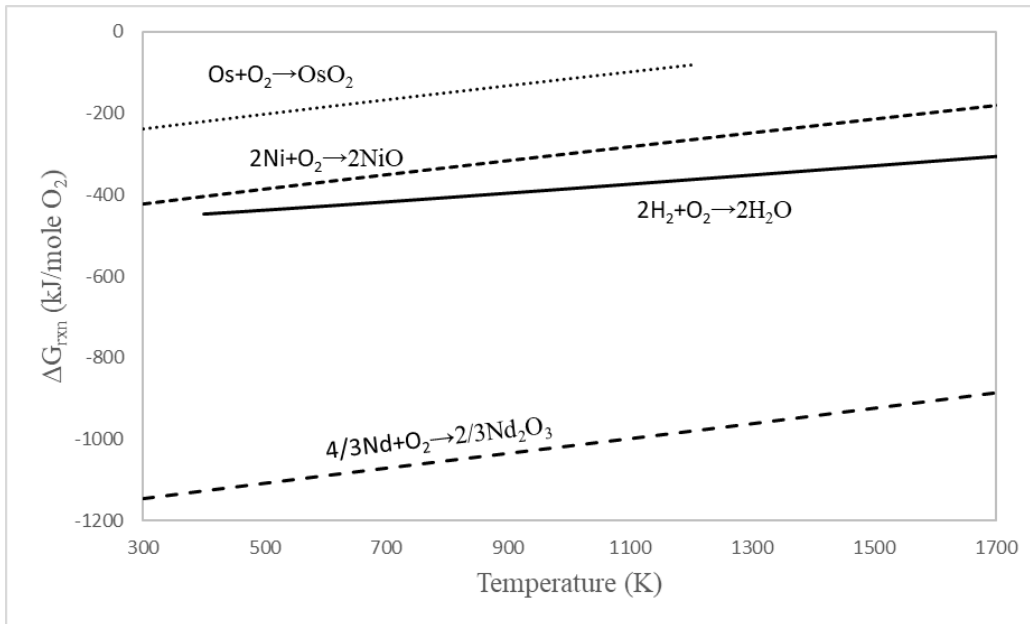


Figure D.20 Ellingham diagram of nickel, neodymium and osmium

Lead: Relative oxidation strength of lead is shown in Figure D.21. PbO_2 and Pb_3O_4 can thermally decomposed around 500 K and 700 K respectively. The change in reaction Gibbs free energy of $Pb \rightleftharpoons PbO$ is close to H_2O line. Nevertheless, only partial oxidation can be achieved by H_2O between 300 and 1100K.

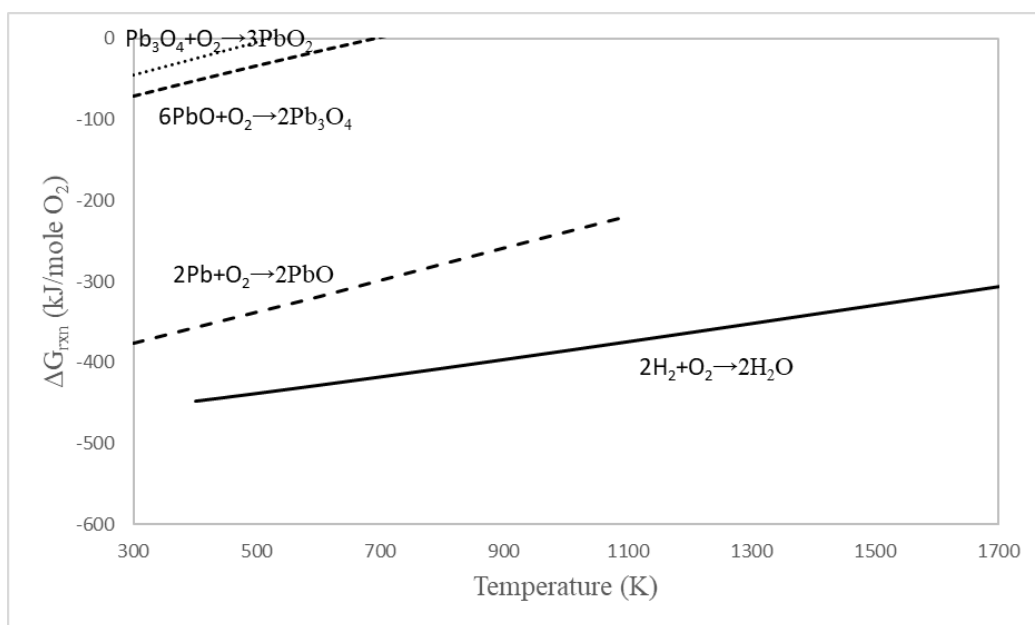


Figure D.21 Ellingham diagram of lead

Palladium and Praseodymium: In the reference book [294], the intermediate oxidation states between Pr and Pr_2O_3 could not be found. Thus, oxidation of $\text{Pr} \rightleftharpoons \text{Pr}_2\text{O}_3$ is taken into consideration. Palladium can be used for decreasing thermal decomposition temperature as shown in Figure D.22. Praseodymium has high oxidation states. Especially, $\text{Pr}_2\text{O}_3 \rightleftharpoons \text{Pr}_7\text{O}_{12}$ has nearly same trend with $\text{Pd} \rightleftharpoons \text{PdO}$. Praseodymium oxidation by H_2O is favorable between 300 and 1700K. Palladium can be selected for decreasing the temperature of high temperature step while Pr_2O_3 should be used as support material due to high oxide stability.

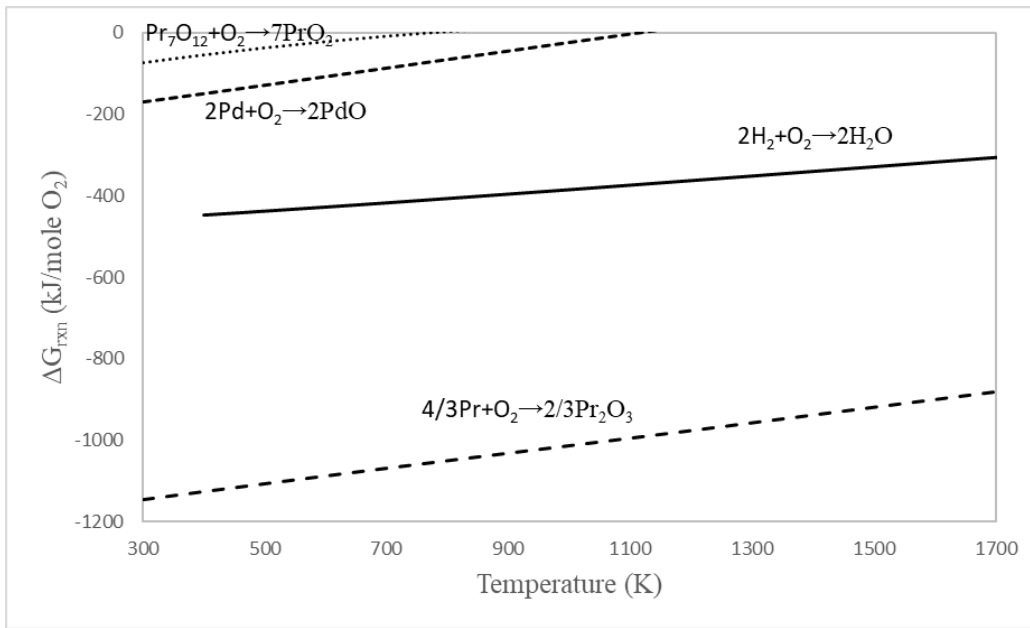


Figure D.22 Ellingham diagram of palladium and praseodymium

Rubidium: Relative oxidation strength of rubidium is shown in Figure D.23. The upper temperature range is limited to 700K since the data in the reference book [294] is available up to 700K. Therefore, it is hard to say about the suitability of rubidium in thermochemical processes.

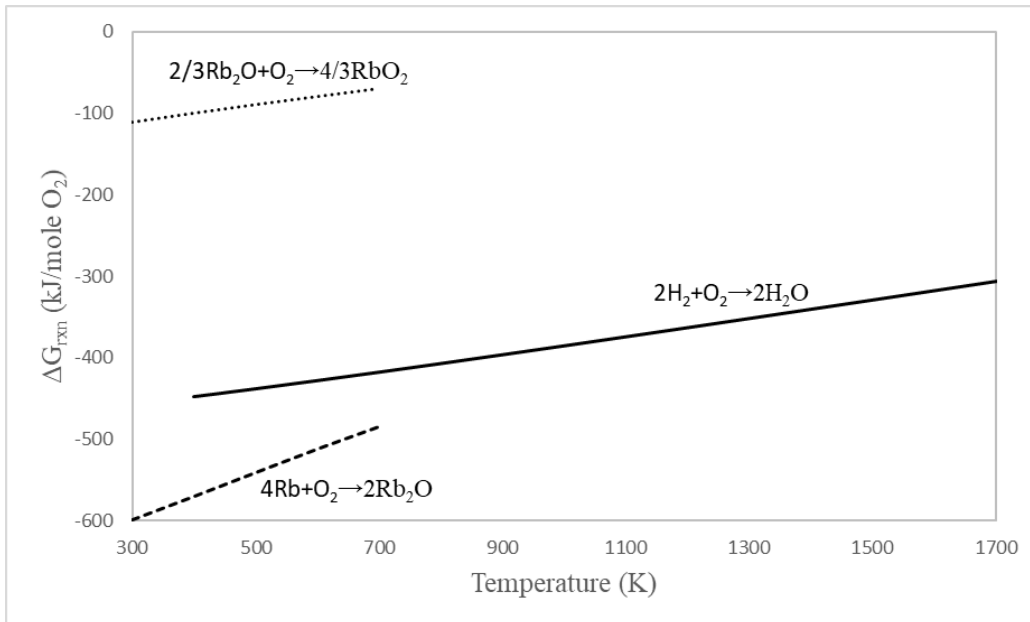


Figure D.23 Ellingham diagram of rubidium

Rhenium: Thermodynamic driving force towards oxidation of rhenium is given in Figure D.24. Rhenium is suitable for decreasing the thermal decomposition temperature. Nevertheless, $Re \rightleftharpoons ReO_2$ transformation has similar tendency with $Pb \rightleftharpoons PbO$ transformation; that is, partial oxidation can be expected by H_2O between 300 and 1400K. Rhenium is suitable for decreasing the high temperature step.

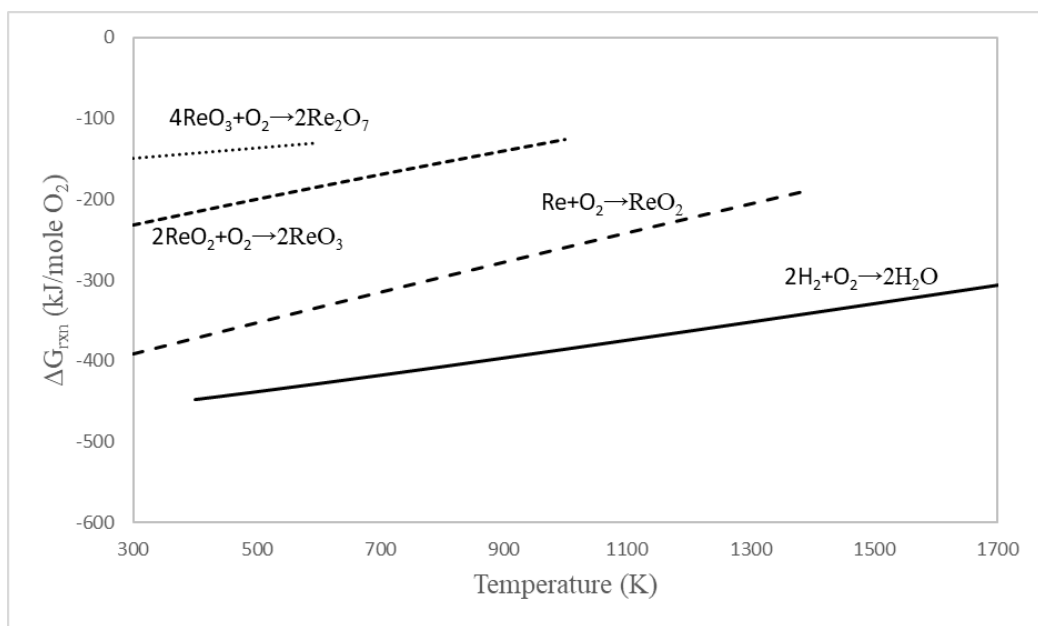


Figure D.24 Ellingham diagram of rhenium

Rhodium and Ruthenium: Relative oxidation strength of rhodium and ruthenium is shown in Figure D.25. In the reference book [294], the intermediate oxidation states of rhodium could not be find. Therefore, the oxidation of $Rh \rightleftharpoons Rh_2O_3$ is taken into consideration. These metals are thermodynamically favorable for decreasing the high temperature step.

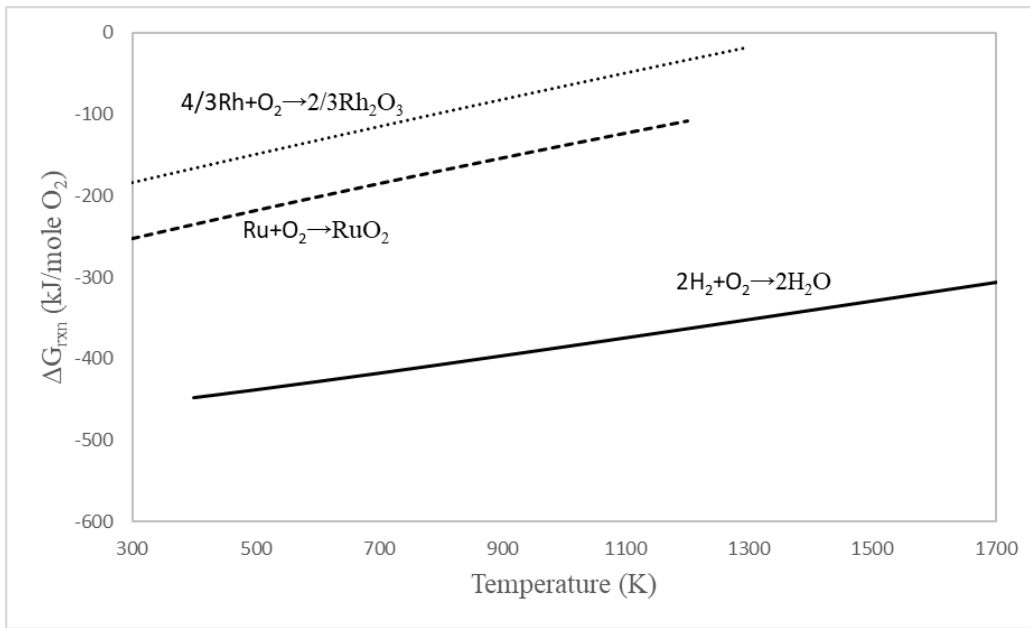


Figure D.25 Ellingham diagram of rhodium and ruthenium

Antimony: The upper temperature range is limited to 900K since the data in the reference book [294] is available up to 900K. Partial oxidation of antimony to Sb_2O_3 and Sb_2O_4 by H_2O is thermodynamically favorable up to 700K as given in Figure D.26. Antimony is more suitable for decreasing the high temperature step.

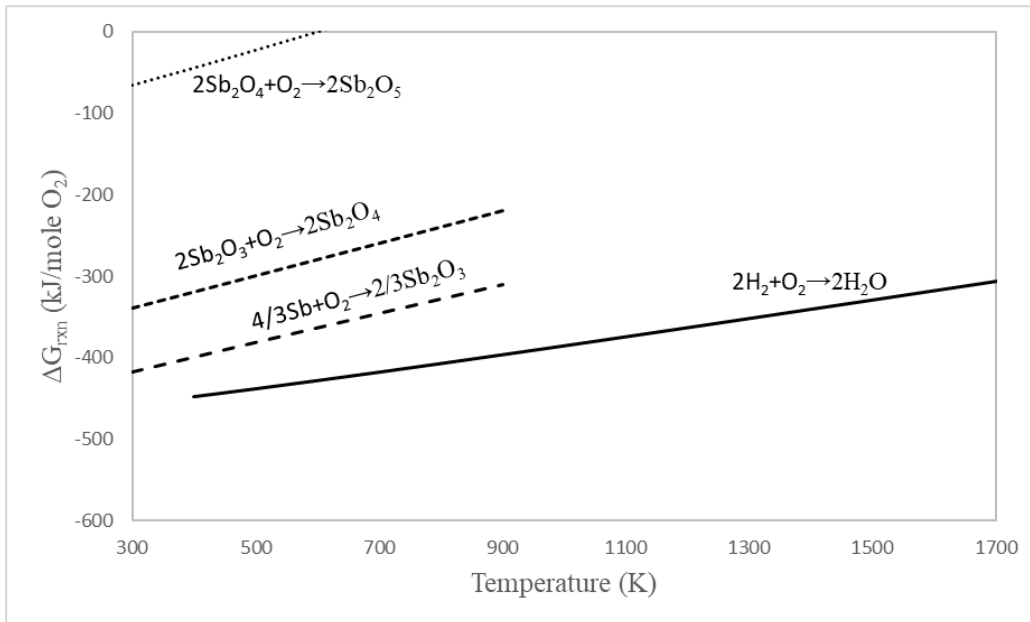


Figure D.26 Ellingham diagram of antimony

Scandium, Selenium, Silicon and Samarium: Relative oxidation strength of scandium, selenium, silicon and samarium is shown in Figure D.27. The data available for selenium is limited to 600K so that it is hard to say about the suitability of selenium in thermochemical processes. Scandium, silicon and samarium oxidation by H_2O is thermodynamically favorable between 300 and 1700K. Sc_2O_3 , SiO_2 and Sm_2O_3 should be used as support material due to high oxide stability.

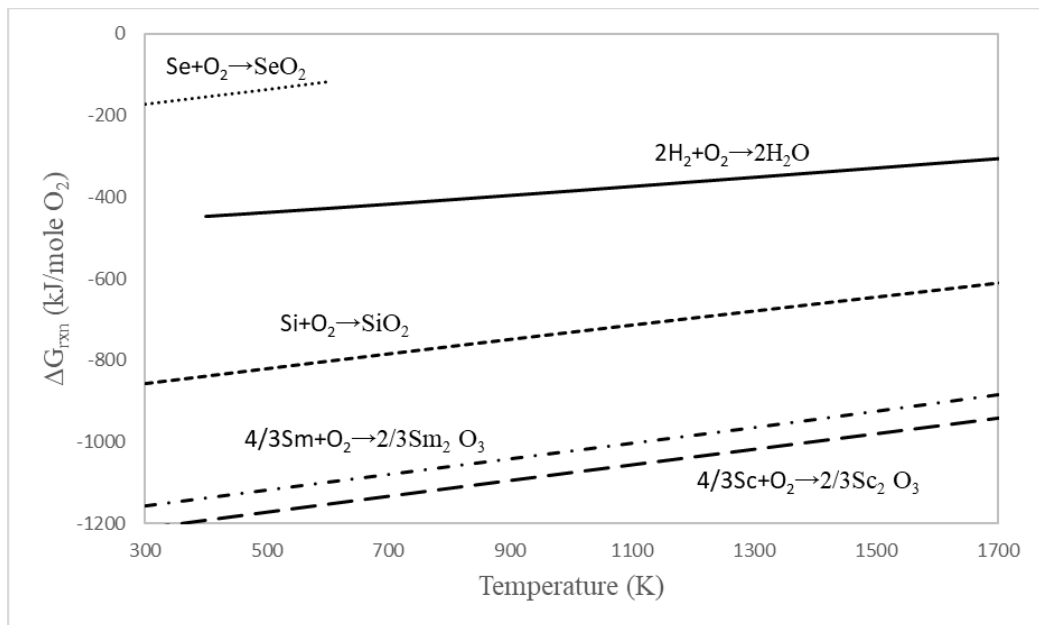


Figure D.27 Ellingham diagram of scandium, selenium, silicon and samarium

Tin: The reaction Gibbs free energy lines of $Sn \rightleftharpoons SnO$ and $SnO \rightleftharpoons SnO_2$ are almost same as shown in Figure D.28. One should be careful about the behavior of tin since it can be fully oxidized to SnO_2 by H_2O between 300 and 1700K as well as SnO_2 can be thermally decomposed to Sn which has low melting point. Tin is suitable for water splitting processes.

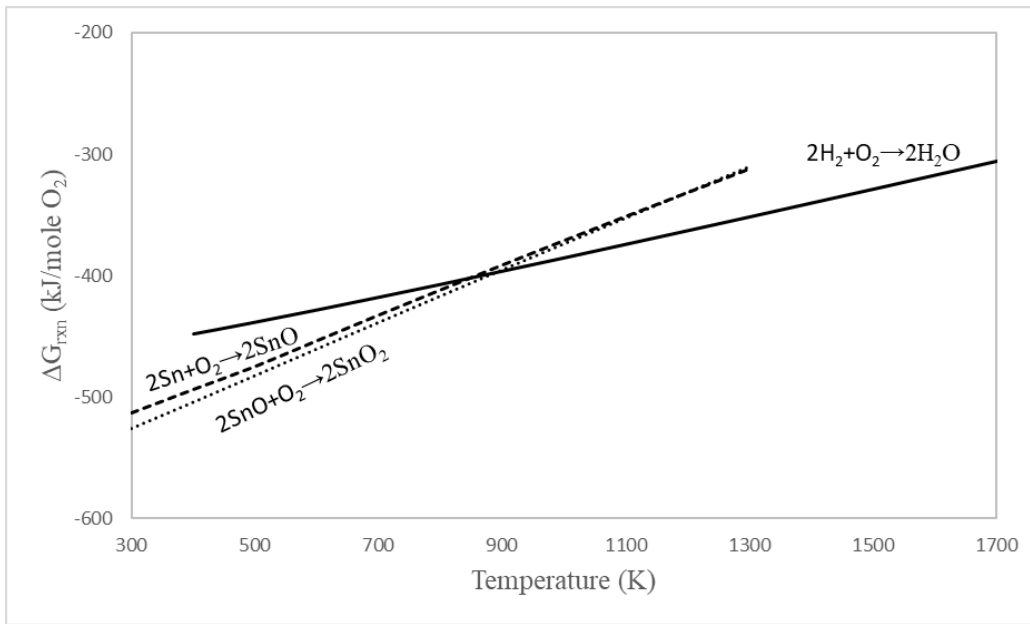


Figure D.28 Ellingham diagram of tin

Strontium: Relative oxidation strength of strontium is shown in Figure D.29. The thermodynamic decomposition temperature of SrO_2 to SrO is around 460K. Strontium can be easily oxidized by H_2O between 300 and 1700K. Strontium is suitable for thermochemical processes as well as a support material.

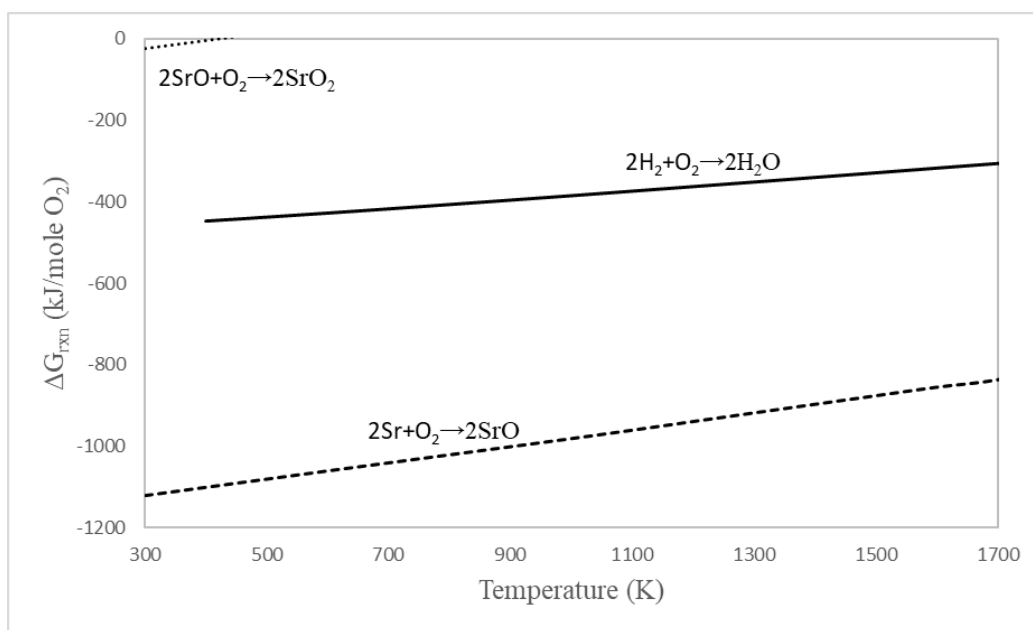


Figure D.29 Ellingham diagram of strontium

Tantalum and Terbium: Thermodynamic driving force towards oxidation of tantalum and terbium is shown in Figure D.30. In the reference book [294], the intermediate oxidation states of tantalum could not be find. Therefore, oxidation of $Ta \rightleftharpoons Ta_2O_5$ is taken into consideration. The oxidation of tantalum by H_2O is thermodynamically favorable in the studied temperature range. The thermodynamic decomposition temperature of TbO_2 to Tb_2O_3 is around 860K. Further reduction seems unfeasible due to the oxide stability of Tb_2O_3 . Terbium is easily oxidized to Tb_2O_3 by H_2O between 300 and 1700K. Tantalum is used for thermochemical processes while terbium has a high potential for use as a support material

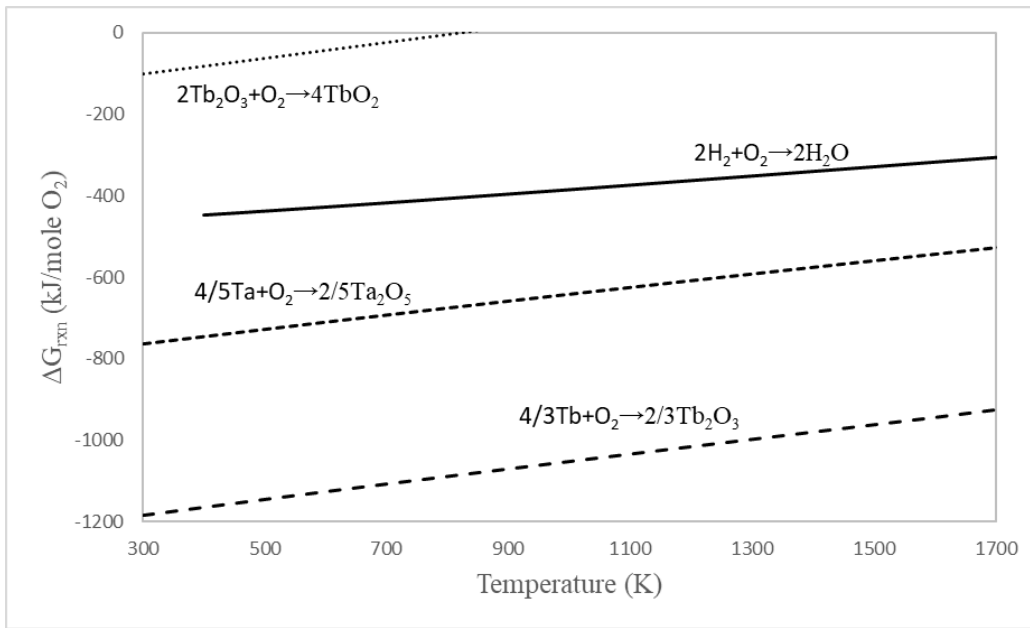


Figure D.30 Ellingham diagram of tantalum and terbium

Thallium and Tellurium: Thallium and tellurium are suitable for decreasing the decomposition temperature of solar thermal hydrogen production as in Figure D.31.

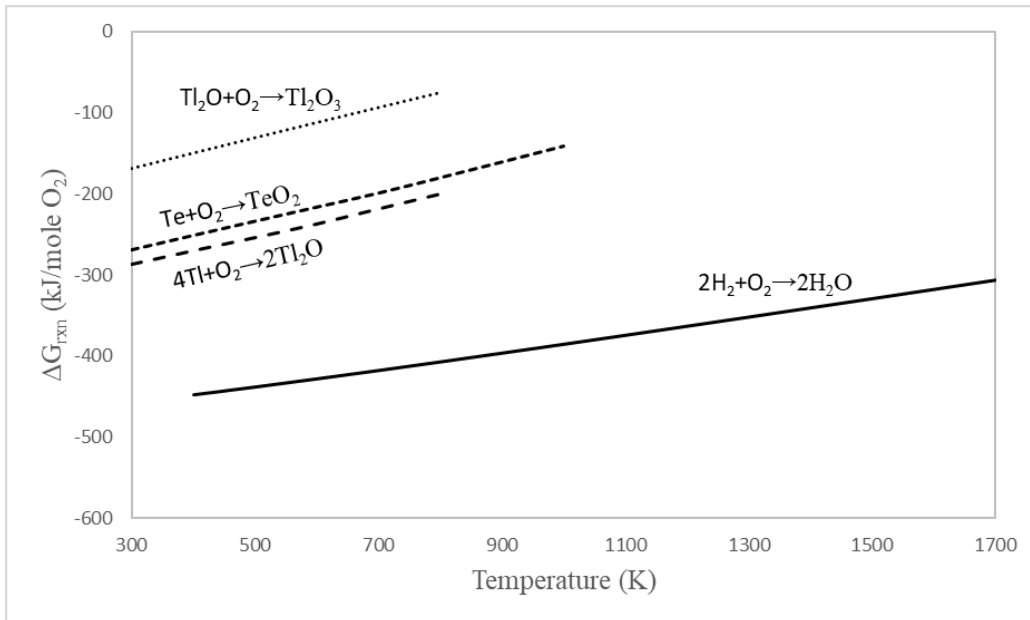


Figure D.31 Ellingham diagram of thallium and tellurium

Titanium: Relative oxidation strength of titanium is demonstrated in Figure D.32. The multiple oxidation steps of titanium offer an advantage during the water splitting reaction. Thermodynamic favorability of these transformations changes up to 900K. Therefore, one should be careful about the change in the intermediate oxidation states. The oxidation of titanium by H₂O is favorable between 300 and 1700K. Titanium can be used for thermochemical processes.

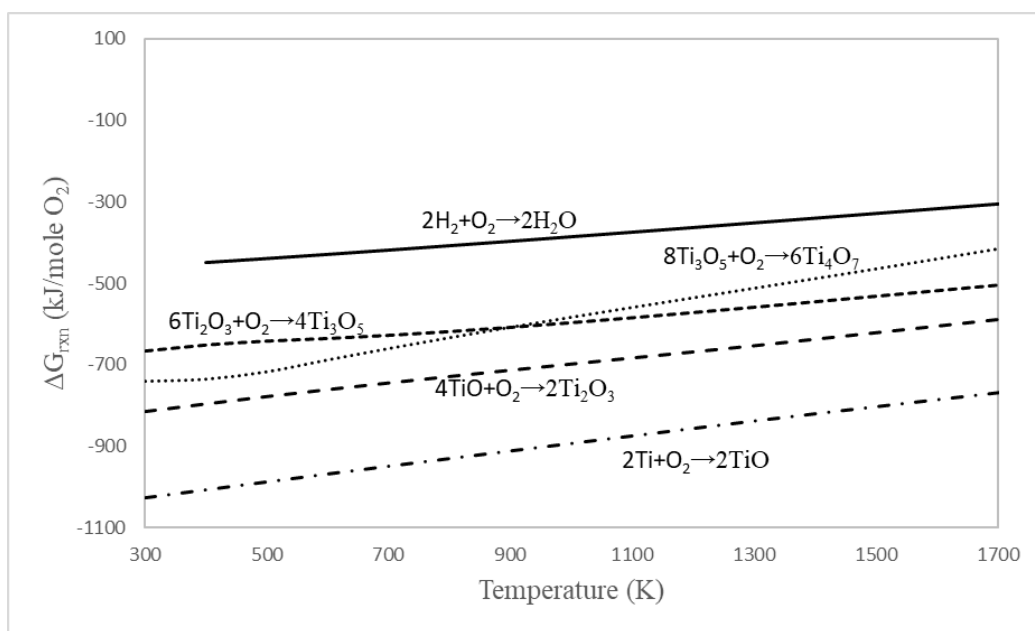


Figure D. 32 Ellingham diagram of titanium

E. Coke Removal Algorithm

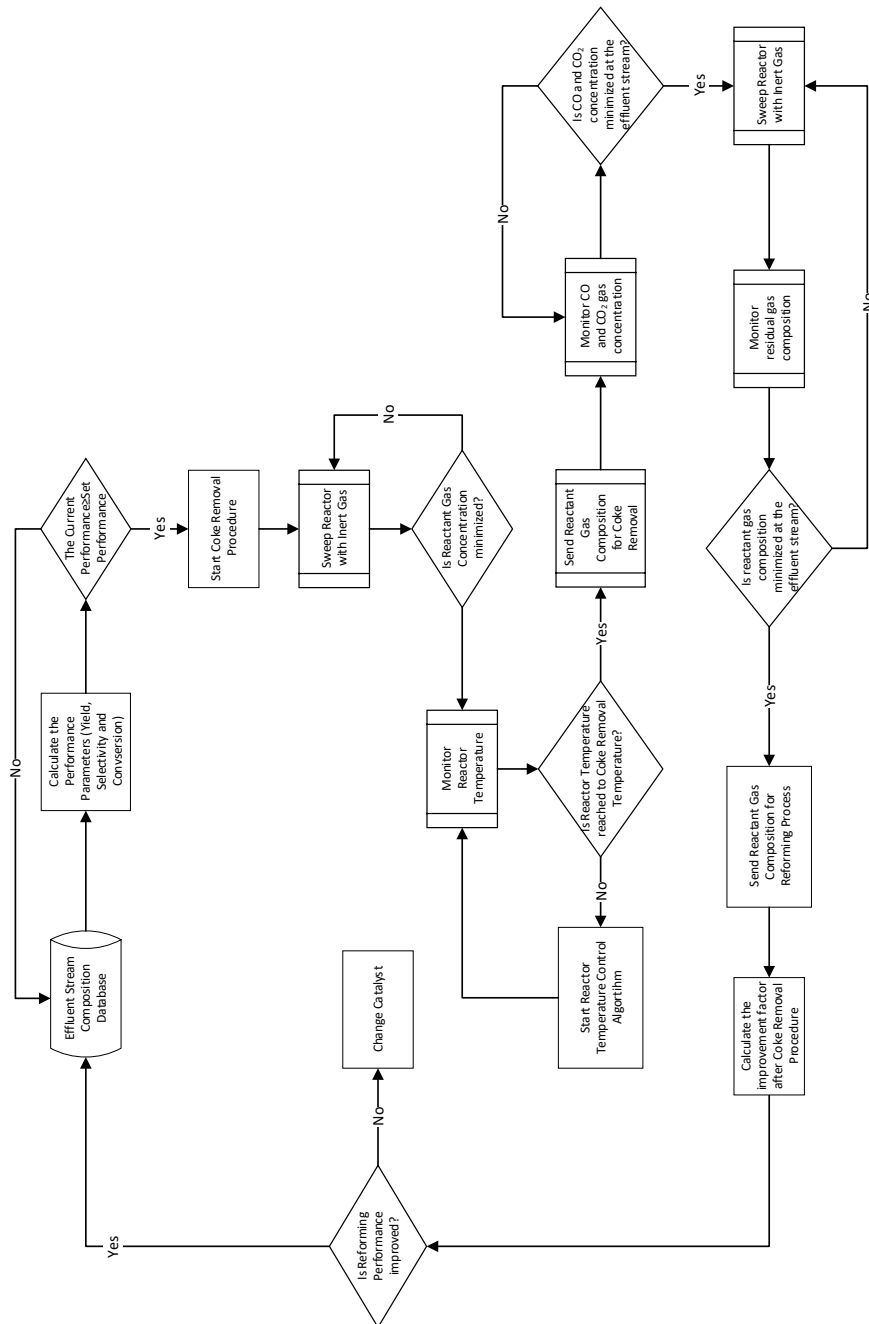


Figure E.1 Main control algorithm for coke removal

Coke formation is an inevitable event for reforming reaction. In the proposed plant, online coke removal algorithm is added to the process control algorithm as given in Figure E.1. This algorithm monitors the product gas composition and calculates the reforming performance continuously. Depending on the minimum performance criteria, the coke removal sequence is started. In Figure E.1, coke removal by oxidation is proposed. However, the coke removal can also be performed by increasing the steam concentration in the system also. Coke removal sequence is finished by tracking effluent stream in terms of CO and CO₂. After those gases in the effluent stream is minimized, system operates a control reforming reaction in order to calculate the improvement factor. This factor mainly measures the reforming efficiency and calculates the enhancement. Depending on the scale of improvement factor, plant starts to operate or shutdown for a catalyst change process

CURRICULUM VITAE

PERSONAL INFORMATION

Surname, Name : Çalışan, Atalay
Nationality : Turkish (TC)
Date and Place of Birth : 4 August 1987, Bursa
Phone : +90 543 409 55 78
E-mail : atalaycalisan@hotmail.com

EDUCATION

Degree	Institution	Year of Graduation
MS	METU, Chemical Engineering, Ankara, Turkey	2013
BS	METU, Petroleum and Natural Gas Engineering (Double Major), Ankara, Turkey	2011
BS	METU, Chemical Engineering, (Major) Ankara, Turkey	2010
High School	Bursa Erkek High School, Bursa	2005

WORK EXPERIENCE

Year	Place	Enrollment
2019-Present	TRL Instruments	Process Engineer
2017-Present	Talassa Ltd.	Director
2011-2017	METU Chemical Engineering	Research and Teaching Assistant

FOREIGN LANGUAGES

Advanced English

PUBLICATIONS

1. A. Calisan, TÜPRAŞ Rafinerici Yetiştirme Programı, Baz Yağ Üretim Tesisi, TÜRKİYE: TÜPRAŞ, 01 Aralık 2016, Book
2. A. Calisan, TÜPRAŞ Rafinerici Yetiştirme Programı, İzomerizasyon Ünitesi, TÜRKİYE: TÜPRAŞ, 01 Aralık 2016, Book
3. A. Calisan, C. G. Ogulgonen, A. Yilmaz, S. Kincal, D. Uner, Steam Methane Reforming over structured reactors under concentrated solar irradiation, , International Journal of Hydrogen Energy, Volume 44, Issue 34, 12 July 2019, Pages 18682-18693
4. A. Calisan, C. G. Ogulgonen, S. Kincal, D. Uner, Finding the optimum between volatility and cycle temperatures in solar thermochemical hydrogen production: Pb/PbO pair, International Journal of Hydrogen Energy, Volume 44, Issue 34, 12 July 2019, Pages 18671-18681
5. T. Tabari, D. K. Singh, A. Calisan, M. Ebadi, H. Tavakkoli & B. Caglar, Microwave Assisted Synthesis Of La-1 (-) Xcaxmno3 (x=0, 0.2 And 0.4): Structural And Capacitance Properties, CERAMICS INTERNATIONAL, 2017, 0272-8842, 43, 17, 15970-15977.

HOBBIES

Computer Technologies, Movies, Sports